

Evaluating DEM results with FEM perspectives
of load – soil interaction

Promotor: Prof. ir. U. D. Perdok
Hoogleraar in de Bodemtechnologie

Co – promotor: Dr. ir. A. J. Koolen
Universitair hoofddocent,
Leerstoelgroep Bodemtechnologie

Samenstelling
Promotiecommissie: Prof. R. Horn, Christian Albrechts Universiteit, Duitsland
Prof. dr. ir. R. A. Feddes, Wageningen Universiteit
Prof. dr. agr. J. Mueller, Wageningen Universiteit
Dr. ir. J. D. Stigter, Wageningen Universiteit

Het onderzoek is uitgevoerd bij de onderzoekschool Production Ecology and Resource Conservation

Evaluating DEM results with FEM perspectives of load – soil interaction

Dawit Tadesse

Proefschrift

ter verkrijging van de graad van doctor
op gezag van de rector magnificus
van Wageningen Universiteit,
prof. dr. ir. L. Spielman
in het openbaar te verdedigen
op woensdag 23 juni 2004
des namiddags te 16.00 uur in de Aula.

Tadesse, D.

Evaluating DEM results with FEM perspectives of load – soil interaction.

Dissertation Wageningen University – With ref. – With summaries in English and Dutch.

ISBN 90-8504-011-6

To my family Etete, Chally, Enu and Gelila

ABSTRACT

For researchers concerned with soil compaction, soil structure is assessed by indirect measurement of parameters related to soil mechanical properties. In this study the mechanical properties of soil are investigated for the dynamic load – soil interaction of tyre – soil systems, tool penetration, shearing and soil cutting by a pendulum type machine. The methods selected for analyses are the Finite Element Method (FEM) and the Distinct Element Method (DEM). The dynamic module of Plaxis (a special purpose finite element program released in 2000), is more advanced than the previous version of Plaxis. In Plaxis calculations, the Mohr – Coulomb model is selected for deformable soil and the Cam – Clay type model is selected for compactable soil properties. Results of these model studies are presented briefly for the above load – soil interactions. Although the dynamic module of Plaxis performs better, the problems of analysing the discontinuous properties of soil such as shearing (sliding), cutting and cracking (fracturing) still remain unsolved due to the continuous nature of the medium. In such cases, representing soil as a discontinuous medium as in DEM is more realistic.

In DEM, soil is an assembly of discrete particles (discontinuous medium) with the possibility of cyclic contact and failure, by updating contact interactions throughout the simulation. The appropriate models selected are: the original DEM for cohesionless particles and the modified Kyoto DEM in which the adhesion force between particles is considered.

The simulation results show that the mechanical properties of the particles are dependent on the micromechanics of deformation. Shear stress and failure appear largely to be influenced by interparticle sliding and rolling. Sliding contacts are always greater for the low values of interparticle friction coefficient. If this value is sufficiently high, especially for coarse and medium granular particles sliding will be very low and rolling of particles dominates the system which results in low shear stress values. Moreover the contact stiffness and the particle size have an important influence on the deformation mechanisms. For instance, for coarse and medium granular particles, soft stiffness shows compaction whereas hard stiffness shows dilatancy during the shearing process. In the simulation of soil cutting by a pendulum type machine adhesive particles are displaced more or less together by forming soil clods. The deformation behaviour of particles and the crack propagation during the cutting process are significantly affected by the adhesion coefficient between particles, the interparticle friction coefficient and the particle size.

In our simulation, parameter analyses were performed by varying the most relevant model inputs. Normal and tangential stiffness between particles, interparticle friction coefficient, adhesion coefficient between particles and particle size turned out to be the most influential input parameters. Finally results from this simulation are qualitatively compared with those of Plaxis and also some similar laboratory test results reviewed from literature are selected for benchmarking. By evaluating the model results using comparisons, the potential capability of the DEM model on showing the actual soil properties during the above load – soil interaction could be approved.

Keywords: Load – soil interaction, soil structure, soil mechanical properties, FEM (Finite Element Method), Plaxis (Finite Element Code), granular particles, shear stress, DEM (Distinct Element Method), micromechanics of deformation, interparticle friction coefficient

CONTENTS

| | | |
|------------|--|-----------|
| I | BACKGROUND | 1 |
| II | OBJECTIVES OF THE RESEARCH | 3 |
| III | OUTLINE OF THE THESIS | 3 |
| IV | ACKNOWLEDGEMENT | 5 |
| 1 | FINITE ELEMENT METHOD (FEM) | 7 |
| 1.1 | Introduction | 7 |
| 1.2 | Basic steps in a finite element analysis | 7 |
| 1.3 | stresses and equilibrium | 10 |
| 1.3.1 | displacement and strains (compatibility) | 12 |
| 1.3.2 | Stress and strain relations | 13 |
| 1.4 | Constitutive models for agricultural soil | 18 |
| 1.4.1 | Elastic models | 18 |
| 1.4.1.1 | Linear elastic model | 18 |
| 1.4.1.2 | Non – linear elastic model | 19 |
| 1.4.2 | Plastic models | 20 |
| 1.4.2.1 | Rigid, perfectly plastic models | 21 |
| 1.4.2.2 | Elasto – plastic models | 21 |
| 2 | PLAXIS FOR DYNAMIC LOADING | 25 |
| 2.1 | Introduction | 25 |
| 2.2 | The dynamic module used in Plaxis | 25 |
| 2.2.1 | Finite element discretisation | 26 |
| 2.2.2 | Interface elements | 26 |
| 2.2.3 | Boundary conditions | 27 |
| 2.2.4 | The dynamic calculation | 28 |
| 2.2.4.1 | Time integration | 28 |
| 2.2.4.2 | Time step | 30 |
| 2.3 | Soil material models | 30 |
| 2.3.1 | Mohr – Coulomb model | 30 |
| 2.3.1.1 | Parameters of the Mohr – Coulomb model | 33 |
| 2.3.2 | Cam – Clay type model | 34 |
| 2.3.2.1 | Parameters of the Cam – Clay type model | 37 |
| 2.4 | User related characteristics of the FEM models | 38 |
| 2.4.1 | The input step | 38 |
| 2.4.1.1 | Geometry | 39 |
| 2.4.1.2 | Material properties | 40 |
| 2.4.1.3 | Mesh generation | 40 |
| 2.4.1.4 | Initial conditions | 40 |
| 2.4.2 | The calculation step | 41 |
| 2.4.2.1 | Selecting the dynamic analysis | 41 |
| 2.4.2.2 | Selecting points for curves | 41 |
| 2.4.2.3 | Execution of the calculation process | 42 |
| 2.4.3. | The output step | 42 |
| 2.4.3.1 | Deformed mesh | 42 |
| 2.4.3.2 | Total stress | 42 |

| | | |
|----------|--|------------|
| 3 | ANALYSIS OF MODELLING DYNAMIC LOADING CASES IN PLAXIS | 45 |
| 3.1 | Introduction | 45 |
| 3.2 | Soil material properties used for the Mohr – Coulomb model | 45 |
| 3.3 | Soil material properties used for the Cam – Clay type model | 46 |
| 3.4 | Modelling tyre – soil system | 46 |
| 3.4.1 | Creating a geometry model | 46 |
| 3.4.2 | Basic calculation | 47 |
| 3.4.3 | Figures presenting calculation results | 48 |
| 3.4.3.1 | Using the Mohr – Coulomb model | 48 |
| 3.4.3.2 | Using the Cam – Clay type model | 55 |
| 3.4.4 | General discussion and conclusion | 62 |
| 3.4.4.1 | Dynamic tyre – soil system | 62 |
| 3.4.4.2 | Basic conclusion | 65 |
| 3.5 | Modelling wedge penetration test | 66 |
| 3.5.1 | Creating a geometry model | 67 |
| 3.5.2 | Basic calculation | 68 |
| 3.5.3 | Figures presenting calculation results | 69 |
| 3.5.3.1 | Using the Mohr – Coulomb model | 69 |
| 3.5.3.2 | Using the Cam – Clay type model | 73 |
| 3.5.4 | General discussion and conclusion | 77 |
| 3.5.4.1 | Penetration of Wageningen clay soil | 77 |
| 3.5.4.2 | Penetration of Silty loam soil | 80 |
| 3.5.4.3 | Basic conclusion | 81 |
| 3.6 | Modelling shear box test in Plaxis | 82 |
| 3.6.1 | Creating a geometry model | 82 |
| 3.6.2 | Basic calculation | 83 |
| 3.6.3 | Figures presenting calculation results | 84 |
| 3.6.3.1 | Using the Mohr – Coulomb model | 84 |
| 3.6.3.2 | Using the Cam – Clay type model | 88 |
| 3.6.4 | Discussion and conclusion | 90 |
| 3.7 | Modelling soil block cutting by a pendulum type machine | 91 |
| 3.7.1 | Creating a geometry model | 91 |
| 3.7.2 | Basic calculation | 92 |
| 3.7.3 | Figures presenting calculation results | 93 |
| 3.7.4 | Discussion and conclusion | 96 |
| 3.8 | Accuracy of FEM results according to benchmark evaluation | 97 |
| 3.8.1 | Elastic benchmark problems | 97 |
| 3.8.1.1 | Example ‘footing’ | 97 |
| 3.8.2 | Plastic benchmark problems | 98 |
| 3.8.2.1 | Example ‘cavity’ | 98 |
| 3.8.3 | Validation for agricultural soil properties | 99 |
| 4 | EXPERIMENTAL RESULTS | 101 |
| 4.1 | Analysis of soil cutting by a pendulum type machine | 101 |
| 4.1.1 | Introduction | 101 |
| 4.1.2 | Soil properties and the experimental set up | 101 |
| 4.1.2.1 | Soil properties used in the experiment | 101 |
| 4.1.2.2 | The experimental set-up | 103 |
| 4.1.3 | Results and discussion | 103 |
| 4.1.3.1 | The pendulum motion and absorbed energy during the cutting process | 103 |
| 4.1.3.2 | Crack formation during the cutting process | 105 |
| 4.1.3.3 | Motion of soil particles during the cutting process | 105 |
| 4.1.4 | Conclusion | 107 |

| | | |
|----------|--|------------|
| 4.2 | Analysis of dynamic tyre – soil system under field conditions and laboratory experiments | 108 |
| 4.2.1 | Introduction | 108 |
| 4.2.2 | Field experiments | 108 |
| 4.2.2.1 | Materials and methods | 108 |
| 4.2.2.2 | Results and discussion | 109 |
| 4.2.3 | Laboratory experiments | 109 |
| 4.3 | Laboratory experiments of the shear box test | 110 |
| 4.3.1 | Introduction | 110 |
| 4.3.2 | Materials and methods | 110 |
| 4.3.3 | Results and discussion | 111 |
| 5 | DISTINCT ELEMENT MODELLING (DEM) | 113 |
| 5.1 | Introduction | 113 |
| 5.2 | Granular materials and their structure | 114 |
| 5.2.1 | Description of contact between discs (particles) | 115 |
| 5.2.1.1 | The force displacement law and equations of particle motion | 116 |
| 5.2.1.2 | Numerical stability | 120 |
| 5.3 | Principles of DEM calculation | 120 |
| 5.4 | Review of the DEM models | 121 |
| 5.4.1 | Review contact models of particles in DEM | 122 |
| 5.4.2 | Review initial structure of particles in DEM | 126 |
| 5.5 | Selection of appropriate DEM models | 129 |
| 5.5.1 | The force – displacement equations implemented in the selected DEM models | 130 |
| 5.6 | The <i>Kyoto</i> DEM program | 133 |
| 5.6.1 | The C programming language | 133 |
| 5.6.1.1 | Main steps in creating the <i>Kyoto DEM</i> program | 134 |
| 5.6.1.2 | User related characteristics of the <i>Kyoto DEM</i> program | 135 |
| I | <i>Shear box test</i> | 135 |
| II | <i>Soil cutting by pendulum type machine</i> | 139 |
| 6 | SIMULATION OF SHEAR BOX TEST AND SOIL CUTTING BY PENDULUM TYPE MACHINE USING <i>KYOTO DEM</i> | 143 |
| 6.1 | Simulation of shear box test | 143 |
| 6.1.1 | Selection of parameters for the simulation | 144 |
| 6.1.1.1 | The normal stiffness value between particles | 144 |
| 6.1.1.2 | The damping coefficient value between particles | 145 |
| 6.1.2 | Generation and consolidation of the initial sample | 146 |
| 6.1.3 | The shearing process | 147 |
| 6.1.3.1 | Effect of parameter variation on the shearing process | 147 |
| 6.1.4 | Output and discussion of the shear box simulation | 149 |
| 6.1.4.1 | Simulated maximum shear strength of DEM particles | 150 |
| I | <i>Coarse granular particles</i> | 150 |
| II | <i>Medium granular particles</i> | 152 |
| III | <i>Fine granular particles</i> | 153 |
| 6.1.4.2 | Discussion of simulated shear strength | 154 |
| 6.1.4.3 | Discussion of volume change of DEM particles | 156 |
| I | <i>Coarse granular particles</i> | 156 |
| II | <i>Medium granular particles</i> | 157 |
| III | <i>Fine granular particles</i> | 158 |
| 6.1.4.4 | Discussion of micro – mechanics of deformation of DEM particles | 159 |
| 6.1.4.5 | Discussion of failure point of DEM particles | 162 |

| | | |
|----------|---|------------|
| 6.2 | Simulation of soil cutting by a pendulum type machine | 163 |
| 6.2.1 | Generation of the initial sample | 163 |
| 6.2.2 | The cutting process | 164 |
| 6.2.3 | Output and discussion of the cutting process | 165 |
| 7 | DEM RESULTS FROM LITERATURE | 171 |
| 7.1 | Introduction | 171 |
| 7.2 | Simulation of tyre – soil system using DEM | 171 |
| 7.3 | Simulation of penetration test using DEM | 173 |
| 8 | EVALUATION OF DEM RESULTS | 175 |
| 8.1 | Comparison between FEM and DEM results | 175 |
| 8.1.1 | Introduction | 175 |
| 8.1.2 | Model limitations and methods of comparison | 175 |
| 8.1.2.1 | Model limitations | 175 |
| 8.1.2.2 | Methods of comparison | 176 |
| 8.2 | Types of simulation and results selected for comparison | 177 |
| 8.2.1 | Shear box simulation | 177 |
| 8.2.1.1 | Deformation behaviour and particle displacement vectors during shearing | 178 |
| 8.2.1.2 | Shear stresses and failure properties | 180 |
| 8.2.1.3 | Volume change and stiffness | 182 |
| 8.2.2 | Simulation of soil cutting | 185 |
| 8.2.2.1 | Particles displacement direction | 185 |
| 8.2.2.2 | Particles velocity vector | 188 |
| 8.2.3 | Simulation of tyre – soil system | 198 |
| 8.2.3.1 | Vertical stress and volume change | 198 |
| 8.2.4 | Simulation of penetration test | 198 |
| 8.2.4.1 | Resistance force and particle motion during penetration | 198 |
| 8.2.5 | Discussion and conclusion | 202 |
| 9 | GENERAL DISCUSSION AND CONCLUSION | 203 |
| | RECOMMENDATIONS ON FURTHER STUDIES | 205 |
| | SUMMARY | 207 |
| | SYMBOLS | 209 |
| | REFERENCES | 215 |
| | SAMENVATTING | 227 |
| | CURRICULUM VITAE | 231 |

I BACKGROUND

During the last decade granular materials have drawn interest, not only of engineers trying to solve practical problems, but also to physicists, realising that granular matter poses numerous interesting questions of fundamental nature (Thornton, 1993) and to researchers concerned with scientific modelling of granular systems (Williams et al, 1999 and Ferrez et al, 1999). Solving practical problems in real life requires expert knowledge in each of these domains. Granular materials abound in nature, soil is just one of the best examples of it. Granular matter is generally thought of as a simple and unsophisticated form of matter, being just an assembly of discrete macroscopic grains. This discrete assembly of macroscopic grains (soil in this case) can be treated using two basic models (FEM and DEM) when it interacts with different loading systems (for example soil – tool interaction, tyre – soil interaction, etc.).

The Finite Element Method (FEM) is a numerical procedure for solving linear as well as non – linear ordinary and partial differential equations describing physical problems (Zienkiewicz, 1991). The physical problems can be subdivided into static problems in which a state of equilibrium is sought, and dynamic problems in which inertia effects become important (Braja, 1995). In FEM soil is generally modelled as a continuum and represented by a mesh of finite elements. FEM is a powerful tool to approximate solutions especially when the system is too complex to be solved analytically, which usually is the case for non – linear load – soil interaction.

Problems occur with the assumption of soil as a continuum medium due to soil's inherent granular nature and consequent deformation and failure modes. In this case it may be advantageous to treat soil as an assemblage of particles with the ability to break and reform contacts. This discrete particulate modelling was first developed by Cundall (1971 & 1974) for the analysis of rock mechanics by using it to analyse the stability of fractured rock slopes. Even though Cundall pioneered DEM for particles of any shape, Cundall and Strack (1979a & 1979b) extended DEM to soil using 2D discs and 3D spheres to study the structure of granular media during loading.

In DEM soil is represented by assemblies of discs and or spheres with different diameters which is analogous to the most actual soil particle shape. Tanaka et al (2000) presented a simulation of the reaction of tool penetration by representing soil as an assembly of discs with two kinds of diameters in 2D state. In his simulation, discs were randomly distributed and each disc was assumed rigid. An overlap between discs was allowed. This overlap causes a contact force and forces acting on a disc appear only when the disc makes contact with another disc (tool). Furthermore, the magnitudes of forces depend on the relative positions and velocities of the discs to the others. In the DEM model an elastic spring in between discs is introduced in order to estimate the force produced by the adjacent discs.

II OBJECTIVES OF THE RESEARCH

The main aims of this study are given below:

- Analysis of simulation of dynamic loading cases using the more advanced version of FEM (The Dynamic Module of Plaxis, a finite element code for soil and rock deformation analysis) for better understanding of soil mechanical properties during dynamic load – soil interaction
- Extensive review of the available DEM models based on contact modelling and initial arrangement of particles with the knowledge of selecting the appropriate DEM models for application of modelling agricultural soil structure and soil mechanical properties
- Analysis of simulation of agricultural dynamic loading cases using the selected DEM (*Kyoto DEM*) model with the intention of estimating soil mechanical properties from the simulation results
- Evaluating the DEM results from the simulation and from literature review, using the FEM results and some analogous experimental results as benchmarking to show the potential capability of the DEM model for its advantage of modelling granular soil

III OUTLINE OF THE THESIS

Chapter one: deals with the basic concepts of the finite element method (FEM) which includes the basic steps in a finite element analysis i.e. stress – strain relations. The final part of this chapter includes basic models for agricultural soils which are elastic and plastic models. The content of this chapter can be used as stepping stone for the introduction to detailed working principles of Plaxis which are explained in the next chapter.

Chapter two: deals with the basics of the dynamic modules of Plaxis (a finite element code for soil and rock analysis) and includes the two basic soil material models used in the Plaxis calculation, the Mohr – Coulomb and the Cam Clay type models.

Chapter three: deals with modelling some of selected agricultural dynamic loading cases; tyre – soil system, wedge penetration, simple shear test and soil cutting by a pendulum type machine. Analysis of the results and basic conclusions are given at the end of each topic.

Chapter four: deals with analysis of the experimental or laboratory test results of some of the loading cases mentioned in the previous chapter for later use of qualitative comparison of the FEM and DEM results obtained in this thesis.

Chapter five: deals with the basic concepts of the distinct element method (DEM) which include the contact force description and equations of particle motion, the working principles, review of the available DEM models and finally selection of the appropriate DEM models for modelling granular soil which is compatible with structured agricultural soil. The selected DEM models are jointly said to be the Kyoto DEM. The equations of particle motion and a summary of the user related characteristics of this model are also given in the final part of this chapter. The contents of this chapter can be used as the working principle or background information of the simulation given in the next chapter.

Chapter six: deals with analysis of simulation of the two dynamic loading cases (the shear box test and the soil cutting by pendulum type machine) using the *Kyoto DEM* program. Simulation results, discussion of results and basic conclusions are included. Among the output of the shear box simulation, the effect of parameter variation, the simulated shear strength of coarse, medium and fine granular DEM particles, the volume change of these particles, the micromechanics of deformation of these particles and the failure point of these particles during shearing are very important. For simulation of the soil cutting by a pendulum type machine, snapshots of the cutting process with different values of coefficient of adhesion area (C_{ad}) are important.

Chapter seven: deals with analysis of a literature review of the DEM results of a tyre – soil system and a penetration test; some general discussion and conclusion is included. The content of this chapter help for later evaluation of DEM results in the next chapter.

Chapter eight: deals with evaluation of the DEM results; model limitations and methods of comparison are included. Evaluation of DEM results has been carried out for all the available simulations. Results used for comparison are different depending on the type of simulation selected. Results from FEM simulation and from experimental or laboratory tests are used as benchmarking. This evaluation has been done by qualitative comparison of simulation results of the same load – soil interaction.

Chapter nine: deals with general discussion and conclusion, recommendations on further studies and summary of the whole thesis.

IV ACKNOWLEDGEMENT

I humbly give all the glory and honour to my precious LORD JESUS CHRIST for his infinite mercy and grace on my life to reach on this stage of life.

My appreciation goes to Prof. Perdok and Dr. Koolen for their continuous support and guidance during my study. I am also grateful for the Soil Technology group of the department of Agrotechnology and Food science of Wageningen University who sponsored this research.

My appreciation also goes to the Mohammed Yakoubi Foundation for their financial assistance of my accommodation. My special thanks to Dr. Hans Stigter for his help and allowance to use Hamilton account and Unix environment, to Sam Blaauw, Albert Boers, Corrie Seves, Miranda Tap for their kind assistance in my study during my study period. Also to Jan van Bommel, rev. Josine van de Horst and for their help of providing financial assistance from different foundations and church groups.

I am honoured to my family Etete, Chally, Enu and Gelila for their persistent help and encouragement.

1 FINITE ELEMENT METHOD (FEM)

1.1 INTRODUCTION

In all branches of engineering the finite element method is becoming increasingly popular as a method of solving the systems of partial differential equations which describe various physical phenomena (Atkison et al, 1978); (Zienkiewicz, 1991). These equations may describe the deformation of solid bodies, the flow of fluids or almost any effect which can be described by the laws of classical physics.

In the 1950s the basic idea of the FEM originated from the matrix analysis of aeroplane structures in aviation engineering. According to the structure matrix analysis method an entire structure can be considered as an assembly formed by linking many finite mechanical elements together; the function of each element is similar to the role of a brick for a building. In 1960 this idea was extended in solving plane stress problems in elastic mechanics and a terminology of “Finite Element Method” was adopted.

However for a continuum medium which is actually composed of infinite number of elements the FEM can be used only after the continuum medium is discretized in the following manner:

- The continuum medium is divided into a finite number of blocks (elements) which are linked to each other only at certain specified points, nodes;
- Inside each element the displacement distribution is approximated using a simple function and the relation between nodal force and nodal displacement is determined by the variation principle;
- Assembling the nodal force displacement relation of all elements yielding a set of algebra equations with nodal displacement being unknowns. Solving such a set of equations provides the displacement information at a finite number of nodes within the continuum medium, (i.e., the approximate solution to the problem).

1.2 BASIC STEPS IN A FINITE ELEMENT ANALYSIS

Analysis of the Finite Element Method can be generally outlined into the following six steps (Shen et al, 1998); (Zienkiewicz, 1991).

1. Discretization of a system

The discretization of a system is the first step in a finite element analysis. It consists of the following: (1) the domain of a system is divided into a finite number of elements; (2) nodes are set up at specified points on each element; (3) adjacent elements are linked together only through these nodes and (4) the assembly of all elements is used to replace the original system.

2. Determination of a displacement model

After the discretization of a system, the next step is to analyse the characteristics of a typical element.

In order to express displacements, strains and stresses inside an element by using the nodal displacements, a displacement distribution within the element has to be assumed for a problem of continuum medium, that is the displacement in the element is assumed to be a simple function of co – ordinates. This function is called a displacement model or displacement function.

The proper choice of a displacement function is a key step in an entire FEM. Most often a displacement function is chosen as a polynomial because it provides some convenience with regard to mathematical operations such as derivation and integration and it can locally approximate all continuous functions using Taylor series.

The maximum power and total number of terms in a polynomial are chosen on the consideration of the degrees of freedom of elements and the requirement for the solution convergence. Generally speaking, the total number of terms in a polynomial should be equal to the degrees of freedom of an element by counting both constant and linear terms. On the basis of the chosen displacement function, displacements at any point within an element can be expressed by the nodal displacements in the following matrix notation:

$$u_f = Nu \tag{1.1}$$

where

- u_f = the displacement column matrix for any point in an element
- N = a shape function matrix, a function of co-ordinates
- u = nodal displacement column matrix of an element

In the aspect of approximating the displacement distribution in a system, the FEM has obvious advantages over the conventional approximation methods. For example in the classic Ritz method, a function is chosen to describe displacements in an entire system and to satisfy all the boundary conditions, while in the FEM an approximate displacement function is chosen with regard to an element (not the whole system) and such function needs not satisfy the boundary conditions of the entire system except for those at the interconnections with adjacent elements.

3. Analysis of mechanical properties of an element

After the displacement function is determined, it is ready for the analysis of mechanical properties of an element, which mainly includes the following three parts:

1. On the basis of the geometric equation and Equation (1.1) the relation between element strains and nodal displacements is derived as follows:

$$\varepsilon = Bu \tag{1.2}$$

where

- ε = the strain vector at any point in an element
- B = the element strain matrix
- u = nodal displacement column matrix

2. By combining the physical equation and Equation (1.2) the relation between the element stresses and the nodal displacements can be expressed as:

$$\sigma = CBu \quad (1.3)$$

where

σ = the stress vector at any point in an element
 C = a constitutive matrix depending on the material properties of the element

3. With reference to the virtual work principle and after some steps of derivations, the element stiffness equation, i.e., the relation between nodal force f_n and nodal displacement u on an element is expressed as:

$$f_n = ku \quad (1.4)$$

where

f_n = element nodal force column matrix
 k = the element stiffness matrix

4. Calculation of equivalent nodal forces

After a continuum medium is discretized, forces are assumed to pass from one element to another only through the nodes connecting these two elements.

However, the forces in a continuum medium are actually transferred through the common boundary between two adjacent elements. Therefore the surface forces acting on the boundary of an element, volumetric forces as well as concentrated forces on the element are all needed to be equivalently translated to forces acting on the nodes associated to that element. In other words all forces acting on an element are replaced by their equivalent nodal forces. Such replacement is based upon the principle that the virtual work by two types of forces should be the same upon any virtual displacement.

5. Assembly of element stiffness equations and establishment of the equilibrium equations for an entire system

For a simple static problem, the establishment of equilibrium equations include both assembling element stiffness matrices into the global stiffness matrix K and assembling the equivalent nodal force vectors of all elements into the global load column matrix F . The underlying reason for doing the assembly is that for all pairs of adjacent elements, the displacement at a common node is the same.

After K and F are known, the static equilibrium equation for the entire system is:

$$KU = F \quad (1.5)$$

where

K = global stiffness matrix
 U = the column matrix composed of nodal displacements
 F = the global load column matrix caused by external forces acting on the nodes

6. Solution of unknown nodal displacements and calculation of element stresses

In a linear equilibrium problem in which the matrix K is considered constant, algorithms for solving linear equations can be used to solve the unknown displacement column matrix in Equation (1.5).

For a non-linear equilibrium problem with the matrix K being variant, an incremental procedure should be adopted to account for the gradual change of stiffness with stress states and paths. Finally the element stresses are calculated by using Equation (1.3) and the nodal displacements.

1.3 STRESSES AND EQUILIBRIUM

The traditional equations of continuum mechanics need some modification when applied to soils. Some of these modifications are straight forward in nature: for example, the sign convention for stress and strains for most engineering materials, tensile stresses and strains are taken to be positive. Soil mechanics uses the opposite sign convention (i.e., compressive stresses and strains are positive).

The next section sets out the basic definitions and equations for an elastic material using this sign convention. The basic soil stress – strain relation is taken as elastic however soil behaviour is markedly non linear.

Figure 1.1 shows a body of material that is acted on by a number of forces. If the body is in equilibrium then six equations of equilibrium can be written which relate the forces acting on the body to one another.

Three of these equations state that the sum of all the forces in three mutually orthogonal directions is zero. The other three equations state that the sums of the moments of the forces about three orthogonal axes are also zero. If the body is not statically in equilibrium then these equations can be replaced by the appropriate forms of Newton’s second law of motion.

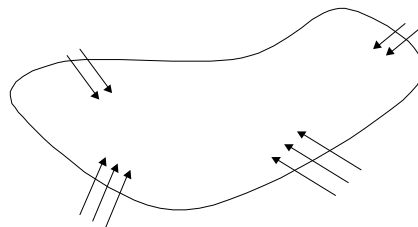


Figure 1.1 Forces acting on a body (Atkison et al, 1978)

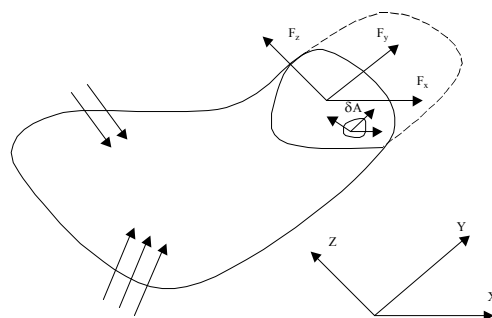


Figure 1.2 Internal forces acting on a body (Atkison et al, 1978)

Figure 1.2 shows a planar cut across a similar body of material. Since the part of the body on either side of the cut must be in equilibrium, there must be internal forces acting in the body (i.e., across the plane) to maintain the state of equilibrium. Using the equations of equilibrium described above, six resultants equivalent to this system of forces can be found.

Considering the forces transmitted across a small area δA inscribed on this plane, it is possible to define a measure of the local intensity of the internal force system. These are of course the internal stresses acting on the material. Taking the plane to be perpendicular to the x -axis internal stresses are obtained.

$$\sigma_x = \lim_{\delta A \rightarrow 0} \left(\frac{-\delta F_x}{\delta A} \right) \quad (1.6)$$

$$\tau_{xy} = \lim_{\delta A \rightarrow 0} \left(\frac{-\delta F_y}{\delta A} \right) \quad (1.7)$$

$$\tau_{xz} = \lim_{\delta A \rightarrow 0} \left(\frac{-\delta F_z}{\delta A} \right) \quad (1.8)$$

While six force resultants were necessary to describe the interaction of the two parts of the body only three stresses are needed to describe the local intensity of forces at one particular point on the surface. This is because the force distribution is considered to be essentially continuous and as the small area δA shrinks in size the force distribution over the area approaches a constant value.

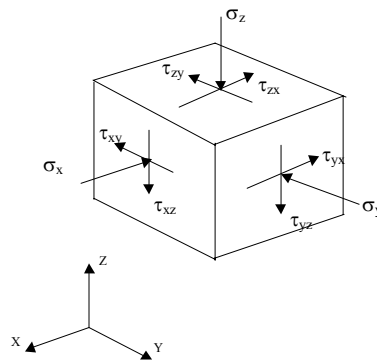


Figure 1.3 Stress components on a soil element

To completely define the state of stress at a point in the material it is necessary to consider the internal forces acting on three mutually perpendicular planes through the point. Thus stress components σ_y , τ_{yx} and τ_{yz} act on a plane perpendicular to the y axis and stress components σ_z , τ_{zx} and τ_{zy} act on a plane perpendicular to the z axis. Considering the equilibrium of an infinitesimal cube of material (Fig. 1.3) for τ

$$\tau_{xy} = \tau_{yx}; \quad \tau_{yz} = \tau_{zy}; \quad \tau_{zx} = \tau_{xz}$$

Hence there are six independent components of stress at a point in the material. Usually the state of a stress in a body is not constant but varies from point to point. Considering the equilibrium of an infinitesimal cube of material in a varying stress field, the following equations are obtained:

$$\frac{\partial \sigma_x}{\partial x} + \frac{\partial \tau_{yx}}{\partial y} + \frac{\partial \tau_{zx}}{\partial z} = f_x \quad (1.9)$$

$$\frac{\partial \tau_{xy}}{\partial x} + \frac{\partial \sigma_y}{\partial y} + \frac{\partial \tau_{zy}}{\partial z} = f_y \quad (1.10)$$

$$\frac{\partial \tau_{xz}}{\partial x} + \frac{\partial \tau_{yz}}{\partial y} + \frac{\partial \sigma_z}{\partial z} = f_z \quad (1.11)$$

where

f_x , f_y and f_z = body forces in the directions of the x , y and z axis respectively.

1.3.1 DISPLACEMENT AND STRAINS (COMPATIBILITY)

When a material is strained a typical point with co – ordinates (x,y,z) moves to a new position $(x+u, y+v, z+w)$. Except for the case when the body is given a rigid body translation the displacements u , v and w will vary across the body (i.e., they will each be functions of x , y and z). Figure 1.4 shows three infinitesimal fibres of length δx , δy and δz in a material and their new locations following straining.

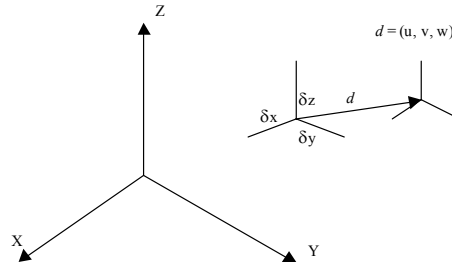


Figure 1.4 Definition of displacements

The principal strains ϵ_{xx} , ϵ_{yy} and ϵ_{zz} and the shear strains γ_{xy} , γ_{yz} and γ_{zx} are given by

$$\epsilon_{xx} = \frac{\partial u}{\partial x} \quad (1.12)$$

$$\epsilon_{yy} = \frac{\partial v}{\partial y} \quad (1.13)$$

$$\epsilon_{zz} = \frac{\partial w}{\partial z} \quad (1.14)$$

$$\gamma_{xy} = \frac{-\partial v}{\partial x} + \frac{-\partial u}{\partial y} \quad (1.15)$$

$$\gamma_{yz} = \frac{-\partial w}{\partial y} + \frac{-\partial v}{\partial z} \quad (1.16)$$

$$\gamma_{zx} = \frac{-\partial u}{\partial z} + \frac{-\partial w}{\partial x} \quad (1.17)$$

A more expressed notation is tensorial shear strains defined by:

$$\varepsilon_{ij} = -\frac{1}{2} \left(\frac{\partial u_i}{\partial x_j} + \frac{\partial u_j}{\partial x_i} \right) \quad (i, j = x, y, z) \quad (1.18)$$

$$\varepsilon = -\frac{1}{2} \begin{bmatrix} \varepsilon_{xx} & \varepsilon_{xy} & \varepsilon_{xz} \\ \varepsilon_{xy} & \varepsilon_{yy} & \varepsilon_{yz} \\ \varepsilon_{xz} & \varepsilon_{yz} & \varepsilon_{zz} \end{bmatrix}$$

Note that a side effect of reversing the normal sign convention for strains is that a positive shear strain γ_{xy} corresponds to an increase in the angle between two fibres initially aligned with the x and y axes.

1.3.2 STRESS – STRAIN RELATIONS

The displacement of a body may be a consequence of deformation, rigid body motion or some combination of both. The deformation is described by the strain which is of two classes: engineering strain and tensorial shear strain as defined by Equations (1.12) to (1.17) and (1.18). If elastic material is stressed in the x direction by a direct stress σ_x then it experiences strains

$$\varepsilon_x = \frac{\sigma_x}{E} \quad (1.19)$$

$$\varepsilon_y = \frac{-\nu\sigma_x}{E} \quad (1.20)$$

$$\varepsilon_z = \frac{-\nu\sigma_x}{E} \quad (1.21)$$

$$\gamma_{xy} = \frac{\tau_{xy}}{E} 2(1+\nu) \quad (1.22)$$

where

E = Young's modulus of the material; ν = the Poisson's ratio;
 τ_{xy} = shear stress; σ_x = stress in x – direction; γ_{xy} = shear strain

The effects of three direct stresses and shear stresses can be superposed to give the generalised form of Hook's law:

$$\varepsilon_x = \frac{\sigma_x}{E} - \nu \frac{\sigma_y}{E} - \nu \frac{\sigma_z}{E} \quad (1.23)$$

$$\varepsilon_y = \frac{-\nu\sigma_x}{E} + \frac{\sigma_y}{E} - \frac{\nu\sigma_z}{E} \quad (1.24)$$

$$\varepsilon_z = \frac{-\nu\sigma_x}{E} - \frac{\nu\sigma_y}{E} + \frac{\sigma_z}{E} \quad (1.25)$$

$$\gamma_{xy} = \frac{\tau_{xy}}{E} 2(1+\nu) \quad (1.26 \text{ a})$$

$$\gamma_{yz} = \frac{\tau_{yz}}{E} 2(1+\nu) \quad (1.26 \text{ b})$$

$$\gamma_{zx} = \frac{\tau_{zx}}{E} 2(1+\nu) \quad (1.26 \text{ c})$$

These equations can be written in matrix form:

$$\begin{bmatrix} \varepsilon_x \\ \varepsilon_y \\ \varepsilon_z \\ \gamma_{xy} \\ \gamma_{yz} \\ \gamma_{zx} \end{bmatrix} = \begin{bmatrix} 1/E & -\nu/E & -\nu/E & 0 & 0 & 0 \\ -\nu/E & 1/E & -\nu/E & 0 & 0 & 0 \\ -\nu/E & -\nu/E & 1/E & 0 & 0 & 0 \\ 0 & 0 & 0 & 1/G & 0 & 0 \\ 0 & 0 & 0 & 0 & 1/G & 0 \\ 0 & 0 & 0 & 0 & 0 & 1/G \end{bmatrix} \begin{bmatrix} \sigma_x \\ \sigma_y \\ \sigma_z \\ \tau_{xy} \\ \tau_{yz} \\ \tau_{zx} \end{bmatrix}$$

where $G = \frac{E}{2(1+\nu)}$, is the elastic shear modulus.

The above relations can be inverted to give stresses in terms of strains:

$$\begin{bmatrix} \sigma_x \\ \sigma_y \\ \sigma_z \\ \tau_{xy} \\ \tau_{yz} \\ \tau_{zx} \end{bmatrix} = \frac{E}{(1-2\nu)(1+\nu)} \begin{bmatrix} 1-\nu & \nu & \nu & 0 & 0 & 0 \\ \nu & 1-\nu & \nu & 0 & 0 & 0 \\ \nu & \nu & 1-\nu & 0 & 0 & 0 \\ 0 & 0 & 0 & 1/2-\nu & 0 & 0 \\ 0 & 0 & 0 & 0 & 1/2-\nu & 0 \\ 0 & 0 & 0 & 0 & 0 & 1/2-\nu \end{bmatrix} \begin{bmatrix} \varepsilon_x \\ \varepsilon_y \\ \varepsilon_z \\ \gamma_{xy} \\ \gamma_{yz} \\ \gamma_{zx} \end{bmatrix}$$

The above relation is written in matrix notation:

$$\sigma = D\varepsilon \quad (1.27)$$

where

σ = total stress; D = stiffness matrix; ε = total strain

Principal stresses

A principal stress is defined as the normal stress on a plane in which the shear stress has vanished. Such a plane is called principal plane. In three dimensions it is always possible to rotate the co – ordinate system in such a way that there are three mutually perpendicular planes found such that all three shear stresses are simultaneously zero and there only remain three principal stresses with their principal directions.

Consider the stress σ in an original $x - y - z$ co – ordinate system is transformed into σ' in another $x' - y' - z'$ system by

$$\sigma' = T\sigma T^T \quad (1.28 a)$$

$$T = \begin{bmatrix} \cos(x, x') & \cos(y, x') & \cos(z, x') \\ \cos(x, y') & \cos(y, y') & \cos(z, y') \\ \cos(x, z') & \cos(y, z') & \cos(z, z') \end{bmatrix} \quad \text{in 3D} \quad (1.28 b)$$

$$T = \begin{bmatrix} \cos(x, x') & \cos(y, x') \\ \cos(x, y') & \cos(y, y') \end{bmatrix} \quad \text{in 2D} \quad (1.28 c)$$

where

T = the rotational matrix consisting of the direction cosines between two co – ordinate systems

The angle between two arbitrary co-ordinates is represented by parenthesis enclosing the corresponding co – ordinate labels separated by a comma as shown in Figure 1.5

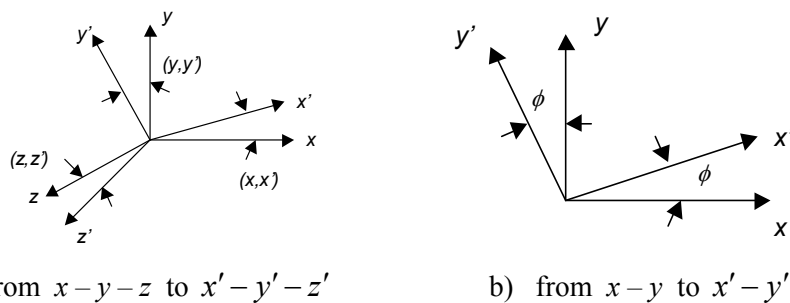


Figure 1.5 Rotation of co-ordinates , a) 3D and b) 2D

According to the matrix theory , a specific set of rotations of co – ordinates exists such that σ' becomes:

$$\sigma' = \begin{bmatrix} \sigma_1 & 0 & 0 \\ 0 & \sigma_2 & 0 \\ 0 & 0 & \sigma_3 \end{bmatrix}$$

where

σ_1 , σ_2 , and σ_3 = principal stresses

The magnitudes of principal stresses become:

$$\sigma_{1,2} = \frac{\sigma_{xx} + \sigma_{yy}}{2} \pm \sqrt{\left(\frac{\sigma_{xx} - \sigma_{yy}}{2}\right)^2 + \sigma_{xy}^2} \quad (1.29)$$

Principal strains

The magnitudes of principal strains in two dimensional cases are:

$$\varepsilon_{1,2} = \frac{\varepsilon_{xx} + \varepsilon_{yy}}{2} \pm \sqrt{\left(\frac{\varepsilon_{xx} - \varepsilon_{yy}}{2}\right)^2 + \varepsilon_{xy}^2} \quad (1.30)$$

Volumetric strain

The definition of volumetric strain is as follows:

$$\varepsilon_{vol} = \frac{\Delta V}{V} = \varepsilon_{xx} + \varepsilon_{yy} + \varepsilon_{zz} = 3\varepsilon_{oct} \quad (1.31)$$

Octahedral stresses

Octahedral stresses refer to the stresses on an octahedral plane which can be easily determined in the σ_1 - σ_2 - σ_3 co-ordinate system. They include octahedral normal stress σ_{oct} and octahedral shearing stress τ_{oct} . The orientations of σ_{oct} and τ_{oct} are respectively normal and tangential to an octahedral plane, their magnitudes are given by:

$$\sigma_{oct} = \frac{\sigma_1 + \sigma_2 + \sigma_3}{3}, \quad \tau_{oct} = \frac{1}{3} \sqrt{(\sigma_1 - \sigma_2)^2 + (\sigma_2 - \sigma_3)^2 + (\sigma_3 - \sigma_1)^2},$$

$$\sigma_{oct} = \begin{bmatrix} \sigma_{oct} & 0 & 0 \\ 0 & \sigma_{oct} & 0 \\ 0 & 0 & \sigma_{oct} \end{bmatrix} \quad (1.32)$$

Octahedral strains

An octahedral strain plane can be determined in the ε_1 - ε_2 - ε_3 co-ordinate system.

The orientations of octahedral normal strain ε_{oct} and shear strain γ_{oct} are respectively normal and tangential to an octahedral plane, while their magnitudes are given by:

$$\varepsilon_{oct} = \frac{\varepsilon_1 + \varepsilon_2 + \varepsilon_3}{3}, \quad \gamma_{oct} = \frac{1}{3} \sqrt{(\varepsilon_1 - \varepsilon_2)^2 + (\varepsilon_2 - \varepsilon_3)^2 + (\varepsilon_3 - \varepsilon_1)^2} \quad (1.33)$$

The ***deviator stresses*** are defined as:

$$\sigma'_{ij} = \begin{bmatrix} \sigma_{xx} - \sigma_{oct} & \sigma_{xy} & \sigma_{xz} \\ \sigma_{xy} & \sigma_{yy} - \sigma_{oct} & \sigma_{yz} \\ \sigma_{xz} & \sigma_{yz} & \sigma_{zz} - \sigma_{oct} \end{bmatrix} \quad (1.34)$$

The ***deviator strains*** are defined as:

$$\varepsilon'_{ij} = \begin{bmatrix} \varepsilon_{xx} - \varepsilon_{oct} & \varepsilon_{xy} & \varepsilon_{xz} \\ \varepsilon_{xy} & \varepsilon_{yy} - \varepsilon_{oct} & \varepsilon_{yz} \\ \varepsilon_{xz} & \varepsilon_{yz} & \varepsilon_{zz} - \varepsilon_{oct} \end{bmatrix} \quad (1.35)$$

1.4 CONSTITUTIVE MODELS FOR AGRICULTURAL SOILS

Constitutive models refer to the description of the relation between stress and strain with time being considered for dynamic cases. They are the central part of setting up a finite element analysis of a physical problem because they entirely determine the formulation of a constitutive matrix C which is a key component of the basic FEM analytical equation as in Equation (1.3). Constitutive models can be classified as elastic, plastic and elasto – plastic models which depend on whether only elasticity or plasticity or both are considered in modelling or not.

1.4.1 ELASTIC MODELS

The most distinguished feature of elastic models is that all strains are recovered when the load is removed. Within the scope of elasticity, models may be of linear or non – linear form as in Figure 1.6

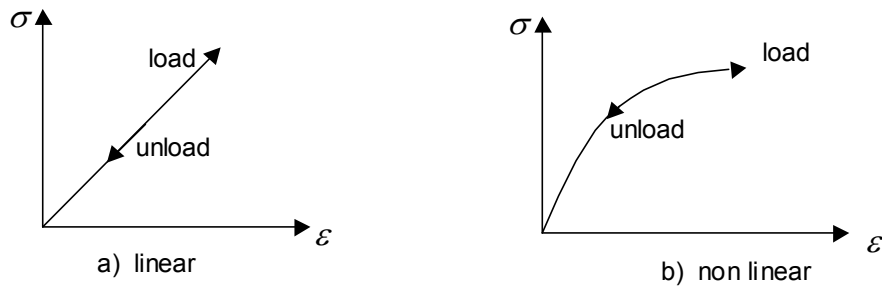


Figure 1.6 a, b. Elastic stress – strain models

1.4.1.1 Linear elastic model

The stress – strain relation in a linear elastic model is linear as in Figure 1.6a. If soil is considered to be completely isotropic, only two material parameters, shear modulus G and bulk modulus K , are required in the modelling as follows:

$$\sigma_{xy} = 2G\varepsilon_{xy} = G\gamma_{xy} ; \quad \sigma_{oct} = K\varepsilon_{vol}$$

In another way, a linear elastic model can be expressed in terms of Young's modulus E and Poisson's ratio ν

$$\sigma_{xx} = E\varepsilon_{xx} ; \quad \varepsilon_{yy} = \varepsilon_{zz} = -\nu\varepsilon_{xx}$$

The following relations exist between the above sets of material parameters:

$$G = \frac{E}{2(1+\nu)} \quad (1.36)$$

$$K = \frac{E}{3(1-2\nu)} \quad (1.37)$$

The constitutive matrix for complete isotropic material is:

$$C = \frac{E}{(1+\nu)(1-2\nu)} \begin{bmatrix} 1-\nu & \nu & \nu & 0 & 0 & 0 \\ \nu & 1-\nu & \nu & 0 & 0 & 0 \\ \nu & \nu & 1-\nu & 0 & 0 & 0 \\ 0 & 0 & 0 & 1-2\nu & 0 & 0 \\ 0 & 0 & 0 & 0 & 1-2\nu & 0 \\ 0 & 0 & 0 & 0 & 0 & 1-2\nu \end{bmatrix}$$

If soil is not considered completely isotropic, more material parameters are required to fill in the constitutive matrix. For example in the situation of cross anisotropy where there is some plane in which stress – strain relations are isotropic and outside which the elastic constants for stresses and strains are different, the constitutive matrix needs five independent constants. If the x - y plane is the plane of isotropy, the matrix is of the following form:

$$C = \begin{bmatrix} C_{11} & C_{12} & C_{12} & 0 & 0 & 0 \\ C_{12} & C_{11} & C_{12} & 0 & 0 & 0 \\ C_{12} & C_{12} & C_{11} & 0 & 0 & 0 \\ 0 & 0 & 0 & C_{11} - C_{12} & 0 & 0 \\ 0 & 0 & 0 & 0 & C_{11} - C_{12} & 0 \\ 0 & 0 & 0 & 0 & 0 & C_{11} - C_{12} \end{bmatrix}$$

1.4.1.2 Non linear elastic models

The simplest type of a non – linear relation is a bilinear one as shown in Figure 1.7a. Soil has an initial constitutive matrix C_1 until the stresses reach a yield value σ_y , after which the constitutive matrix is changed to C_2 .

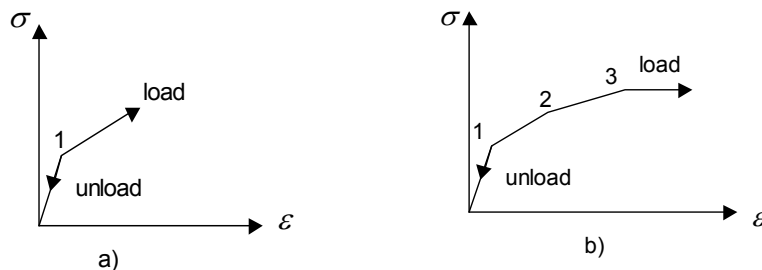


Figure 1.7 a, b. Bilinear and multi – linear elastic models

The incremental stress – strain relation can be written as:

$$\Delta\sigma = C_1\Delta\varepsilon \quad \sigma < \sigma_y \quad (1.38)$$

$$\Delta\sigma = C_2\Delta\varepsilon \quad \sigma \geq \sigma_y \quad (1.39)$$

If the constitutive matrix is expressed in terms of E and ν , the Young's modulus is usually reduced and the Poisson's ratio considered constant before and after the stresses reach σ_y . However the drawback associated to this treatment is that the bulk modulus is reduced as much as the shear modulus. The soil element therefore becomes highly compressible and often an unrealistic solution may follow. A better way to overcome this shortcoming is to express the constitutive matrix in terms of the shear modulus G and the bulk modulus K by reducing G and keeping K constant.

The dominant advantage of a bilinear model is its simplicity. However the modulus E and G of real agricultural soils usually change gradually with the strains. To extend the bilinear models to accommodate this situation, multilinear or piece-wise linear models are introduced as shown in Figure 1.7b. The tangent modulus E_t which can be E or G on a given n-piece-wise stress-strain curve is defined as the slope of the chord between two successive computed points as:

$$E_t = \frac{\sigma_i - \sigma_{i-1}}{\varepsilon_i - \varepsilon_{i-1}} \quad 3 \leq i \leq n \quad (1.40)$$

1.4.2 PLASTIC MODELS

The theory of plasticity was originally developed on the basis of experiments on metals. Therefore, some basic concepts in soil plasticity were borrowed from those of metal plasticity. Figure 1.8 shows a typical stress – strain relation for a metal bar. The initial state of the bar is supposed to be at point O. At the beginning portion of loading, designated by \overline{OA} , the stress – strain relation is invertible that means, loading is reversible.

However, experiments revealed the existence of a certain point B beyond which the loading is irreversible. This point is called yield point. When the loading exceeds the yield point, any following unloading can only partially restore the developed total strain.

The recovered and non – recovered component of the total strain are called elastic strain and plastic strain, respectively, as designated by \overline{DE} and \overline{OD} in the figure. The maximum stress that the material is able to sustain, is called failure point, as illustrated by point F in the figure.

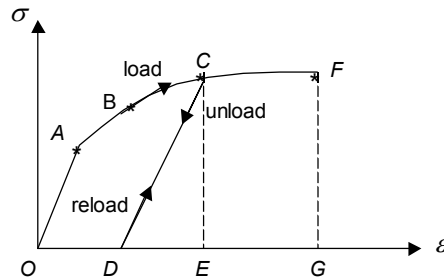


Figure 1.8 A stress – strain curve of a typical metal bar

One distinguished feature of soil manipulation in agricultural production is that soil undergoes substantial deformation before the external load is removed, and a large amount of irreversible deformation remains after the removal of the load.

In common laboratory experiments of triaxial shear and hydrostatic compression tests, researchers showed loading-reloading behaviour of soil after undergoing a noticeable amount of deformation (Chi et al, 1993). In both types of experiments, only a small amount of deformation is reversible, i.e., elastic, and most part of deformation is irreversible, i.e., plastic. This indicates that the plastic deformation dominates the soil deformation in agricultural operations and more attention is required for these phenomena.

Classification of plastic models

Constitutive models associated to plasticity can generally be divided into two types:

- Rigid, perfectly plastic models
- Elasto – plastic models

1.4.2.1 Rigid, perfectly plastic models

The simplest form of plasticity is a rigid, perfect plastic model as shown in Figure 1.9. In the model there are no elastic or recovered strains and no changes related to a fixed yield surface. Before stresses reach the yield point, soil is assumed not to deform like a rigid object; beyond the yield point, pure plastic deformation is assumed to occur in soil without any limitation. This model can be used to estimate the limit capacity or load of soil, but generally it oversimplifies the stress – strain behaviour of agricultural soils.

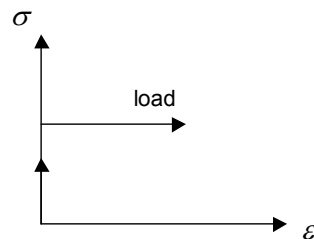


Figure 1.9 Rigid, perfectly plastic stress – strain model

1.4.2.2 Elasto – plastic models

There are some elastic and some plastic strains in the stress – strain relation for agricultural soils. After stresses have reached the yield stress, there exist three cases:

Perfectly plastic; Strain hardening and Strain softening

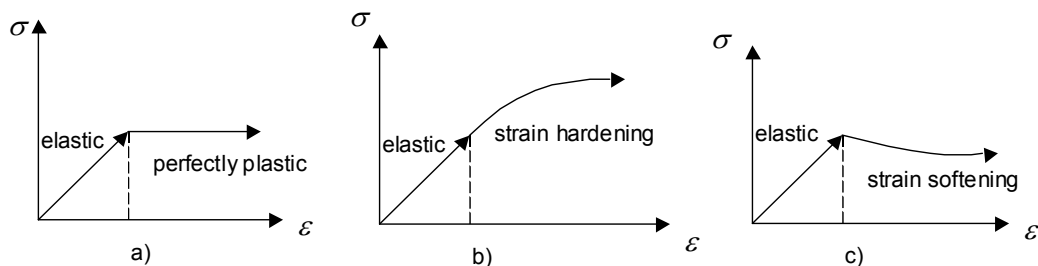


Figure 1.10 a, b and c. Elasto – plastic stress – strain model

Figure 1.10 show all the three cases respectively.

These types of model can be used to analyse all cases with or without reloading, at the cost of complexity in constitutive models and FEM calculations.

Assumptions of soil plasticity

Unlike the stress – strain relation of elasticity, the relations arising from plasticity theory usually are incremental that is the stress and strain are entirely related by their incremental or differential components. The incremental stress – strain relations for an elasto – plastic material are established on the basis of three basic assumptions:

- Yield and failure criteria
- Flow rule
- Hardening law

Yield and failure criteria

A yield criteria f is a function of stress-strain and other parameters such that when $f < k$ soil is elastic and when $f = k$ soil is in plastic state. Here, k is a yielding constant depending on material properties. The function f cannot be greater than k this requirement is known as the consistency condition. The yield criteria f designates a yield surface in stress space which divides the region into two parts. Inside the yield surface, only elastic strains occur; at the surface both elastic and plastic strains are possibly generated.

A failure criteria F is a function of stress-strain and other parameters such that when $F < k_0$ soil failure does not occur and when $F = k_0$ soil is in a failure state. Here k_0 is a failure constant depending on material properties. The failure function F corresponds to a failure surface in stress space which is the bound or limit to the yield surface.

A yield surface must lie inside or, at most coincide with the failure surface. The shapes of yield and failure surfaces are usually defined to be similar.

The existing yield and failure criteria can be classified into two types: non-frictional and frictional models, according to whether models take account of frictional components to their shear strength, all the yield and failure criteria considered here are shear (frictional) type.

Mohr – Coulomb failure criterion

It is a frictional model based on the following Mohr – Coulomb law:

$$\tau = c + \sigma \tan \phi \quad (1.41)$$

which can be transformed into the following form in the 3D stress space:

$$F_1(\sigma_{ij}) = \sigma_1 - \sigma_3 - [\sin \phi (\sigma_1 + \sigma_3) + 2c \cos \phi] \quad (1.42)$$

This equation is equivalent to an irregular hexagonal pyramid surface centred on the hydrostatic axis in principal stress space shown in Figure 1.11.

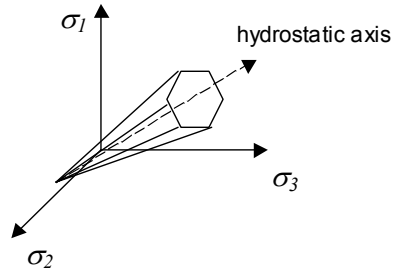


Figure 1.11 Mohr – Coulomb failure surface

Flow rule

In most models of soil plasticity, it is assumed that the total soil strain increment is composed of elastic and plastic strain increments:

$$d\varepsilon_{ij} = d\varepsilon_{ij}^e + d\varepsilon_{ij}^p \quad (1.43)$$

The direction of elastic strain increment generally coincides with the direction of the stress increment, and the magnitude of elastic strain increment is determined by:

$$d\varepsilon_{ij}^e = \frac{d\sigma'_{ij}}{2G} \quad (1.44)$$

The direction of plastic strain increment is usually not coaxial with the direction of the stress increment, and its magnitude is not as easily determined as that of elastic strain increment. Therefore a flow rule is proposed to determine the direction and relative magnitude of plastic strain increment after the yield surface is contacted.

Since plastic flow is somehow similar to fluid flow, the use of a plastic potential function $g(\sigma_{ij})$ is a natural way to describe a vector quantity which depends only on the location of a point in space. A plastic potential function defines a plastic potential surface in stress space. The direction of the plastic strain increment is assumed to be the direction of maximum gradient of the plastic potential function at the point where a stress state contacts it. According to Drucker et al (1955), the plastic strain increment is given by a scalar constant β times a vector m_{ij} normal to the potential surface at the stress point:

$$d\varepsilon_{ij}^p = \beta m_{ij} = \beta \frac{\partial g(\sigma_{ij})}{\partial \sigma_{ij}} \quad (1.45)$$

If the plastic potential function is known, the magnitude of plastic strain increment $d\varepsilon_{ij}^p$ is entirely dependent on the constant β which can be determined by the plastic potential function and a work – hardening law.

Hardening law

A yield surface is encountered in a work – hardening soil when the first plastic deformation occurs. Then if the stress continues to increase, the yield surface will expand away from the hydrostatic axis until it meets the failure surface.

Yield surface hardening is mainly concerned with how the yield surface grows, if deformational stress of soil increases.

2 PLAXIS FOR DYNAMIC LOADING

2.1 INTRODUCTION

The Finite Element Method (FEM) is one of the best tools to study the deformation of soil mass. Plaxis is a special purpose finite element computer program suitable for the analysis of deformation problems in soil and rock (Plaxis, 1998). A restriction is made in the sense that deformations are considered to be small. This enables a formulation with reference to the original undeformed geometry. It was explained in the previous chapter that displacements and stresses are maintained in a limited number of points in a finite element calculation. By interpolation of the displacements from the nodes, the displacements can be calculated everywhere throughout the element (Zienkiewicz, 1991). This interpolation is done by means of shape functions. The displacements within an element are determined solely by the nodes in that element. Depending on the number of nodes a certain degree of interpolation is possible. Because the displacements are known throughout, the strains at any point can be determined. The strains at one point are calculated from the derivatives of the displacement at that point. The main output quantities of a finite element calculation (Plaxis) are the displacements at the nodes and the stresses at the stress points.

2.2 THE DYNAMIC MODULE USED IN PLAXIS

Although Plaxis was first developed for static loading cases, further improvement on the area of interest proved that it also works for dynamic loads. The basic functionality of the dynamic module is explained in this part of the thesis.

For the general explanation of the basic functionality of Plaxis you are referred to Plaxis scientific manual version 7 (Plaxis, 1998). With the dynamic module the inertia effect is also included (Braja, 1995). Inertia effect refers to the influence of inertia forces of soil mass on the load – soil interactions.

The dynamic equilibrium equation for a finite element system can be expressed as:

$$M\ddot{u} + C\dot{u} + Ku = F \quad (2.1)$$

where

M = the mass matrix (soil + water + any added object) ;
 u, \dot{u}, \ddot{u} = displacement, velocity and acceleration vectors ;
 C = the damping matrix ($C = \alpha_R M + \beta_R K$): α_R, β_R are Rayleigh coefficients; K = the stiffness matrix ; F = the load vector

The term ($Ku = F$) corresponds to the static deformation calculation. According to Newton's Second Law ($F = ma$), the greater the mass the less the acceleration brought about when a particular force is applied. The material damping matrix C is caused by friction or viscosity. The greater the viscosity of the soil, the more vibration energy is dissipated and the less the materials move after applying a particular load.

As written above C is a combination of mass matrix and stiffness matrix (Rayleigh damping with Rayleigh coefficients).

In the standard setting of Plaxis calculation there is no Rayleigh damping ($\alpha_R = \beta_R = 0$) which is the condition applied in this thesis.

With respect to the stress – strain relationship in the soil, the theory applied here is based on what was explained in chapter one. Furthermore for more detailed description of the dynamic calculation you are referred to Hughes (1987)

2.2.1 FINITE ELEMENT DISCRETISATION

In order to carry out a finite element simulation in Plaxis a continuum is divided into a number of triangular elements. Each element consists of a number of nodes and stress points. The basic elements are the 6 – node triangular element and the 15 – node triangular element (Fig 2.1).

The 6 – node triangle is the default element for 2D analysis. It provides a second order interpolation for displacements and the element stiffness matrix is evaluated by numerical integration at three stress points. For the 15 – node triangle the order of interpolation is four and the integration involves twelve stress points. The 15 – node triangle is a very accurate 2D element which has been shown to produce high quality stress results, however using 15 – node triangles leads to relatively high memory consumption and slow calculation performance.

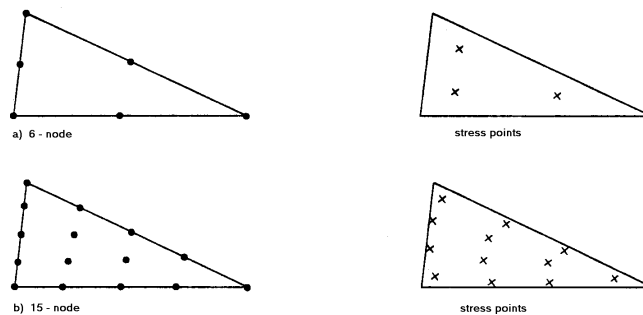


Figure 2.1 a, b. Location of nodes and stress points in triangular elements of Plaxis

2.2.2 INTERFACE ELEMENTS

Interfaces are used to model the interaction between the structure and the soil (Plaxis, 1998). Interfaces are composed of interface elements. Figure 2.2 shows how interface elements are connected to soil elements. When using 6 – node soil elements the corresponding interface elements are defined by three pairs of nodes, whereas for 15 – node soil elements the corresponding interface elements are defined by five pairs of nodes. In the Figure the interface elements are shown to have a finite thickness, but in the finite element formulation the co-ordinates of each pair are identical which means the element has a zero thickness. Each interface has assigned to a ‘virtual thickness’ which is an imaginary dimension used to obtain the material properties of the interface.

The virtual thickness is defined as the virtual thickness factor times the average element size. For Plaxis the default value of the virtual thickness factor is 0.1.

A typical application of interfaces is placed at the sides of the structure – soil interaction. The roughness of the interaction is modelled by choosing a suitable value for the strength reduction factor R in the interface. The factor relates the interface strength (friction and cohesion of interface) to the soil strength (friction angle and cohesion of the soil).

According to the Plaxis manual the following relations are applied between interface strength and soil strength.

$$c_i = R c_{soil} \quad (2.2)$$

$$\tan \phi_i = R \tan \phi_{soil} \quad (2.3)$$

where

c_i = cohesion of the interface; R = strength reduction factor ;

c_{soil} = cohesion of soil; ϕ_i = angle of friction of the interface;

ϕ_{soil} = angle of internal friction of the soil

If R is set to unity the interface properties are the same as those within the associated data set. In the case R is set to a value less than unity then the interface is weaker and more flexible than the associated soil.

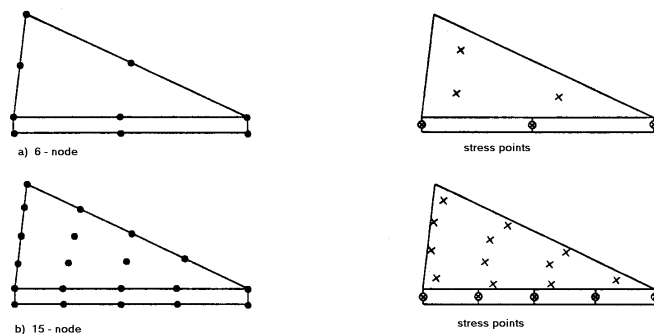


Figure 2.2 a , b. Distribution of nodes and stress points in the interface elements connected to the soil elements (Plaxis, 1998)

2.2.3 BOUNDARY CONDITION

Applying appropriate boundary conditions are among the essential features of modelling dynamic loading cases in Plaxis. For dynamic loading cases the boundaries should in principle be much further away from the loading than for static loading. This is because vibrations generally disperse very quickly in the former case, giving rise to unnatural reflections that lead to distortion of the results (Plaxis dynamic module version 7.2, 2000).

However, locating the boundaries far away requires many extra elements and therefore a lot of extra memory and calculating time. To counteract such reflections special measures are needed at the boundaries which are called ‘absorbent boundaries’ (Plaxis dynamic module version 7.2, 2000). An absorbent boundary aims at absorbing the reflection waves on the boundaries caused by dynamic loading, that otherwise would be reflected inside the soil body. The use of absorbent boundaries in Plaxis means using a damper on the boundaries. The damper ensures that an increase in stress on the boundary is absorbed without rebounding. The boundary then starts to move (Plaxis dynamic manual version 7.2, 2000)

2.2.4 THE DYNAMIC CALCULATION

Problems of interest like tyre – soil or tool – soil systems are usually dynamic, that is an interaction between a tyre or a tool and a specific portion of soil is completed within a limited stretch of time (Shen et al, 1998); (Wiermann et al, 1999). The response of soil for such dynamic loads can be simulated by one of four direct time integration methods.

2.2.4.1 Time integration

For the numerical calculation of dynamics, the form of time integration is the determining factor for the stability and accuracy of the calculation process. Soil reaction to dynamic loads can be simulated by one of the four direct time integration methods.

These are: the central difference method, the Haubolt method, the Newmark method and the Wilson- θ method. The main weakness of the central difference method is that its solution is only conditionally stable, i.e., the time step must be smaller than a critical time step to obtain a stable solution. The weakness associated to the Houbolt method is the requirement of a special starting procedure to obtain the displacement at two instants Δt and $2\Delta t$ where Δt is the time interval.

On the other hand the Newmark and the Wilson- θ method belong to the class of linear acceleration methods and are unconditionally stable if $\beta \geq 0.5$; $\alpha \geq 0.25(0.5 + \beta)^2$ for the Newmark method where, α and β determine the accuracy of the numeric time integration, (and are not equal to α and β of the Rayleigh damping) and $\theta \geq 1.37$ for the Wilson- θ method. The main difference between the Newmark method and Wilson - θ method is that the latter assumes linear change of acceleration in time range $[t, t + \theta\Delta t]$, where θ determines the accuracy of the numerical time integration.

In this section only the algorithm implementation based on the Newmark method is discussed. The Newmark method is a frequently used method of implicit time integration (Sluys, 1992). The conventional Newmark step-by-step integration method is not well suited in solving problems with dynamic loading and material non-linearity. Therefore an incremental and iterative algorithm is proposed. For all kinematic and static variables at time t and $t + \Delta t$ Equation (2.1) is expressed as:

$$M^t \ddot{u}^t + C^t \dot{u}^t + K^t u^t = F^t \quad (2.4)$$

$$M^{t+\Delta t} \ddot{u}^{t+\Delta t} + C^{t+\Delta t} \dot{u}^{t+\Delta t} + K^{t+\Delta t} u^{t+\Delta t} = F^{t+\Delta t} \quad (2.5)$$

Assuming $M^{t+\Delta t} \approx M^t$; $C^{t+\Delta t} \approx C^t$; $K^{t+\Delta t} \approx K^t$ if the incremental step is small enough. The subtraction of Equation (2.4) from Equation (2.5) yields the following basic dynamic equation in increment form

$$M^t (\ddot{u}^{t+\Delta t} - \ddot{u}^t) + C^t (\dot{u}^{t+\Delta t} - \dot{u}^t) + K^t (u^{t+\Delta t} - u^t) = F^{t+\Delta t} - F^t \quad (2.6)$$

According to the Lagrangian median theorem,

$$\dot{u}^{t+\Delta t} = \dot{u}^t + \tilde{\ddot{u}} \Delta t \quad (2.7)$$

where

$$\tilde{\ddot{u}} = \text{value of } \ddot{u} \text{ at certain point in the domain } (t, t + \Delta t)$$

The Newmark method assumes

$$\tilde{u} = (1 - \beta)\dot{u}^t + \beta\dot{u}^{t+\Delta t} \quad 0 \leq \beta \leq 1 \quad (2.8)$$

therefore Equation (2.7) is written as:

$$\dot{u}^{t+\Delta t} - \dot{u}^t = \Delta t \ddot{u}^t + a_0 (\dot{u}^{t+\Delta t} - \dot{u}^t) \quad (2.9)$$

where

$$a_0 = \beta \Delta t$$

According to Taylor expansion of the displacement vector

$$u^{t+\Delta t} = u^t + \dot{u}^t \Delta t + (0.5 \Delta t^2) \ddot{u}^{t+h\Delta t} \quad 0 < h < 1 \quad (2.10)$$

By further assumption of the Newmark method

$$\ddot{u}^{t+h\Delta t} = (1 - 2\alpha)\ddot{u}^t + 2\alpha \ddot{u}^{t+\Delta t} \quad 0 \leq 2\alpha \leq 1 \quad (2.11)$$

Thus Equation (2.10) can be written as

$$\ddot{u}^{t+\Delta t} - \ddot{u}^t = a_1 (u^{t+\Delta t} - u^t) + a_2 \dot{u}^t + a_3 \ddot{u}^t \quad (2.12)$$

where

$$a_1 = \frac{1}{\alpha \Delta t^2} ; \quad a_2 = -\frac{1}{\alpha \Delta t^2} ; \quad a_3 = -\frac{1}{2\alpha}$$

By substitution of Equations (2.9) and (2.12) into Equation (2.6) the final equation becomes

$$\begin{aligned} (a_1 M^t + a_4 C^t + K^t) (u^{t+\Delta t} - u^t) &= (F^{t+\Delta t} - F^t) + \\ M^t (-a_2 \dot{u}^t - a_3 \ddot{u}^t) + C^t (-a_5 \dot{u}^t - a_6 \ddot{u}^t) & \end{aligned} \quad (2.13)$$

where

$$a_4 = a_0 a_1 ; \quad a_5 = a_0 a_2 ; \quad a_6 = \Delta t + a_0 a_3$$

The unknown displacement column matrix $(u^{t+\Delta t} - u^t)$ can be solved from Equation (2.13) if u^t, \dot{u}^t , and \ddot{u}^t are known. Then on the basis of Equation (2.9) and (2.12) $u^{t+\Delta t}, \dot{u}^{t+\Delta t}$ and $\ddot{u}^{t+\Delta t}$ are determined by the following Equations

$$\begin{aligned} u^{t+\Delta t} &= u^t + \dot{u}^{t+\Delta t} - \dot{u}^t \\ \dot{u}^{t+\Delta t} &= \dot{u}^t + a_8 \ddot{u}^t + a_0 \ddot{u}^{t+\Delta t} \\ \ddot{u}^{t+\Delta t} &= a_1 (u^{t+\Delta t} - u^t) + a_2 \dot{u}^t + a_7 \ddot{u}^t \end{aligned} \quad (2.14)$$

where

$$a_7 = a_3 + 1 ; \quad a_8 = \Delta t - a_0$$

2.2.4.2 Time step

Based on the above discussion of the Newmark method the time integration is the determining factor for the stability and accuracy of the calculation process. Despite the implicit integration the time step used in the calculation is subject to limitations. If the time step is too large, the solution will display major deviations and the calculated response will be unreliable (Plaxis dynamic module version 7.2, 2000).

The critical time step depends on the maximum frequency occurring in the model and the accuracy of the finite element mesh. The chosen time step is so small that a wave in a single step displaces less than one single element.

$$\Delta t_{crit} = \frac{B}{\zeta \sqrt{\frac{E(1-\nu)}{\rho(1+\nu)(1-2\nu)} \sqrt{1 + \frac{B^4}{4S^2} - \frac{B^2}{2S} \left[1 + \frac{1-2\nu}{4} \frac{2S}{B^2} \right]}}} \quad (2.15)$$

where

ζ = multiplying factor depends on finite element type ; B = the average length of the element ; S = surface area of the element ; ρ = density of the material ;
 E = Young's modulus ; ν = Poisson's ratio

2.3 SOIL MATERIAL MODELS

A material model is a set of mathematical equations that describes the relationship between stress and strain. All material models implemented in Plaxis are often expressed in a form in which infinitesimal increments of stress rates are related to infinitesimal increments of strain rates.

In this thesis, the two types of soil models used for the Plaxis calculation are the Mohr-Coulomb and the Cam Clay type models. Details of the models with some mathematical formulations are given below.

2.3.1 MOHR – COULOMB MODEL

The Mohr-Coulomb model is a perfectly plastic model, which is used as a first approximation of soil behaviour in general. Soil plasticity is associated with the development of irreversible strains. In order to evaluate whether or not plasticity occurs in a calculation a yield function is introduced as a function of stress and strain (Plaxis material model manual version 5, 1994).

A perfectly plastic model is a constitutive model with a fixed yield surface that is fully defined by model parameters and not affected by plastic straining. For stress states represented by points within the yield surface the behaviour is purely elastic and all strains are reversible.

Elastoplasticity of the Model

The basic principle of elastoplasticity is that strains and strain rates are decomposed into an elastic and a plastic part.

$$\underline{\varepsilon} = \underline{\varepsilon}^e + \underline{\varepsilon}^p \quad \underline{\dot{\varepsilon}} = \underline{\dot{\varepsilon}}^e + \underline{\dot{\varepsilon}}^p \quad (2.16)$$

Substitution of Equation (2.16) into Hook's law Equation (1.27) gives:

$$\underline{\underline{\dot{\sigma}'}} = \underline{\underline{D}}^e \underline{\underline{\dot{\epsilon}}}^e = \underline{\underline{D}}^e (\underline{\underline{\dot{\epsilon}}} - \underline{\underline{\dot{\epsilon}}}^p) \quad (2.17)$$

According to the classical theory of plasticity (Hill, 1950) plastic strain rates are proportional to the derivative of the yield function with respect to the stresses. This means that the plastic strain rates can be represented as vectors perpendicular to the yield surface.

This classical form of the theory is referred to as associated plasticity. However for Mohr-Coulomb type yield functions the theory of associated plasticity leads to an overprediction of dilatancy. Therefore in addition to the yield function a plastic potential function is introduced. For the cases f is the yield function and g is plastic potential function, $g \neq f$ is denoted as non-associated plasticity. In general the plastic strain rates are written as:

$$\underline{\underline{\dot{\epsilon}}}^p = \lambda \frac{\partial g}{\partial \underline{\underline{\sigma}'}} \quad (2.18)$$

in which λ is the plastic multiplier. For purely elastic behaviour $\lambda = 0$, where as in the case of plastic behaviour λ is positive:

$$\lambda = 0 \text{ for } f < 0 \text{ or } \frac{\partial f^T}{\partial \underline{\underline{\sigma}'}} \underline{\underline{D}}^e \underline{\underline{\dot{\epsilon}}} \leq 0 \quad (\text{elasticity}) \quad (2.19)$$

$$\lambda > 0 \text{ for } f = 0 \text{ and } \frac{\partial f^T}{\partial \underline{\underline{\sigma}'}} \underline{\underline{D}}^e \underline{\underline{\dot{\epsilon}}} > 0 \quad (\text{plasticity}) \quad (2.20)$$

Considering only elastic perfectly plastic behaviour and the consistency condition for plastic flow, the plastic multiplier λ can be formulated as:

$$\lambda = \frac{1}{d} \frac{\partial f^T}{\partial \underline{\underline{\sigma}'}} \underline{\underline{D}}^e \underline{\underline{\dot{\epsilon}}} \quad (2.21)$$

where

$$d = \frac{\partial f^T}{\partial \underline{\underline{\sigma}'}} \underline{\underline{D}}^e \frac{\partial g}{\partial \underline{\underline{\sigma}'}} \quad (2.22)$$

By substituting Eqn (2.22) into Eqn (2.21) and further substituting Eqn (2.21) into Eqn (2.18), with further substituting into Eqn (2.17) gives Eqn (2.23), which is the general elastoplastic relation between stress rates and strain rates, see Smith and Griffith (1982); Vermeer and De Borst (1984).

$$\underline{\underline{\dot{\sigma}'}} = \left(\underline{\underline{D}}^e - \frac{\alpha}{d} \underline{\underline{D}}^e \frac{\partial g}{\partial \underline{\underline{\sigma}'}} \frac{\partial f^T}{\partial \underline{\underline{\sigma}'}} \underline{\underline{D}}^e \right) \underline{\underline{\dot{\epsilon}}} \quad (2.23)$$

The parameter α is used as a switch. If the material behaviour is elastic as defined by Equation (2.19) the value of α is equal to zero, whilst for plasticity the value of α is unity.

Mathematical formulation of the yield function

The Mohr-Coulomb yield condition is an extension of Coulomb's friction law to general states of stress. In fact this condition ensures that Coulomb's friction law is obeyed in any plane within a material element.

The full Mohr-Coulomb yield condition can be defined by three yield functions when formulated in terms of principal stresses:

$$f_1 = \frac{1}{2} |\sigma'_2 - \sigma'_3| + \frac{1}{2} (\sigma'_2 + \sigma'_3) \sin \phi - c \cos \phi \leq 0 \quad (2.24)$$

$$f_2 = \frac{1}{2} |\sigma'_3 - \sigma'_1| + \frac{1}{2} (\sigma'_3 + \sigma'_1) \sin \phi - c \cos \phi \leq 0 \quad (2.25)$$

$$f_3 = \frac{1}{2} |\sigma'_1 - \sigma'_2| + \frac{1}{2} (\sigma'_1 + \sigma'_2) \sin \phi - c \cos \phi \leq 0 \quad (2.26)$$

The two plastic model parameters appearing in the yield functions are the well known friction angle ϕ and the cohesion c .

In addition to the yield functions (f) three plastic potential functions (g) are defined for the Mohr-Coulomb model:

$$g_1 = \frac{1}{2} |\sigma'_2 - \sigma'_3| + \frac{1}{2} (\sigma'_2 + \sigma'_3) \sin \psi \quad (2.27)$$

$$g_2 = \frac{1}{2} |\sigma'_3 - \sigma'_1| + \frac{1}{2} (\sigma'_3 + \sigma'_1) \sin \psi \quad (2.28)$$

$$g_3 = \frac{1}{2} |\sigma'_1 - \sigma'_2| + \frac{1}{2} (\sigma'_1 + \sigma'_2) \sin \psi \quad (2.29)$$

The plastic potential functions contain a third plasticity parameter, the dilatancy angle ψ .

This parameter is required to model positive plastic volumetric strain increments for $\psi > 0$ and volume decrease for $\psi < 0$ and no volume change for $\psi = 0$.

By differentiating the plastic potential function g according to Equation (2.18) the parameter ψ is obtained as:

$$\sin \psi = \frac{\dot{\epsilon}_v^p}{\dot{\gamma}^p} \quad (2.30)$$

where

$\dot{\epsilon}_v^p$ is the increment of plastic volumetric strain ; $\dot{\gamma}^p$ is the plastic distortion increment

2.3.1.1 Parameters for the Mohr – Coulomb model

The Mohr-Coulomb model requires a total of five basic parameters. These parameters with their standard units are listed below:

| | | |
|--------|-------------------|----------------|
| E | Young's modulus | [kPa] |
| ν | Poisson's ratio | [-] |
| ϕ | Angle of friction | [$^{\circ}$] |
| c | Cohesion | [kPa] |
| ψ | Dilatancy | [$^{\circ}$] |

Young's modulus of elasticity

Plaxis uses the Young's modulus as the basic stiffness modulus in the Mohr-Coulomb model. A stiffness modulus has the dimension of stress. A value is derived from a standard triaxial test as shown in the Fig 2.3.

In such a test the sample is first loaded by a hydrostatic pressure ($\sigma_1 = \sigma_2 = \sigma_3$) and then an increasing deviatoric stress ($\sigma_1 - \sigma_3$) is added by increasing σ_1 .

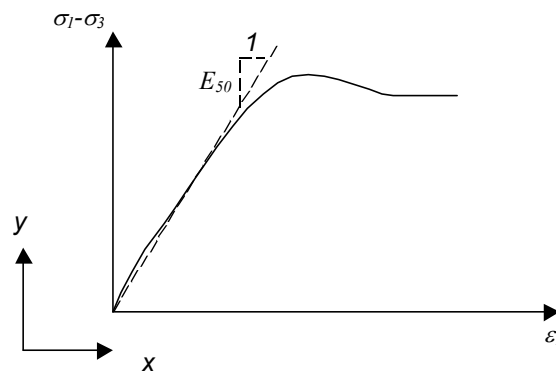


Figure 2.3 Elasticity modulus from results of standard triaxial test (Plaxis material models manual version 5, 1994).

The secant modulus at 50% strength, denoted as E_{50} is a suitable stiffness parameter in many problems (Plaxis material models manual version 5, 1994). For moist or wet rather dense clay soils an E value is obtained by recognising that under these conditions the soil compressibility is mainly caused by the compressibility of entrapped air bubbles in the soil pores. Barneveld (2000) assumed that the entrapped air follows Boyle's gas law and that the external mean normal stress is fully transmitted to the entrapped air bubbles. In this way he could calculate E from a standard triaxial test and the initial soil air content.

Poisson's ratio

The other elastic property in the relationships of elastic theory is Poisson's ratio, which is defined as the ratio of lateral strain to axial strain. It has values between 0 and 0.5 depending on the material. The value 0.5 corresponds to a material showing no volume change and the value 0 represents a perfect rigid material.

In Plaxis in many cases ν is determined from the coefficient of lateral earth pressure K_0 .

As the Mohr – Coulomb model gives the well known ratio of $\frac{\sigma_3}{\sigma_1} = \frac{\nu}{(1-\nu)}$ for one

dimensional compression; it is easy to select Poisson's ratio such that a realistic value of K_0 is obtained. For agricultural soils a usual value of this coefficient is 0.5. In clay type, rather dense, wet agricultural soils a loading will generate compressive water stresses in the pore system. Under these conditions K_0 may reach values up to 0.9 (Klajj, 1975).

Application of Boyle's law to the entrapped air in a quick standard triaxial test at this soil condition will also give a value for ν because ε_3 may be derived from the air volume reduction and ε_1 (Barneveld, 1994).

Cohesion and Angle of Internal Friction

Cohesion and angle of internal friction are parameters which determine the shear strength of the soil. Koolen and Kuipers (1983) presented values of c and ϕ .

Several authors measured the cohesion in the range between 9 to 140 kPa depending on the type of the soil. A minimum value of cohesion may be estimated as $c = \chi s_w \tan \phi$, where χ is degree of saturation and s_w is suction in the soil water.

For unsaturated soil the angle of internal friction varies between 25° for moist, relatively loose and fine particles to 45° for drier, relatively dense and coarse particles.

Dilatancy angle

According to Plaxis manual clay and silty soils that are not heavily overconsolidated tend to show little dilatancy (Plaxis materials model manual version 5, 1994). Furthermore the dilatancy of sand depends on both the density and on the friction angle. For quartz sands the order of magnitude is $\psi = \phi - 30$. A small negative value for ψ may be realistic for extremely loose sands. ψ is a measure of plastic volume change in a plastic state of a material; if $\psi = 0$, no volume change, $\psi > 0$, volume increase and $\psi < 0$ implies volume decrease.

2.3.2 CAM – CLAY TYPE MODEL

The Cam – Clay type models are derived from the critical state theory (Atkinson and Bransby, 1978). Critical state soil mechanics may be treated as an empirical description that unifies different aspects of soil deformation. Soil exhibits permanent (plastic) deformation, non-permanent (elastic) deformation, yield surfaces that mark the onset of permanent plastic deformation at critical state on which shear deformation occurs without volume change.

The Soft – Soil model in the FEM package named Plaxis (Plaxis scientific manual version 7) is one of the Cam – Clay type models which can be used to simulate the behaviour of soft soils like normally consolidated clays. The model performs best in situations of primary compression.

Some of the basic characteristics of the soft-soil model are:

- Stress dependent stiffness (logarithmic compression behaviour)
- Distinction between primary loading and unloading – reloading
- Memory for pre – consolidation stress
- Failure behaviour according to the Mohr-Coulomb criterion

Based on isotropic states of stress and strain ($\sigma'_1 = \sigma'_2 = \sigma'_3$) in the soft-soil model it is assumed that there is a logarithmic relation between the volumetric strain and the mean effective stress, which can be formulated as:

$$\varepsilon_v - \varepsilon_v^0 = -\lambda^* \ln\left(\frac{p'}{p^0}\right) \quad \text{primary compression / loading} \quad (2.31)$$

$$\varepsilon_v^e - \varepsilon_v^{e0} = -\kappa^* \ln\left(\frac{p'}{p^0}\right) \quad \text{unloading and reloading} \quad (2.32)$$

where

- ε_v = the volumetric strain ; p' = the mean effective stress ;
- λ^* = the modified compression index, which determines the compressibility of the material in primary loading ;
- κ^* = the modified swelling index, which determines the compressibility of the material in unloading and subsequent reloading

Note that the soil response during unloading and reloading is assumed to be elastic, which explains the superscript e in Equation (2.32). The elastic behaviour is described by Hook's law of elasticity (see section 1.3.2).

When plotting Equation (2.31) and Equation (2.32) one obtains a straight line as shown in Fig 2.4. In order to maintain the validity of Equation (2.31) and Equation (2.32) a minimum effective stress value of one stress unit is incorporated. An infinite number of unloading-reloading lines exist in Fig 2.4 each corresponding to a particular value of isotropic preconsolidation stress (p_{pre}).

The preconsolidation stress represents the largest stress level experienced by the soil. During unloading and reloading this preconsolidation stress remains constant. In primary loading however the preconsolidation stress increases with the stress level, causing irreversible volumetric strains.

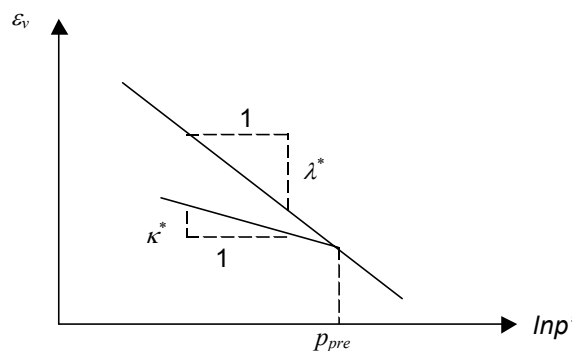


Figure 2.4 Logarithmic relation between volumetric strain and mean stress.

As explained before the soil response during unloading and reloading is assumed to be elastic. The elastic behaviour of soil is explained by Hook's law of elasticity in section 1.3.2

Yield function and yield surface of the soft-soil model

For convenience the stress state selected here is the triaxial loading condition with $\sigma'_2 = \sigma'_3$.

For such state of stress the yield function of the soft-soil model is defined as:

$$f = \bar{f} - p_{pre} \quad (2.33)$$

where

$$\bar{f} = \frac{q^2}{M^2(p' + c \cot \phi)} + p' \quad (2.34)$$

$$p_{pre} = p_{pre}^0 \exp\left(\frac{-\varepsilon_v^p}{\lambda^* - \kappa^*}\right) \quad (2.35)$$

The yield function f describes an ellipse in $p' - q$ plane as shown in Fig 2.5.

The development of plastic strains is evaluated by means of a yield function f and the direction of the plastic strain increments is evaluated from the plastic potential function g (Eqn. 2.18). For a negative value of the yield function no plastic strain increments occur and the response is purely elastic (Eqn. 2.19).

In the Soft – Soil model the yield surface is the boundary of the elastic stress area, which has a limit of the Mohr – Coulomb failure line as shown in the Fig 2.5. Stress paths within this boundary only give elastic strain increments whereas stress paths that tend to cross the boundary generally give both elastic and plastic strain increments.

The parameter M in Equation (2.34) determines the height of the ellipse. The height of the ellipse is responsible for the ratio of horizontal and vertical stresses in primary one dimensional compression.

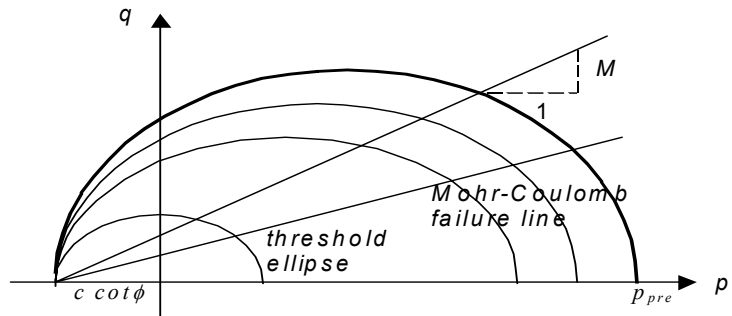


Figure 2.5 Yield surface of the Soft – Soil model in $p' - q$ plane (Plaxis, 1998)

The tops of all ellipses are located on a line with inclination M in the $p' - q$ plane.

In the modified Cam – Clay model (Burland, 1965 and 1967) the M line is referred to as the critical state line and represents stress state at post peak failure. The parameter M is then based on the critical state friction angle. In the Soft – Soil model however failure is not necessarily connected to critical state. The Mohr – Coulomb failure criterion is used with strength parameters ϕ and c which does not correspond to the M line.

The isotropic preconsolidation stress, p_{pre} determines the magnitude of the ellipse. In fact an infinite number of ellipses exists (see Fig 2.5) each one corresponding to a particular value of p_{pre} . The left hand side of the ellipse is extended into the tension zone of the principal stress space ($p' < 0$) by means of the term $c \cot \phi$ in Equation (2.34).

In order to make sure that the right hand side of the ellipse will remain in the compression zone ($p' > 0$) a minimum value of $c \cot \phi$ is adopted for p_{pre} .

For $c = 0$ a minimum value of p_{pre} equal to 1 stress unit is adopted. Hence there is a threshold ellipse as shown in the Fig 2.5.

The value of p_{pre} is affected by volumetric plastic straining and follows from the hardening relation as formulated in Equation (2.35). This equation reflects the principle that the preconsolidation stress increases exponentially with decreasing volumetric plastic strain (compaction). The value p_{pre}^0 can be regarded as the initial value of the preconsolidation stress. The value of the initial volumetric plastic strain is assumed to be zero.

In Soft – Soil model the yield function as defined in Equation (2.33) is only active to model the irreversible volumetric straining in primary compression and is used as the cap of the yield contour. In order to model failure behaviour a perfectly plastic Mohr – Coulomb type yield function is introduced. This yield function represents a straight line in $p' - q$ plane. This line is indicated in Fig 2.5 as a Mohr – Coulomb failure line.

2.3.2.1 Parameters for the Cam – Clay type model

This Soft – Soil model requires a total of seven parameters. These parameters with their standard units are listed below:

| | | |
|-------------|----------------------------|--------------|
| ν | Poisson's ratio | [-] |
| ϕ | Angle of friction | [$^\circ$] |
| c | Cohesion | [kPa] |
| ψ | Dilatancy | [$^\circ$] |
| λ^* | Modified Compression index | [-] |
| κ^* | Modified Swelling index | [-] |
| p_{pre} | Preconsolidation stress | [kPa] |

Poisson's ratio

For the Soft – Soil model Poisson's ratio plays a minor role when normally consolidated soils are loaded but Poisson's ratio is important for unloading problems. It is observed that in unloading of a uni-axial compression test the decrease of the lateral stress is relatively small compared with the decrease in vertical stress; this implies a low ν value. According to Plaxis manual ν will usually be in the range between 0.1 and 0.2.

Cohesion and Angle of Internal Friction

The cohesion has the dimension of stress. Entering a cohesion will result in an elastic region that is partly located in the tension zone of the stress space as shown in the Fig 2.5.

The effective angle of internal friction is specified in degrees and represents the increase of shear strength with effective stress level. All the other remarks are the same as that of the Mohr – Coulomb model, see section 2.3.1.1.

Dilatancy angle

For the type of materials where the soft soil model should be used, dilatancy can generally be neglected. A dilatancy angle of zero degree is included in the standard settings for the Soft-Soil model.

Modified Compression and Swelling index

These parameters can be obtained from uniaxial compression test with loading and unloading stages as shown in Fig 2.4. The slope of the primary loading line gives the modified compression index and the slope of the unloading line gives the modified swelling index.

Note that there is a difference between the modified indices λ^* and κ^* defined in Equation (2.31) and (2.32) and the original Cam-Clay parameters λ and κ . The latter parameters are defined in terms of the void ratio instead of the volumetric strain ε_v ; for details refer the Plaxis material manual version 7 (Plaxis, 1998).

2.4 USER RELATED CHARACTERISTICS OF THE FEM MODEL

In order to carry out FEM calculations using Plaxis dynamic module the following three basic steps have to be fulfilled: the input step, the calculation step and the output step

2.4.1 THE INPUT STEP

General settings

In the general settings of the new project the user can define the basic conditions for the dynamic analyses to be performed. These are: the dimensions of the draw area, basic units (for length, force and time) , the type of the model and the type of elements.

In addition to these the user may input an independent acceleration component or he can consider the default gravity acceleration (9.8 m/s^2) to calculate the wave velocities.

Units

In a dynamic analysis the units are usually [s] for time, [m] for length, and [kN] for force. These units can be changed by the user if necessary. The two well known models used to run Plaxis are a plane strain model and an axisymmetric model.

Models

A plane strain model is used for structures with uniform cross section and corresponding stress state and loading scheme over a certain length perpendicular to the cross section.

An axisymmetric model is used for circular structures with uniform radial cross section and loading scheme around the central axis, where the deformation and stress state are assumed to be identical in any radial direction.

Elements

6 – node triangular element is the default element for a 2D analysis of either plane strain or axisymmetric models. It provides a second order interpolation for displacements. The element stiffness matrix is evaluated by numerical integration using a total of three stress points (see Fig 2.1 a). 15 – node triangular element is also used for 2D analysis of either plane strain or axisymmetric models. The element stiffness matrix is evaluated by numerical integration using a total of twelve stress points (see Fig 2.1 b)

2.4.1.1 Geometry model

After completing the general settings the user has to create a 2D geometry model which is a representation of the problem of interest. A geometry model consists of points, lines and clusters. Points and lines are entered by the user whereas clusters are generated by the program. In addition to these basic components, structural objects or special conditions can be assigned to the geometry model.

Loads and boundary conditions

Based on the problem of interest the user has to select the right loading and boundary conditions. The load submenu in the input program contains distributed loads (tractions), point forces and prescribed displacements. Loads and prescribed displacements can be applied within the model as well as the model boundaries.

Loads

Based on the problem of interest the user has to select the right loading conditions. Tractions are distributed loads that can be applied to geometry lines. The input values of tractions are given in force per area (kPa). Two load systems are available for tractions (A and B) which can be activated independently. Traction loads are controlled by the load multipliers $MloadA$ ($\sum MloadA$) or $MloadB$ ($\sum MloadB$) respectively. The applied magnitude of traction loads during calculations is the product of the input value and the corresponding load multiplier.

Point forces are concentrated forces that act on a geometry point. The input values of point forces are given in force per unit of length (kN/m). Two load systems are available for tractions (A and B) which can be activated independently. Point forces are controlled by the load multipliers $MloadA$ ($\sum MloadA$) or $MloadB$ ($\sum MloadB$) respectively. The applied magnitude of point forces during calculations is the product of the input value and the corresponding load multiplier.

Prescribed displacements are conditions that can be imposed on geometry lines to control the displacement of these lines. The input values of the prescribed displacements are given in meter (m). Prescribed displacements are controlled by the load multipliers $Mdispl$ ($\sum Mdispl$). The applied magnitude of prescribed displacements during calculations is the product of the input value and the corresponding load multiplier.

Boundary conditions

Based on the problem of interest the user has to select the right boundary conditions.

Fixities

Plaxis automatically imposes a set of general boundary conditions to the actual geometry model. These boundary conditions can be applied to geometry lines as well as to geometry points. Distinction can be made between horizontal fixity ($u_x = 0$), vertical fixity ($u_y = 0$) and total fixity ($u_x = u_y = 0$). Fixities are prescribed displacements equal to zero.

Absorbent boundaries

The user has to use geometry model boundaries sufficiently distant to the area of interest or uses special boundary conditions (absorbent boundaries) at the bottom and right hand side boundaries to avoid disturbances due to the boundary conditions (Plaxis dynamic module version 7.2, 2000). Without these special boundary conditions the waves would be reflected on the model boundaries, returning into the model and disturbing the results.

2.4.1.2 Material properties

After the geometry has been completed the user should compose data sets of material parameters. In Plaxis soil properties and material properties of structures are stored in material data sets.

All data sets are stored in a material data base. From the data base the data sets can be assigned to the soil clusters or to the corresponding structural objects in the geometry model.

Soil material models

In this section the user has to select the right soil material model based on the properties of the soil. The two well known soil material models are the Mohr – Coulomb soil model and the Cam – Clay type soil model.

The Mohr – Coulomb model can be considered as a first order approximation of real soil behaviour. This elastic perfectly – plastic model requires five basic input parameters namely a Young's modulus, Poisson's ratio, Cohesion, Friction angle and Dilatancy angle. For details see section 2.3.1.1.

The Cam – Clay type model can be used to simulate the behaviour of soft soils. The model performs best in situations of primary compression. The model has seven basic parameters namely Poisson ratio, Cohesion, Friction angle, Dilatancy, Modified compression index, Modified swelling index and Preconsolidation stress. For details see section 2.3.2.1.

2.4.1.3 Mesh generation

When the full geometry is defined, all geometry components have their properties and the geometry model is complete, mesh can be generated. Plaxis allows for a fully automatic generation of finite element meshes which means the geometry model has to be divided into elements. A composition of finite elements is called a finite element mesh. The basic elements are the 6 - node triangular element and the 15 – node triangular element. Their difference is that a mesh composed of 15 – node elements gives a much finer distribution of nodes and thus much more accurate results than a similar mesh composed of the same number of 6 – node elements.

Global coarseness

Distinction is made between five levels of global coarseness: very coarse, coarse, medium, fine and very fine. The average element size and the number of generated elements depend on this global coarseness setting.

2.4.1.4 Initial conditions

Once the geometry model has been created and the finite element mesh has been generated, the initial stress and the initial situation must be specified.

The generation of initial stresses by means of the K_0 – procedure using the K_0 value from Jaky's formula $(1 - \sin \phi)$ is the last part of the input step. The initial stress in a soil body is influenced by the weight of the material ($\sum Mweight$) and the history of its formation.

This stress state is usually characterised by an initial vertical stress (σ_v) which is related to the coefficient of lateral earth pressure K_0 , by $\sigma_h = K_0 \sigma_v$.

2.4.2 THE CALCULATION STEP

With the generation of the initial stresses, the generation of the initial situation of the finite element model is complete. After this step the actual finite element calculations can be executed by using the calculation program. The calculation program contains all facilities to define and start up finite element calculations. When all parameters have been set the user starts the calculation process. In Plaxis a calculation process is divided into calculation phases and each phase is generally divided into a number of calculation steps. This is necessary because the non – linear behaviour of the soil requires loading to be applied in small portions (load increments).

2.4.2.1 Selecting the dynamic analysis

The dynamic calculation can be defined by selecting dynamic analysis together with automatic time stepping.

Dynamic analysis parameters

In the calculation program the user can define the control parameters of the dynamic calculation.

Time stepping

The time step used in a dynamic calculation is constant and equal to

$$\delta t = \frac{t}{n * m} \quad \text{where } t \text{ is the duration of the dynamic loading, } n \text{ is the number of additional}$$

steps and m is the number of dynamic sub steps.

Time duration

For each phase in the calculation program the user has to specify the duration of the dynamic load. The estimated end time is calculated automatically by adding the duration time of all consecutive phases.

Additional steps

Plaxis stores the calculation results in several steps. By default the number of additional steps is 100 but the user can enter any value between 1 and 250 in the calculation program.

Dynamic sub steps

For each additional step Plaxis can calculate the number of sub steps necessary to reach the estimated end time with a sufficient accuracy on the basis of the generated mesh and the calculated time step (δt_{crit}). The time step used in the calculation must be less than the calculated time step ($\delta t \leq \delta t_{crit}$). For δt_{crit} , see Eqn (2.15).

Dynamic loads

In Plaxis a dynamic load can consist of an harmonic load, a block load or a special user defined load. A dynamic load is activated in the calculation program by means of multipliers.

2.4.2.2 Selecting points for curves

After the calculation phases have been defined and setting all necessary input dynamic parameters and before the calculation process is started, some points may be selected for the generation of load – displacement curves or stress paths. These points could be nodes or stress points depending on the users interest.

During the calculations information for the selected points is stored in a separate file. After the calculation the curve program may be used to generate load – displacement curves or stress paths. It is therefore not possible to generate curves for points that have not been pre-selected. Because of limitations in the computer memory only a few points can be selected to store data during the calculation process.

2.4.2.3 Execution of the calculation process

When all the calculation phases have been defined and points for curves have been selected, the calculation process can be executed starting the calculation program.

2.4.3 THE OUTPUT STEP

The main output quantities of a finite element calculation are the displacements at the nodes and the stresses at the stress points. In addition, when a finite element model involves structural elements, structural forces are calculated in these elements.

An extensive range of facilities exist within Plaxis to display the results of a finite element analysis. The output program contains all facilities to view and to list the results of generated input data and finite element calculations. Among the many output possibilities some are described below.

2.4.3.1 Deformed mesh

The deformed mesh is a plot of the finite element mesh in the deformed shape, super-imposed on a plot of undeformed geometry. If it is desired to view the deformations on the true scale or larger scale then the scale option may be used.

Total displacements

The total displacements are the total vectorial displacements $|u|$ at all nodes at the end of the current calculation step, displayed in a plot of the undeformed geometry.

The total displacement may be presented as arrows or contours or shadings by selecting the appropriate option from the output program.

In addition to the vectorial components, the horizontal component (u_x) and the vertical component (u_y) of the total displacement may be viewed separately by selecting the corresponding option from the output program.

Total strains

The total strains are the total strains in the geometry at the end of the current calculation step, displayed in a plot of the undeformed geometry. In Plaxis by default the total strains are presented as principal strains. The length of each line represents the magnitude of the principal strain and the direction indicates the principal direction. In addition to this the horizontal strain (ε_x), vertical strain (ε_y), shear strain (γ_{xy}) and volumetric strain (ε_v) can be viewed separately from the output program.

2.4.3.2 Total stresses

The total stresses are the total stresses in the geometry at the end of the current calculation step, displayed in a plot of the undeformed geometry. By default the total stresses are presented as principal stresses. The length of each line represents the magnitude of the principal stress and the direction indicates the principal direction.

In addition to the total stresses, the vertical stress (σ_y), the horizontal stress (σ_x) and the shear stress (τ_{xy}) can be viewed separately by selecting the corresponding output form from the output program

Total effective stresses

The effective stresses are the effective stresses in the geometry at the end of the current calculation step, displayed in a plot of the undeformed geometry. By default effective stresses are presented as principal stresses calculated from the Cartesian stress components. The horizontal effective stress (σ'_x) and the vertical effective stress (σ'_y) can also be viewed from the output program

Plastic points

The plastic points are the stress points in a plastic state, displayed in a plot of the undeformed geometry. The plastic stress points are indicated by small symbols that can have different shapes and colours depending on the type of plasticity that has occurred.

An open square indicates that the stress lies on the surface of the Coulomb failure envelope. A white solid square indicates that the tension cut – off criteria was applied. A crossed square represents a state of normal consolidation where the preconsolidation stress is equivalent to the current stress state.

3 ANALYSES OF MODELLING DYNAMIC LOADING CASES IN PLAXIS

3.1 INTRODUCTION

Apart from the dynamic aspects like inertia and dynamic loads it is possible to model dynamic load soil interaction with Plaxis. When soil is subjected to different loading cases non – linear soil behaviour will result. However Plaxis can cope with problems involving non – linear soil behaviour under even complex dynamic loads.

In order to describe this behaviour of soil in a constitutive model a distinction can be made between elasticity, plasticity, hardening and softening behaviour. Details of these models are given in chapter one. A very detailed soil model contains all these aspects but simpler models can be formulated by adopting only elasticity or by simple combination of elasticity and plasticity. Examples of such models are Mohr – Coulomb and Cam – Clay type models.

Based on the user related characteristics of the FEM model explained in the previous chapter, we are now performing Plaxis calculations for selected load – soil interactions.

These are: tyre – soil system, tool – soil system, simple shear box test and soil cutting by a pendulum type machine.

3.2 SOIL MATERIAL PROPERTIES USED FOR THE MOHR – COULOMB MODEL

For the Mohr – Coulomb model the reference soil for all the presented simulations is a Wageningen clay. This soil was taken from the 7 – 17 cm depth of a Wageningen silty clay loam in a field of mature sugarbeets (Dawidowski and Koolen, 1987).

Soil stress – strain behaviour at low stress levels, or in a first part of severe loading, is usually considered to be elastic. Realistic values of elastic modulus E and Poisson’s ratio ν for agricultural soils are hardly available. Barneveld (1994) mentioned the values $E = 2.20$ MPa and $\nu = 0.45$ for wet dense clay soil having an air content of 5%. These values have been derived from triaxial tests of Dawidowski and Koolen (1987). Realistic values of the lateral earth pressure at rest K_0 are also hardly available for agricultural soil conditions.

A classic way to describe plastic behaviour without hardening uses the concepts of cohesion c and angle of internal friction ϕ . Therefore using the lateral earth pressure derived from Jaky’s formula ($K_0 = 1 - \sin \phi$) is reasonable. The obtained parameter set is shown in Table 3.1 below.

Table 3.1 Soil material properties of the Mohr – Coulomb model

| Parameters | Symbol | Value | Unit |
|--------------------|------------|----------------|-------------------|
| Material behaviour | Type | Drained | - |
| Material model | Model | Mohr – Coulomb | - |
| Young’s modulus | E | 2200 | kPa |
| Poisson’s ratio | ν | 0.45 | - |
| Cohesion | c | 82 | kPa |
| Friction angle | ϕ | 0 | $^{\circ}$ |
| Dilatancy angle | ψ | 0 | $^{\circ}$ |
| Wet soil weight | γ_w | 18.74 | kN/m ³ |
| Dry soil weight | γ_d | 18 | kN/m ³ |

3.3 SOIL MATERIAL PROPERTIES USED FOR THE CAM – CLAY TYPE MODEL

For the Cam – Clay type model the reference soil for all the presented simulations is a silty loam soil.

Konijn (1978) took core samples at different depths of the 20 – 60 cm layer of loam soil after potato harvesting and measured the preconsolidation stress on the sample at field water content. Poodt (1999) estimated for this soil c , ϕ , λ^* , and κ^* .

For details of parameter estimation one can see Koolen et al (2000). The numerical results of Poodt's estimate for the above parameters are shown in Table 3.2

Table 3.2 Soil material properties of the Cam – Clay type model

| Parameters | Symbol | Value | Unit |
|----------------------------|-------------|-------------|-------------------|
| Material behaviour | Type | Drained | - |
| Mataerial model | Model | Soft – Soil | - |
| Poisson's ratio | ν | 0.15 | - |
| Cohesion | c | 23 | kPa |
| Friction angle | ϕ | 35 | $^{\circ}$ |
| Dilatancy angle | ψ | 0 | $^{\circ}$ |
| Wet soil weight | γ_w | 17.79 | kN/m ³ |
| Dry soil weight | γ_d | 17 | kN/m ³ |
| Preconsolidation stress | P_{pre} | 187 | kPa |
| Modified compression index | λ^* | 0.07 | - |
| Modified swelling index | κ^* | 0.0047 | - |

3.4 MODELLING TYRE – SOIL SYSTEM

In this section the dynamic tyre – soil system is modelled by a drained uniaxial loading test using real soil parameters. The two selected soils are the Wageningen clay soil and the Silty loam soil. The default parameters of these soils are listed in Table 3.1 and Table 3.2.

3.4.1 CREATING A GEOMETRY MODEL

As explained in the input step of the user related characteristics of the FEM model, for each new project to be analysed it is important to create a geometry model first. A geometry model is a representation of a real problem and consists of points, lines and clusters.

The real problem in this case was the tyre – soil system. The tyre – soil system is modelled by an axisymmetric loading where the tyre is simulated by a circular area with uniformly distributed vertical stresses and the soil is modelled by vertical cylinder with fixed bottom boundaries in horizontal and vertical directions and with two horizontally fixed lateral walls.

Special boundary conditions have to be defined to account for the fact that in reality the soil is a semi-infinite medium. Without these special boundary conditions the waves would be reflected on the model boundaries which means, returning into the model and disturbing the results.

To avoid these spurious wave reflections absorbent boundaries are specified at the bottom and right hand side boundaries.

The radius (r) of the loaded area is calculated as:

$$L = aT_{IP}r^2 \quad (3.1)$$

where

L = Vertical load ; T_{IP} = Tyre inflation pressure ; a = Tyre constant

The diameter and height of the soil cylinder are 6 m and 2 m respectively. Because of the existing axisymmetry the calculation only considers the cylinder half to the right of the vertical cylinder axis.

The assumed total dynamic load (L) is 96 kN, the inflation pressure (T_{IP}) is 150 kPa and the tyre constant (a) is 4. The radius (r) of the loaded area could be estimated by using Equation (3.1) of Chancellor (1977)

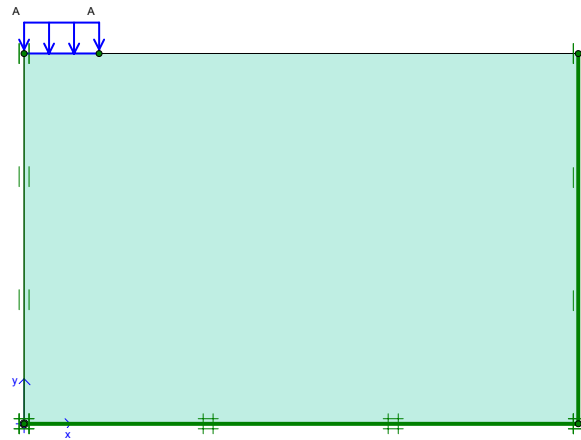


Figure 3.1 The geometry model of a uniaxial loading test with absorbent boundaries

3.4.2 BASIC CALCULATION

After creation of the geometry model a finite element mesh composed of 15-node triangular soil elements is used in the discretization. The mesh is generated with the global coarseness set to 'medium coarse' and of 228 total elements. The initial state of stress is generated by the K_0 - procedure that was derived from Jaky's formula ($K_0 = 1 - \sin \phi$).

The loading consists of a vertical traction of 187.5 kPa and is controlled by the load multiplier $\sum MloadA$. The calculation has been carried out using the dynamic analysis with automatic time stepping procedure. The time step used in the calculation is 0.0001 s and the duration of the vertical load is vary between 0.01 and 0.1 s. The calculation results are illustrated by using figures and curves in the following section

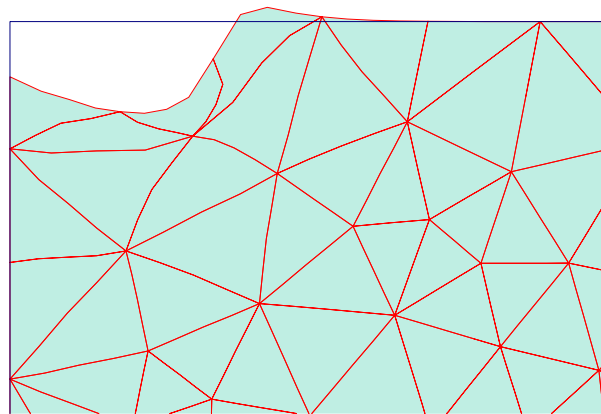
3.4.3 FIGURES PRESENTING CALCULATION RESULTS

The following figures show the soil deformation behaviour during loading

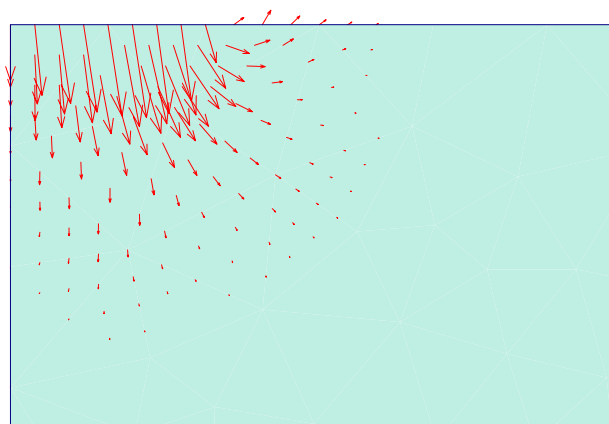
3.4.3.1 Using the Mohr – Coulomb model

The soil used for the Mohr – Coulomb model is the Wageningen clay soil of Table 3.1

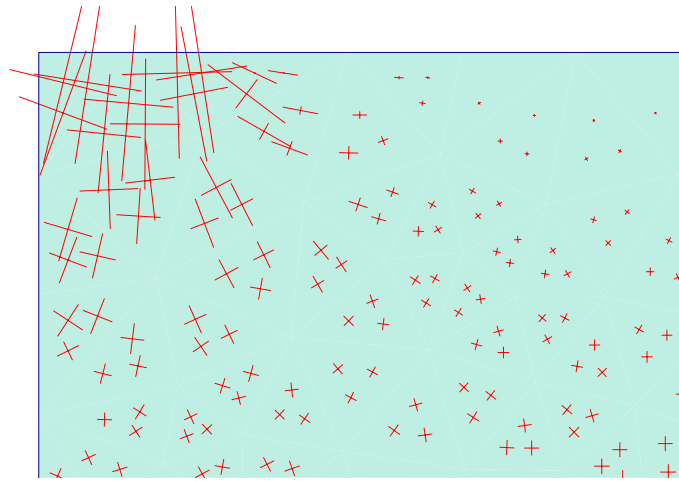
For relatively shorter duration (loading time = 0.01 s)



a) Deformed mesh , extreme total displacement = 9.71 mm



b) Total displacement vectors



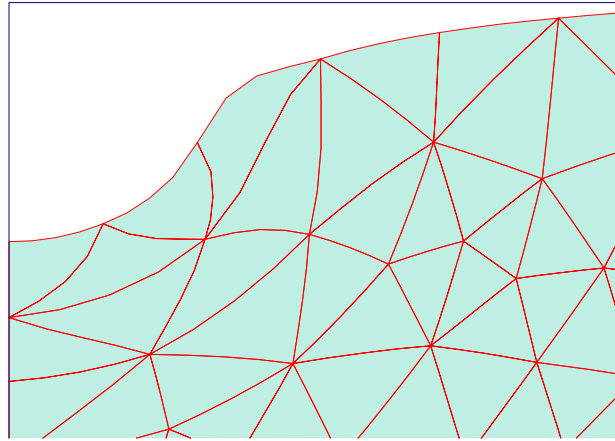
c) Total stress distribution



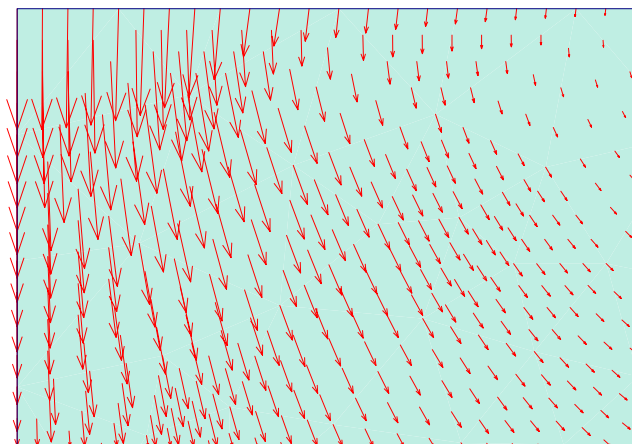
d) Tension failure points

Figure 3.2 a – d. Deformation behaviour of Wageningen clay soil after loading duration of 0.01 s

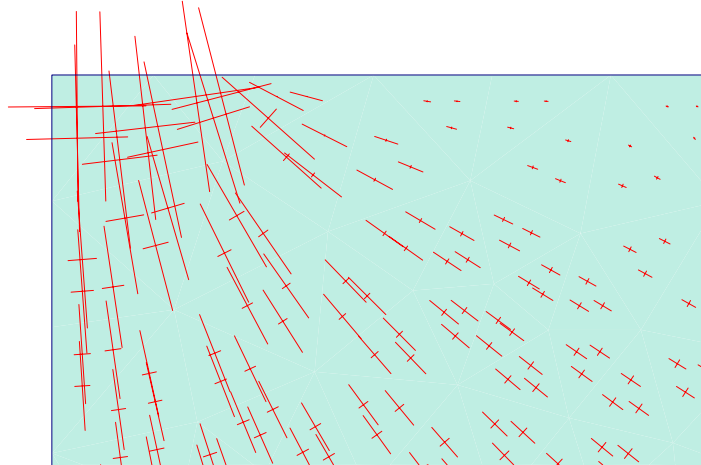
For relatively longer duration of loading (Loading time = 0.1 s)



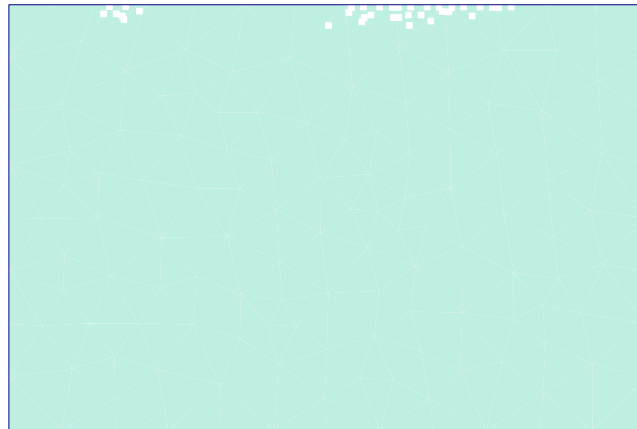
a) Deformed mesh , extreme total displacement = 48.06 mm



b) Total displacement vectors



c) Total stress distribution



d) Tension failure points

Figure 3.3 a – d. Deformation behaviour of Wageningen clay soil after loading duration of 0.1 s

Time effect on load bearing capacity

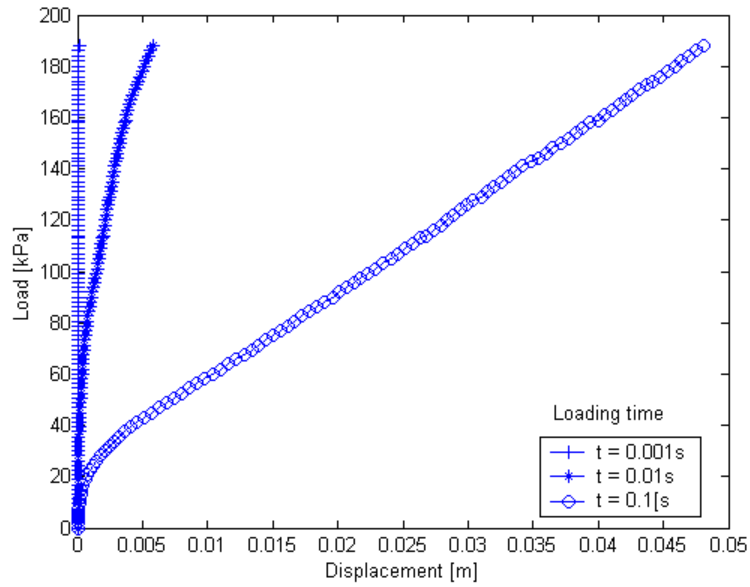
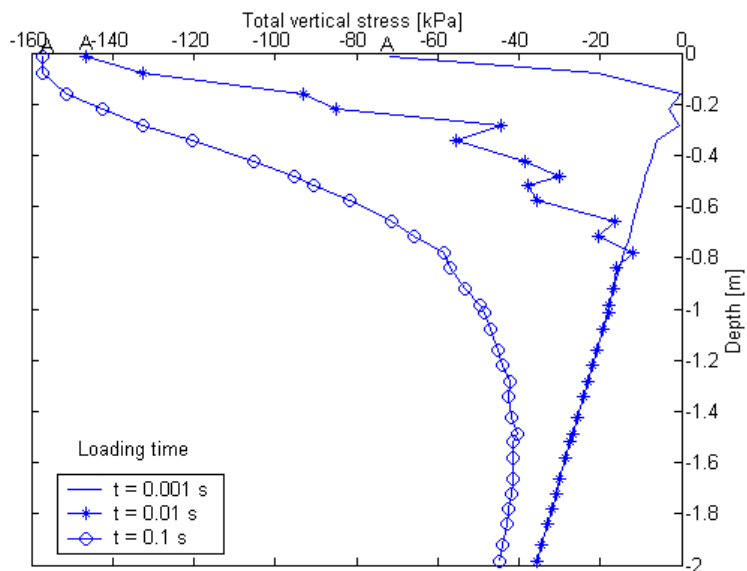
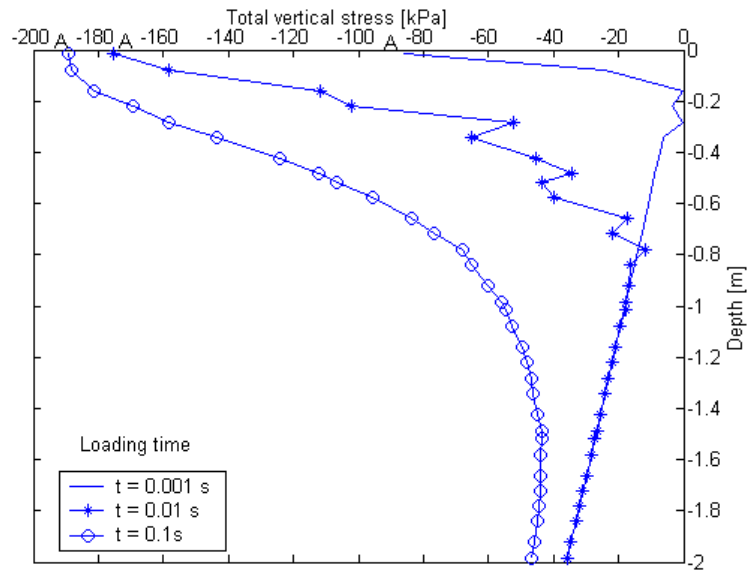


Figure 3.4 Load-displacement curves of the tyre load for Wageningen clay soil

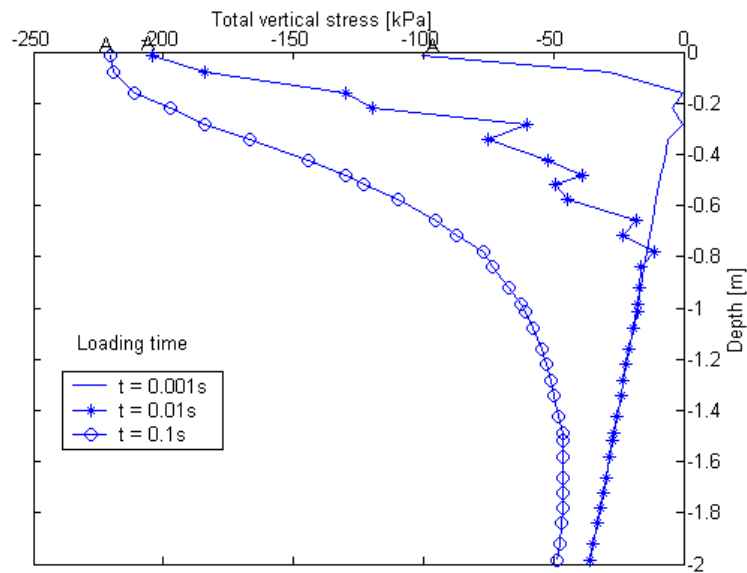
Effect of tyre inflation pressure



a) Tyre inflation pressure (IP) = 125 kPa



b) Tyre inflation pressure (IP) = 150 kPa



c) Tyre inflation pressure (IP) = 175 kPa

Figure 3.5 a – c. Total vertical stress (σ_{yy}) distribution versus depth of Wageningen clay soil. Point A is the nodal point just at the centre of the load

Loading time and shear stress

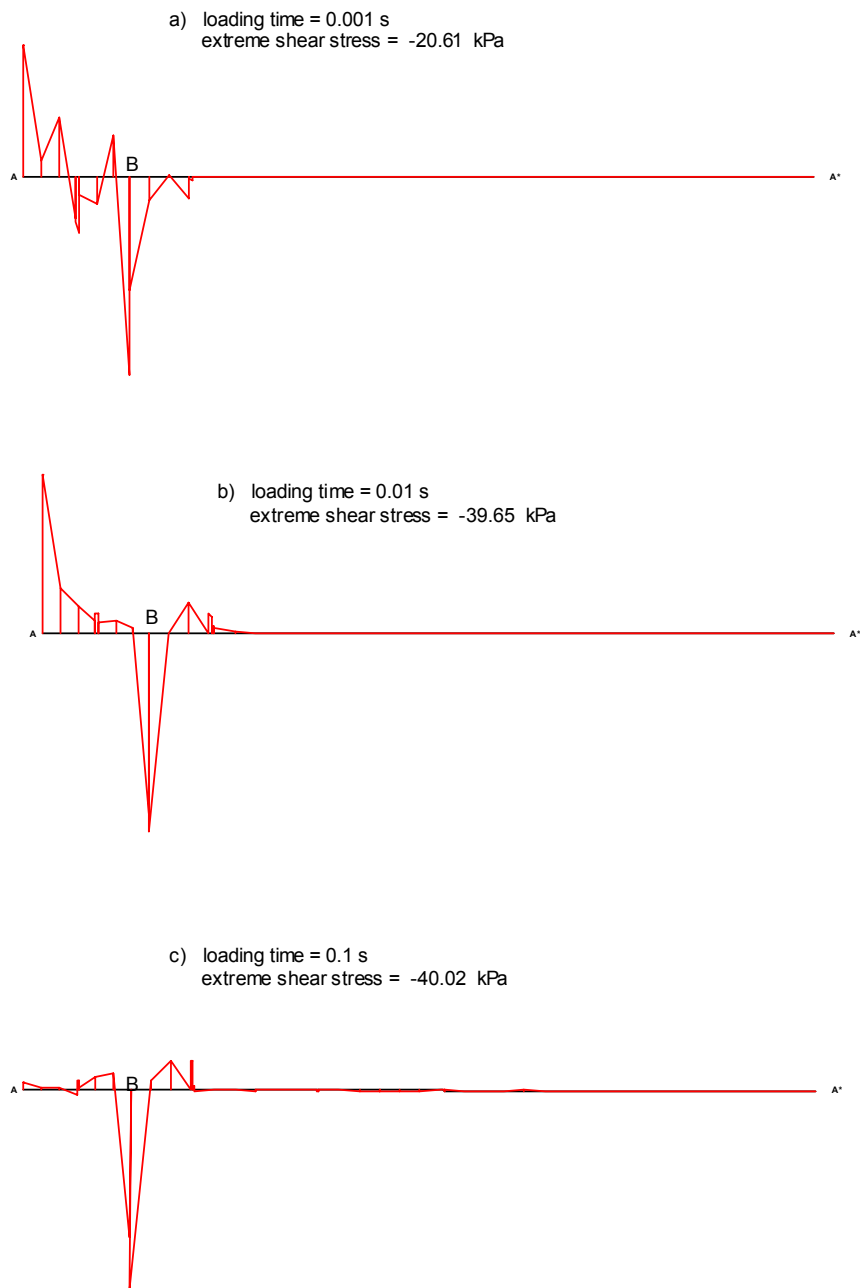
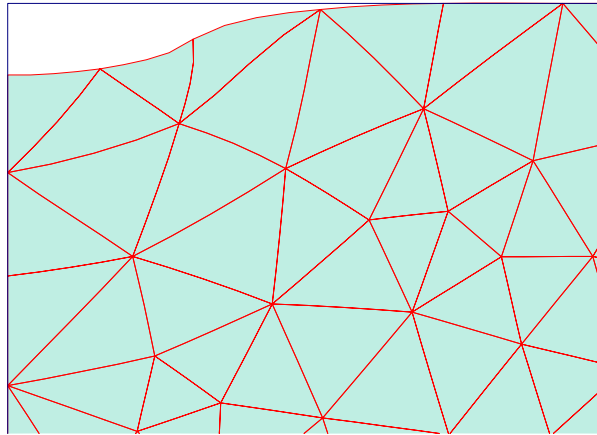


Figure 3.6 a – c. Shear stress distribution of Wageningen clay soil on the cross-section of the surface plane

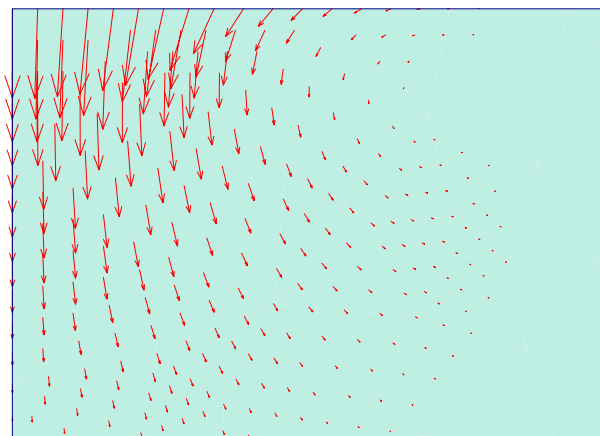
3.4.3.2 Using the Cam – Clay type model

The soil used for the Cam – Clay type model is the Silty loam soil of Table 3.2

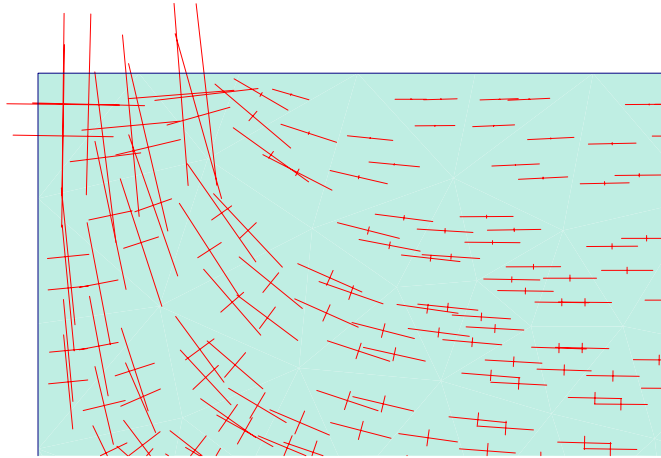
For relatively shorter duration (loading time = 0.01 s)



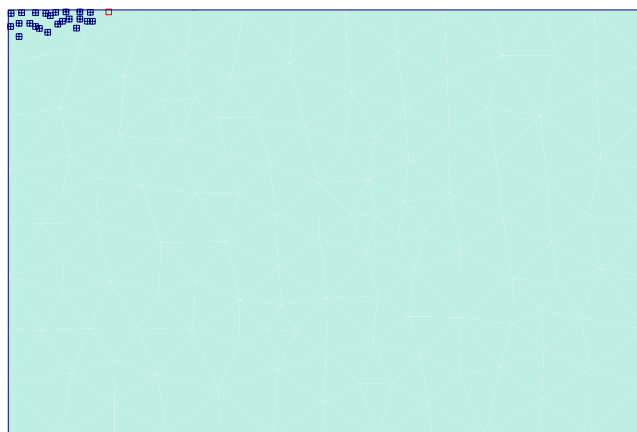
a) Deformed mesh , extreme total displacement = 3.57 mm



b) Total displacement vectors



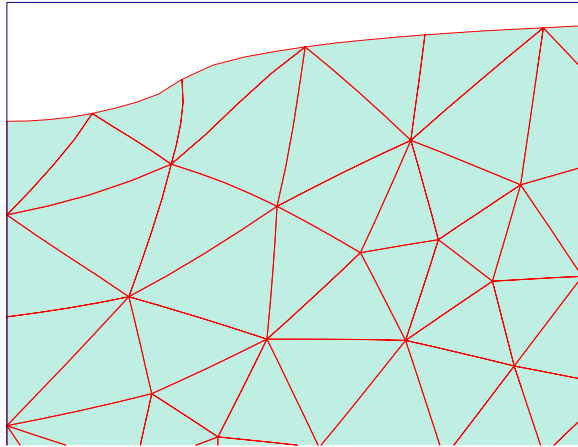
c) Total stress distribution



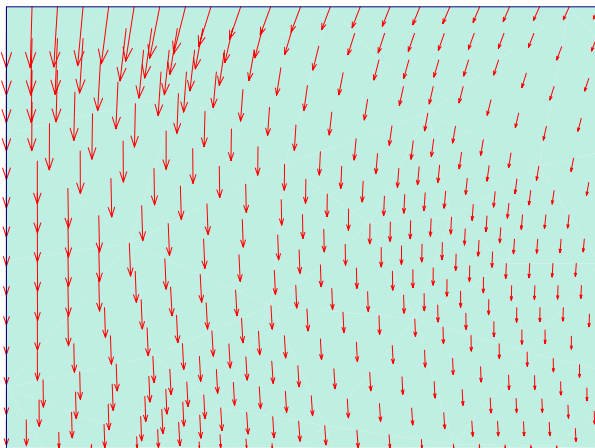
d) Mohr – Coulomb (empty) and plastic cap (filled) failure points

Figure 3.7 a – d. Deformation behaviour of Silty loam soil after loading duration of 0.01 s.

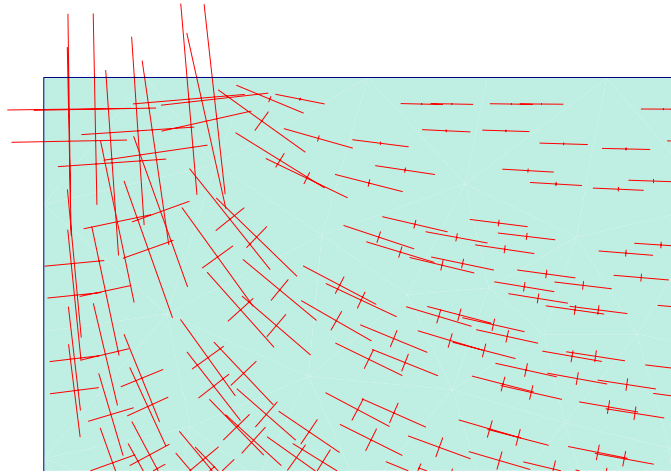
For relatively longer duration (Loading time = 0.1 s)



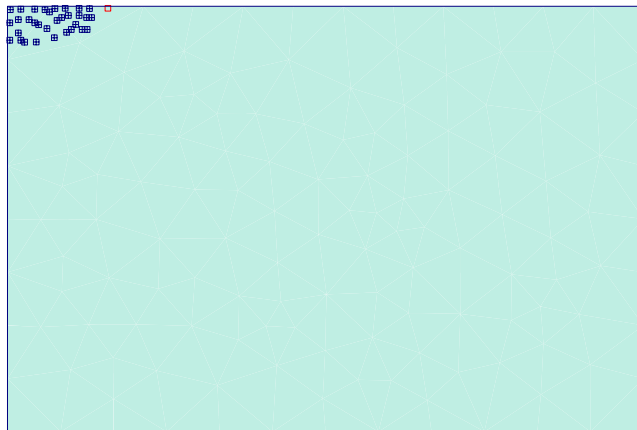
a) Deformed mesh , extreme total displacement = 6.02 mm



b) Total displacement vectors



c) Total stress distribution



d) Mohr – Coulomb (empty) and plastic cap (filled) failure points

Figure 3.8 a – d. Deformation behaviour of Silty loam soil after loading duration of 0.1 s

Time effect on load bearing capacity

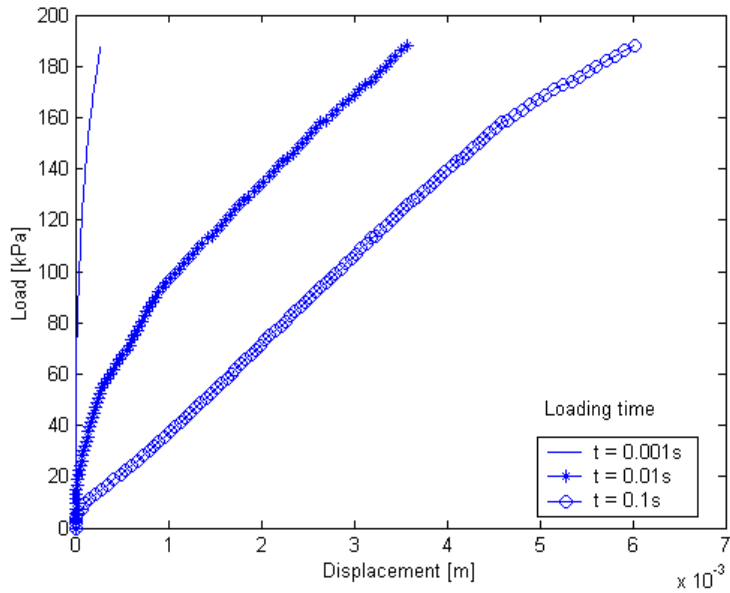
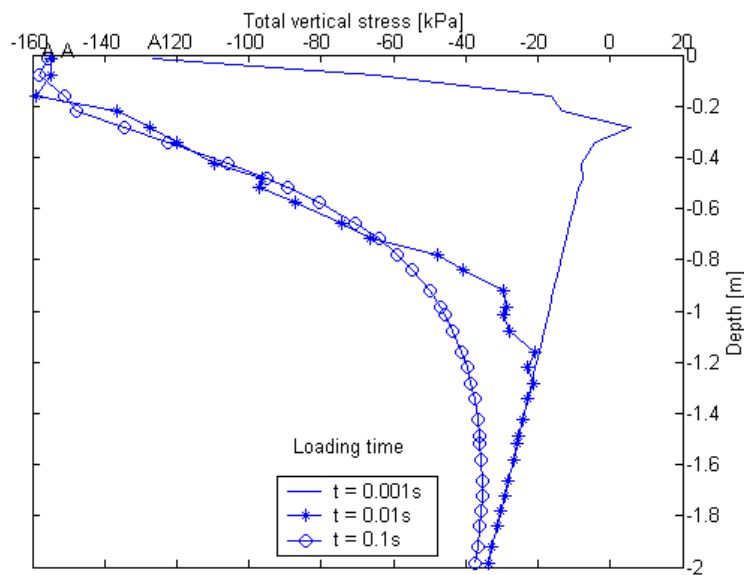
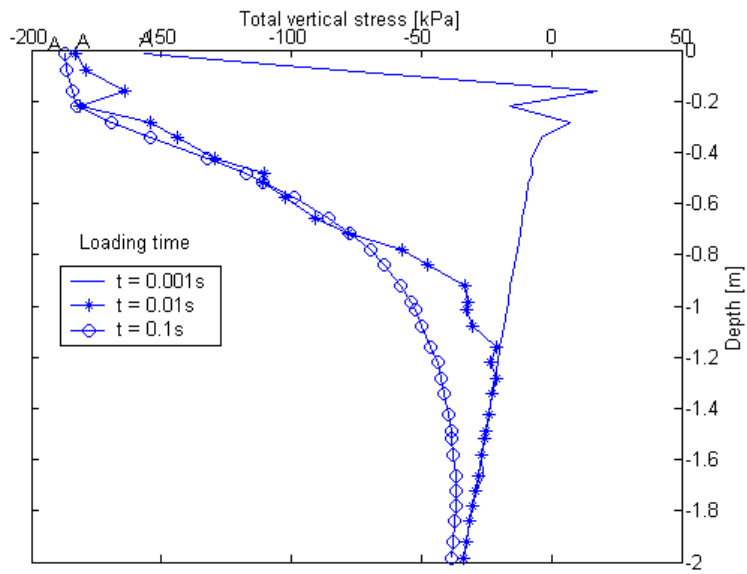


Figure 3.9 Load – displacement curves of the tyre load on silty loam soil

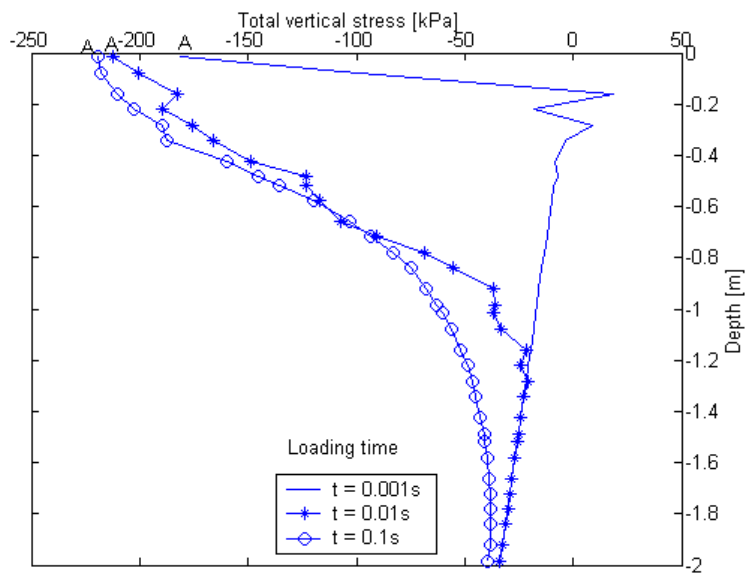
Effect of tyre inflation pressure



a) Tyre inflation pressure (IP) = 125 kPa



b) Tyre inflation pressure (IP) = 150 kPa



c) Tyre inflation pressure (IP) = 175 kPa

Figure 3.10 a – c. Total vertical stress (σ_{yy}) distribution versus depth of Silty loam soil. Point A is the nodal point just at the centre of the load

Time effect and shear stress

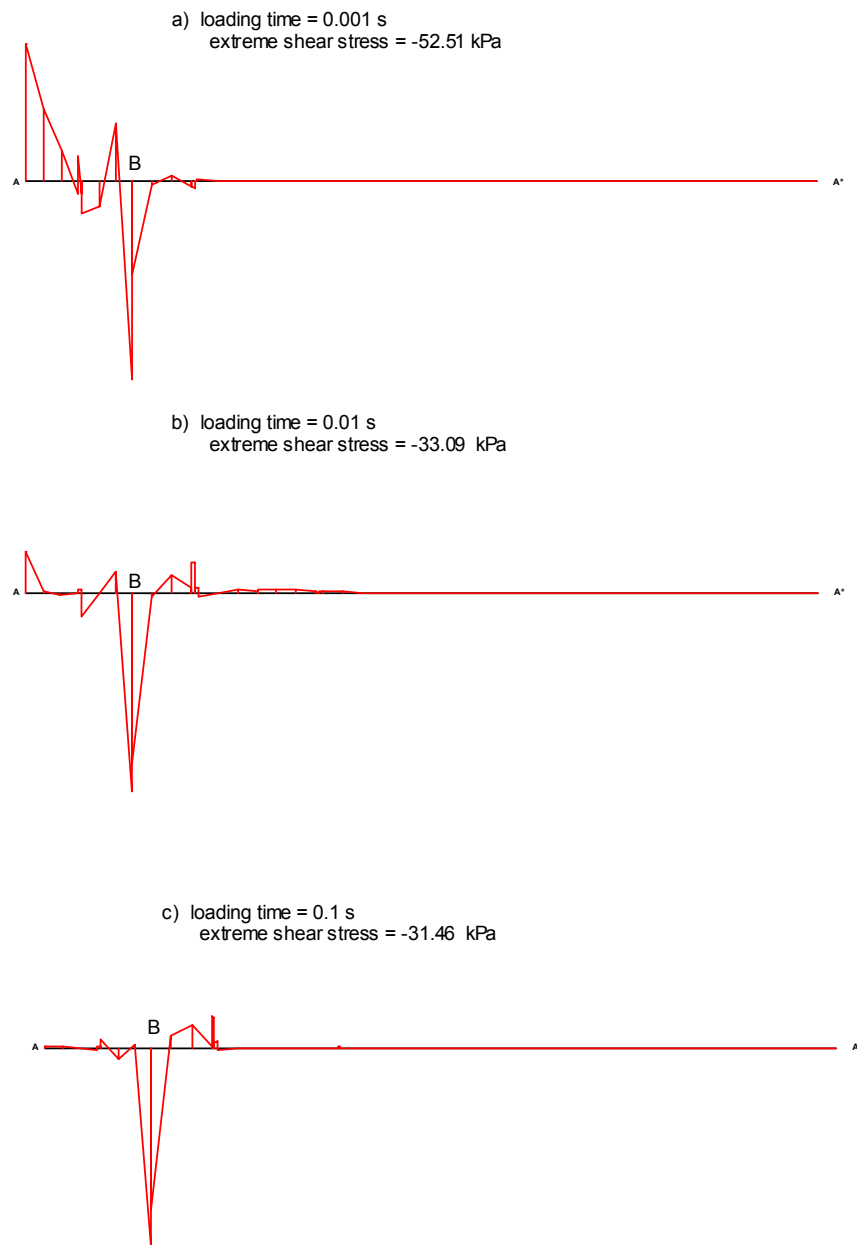


Figure 3.11 a – c. Shear stress distribution of Silty loam soil on the cross-section of the surface plane

3.4.4 GENERAL DISCUSSION AND CONCLUSION

Soil structural deterioration is mainly caused by forces (Febo, 1999). These forces may be applied by tractor tyres, tracks, tillage tools, human or animal traffic, etc.

The reaction of these forces depends on their magnitude, duration, soil type and soil conditions (structure, moisture, etc.).

Dynamic loads applied to the soil surface induce stresses at the load - soil interface as well as deeper in the soil profile. Whether these stresses cause soil deformation or compaction depends on the internal soil strength and on properties of the external applied load and its duration. Dynamic loading events exceeding the internal soil strength induce changes in soil structure, which is the rearrangement of the solid particles due to tension, shear or plastic failure (Wiermann et al, 1999).

3.4.4.1 Dynamic tyre – soil system

The main objective of the present study was to introduce a feasible constitutive relationship of the propagation of vertical stresses within the soil resulting from the applied loads and the duration of such loads. The load transmitted by the moving tyre is dynamic rather than static so effects of soil inertia are included.

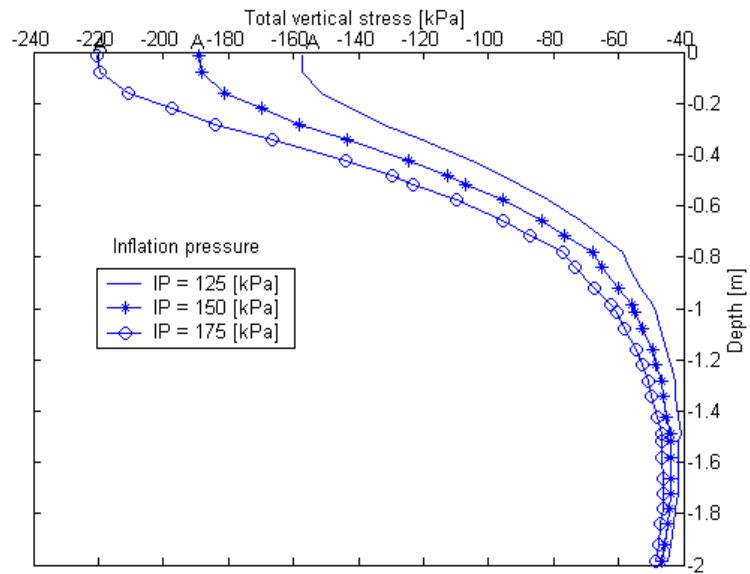
The results discussed here are based on a number of simplifications and idealisations of real dynamic tyre-soil systems. Nevertheless, the results suggest that it should be possible to develop general guide lines for the assessment of the extent of soil structure damage under dynamic loads. Our reference case of modelling dynamic loads on the soil is selected based on similarities with measurements of dynamic tyre pressure on the agricultural fields.

In the present calculation the duration of the load is selected based on short time loading events such as for example wheeling. Time can be an important factor in compaction. For example (Harris, 1971) the time required for a tractor wheel travelling at normal speed to rotate through the angle of effective soil contact (i.e., the duration of loading) is generally less than 0.2 s.

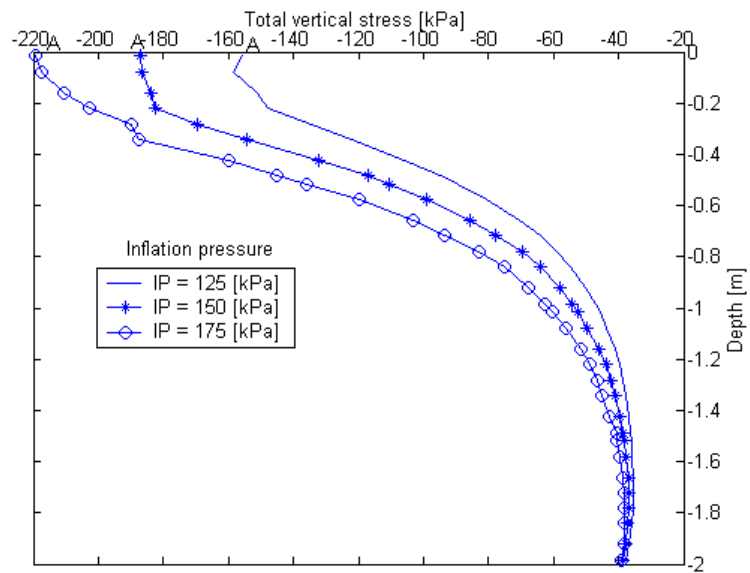
The degree of soil structure deterioration is further determined by increasing dynamic loads and inflation pressures of the tyre. In the present case the dynamic load is increased by increasing the inflation pressure (IP) of the tyre.

In the present study effects of increasing dynamic loads (due to inflation pressure increase) are also investigated. From the calculation results increasing the dynamic load significantly affects especially the first 50 cm depth of the soil and the effect is decreasing when the depth of the soil increases (see Fig. 3.12).

Effect of increasing dynamic loads



a) Wageningen clay soil



b) Silty loam soil

Figure 3.12 a , b. Vertical stress (σ_{yy}) distribution within the depth of the soil profile ; point A is the nodal point just under the centre of the load the load duration is 0.1 s

As we have seen from the deformed mesh of Wageningen clay soil (Fig. 3.2 a) the load sinkage for loading time 0.01s is smaller than that of 0.1s. This is also clearly seen on the load sinkage curves (Fig. 3.4). An area with tensile stresses developed near the surface plane of the soil body (Fig. 3.2 d & 3.3 d). However there are no Mohr – Coulomb failure points, this is because the shear stress is sufficiently small when compared with the cohesion of the soil (Fig. 3.6). Moreover the stress points increased in number when the loading time increased. For instance the number of stress points on the tension state of 0.1 s loading duration is five times as much as that of 0.01 s; this shows deformation of Wageningen clay soil increased when duration of the load increased. However still no Mohr – Coulomb plastic points occurred. This is due to the high cohesion value of the Wageningen clay soil.

In case of Silty loam soil we didn't see significant sinkage difference between 0.01 and 0.1s of loading time (see the comparison between Fig. 3.7 a & 3.8 a). Besides the sinkage is very small in both durations, when comparing with that of Wageningen clay soil (see the comparison between Fig. 3.2 a & 3.7 a for loading time of 0.01s and Fig. 3.3 a & 3.8 a for loading time of 0.1 s). However the number of stress points on the plastic cap state is increased reasonably for loading time of 0.1 s (compare Fig. 3.7 d & Fig. 3.8 d) which means compaction increased.

When comparing soil displacement vectors of the two soils , displacement vectors are generally directed towards the load displacement for both soils. However at small instant of loading time (for example at $t = 0.01s$, Fig. 3.2 a, b) some soil displacement vectors of Wageningen clay soil especially at the edge area of the load have moved upwards. This behaviour of Wageningen clay soil together with the deformed mesh qualitatively agree with Barneveld (2000) and Soehne (1953).

When we see the vertical stress (pressure) distribution under the load (Fig. 3.5 and 3.10), it was also loading time dependent for both soils. However the effect of loading time is lower for the case of Silty loam soil. Especially for relatively longer duration this is due to the high shear strength of Silty loam soil due to its higher friction angle; the results are qualitatively similar to Othman (1999). Furthermore pressure differences have been seen on pressure distributions between 0.01 and 0.1s and the magnitude of pressure distribution at 0.1s is higher than that of 0.01s for both soils. However the pressure distribution was much more in the horizontal direction for Silty loam soil especially at $t = 0.01s$. Of course the magnitude is minimised for silty loam soil. Soehne (1958) also analysed pressure spread much more in the horizontal direction when tyres interacted with dry soil.

The extreme shear stress appeared at the edge of the load-soil contact area (point B of Fig. 3.6 and Fig. 3.11). However no Mohr-Coulomb failure points appeared for Wageningen clay soil. This is because shear stress due to applied load is less than shear strength of the soil. Only plastic tension points are existing; this indicates that soil may also fail in tension instead of shear. For the Mohr – Coulomb model used in Plaxis the tension cut-off is by default selected with a tensile strength of zero.

For Silty loam soil a few number of Mohr – Coulomb failure points are existing at the edge of the load – soil contact area. This implies that the shear stress due to applied load reached the shear strength of the soil at least at this point (point B, Fig. 3.11).

In both soil types the magnitude of shear stresses is very small and very non – linear in distribution compared with that of total vertical stresses.

On the other hand plastic cap points were existing in higher numbers at the load – soil contact area where the uniformly distributed vertical stresses are higher than the preconsolidation stress of the soil (see Fig. 3.7 d & 3.8 d; these show areas of soil structural damage (compaction)).

3.4 .4 .2 Basic conclusion

- Dynamic loads applied to the soil surface induce stresses at the load – soil interface as well as deeper in the soil profile. These stresses increase when the load and the duration increase. Besides such stresses affect the structure of the soil under the load. These structures refer to the arrangement of the soil particles under the area of the load. The voids between particles (called pores) serve as conduit to move water, air and plant nutrients into the root zone, they also provide pathways for root growth and development
- Effect of dynamic load varies depending on soil mechanical properties
- Increase of magnitude of dynamic load increases magnitude of compaction or deformation, depending on the soil type on which the load is applied
- Magnitude of soil stress (pressure) distribution deeper in the soil profile depends on the duration of the load applied
- The type of soil structure deterioration under dynamic load is different for both soil types: structure of Silty loam soil deteriorates easily by compaction whereas that of Wageningen clay soil deteriorates by deformation especially for relatively longer duration of loads
- Soil particle movement during dynamic loading is also time dependent. For example at small instant of loading time some soil displacement vectors have moved upwards and for relatively longer loading time soil displacement vectors have moved towards the loading direction
- In general it is not erroneous to summarise that tractor loads and the duration of such loads are among the factors which predict the extent of soil structure degradation by dynamic loads.

3.5 MODELLING WEDGE PENETRATION TEST

In this section the modelling of a wedge penetration test is presented using real soil parameters. The types of wedges selected are the 60 and 30 degree wedges. For simplicity the wedges are assumed to be fully smooth. The forces acting on the wedge could be separated into several components and these components must be in equilibrium. The force components are shown in Figure 3.13, where N represents normal forces and T represents tangential forces.

$$P = P_1 + P_2 = 2N \sin(\alpha/2) + 2N\mu' \cos(\alpha/2) \quad (3.2)$$

where

P = total force (load) on the wedge

P_1 = component of resistance resulting from the normal force on the wedge

P_2 = component of resistance resulting from the tangential force on the wedge

N = normal force; T = tangential force; α = wedge angle ;

μ' = coefficient of soil-metal friction

For fully smooth wedge $\mu' = 0$, so that

$$P = P_1 = 2N \sin(\alpha/2) \quad (3.3)$$

The selected two soils are the Wageningen clay soil and the Silty loam soil. The default parameters of these soil are listed in Table 3.1 and Table 3.2.

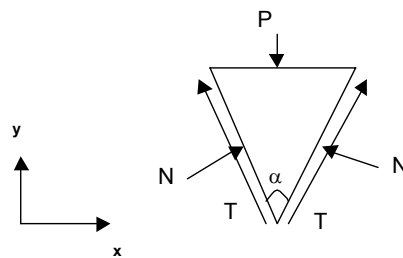


Figure 3.13 Forces on and shape of the wedge (Kostritsyn, 1956).

3.5.1 CREATING A GEOMETRY MODEL

For each new project to be analysed it is important to create a geometry model first. A geometry model is a representation of a real problem and consists of points, lines and clusters. The geometry of the soil bin was 2 m by 6 m dimensions. Furthermore the case is plane strain modelled with 6 - noded triangular elements. The total number of discretized elements is 248 for a 60 degree wedge and 238 for a 30 degree wedge. The finite element mesh used for the discretization is the 'medium coarse' mesh. Element nodes that represent the bottom of the soil bin are fixed in both (vertical and horizontal) directions.

Element nodes representing the raised edge of the soil bin are fixed in horizontal direction and can move freely in vertical direction. For simplicity take one half of the geometry model by assuming a symmetrical wedge penetration. The following Table 3.3 summarises the discretization process. Absorbent boundaries are applied at the bottom and right hand side boundary.

Table 3.3 Soil body discretization for penetration

| Types of wedge | 30 tip angle | 60 tip angle |
|-------------------------|---------------|---------------|
| Model | Plane strain | Plane strain |
| Elements | 6 – node | 6 – node |
| Mesh | Medium coarse | Medium coarse |
| Number of elements | 238 | 248 |
| Number of nodes | 517 | 537 |
| Number of stress points | 714 | 744 |

The finite element model simulation is starting by creating the geometry model



Figure 3.14 The magnified initial geometry model of 30 degree wedge penetration with prescribed displacement

3.5.2 BASIC CALCULATION

After creation of a geometry model and consecutive mesh generation, the initial state of stress was generated by the K_0 - procedure that is derived from Jaky's formula ($K_0 = 1 - \sin \phi$) before starting the penetration process.

The penetration consists of the prescribed vertical wedge displacement of 10 cm.

The calculation is controlled by the displacement multiplier $\sum Mdisp$. The calculation involves the dynamic analysis with automatic time stepping procedure. The time step used in the calculation is 0.0003 s which is less than the critical time step calculated by Eqn (2.15). The ratio of low penetration velocity to high penetration velocity (v_l / v_h) varies between 0.01 & 0.02. The following Table 3.4 shows the penetration velocity for the above prescribed displacement.

Table 3.4 Penetration velocity during wedge penetration

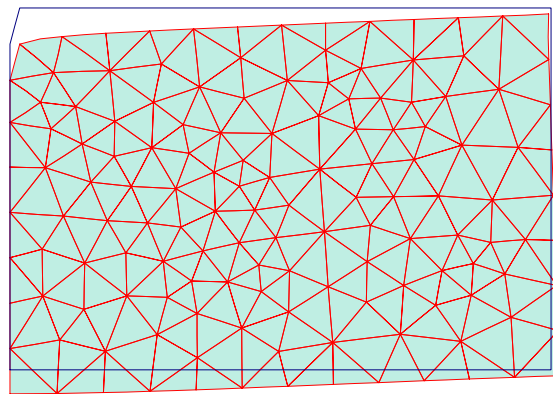
| | | Penetration velocity in [m/s] | | | |
|------------------------------|-------|-------------------------------|-------|--------------|--|
| | | Types of wedge | | | |
| | | 30 tip angle | | 60 tip angle | |
| Penetration time in [s] | Wclay | Sloam | Wclay | Sloam | |
| 0.01 | 5.0 | 5.0 | 5.0 | 8.0 | |
| 0.10 | 0.6 | 0.7 | 0.7 | 0.8 | |
| 1.0 | 0.1 | 0.1 | 0.1 | 0.1 | |
| Where | | | | | |
| Wclay = Wageningen clay soil | | | | | |
| Sloam = Silty loam soil | | | | | |

3.5.3 FIGURES PRESENTING CALCULATION RESULTS

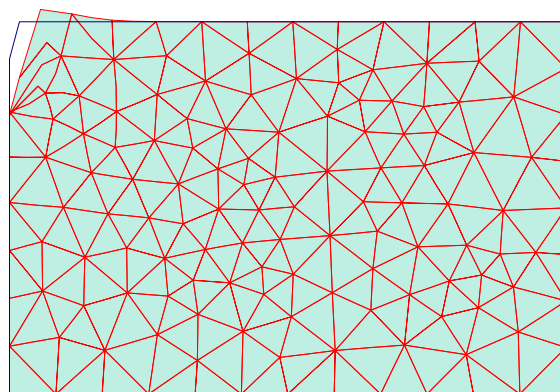
The following Figures 3.15 to 3.18 show the soil penetration behaviour during penetration with low and relatively high velocity.

3.5.3.1 Using the Mohr – Coulomb model

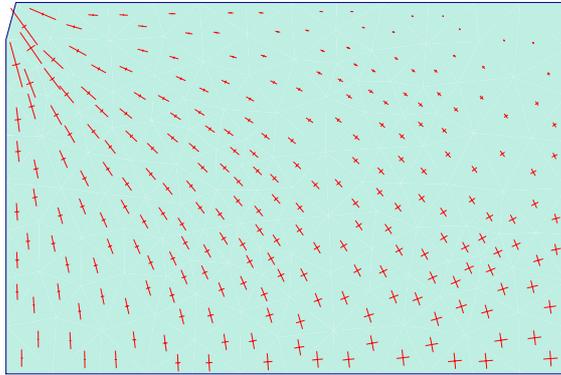
The soil used for this model is the Wageningen clay soil and the wedge used for penetration is the 30 degree wedge.



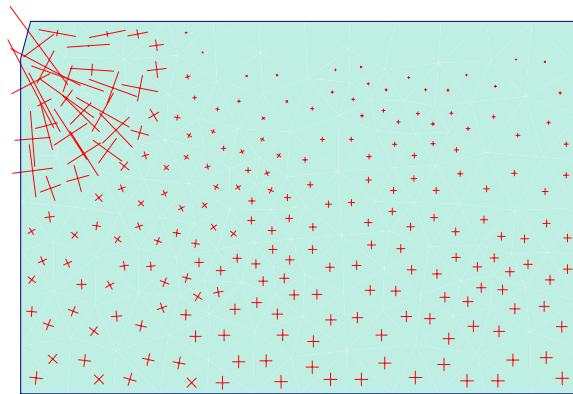
a) Deformed mesh , $v_p = 0.1 \text{ m/s}$



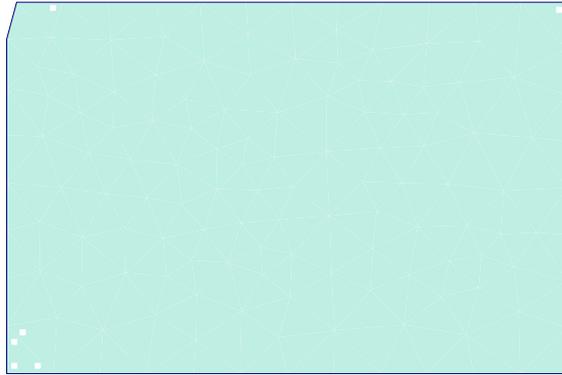
b) Deformed mesh , $v_p = 5.0 \text{ m/s}$



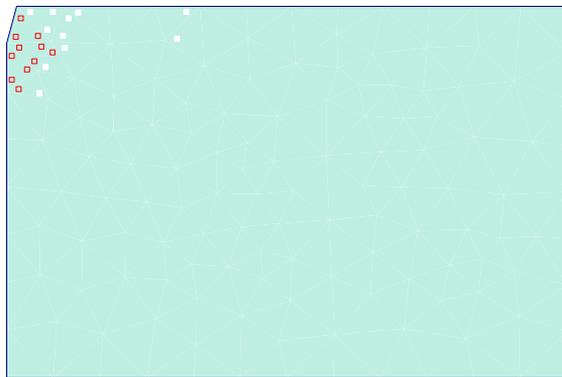
c) Soil total stress distribution , $v_p = 0.1 \text{ m/s}$



d) Soil total stress distribution , $v_p = 5.0 \text{ m/s}$



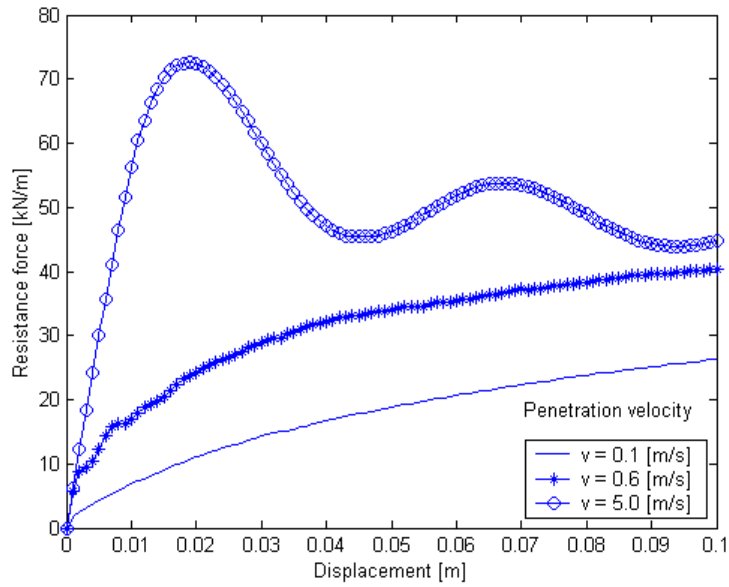
e) Tension failure points , $v_p = 0.1 \text{ m/s}$



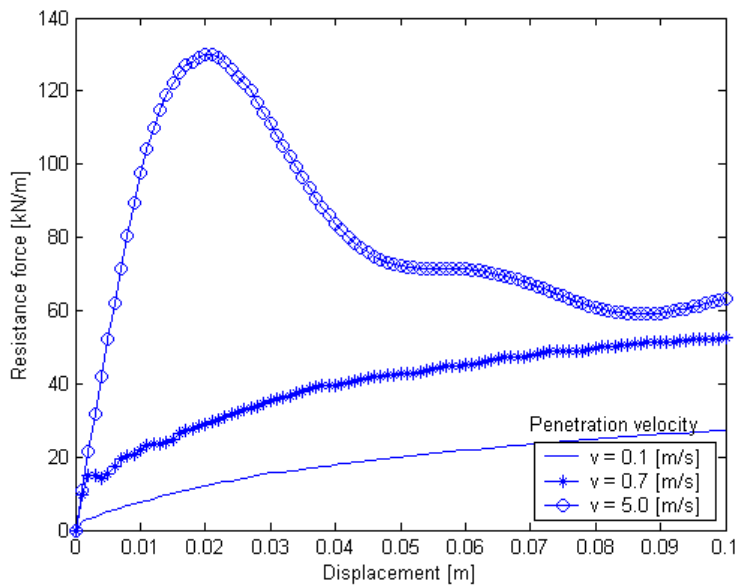
f) Mohr – Coulomb (empty) and tension failure points , $v_p = 5.0 \text{ m/s}$

Figure 3.15 a – f. Deformation behaviour of Wageningen clay soil after penetration of 30 degree wedge with low and relatively high velocity

Effect of penetration velocity to resistance force



a) 30 degree wedge

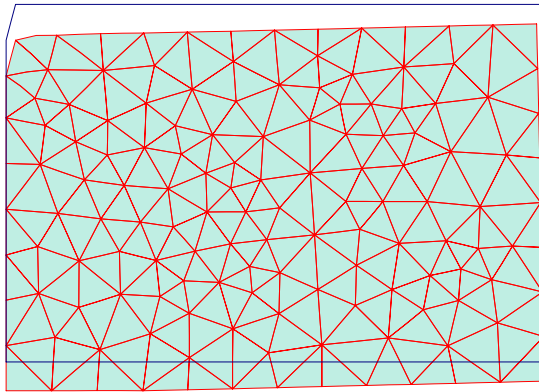


b) 60 degree wedge

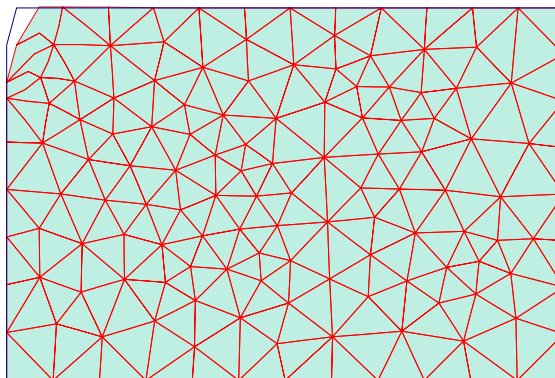
Figure 3.16 a, b. Resistance force versus displacement curves of 30 and 60 degree wedges during penetration of Wageningen clay soil

3.5.3.2 Using the Cam – Clay type model

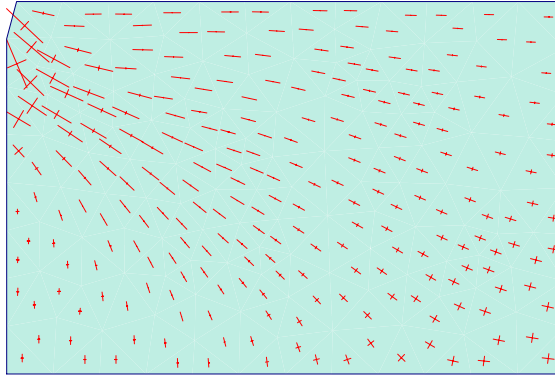
The soil used for this model is the Silty loam soil of Table 3.2 and the wedge used for penetration is the 30 degree wedge.



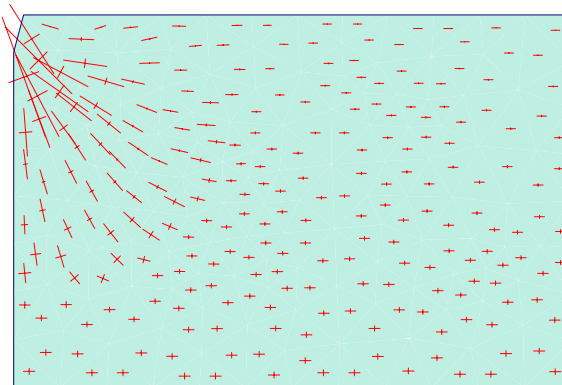
a) Deformed mesh , $v_p = 0.1 \text{ m/s}$



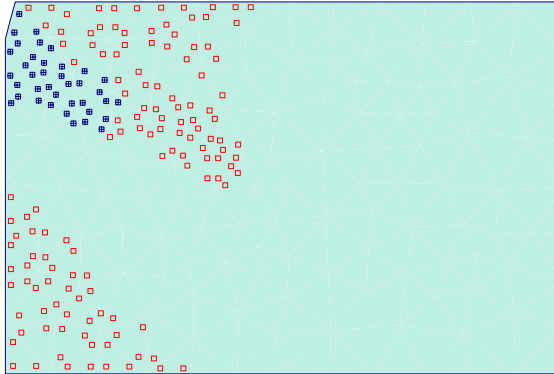
b) Deformed mesh , $v_p = 5.0 \text{ m/s}$



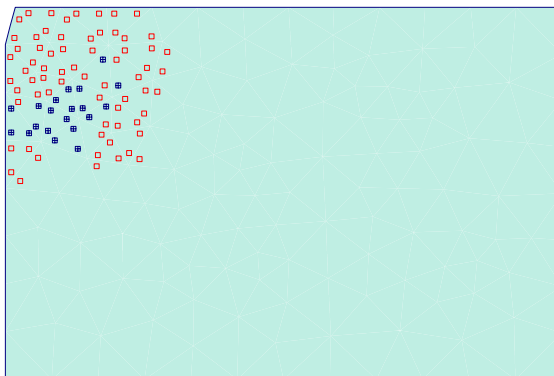
c) Total stress distribution , $v_p = 0.1 \text{ m/s}$



d) Total stress distribution , $v_p = 5.0 \text{ m/s}$



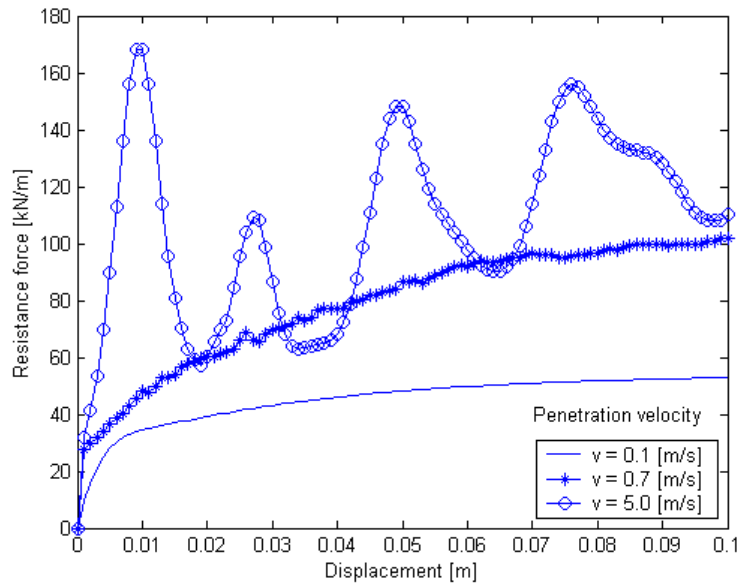
e) Mohr – Coulomb (empty) and plastic cap (filled) failure points, $v_p = 0.1 \text{ m/s}$



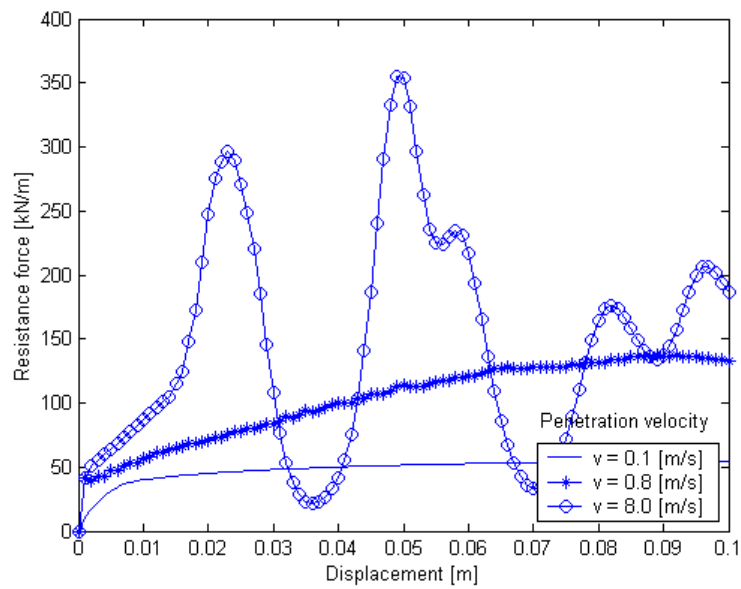
f) Mohr – Coulomb (empty) and plastic cap (filled) failure points, $v_p = 5.0 \text{ m/s}$

Figure 3.17 a – f. Deformation behaviour of Silty loam soil after penetration of 30 degree wedge with low and relatively high velocity

Effect of penetration velocity to resistance force



a) 30 degree wedge



b) 60 degree wedge

Figure 3.18 a, b. Resistance force versus displacement curves of 30 and 60 degree wedges after penetration into Silty loam soil

3.5.4 GENERAL DISCUSSION AND CONCLUSION

Background summary

Soil reactions associated with the overall orientation of tools have been studied with simplified systems (Fig. 3.13). Generally inclined planes have been forced through the soil to determine the force relations that are associated with different tool orientations (William et al, 1968). William and Glen (1968) further showed (depending on the shape and types of the tool used) basic processes of cutting or separation, shear failure, friction failure, compression failure and/or plastic failure. Moreover any combination of these processes may occur as the tool is forced into the soil.

This means when soil is strained by the passage of a tillage tool the soil may react by compacting, deformation or by some type of failure that causes detachment of the soil. When the soil is compacted its strength may be increased and larger draft resistances of tools may result. Soil behaviour can thus be described by expressing the resistance to penetration at a given depth, the type and degree of failure occurring, and the direction of soil particles movement at different penetration times.

Wedges are used frequently as aids to support machines that are studied in the field (Koolen and Kuipers, 1983). Wedges are also applied in a number of trench making machines. A penetrating wedge induces a two dimensional process in the soil and is therefore well – suited for process studies (Koolen and Kuipers, 1983).

Penetration is thus often termed cutting since cutting usually implies a localised soil failure in the neighbourhood of the cutter. Furthermore dynamic penetration is important in a dynamic situation such as the vibratory cutting of soil (Kondner, 1959).

If the penetration is conducted slowly with time allowing for equilibrium, then the penetration should be static penetration.

3.5.4.1 Penetration of Wclay soil

Two types of acute wedges are selected for the process; one with 30 degree and the other with 60 degree. Both wedges have the same height but different width relative to their variations of tip angles.

A displacement of 10 cm inside the soil has been investigated by using different penetration velocity (low and high). The dimensions of the wedge, tip angle and penetration velocity are selected based on their suitability for process studies.

A 30 degree wedge penetration

When the 30 degree wedge penetrates into the Wclay soil, the reaction of the soil depends on the dimensions of the wedge, tip angle, soil properties and penetration velocity. As expected the resistance force of the soil increases as the penetration velocity increases (Fig. 3.16 a & 3.18 a). At the initial phase of penetration (for the first few displacements) the resistance force increases rapidly and thereafter the force changes steadily; this was true especially at low penetration velocity.

At higher penetration velocity, the resistance force rises rapidly in the same way for the low penetration velocity case but with large amplitude at the first instance of penetration. Thereafter it fluctuates with diminishing amplitude to come to residual value.

The following differences were listed at low and high penetration velocity. The nodal point selected for the comparison was the node at the tip of the wedge.

| | Low penetration velocity | High penetration velocity |
|----------------------|---|--|
| Zone of influence: | large zone of influence | relatively small |
| Deformation: | large, tensile cracks appeared at the surface boundary and at the bottom of the symmetry axis (Fig. 3.15 a) | relatively small, tensile cracks as well as shear strain (Fig. 3.15 b) |
| Soil movement: | mainly downward following deformation patterns | mainly upward opposite to the wedge movement |
| Stress distribution: | relatively high around the wedge tip (Fig. 3.15 c) | very high at wedge tip and concentration specified in the zone of influence (Fig. 3.15 d) |
| Failure points: | only few tension points due to tensile cracks (Fig. 3.15 e) | increased number of tension points and shear points around the wedge tip and wedge surface (Fig. 3.15 f) |

NOTE: Zone of influence means area of the soil body influenced by the wedge during penetration at a certain time

60 degree wedge penetration

What has been described above for 30 degree wedge penetration also occurs for 60 degree wedge penetration. The main differences are differences in magnitude (quantitatively). Qualitatively they are similar.

| | 30 degree tip angle wedge | 60 degree tip angle wedge |
|--------------------|--|--|
| Zone of influence: | small | relatively large |
| Deformation: | small | relatively large |
| Penetration force: | fewer in magnitude | relatively large especially at higher penetration velocity and the difference is small at low penetration velocity |
| Failure points: | generally fewer in numbers the difference is significant after Silty loam penetration, fewer cap points and more shear points are resulted | increased in number, more number of cap points and few number of shear points after Silty loam penetration |

3.5.4.2 Penetration of Silty loam soil

30 / 60 degree wedge penetration

What has been described for penetration into Wclay is also listed for penetration into silty loam soil; the main differences are listed below.

| | Silty loam soil | Wageningen clay soil |
|--------------------|--|---|
| Deformation: | small, much compaction especially at low penetration velocity | large, especially at lower penetration velocity and little compaction at higher penetration velocity |
| Penetration force: | at higher penetration velocity, very large in magnitude, increases unsteadily (very fluctuating by large and varying amplitude) whereas at low velocity, increase steadily (Fig. 3.18) | at higher penetration velocity, relatively small in magnitude, increases unsteadily (relatively less fluctuating with smaller amplitude) whereas at lower velocity increases steadily (Fig. 3.16) |
| Failure points: | more number of caps and shear points appeared towards the depth of the soil in front of the wedge tip especially at low penetration velocity (Fig. 3.17 f) | few number of tensile points and few shear points appeared around the wedge tip and wedge surface at high penetration velocity (Fig. 3.15 f) |

3.5.4.3 Basic conclusion

- As the wedge tip angle increases, the penetration force increases, the size of the zone of influence increases, deformation / compaction increases (depends on soil deformability or compactability). At low penetration velocity increase of tip angle among acute wedges is insensitive.
- As acute wedges penetrated into the soil at high velocity, the reaction force reached its maximum during the first instance of penetration and thereafter changes steadily with diminishing amplitude and comes to residual resistance.
- As the wedge tip angle increases, not only penetration force increases but also the amplitude of fluctuation force increases. This was true especially at penetration of hard soil (silty loam) with high velocity.
- At lower penetration velocity, relatively much soil compaction resulted after hard soil (Sloam) penetration and large deformation resulted after soft soil (Wclay) penetration .
- In general soil reactions during acute wedge penetration depend on wedge dimension, tip angle, soil properties and penetration velocity.

3.6 MODELLING SHEAR BOX TEST IN PLAXIS

In this section, the modelling of drained shear box tests is presented using real sets of soil parameters. The two models used for the FEM calculation are the Mohr – Coulomb and the Cam – Clay models, the soil material properties used for these models are given in Table 3.1 and Table 3.2 respectively.

Calculation results are presented in the following section using figures.

3.6.1 CREATING A GEOMETRY MODEL

For each new case to be analysed it is important to create a geometry model first.

A geometry model is a representation of a real problem and consists of points, lines and clusters.

A shear box test can simply be modelled by means of plane strain geometry of 0.1 by 0.1 m dimensions (Figure 3.19).

The boundaries are horizontally fixed during vertical loading and vertically fixed for shearing displacements.

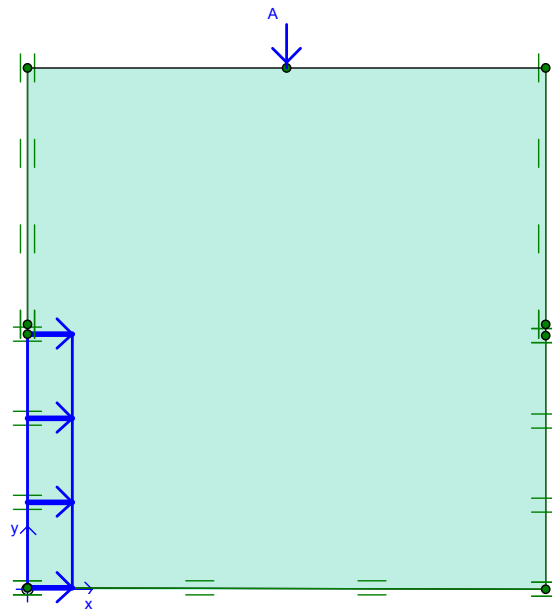


Figure 3.19 Simplified geometry model of shear box test with load A and prescribed displacement

3.6.2 BASIC CALCULATION

After the creation of a geometry model, a finite element mesh composed of 6-node triangular soil elements is used in the discretization. The mesh is generated with the global coarseness set to 'medium coarse' and a total of 284 elements is formed after the discretization. The result is shown in Fig. 3.20. The initial state of stresses is generated by the K_0 - procedure that is derived from Jaky's formula ($K_0 = 1 - \sin \phi$), where K_0 is coefficient of lateral earth pressure and ϕ is internal friction angle.

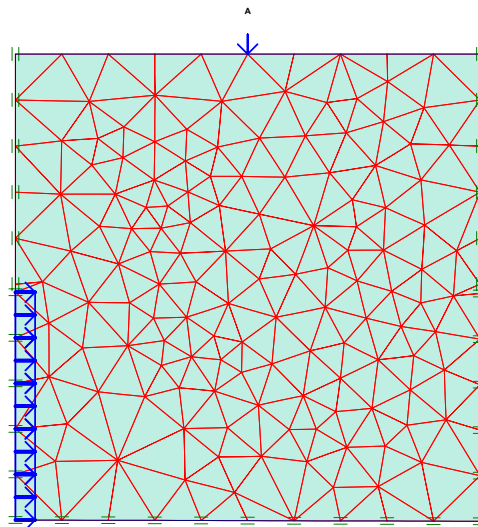


Figure 3.20 The medium coarse undeformed mesh generated for Wageningen clay soil before shear started

The applied values of the point force (vertical load) and the prescribed displacement are controlled by the load multiplier ($\sum MloadA$) and the displacement multiplier ($\sum Mdisp$) respectively. The calculation involves two phases. The loading phase and the shearing phase. Both phases are analysed in dynamic way with automatic time stepping procedure.

The time step used in the calculation is ($\Delta t = 1 * 10^{-4} s$) which is less than the critical time step calculated by Eqn (2.15). If the time step is too large, the solution will display major deviations and the calculated response will be unreliable. Therefore the chosen time step must be small so that a wave in a single step displaces less than a single element.

In the first calculation phase the sample is vertically compressed by vertical pressure of $\sigma_n = 82kPa$ ($\sum MloadA = 82kPa$) for Wageningen clay soil and $\sigma_n = 39kPa$ for Silty loam soil ($\sum MloadA = 39kPa$) and assuming fully drained behaviour of the two soils for a duration of 1 s.

After this phase the displacements are reset to zero. On the second phase the soil specimen of the lower box is horizontally sheared by a horizontal shear velocity of 0.1 cm/s for a displacement of 1 cm.

3.6.3 FIGURES PRESENTING CALCULATION RESULTS

The following Figures 3.21 to 3.24 show the soil deformation behaviour during shearing process

3.6.3.1 Using the Mohr – Coulomb model

The soil used for the Mohr – Coulomb model is the Wageningen clay soil of Table 3.1.

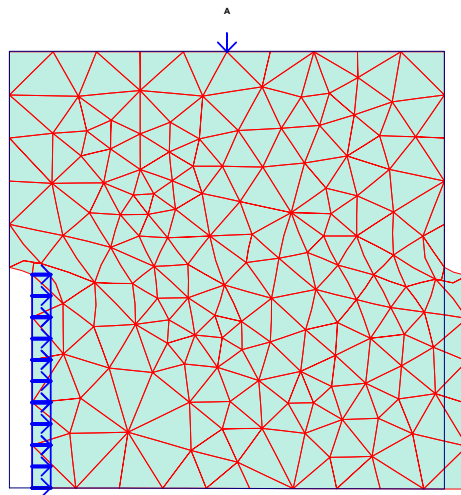


Figure 3.21 The deformed mesh of Wageningen clay soil after shearing for 1cm

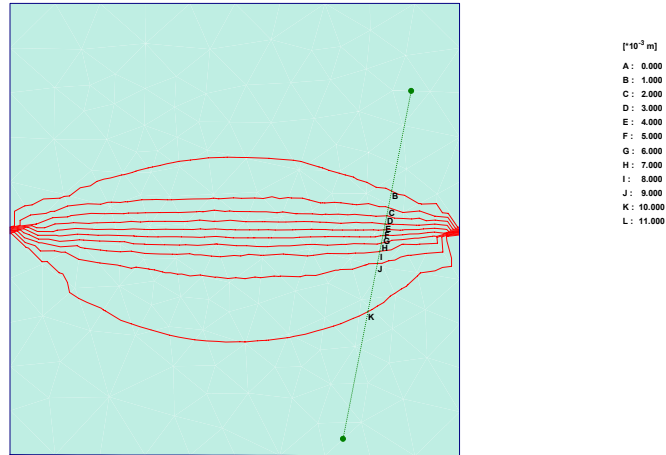


Figure 3.22 Total displacement contour in the shear zone of Wageningen clay soil

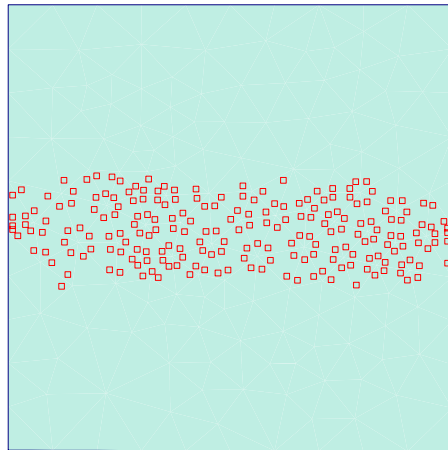


Figure 3.23 Mohr – Coulomb failure points in the shear zone of Wageningen clay soil

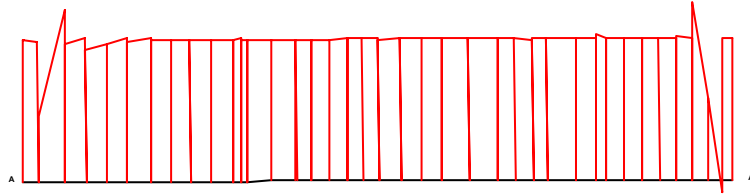


Figure 3.24 The shear stress distribution on the shear plane of Wageningen clay soil

The following curves, from Fig. 3.25 to 3.27 show the effect of stiffness, cohesion and friction angle variation during the shearing process

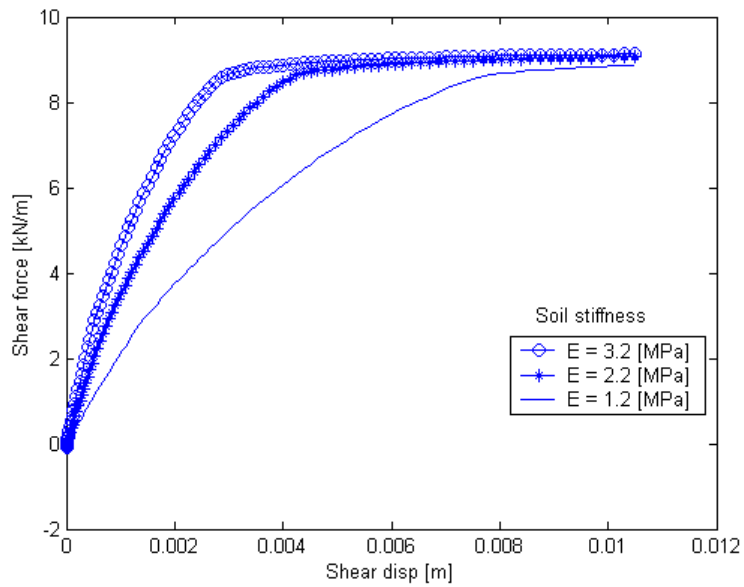


Figure 3.25 Effect of stiffness variation on shear force of Wageningen clay soil

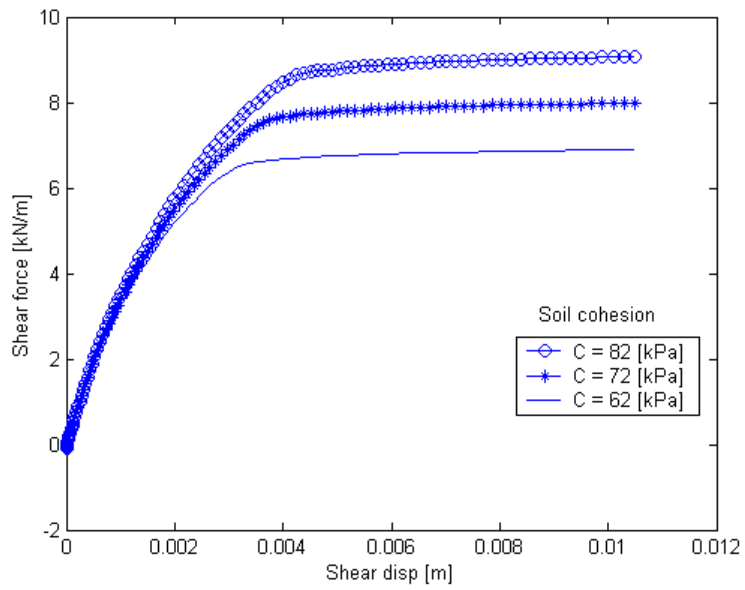


Figure 3.26 Effect of cohesion variation on shear force of Wageningen clay soil

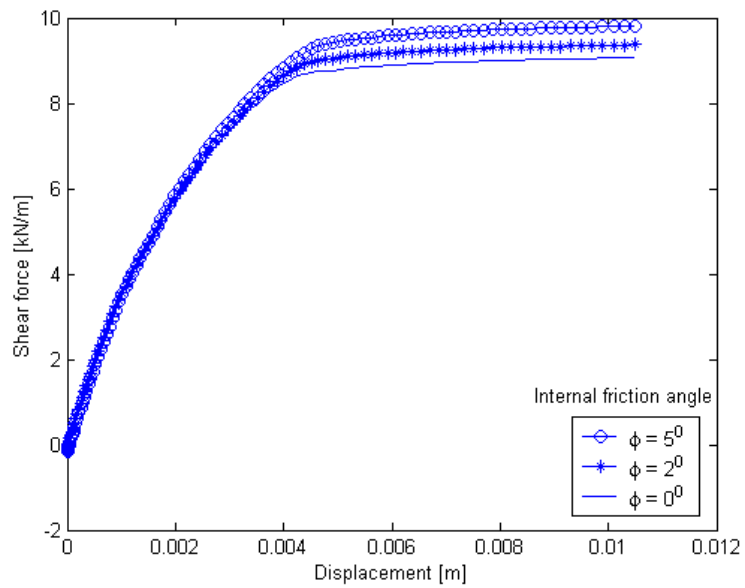


Figure 3.27 Effect of friction angle variation on shear force of Wageningen clay soil

3.6.3.2 Using the Cam – Clay type model

The soil used for the Cam – Clay model is the Silty loam soil of Table 3.2. Figures 3.28 and 3.29 show the soil deformation and shear behaviour.

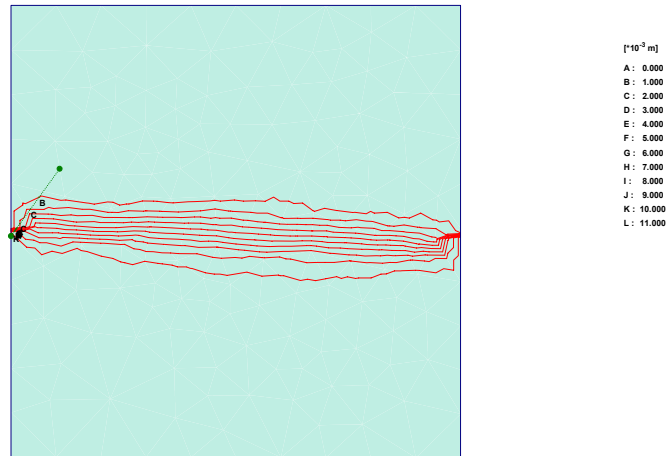


Figure 3.28 Total displacement contour in the shear zone of Silty loam soil

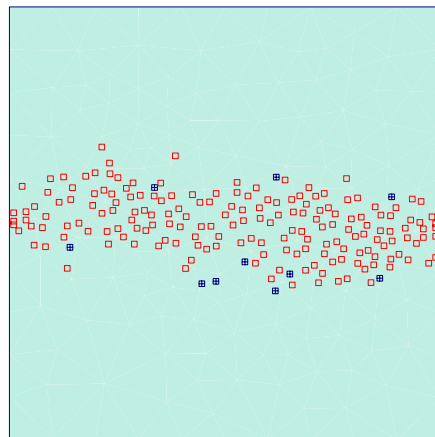


Figure 3.29 Mohr – Coulomb (empty) and plastic cap (filled) failure points in the shear zone of Silty loam soil

The following curves, from Fig. 3.30 to 3.31 show the effect of cohesion and friction angle variation during the shearing process

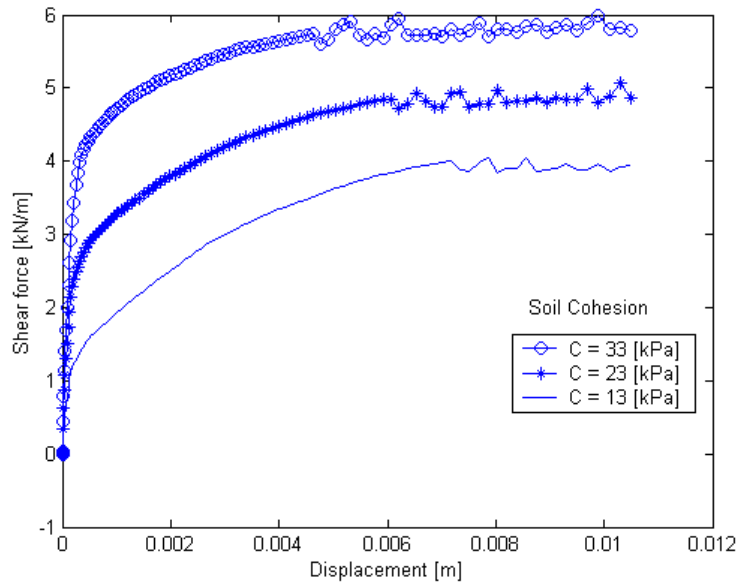


Figure 3.30 Effect of cohesion variation on shear strength of Silty loam soil

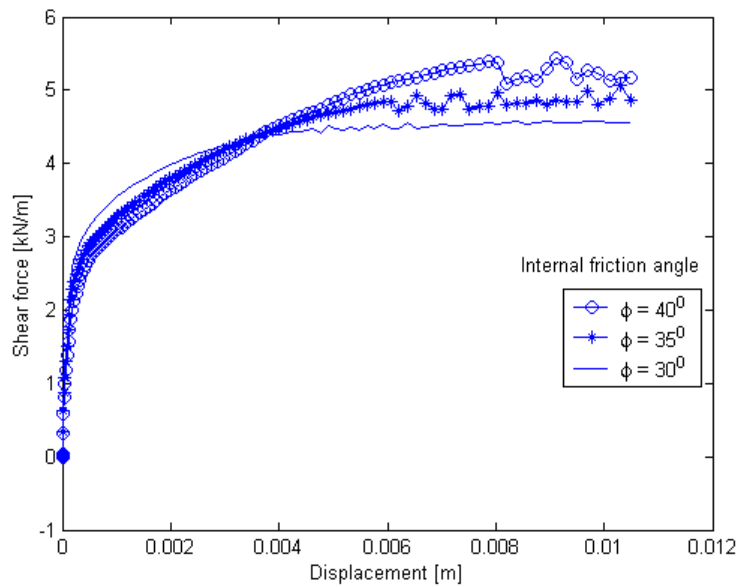


Figure 3.31 Effect of friction angle variation on shear strength of Silty loam soil

3.6.4 DISCUSSION AND CONCLUSION

For investigation of the failure conditions of soils one must know the internal resistance exerted by the soil to displacement, slip, deformation and volume change. Such internal resistance is characterised by the shear strength of the soil.

In soil mechanics the Mohr – Coulomb condition is usually used as the condition of failure. Accordingly the shear strength may be given by two parameters: ϕ , the slope of the Coulomb line and c , the shear strength measured at a zero normal stress. These are called friction angle and cohesion respectively. The shear box test is the simplest laboratory soil test available for the direct measurement of soil cohesive and frictional strength parameters whereas our interest now is modelling of the dynamic shear box test with Plaxis which is used to study the failure and the deformation patterns of the soil. Using Plaxis has lots of advantages; therefore we discuss the merits of Plaxis on modelling shear box test. When we compare sources of error for laboratory shear box test and Plaxis shear box test, Plaxis shear box test gives much more reliable results.

In the laboratory test sometimes coarse particles might be trapped in the clearance of the boxes disturbing the magnitude of shear resistance of the soil during shearing (Kezdi, 1974). This can be corrected in Plaxis by taking very thin clearances using input of digital numbers. Further difficulty of laboratory tests is the precise setting of the plane of forces. If we fail to make the horizontal force exerts its effect precisely in the shear plane specified, then the results would be disturbed. Again this can be corrected in Plaxis by selecting nodal points exactly on the shear plane. In Plaxis soil samples are placed inside the two boxes and a vertical load A is applied on the upper box. The soil is allowed to come to drainage equilibrium after the load A is applied for 1s. Then the lower box is displaced relative to the other with constant velocity of 1mm/s (strain – control method) and the required horizontal force is “measured” by Plaxis incrementally. On the force – displacement curve for each parameter under study the failure point P is determined as indicated for Fig. 3.25 to 3.27 and also for Fig. 3.30 & 3.31. This point is the largest shear force (F_x) or that point where the shear force versus displacement curve increases only slowly.

For the case of the Mohr – Coulomb soil model using different input values of the parameter E (Young’s modulus) we didn’t see failure force difference despite the failure occurred earlier for the higher values of E (Fig. 3.25). For parameters of c and ϕ which are the two strength determining parameters the failure force is different for different values of those parameters. As expected failure force is increasing where c is increasing and the same is true for ϕ (Fig. 3.26 and 3.27). For the case of Silty loam soil the conditions of what was explained for c and ϕ of Wageningen clay soil remain the same. That means when values of these parameters increase the shear strength will be increased (Fig. 3.30 and 3.31).

The force – displacement curves of Silty loam soil also show similar behaviour with that of Wageningen clay besides the failure force differs depending on the magnitude of normal load. Inspection of plastic points (Fig. 3.23 and 3.29) showed that failure is concentrated on the predetermined shear plane and the shear stresses on the plane seem uniformly distributed (Fig. 3.24). However the failure zone of Wageningen clay was larger than that of Silty loam soil; this is due to deformation behaviour of Wageningen clay soil. In fact such shear force – displacement curves reflect how a soil would behave on a predetermined thin shear zone in the field such as under a tractor tyre (Mckyes, 1989).

3.7 MODELLING OF SOIL BLOCK CUTTING BY A PENDULUM TYPE MACHINE

The finite element modelling of soil block cutting by a pendulum type machine is first started by creating the initial geometry model of the soil block together with the shape of the tool. The model used for the FEM calculation is the Mohr – Coulomb model together with the Wageningen clay soil which is given in Table 3.1.

3.7.1 CREATING A GEOMETRY MODEL

For each new case to be analysed it is important to create a geometry model first. A geometry model is created by the input program of Plaxis and it is a representation of a real problem consisting of points, lines and clusters. The initial geometry model of the soil block has the dimensions as shown in the Fig. 3.32 . This and all the other dimensions of the geometry model are equal with the dimensions of the laboratory test of soil block cutting by a pendulum type machine analysed on the MSc thesis of Fissha (1998) and Tadesse (1999). The standard boundary conditions (total fixities) are used to fix the boundaries and the absorbent boundaries are used at the boundaries where total fixities are used.

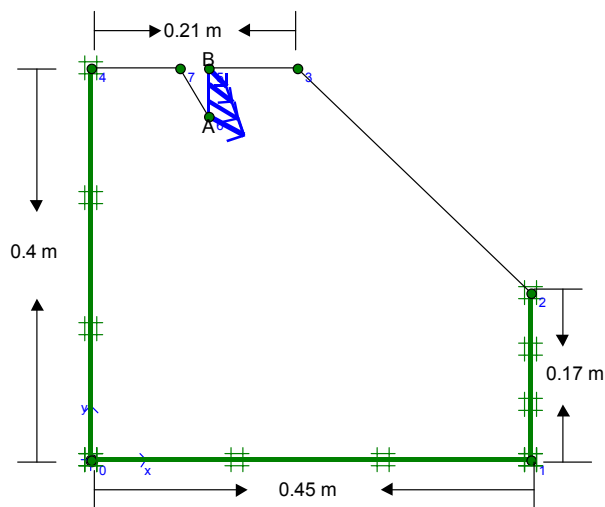


Figure 3.32 The created geometry model with total fixities, absorbent boundaries, and applied prescribed displacement

3.7.2 BASIC CALCULATION

After the creation of a geometry model a finite element mesh composed of 6 – node triangular soil elements is used in the discretization process. The mesh is generated with the global coarseness set to ‘medium coarse’ and a total of 162 elements, 363 nodes and 486 stress points is formed after the discretization.

The initial state of stress is generated by the K_0 – procedure ($K_0 = 1 - \sin \phi$), where K_0 is coefficient of lateral earth pressure and ϕ is internal friction angle.

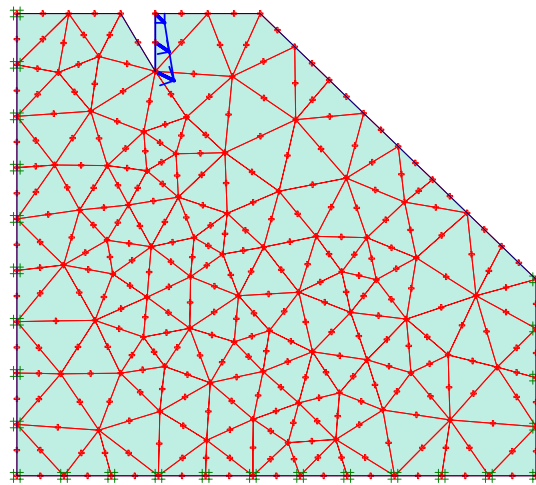
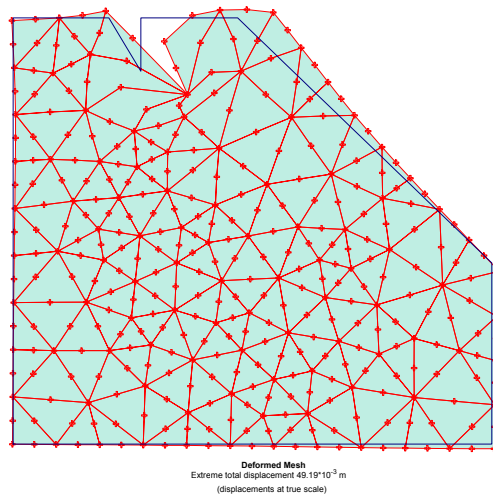


Figure 3.33 Discretized soil block with tool displacement direction, 162 elements and 363 nodes

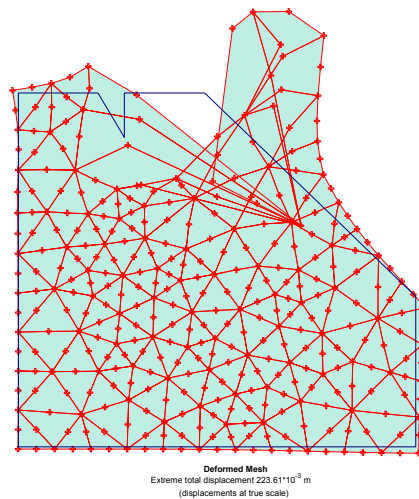
The applied values of the displacements are controlled by the displacement multiplier ($\sum Mdisp = 0.02m$); in this case the tool has been displaced in the tangential direction with a magnitude of 0.049m. The prescribed displacement has the co-ordinates of A (1, -1) and B (-1, 2) where A and B are the two positions of the tool as shown in Fig. 3.32. The tangential motion of the tool is the correct way of estimating soil cutting by pendulum type machine. In Plaxis it is difficult to model the curved motion of the tool, so we used tangential motion with a small displacement that shows a similar effect of the curved motion rather than vertical or horizontal motion of the tool. The calculation involves a single phase dynamic analysis with automatic time stepping procedure. The time step selected is ($\Delta t = 0.0001s$) and the total calculation time would be $t = 0.02s$

3.7.3 FIGURES PRESENTING CALCULATION RESULTS

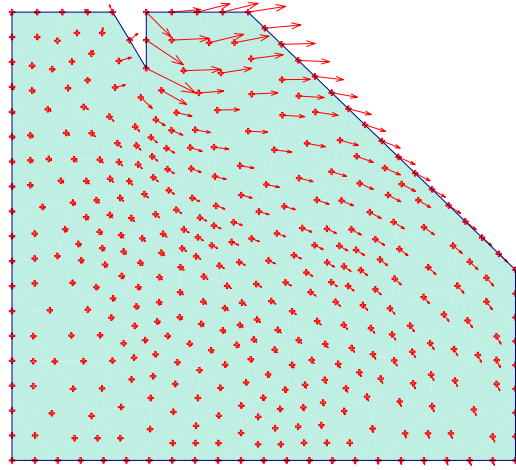
The following Figure 3.34 shows the deformation behaviour of the Wageningen clay soil when cutting by the pendulum type machine.



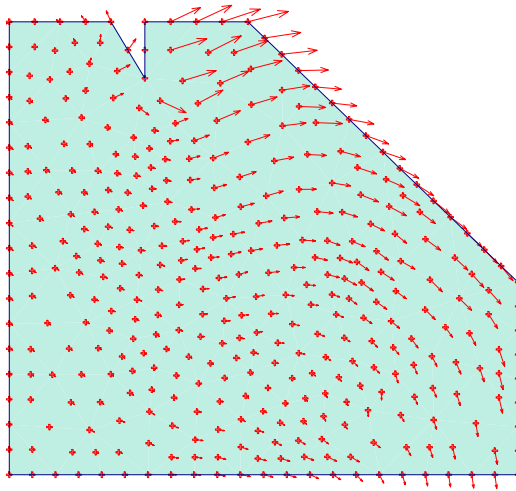
a) Deformed mesh with nodal points after cutting with small displacement



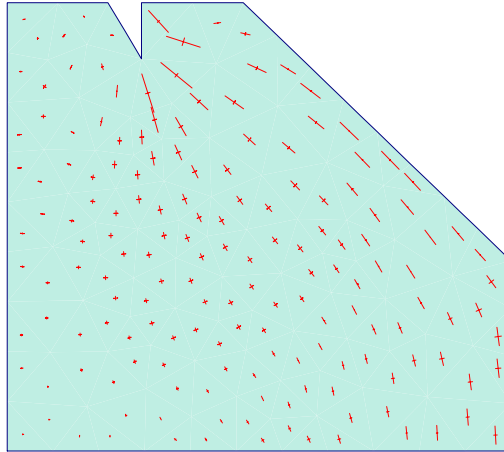
b) Deformed mesh with nodal points after cutting with relatively large displacement



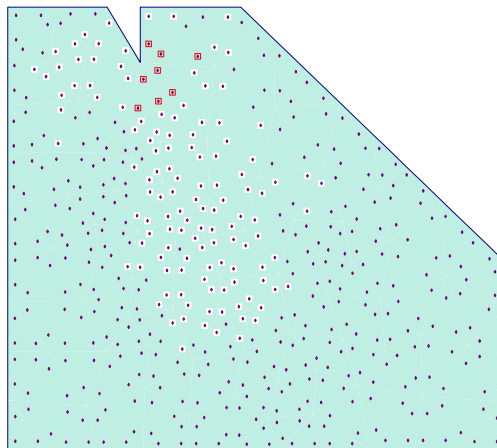
c) Distribution of soil particles displacement vectors for small displacement



d) Distribution of soil particles velocity vectors for small displacement



e) Total stress distribution for small displacement



f) Mohr – Coulomb (open with stress points inside) and tension failure (white with stress points inside) points; the dots are stress points, for small displacement

Figure 3.34 a – f. Soil deformation behaviour of Wageningen clay soil after cutting by a pendulum type machine

3.7.4 DISCUSSION AND CONCLUSION

We analyse the FEM calculation of the cutting process of a soil block by a pendulum type machine and investigate the dynamic behaviour of cohesive soil.

Figure 3.34 a shows the deformed mesh after 5 cm displacement of the tool in tangential direction. The mesh is deformed in the upward direction in front of the tool surface and little deformation occurred behind the tool surface at the instant of displacing the tool. All this deformation behaviour is expected with regard to the tool motion since the tool pushes the soil mass in front of its surface in horizontal as well as upward direction during cutting.

Figure 3.34 b shows the deformation behaviour of the soil mass after cutting with relatively large displacements (22 cm). In this case the irregularity of the mesh deformation is increased. This is due to the increased particle motion resulting from the increased force of the tool during the cutting process.

Figure 3.34 c shows the analogue soil displacement vectors for the deformed mesh with small displacement. The first three nodal points on the surface of the tool show the displacement direction of the tool and the rest of the nodes with arrows shows the displacement direction of the soil particles. It seems that most of these nodes are displaced in the horizontal direction rather than vertically except very few nodes at the surface of the soil mass in front of the tool. However, there should also be an upward and downward movement of soil particles. These movements of soil particles are clearly seen from the velocity vectors diagram (Fig. 3.34 d) which shows the soil particle movement at the time of soil deformation.

Figure 3.34 e shows the total stress concentration area of the soil mass. The area of the soil mass near to the tool tip and in front of the tool surface shows relatively high concentration of stresses which is expected. The length of each line represents the magnitude of the principal stress and the direction indicates the principal direction.

Plastic points are shown by Figure 3.34 f ; these points show the area of the soil mass, where failure occurred. Stress points near the tool tip or in front of the tool surface (where high concentration of stresses occurred) are in a failure state. These failure points are Mohr – Coulomb failure points and located in the Figure as an open square with stress points inside. The Mohr – Coulomb failure points are stress points where the Mohr stress circle touches the Coulomb failure envelope (Plaxis, 1998). The other plastic points are called tension points; these points are located on the figure as white squares with stress points inside. A tension point is a stress point which fails in tension. In the present calculation the tensile strength of Wageningen clay is considered to be 20.5 kPa.

In FEM calculations of the soil cutting process by a pendulum type machine it is difficult to see an open crack formation on the remaining part of the soil block or on the part of the soil block displaced by the tool. This may be due to the continuum nature of the medium, so that there is no distinction between individual elements during the cutting process. Rather elements are displaced at nodal points. In the case of analysing crack formation, DEM or laboratory experiments are more useful than FEM. In DEM calculation of soil block cutting by a pendulum type machine, particles are separated from each other during the cutting process and open crack formation can easily be formed in front of the tool (for details see the Figures of section 6.2.2).

3.8 ACCURACY OF FEM RESULTS ACCORDING TO BENCHMARK EVALUATION

The performance and accuracy of FEM has been carefully tested by carrying out analyses of problems with known analytic, semi – analytic or numerical solutions. Plaxis (1998) gives a selection of these benchmark problems. Section 3.8.1 and 3.8.2 present two of them.

3.8.1 ELASTIC BENCHMARK PROBLEMS

A large number of elasticity problems with known exact solutions is available for use as benchmark problem. Only one example of the elastic calculation has been selected for verification because it resembles the calculation that FEM might be used for in practice.

3.8.1.1 Example ‘footing’

The problem of a smooth strip footing on an elastic soil layer with depth $h = 4$ m and length $l = 14$ m. The soil has elastic properties of Poisson’s ratio $\nu = 0.33$ and bulk modulus $G = 500$ kPa. A uniform vertical displacement of 10 mm is prescribed to the footing and the indentation force, F , is calculated from the results of the finite element calculation.

Results: The footing force calculated from the finite element calculation was $F = 15.26$ kN. The analytical solution to this problem can be found in the formula,

$$\text{settlement} = \frac{F\delta}{2(1+\nu)G} \quad (\text{Giroud, 1972}).$$

For the dimensions and material properties used in the finite element analysis this formula gives a footing force of $F = 15.15$ kN. The error in the numerical solution is therefore about 0.7 %. Figure 3.35 shows that the FEM results agree very well with the analytic solution.

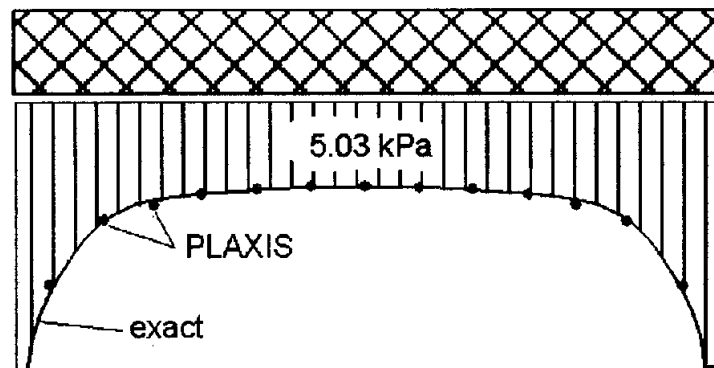


Figure 3.35 The analytical and FEM results for the pressure distribution underneath a smooth rigid footing on an elastic medium (Plaxis version 7, 1998)

3.8.2 PLASTIC BENCHMARK PROBLEMS

A series of benchmark calculations involving plastic material behaviour is described in the Plaxis version 7 material models manual. Only one example with known analytic solution is described below for verification.

3.8.2.1 Example 'cavity'

For the expansion of a cylindrical cavity in an elastic perfectly cohesive soil theoretical solutions exist for both large and small displacement analysis.

A cylindrical cavity of initial radius a_0 is expanded to radius a by the application of an internal pressure p . The radius of the elastoplastic boundary is represented by r . The soil is incompressible with an angle of friction of zero and cohesion c .

In this calculations the ratio G/c is taken to be 100 and Poisson's ratio is $\nu = 0.495$.

Results: Figure 3.36 shows relationships between cavity pressure and radial displacement. The FEM calculated results agree very well with the analytical solutions.

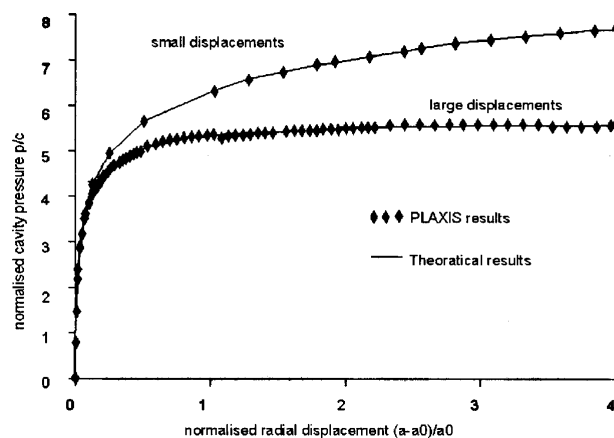


Figure 3.36 FEM and theoretical results of cavity pressure versus radial displacement (Plaxis version 7, 1998)

3.8.3 VALIDATION FOR AGRICULTURAL SOIL PROPERTIES

The Finite Element Method has been used by a number of scientists to study soil compaction by tyre – soil system and the process of soil – tool interaction (Koolen et al, 2003; Koolen,1999; Carol et al, 1999; Fielke, 1997 and Kirby, 1989) Those studies have shown that the FEM results reasonably approximate the real situation in the agricultural fields.

Very recent ones are (Koolen et al, 2003) and (Koolen, 1999) for analysis of soil compaction by tyre – soil system and (Carol et al, 1999) and (Fielke, 1997) for analysis of soil deformation during tool – soil interaction. As many of these researchers agree it is very difficult to study the tyre – soil system or the soil – tool interaction by field experiments whereas the FEM model is a convenient one to do so.

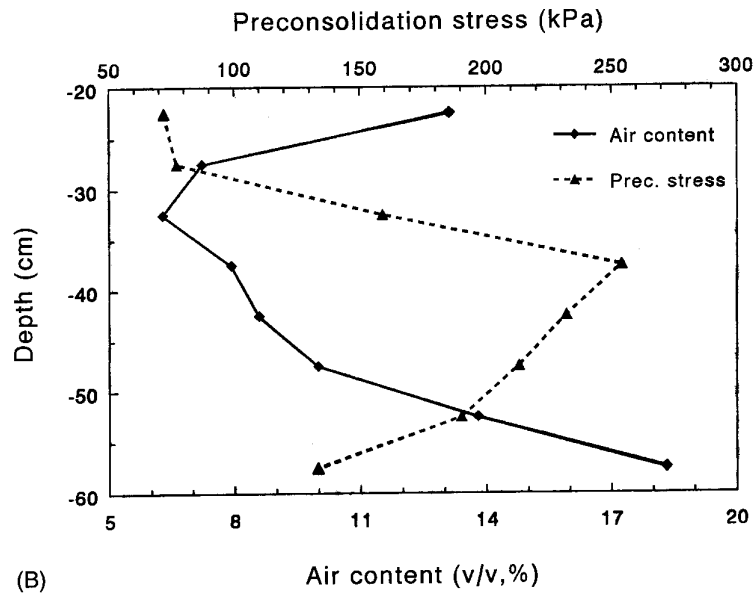
Koolen et al (2003) presented FEM analysis of subsoil reaction on heavy wheel loads that frequently occur in arable farming, Fig. 3.37 b. The results showed that the preconsolidation stress of the subsoil was an upper bound of the vehicle induced stresses in the subsoil. This finding is a result that one will expect. It can therefore be considered as a validation of the FEM analysis (Fig. 3.37 a).

They used the same soil type (Silty loam soil) as was explained in this thesis from different soil depths with different preconsolidation stresses and cohesion values. The FEM calculations were done with automatic mesh generation and with updated mesh analysis, for tyre sizes, inflation pressures and wheel loads that occur with the heaviest sugarbeet harvesters available on the European market in 1999.

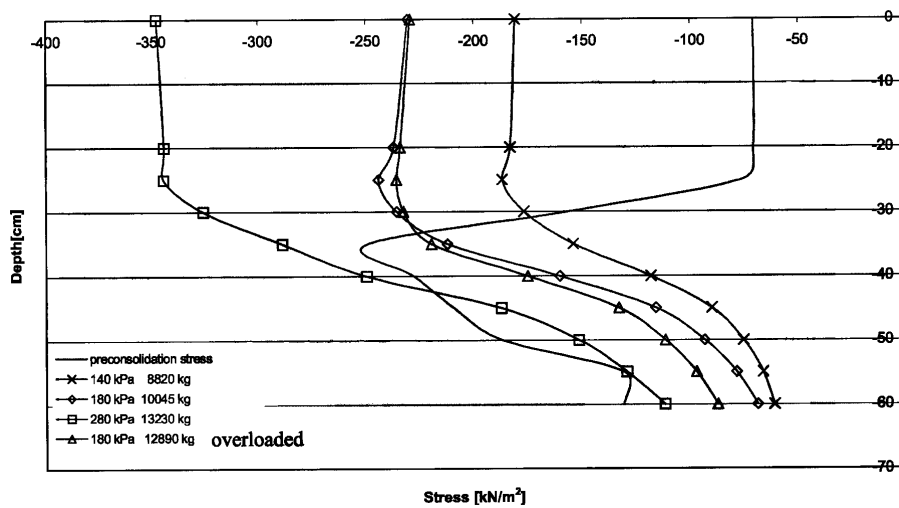
The results of the calculation include the detection of regions with Mohr – Coulomb plasticity regions, with cap plasticity (compaction hardening) and the distribution of soil pressure beneath the centre of the tyre. These results are parallel with the dynamic FEM simulation results presented in this thesis for the tyre – soil system. In the present case the author used Plaxis version 7.2 (2000) that is the dynamic analysis (automatic mesh generation with automatic time stepping) which is even more realistic for dynamic loading cases like tyre – soil system or soil – tool interaction.

Therefore besides the benchmark problems presented in Plaxis (1998) we can use the above already published FEM results as a validation of the FEM calculation results presented in this thesis.

Probably deviation of the FEM calculation results from the actual results are mainly caused by the inaccuracy in measuring soil properties, which is a main problem in FEM calculations.



a) Preconsolidation stress and air content from uniaxial compression test



b) Preconsolidation stress from FEM calculations

Figure 3.37 a, b. Validation of FEM results by comparing a) preconsolidation stress from laboratory test and b) preconsolidation stress from FEM calculations (Koolen et al, 2003)

4 EXPERIMENTAL RESULTS

The laboratory experimental results of soil block cutting by a pendulum type machine, dynamic tyre – soil system and simple shear test are presented in this section. Only selected parts of the results are presented here for later comparison analysis of DEM and FEM results.

For detailed analysis of the experimental results one can read the MSc theses of Fissha (1998) and Tadesse (1999) for soil block cutting by the pendulum type machine, Lebert et al (1988) and Horn et al (1988) for the dynamic tyre – soil system and Kezdi (1974 & 1980) and Craige (1992) for the shear box test.

4.1 ANALYSIS OF SOIL CUTTING BY A PENDULUM TYPE MACHINE

4.1.1 INTRODUCTION

The process of soil loosening has been performed all over the world for many centuries. Operating tools (mouldboard plow, rotary tine, wedge, discplough etc.) have to move through the soil to get the desired loosening process.

Tools are labelled “tines” if the loosening effect reaches considerably further than the width of the body and “plough body” if the loosening effect is mainly confined to the soil within the width of the operating tool (Koolen, 1977).

A tillage tool is labelled as a two dimensional tool if the horizontal cutting edge is always perpendicular to the direction of travel. For two dimensional cutting blades the important characteristics are the shape of the surface, the cutting angle, the working depth in relation to the size, and the height of the tool. The tool used in the experiment (Fig. 4.2) can be considered as a two dimensional tool. Basically all soil loosening processes transfer soil from its original position. Thus mechanical failure of the soil material is involved in the sense that the mass of the soil being moved doesn't retain its original geometric shape.

An experiment was done by Fissha (1998) and later by Tadesse (1999) in the soil Tillage laboratory of Wageningen University in order to analyse the dynamic behaviour of soil under tillage. The difference between the experiments of Fissha and Tadesse was about tool shape. Fissha used the common rotary tillage tool without modification.

Tadesse used a modified rotary tine by increasing the stiffness of the tool.

The case of Fissha is presented in the following section since he used the original rotary tine which is commonly used in soil loosening processes.

4.1.2 SOIL PREPARATION AND THE EXPERIMENTAL SET-UP

4.1.2.1 Soil properties used in the experiment

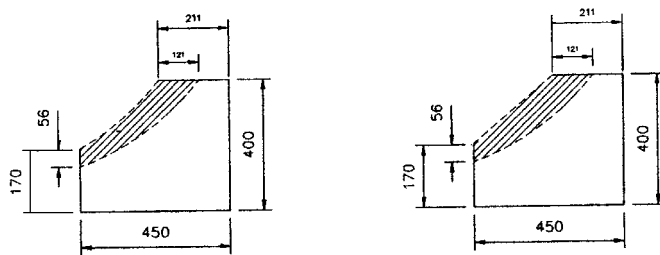
Two different types of soil as described in Table 4.1 are selected among the soils which are prepared to be investigated at moisture content equal to their field capacity and porosity which is convenient for soil handling.

Table 4.1 Soil physical properties used in the experiment

| Soil type | % of mineral content | | | % of soil | | Limit of consistency | | | Porosity % | MC at pF 2 % | Density (g/cm ³) |
|------------------------------|----------------------|------|------|-------------------|-------|----------------------|--------|---------|------------|--------------|------------------------------|
| | clay | silt | sand | calcium carbonate | humus | liquid | sticky | plastic | | | |
| Wageningen (silty clay loam) | 36 | 47 | 16 | 33 | 23 | 43.7 | 32 | 30.5 | 45 | 27 | 1.87 |
| Ede (sand) | 4 | 9 | 87 | | 3.6 | 1.9 | 15.4 | | 41 | 17 | 1.78 |

The next step was preparing the soil block by filling the soil bin. The soil bin was 45 cm long, 40 cm wide and 12 cm deep (Fissha, 1998). The shape of the soil block was such that the blade motion during pendulum rotation was similar to that of the assumed rotary tiller as shown in Fig. 4.2: the shape of the soil block was derived from the impact position, cutting path and bite length of the assumed tiller condition.

The actual shape of soil slice produced by the rotating pendulum in a single strike is shown in Figure 4.1 a. However the laboratory preparation of a soil block with a curved shape has a practical difficulty. This problem was avoided by replacing the curved front face part with a straight line as shown in Figure 4.1 b.



a) Actual shape of soil block

b) Modified shape of soil block

Figure 4.1 a, b. Setting shape of soil block

The main parameters of the blade selected for simulation were derived from the rotary tiller blade which is commonly used for cultivation in the Far East (Nguyen, 1996). Figure 4.2 shows the blade cross sections and Table 4.2 shows its important parameters.

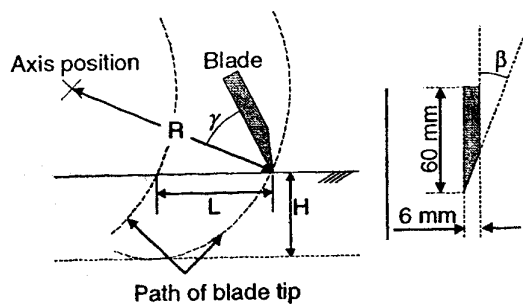


Figure 4.2 Cross section of the rotary tiller blade

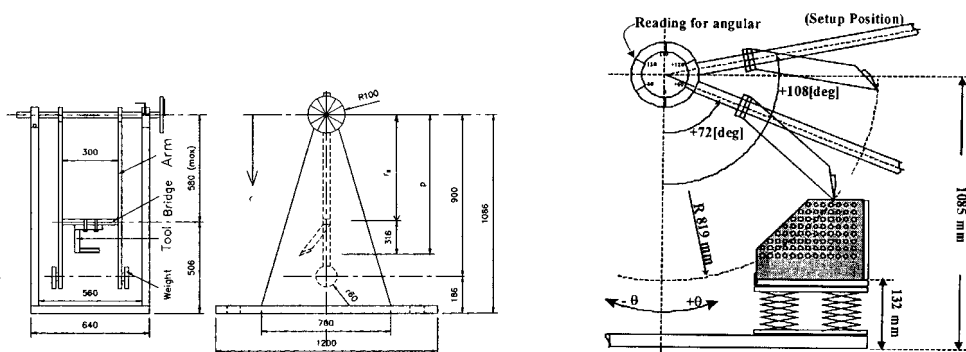
Table 4.2 Rotary tiller blade parameters

| Parameters | Values |
|----------------------------|--------------------|
| Tip angle (β) | 25 ⁰ |
| Setting angle (γ) | 52.11 ⁰ |
| Rotation radius (R) | 22 cm |
| Traveling velocity | 111.11 cm/s |
| Angular velocity | 275 rpm |
| Working depth (H) | 15 cm |
| Bite length (L) | 12.1 cm |

4.1.2.2 The experimental set-up

After the soil block was prepared white headed pins were placed on the front face of the soil block in order to form a grid. The pins are placed at every intersection point of horizontal and vertical lines 2 cm apart.

The soil block was moved and securely placed on the pendulum type impact machine as shown in Fig. 4.3 b, which is arranged to simulate the rotary cutting process. And then the pendulum was released from 105 degree position and strikes the soil block at 72 degree measured from the vertical axis (after rotation of 33 degree) at a velocity of 3 m/s. Based on the pendulum type impact machine and blade – soil impact setup in Fig. 4.3 a and 4.3 b respectively the selected working radius of the pendulum machine is $R = 0.819$ m.



a) Pendulum type impact machine

b) Blade – soil impact setup

Figure 4.3 Pendulum type machine (a) and experimental setup (b)

4.1.3 RESULTS AND DISCUSSION

4.1.3.1 The pendulum motion and absorbed energy during the cutting process

The images of soil behaviour during the cutting process were recorded by a high speed video camera and the angular top position was measured after cutting. The pendulum motion was measured from recorded images after the experiments. If a large reaction force had worked on the blade the pendulum motion would become slower.

In general the motion of the pendulum during a cutting process is controlled by the following kinetic equation (Eqn 4.1)

$$I_0\alpha_t = RF_t - Lmg \cos\theta_t + e\Delta\theta \quad (4.1)$$

where

I_0 is moment of inertia of the pendulum; α_t is angular acceleration of the pendulum; R is distance from axis to blade tip; F_t is resistance force against blade motion; L is length from rotation axis to centre of gravity of the pendulum; m is the mass of the pendulum; g is acceleration due to gravity; θ_t is rotation angle of the pendulum; e is the friction energy lost by the bearings

The energy absorbed by the soil loosening process during the pendulum motion is calculated by using Equation 4.2.

$$E_{abs} = mg\Delta h - e\Delta\theta \quad (4.2)$$

where

m is mass of the pendulum machine; g is the acceleration due to gravity; Δh is the change in heights between the starting and stop positions of the pendulum; $\Delta\theta$ is a rotation angle during pendulum motion

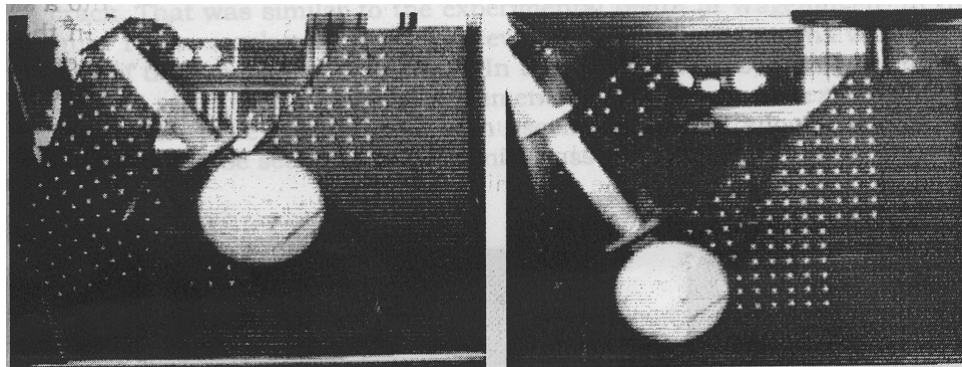
Therefore the energy absorbed by the loosened soil during the cutting process was related to the pendulum stop angle after cutting as shown in Table 4.3. This shows that the absorbed energy of the loosened soil increased as the content of clay in the soil increased.

Table 4.3 Energy absorbed during the cutting process

| Pendulum motion | Wageningen clay soil | | Ede sand soil | |
|------------------------------|----------------------|----------|---------------|----------|
| | Exp. one | Exp. two | Exp. one | Exp. two |
| Pendulum release angle [deg] | 105 | 105 | 105 | 105 |
| Pendulum stop angle [deg] | -34 | -30 | -79 | -79 |
| Absorbed energy [J] | 110.73 | 114.81 | 36.9 | 36.9 |

4.1.3.2 Crack formation during the cutting process

The behaviour of the soil when the cutting blade passed through soil block is shown in Fig. 4.4. Crack formation in the thrown part in front of the blade or in the remaining part behind the blade and the consumption of pendulum kinetic energy varied with soil type. In the case of Wageningen clay soil (since clay content is highest) the crack proceeded faster than the blade motion (Fig. 4.4 a). Shape of the thrown block was kept through the cutting process. Whereas in the case of Ede sand crumbling was found at the top of the thrown block and some cracks were found in the remaining part of soil (Fig. 4.4 b).



a) Wageningen clay soil

b) Ede sand soil

Figure 4.4 Snapshot pictures showing cutting processes visualising with pins

4.1.3.3 Motion of soil particles during the cutting process

Soil particle movement can be analysed from measurements of displacement, compaction, deformation, velocity and acceleration (Koolen, 1977). Displacements and velocities are selected in the present case. The use of white headed pins during the experiment has facilitated measurements of these processes.

Particle flow path

Using successive film frames the flow paths of some soil particles were constructed. A flow path of a particle may be a particle path relative to the blade or to the untouched soil. In the present case the flow path is selected with the assumption that the untouched soil was considered as fixed. The flow path was constructed approximately during the time interval where the blade starts to loosen the soil and the loosened particles start to fall due to gravitation effect. Fig. 4.5 with Table 4.4 and Fig 4.6 with Table 4.5 show the particle flow paths obtained at different points of time for Wageningen clay soil and Ede sand soil respectively.

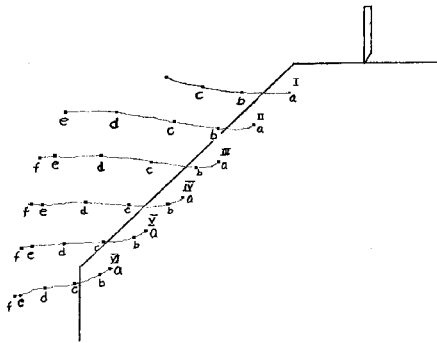


Table 4.4 Particles distance during cutting process

| Segments | Distance (mm) | | | | | | Position | Time (ms) |
|----------|---------------|------|------|------|------|------|----------|-----------|
| | I | II | III | IV | V | VI | | |
| | | | | | | | a | 472 |
| ab | 50.4 | 37.8 | 25.2 | 16.8 | 16.8 | 12.6 | b | 520 |
| bc | 42 | 50.4 | 50.4 | 42 | 33.6 | 29.4 | c | 568 |
| cd | | 58.8 | 58.8 | 46.2 | 42 | 33.6 | d | 616 |
| de | | 58.8 | 50.4 | 46.2 | 37.8 | 29.4 | e | 664 |
| ef | | | 16.8 | 12.6 | 12.6 | 8.4 | f | 680 |

Figure 4.5 Flow paths of six selected particles I – VI during the cutting process of Wageningen clay soil.

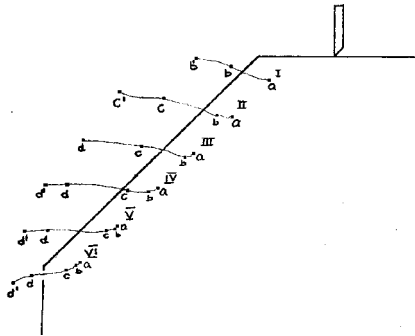


Table 4.5 Particles distance during cutting process

| Segments | Distance (mm) | | | | | | Position | Time (ms) |
|----------|---------------|------|------|------|------|------|----------|-----------|
| | I | II | III | IV | V | VI | | |
| | | | | | | | a | 528 |
| ab | 41 | 16.4 | 8.2 | 8.2 | 4.1 | 4.1 | b | 564 |
| bb' | 36.9 | 50.4 | 50.4 | 42 | 33.6 | 29.4 | b' | 588 |
| bc | | 53.3 | 41 | 20.5 | 8.2 | 12.3 | c | 600 |
| cc' | | 45.1 | | | | | c' | 624 |
| cd | | | 57.4 | 61.5 | 77.9 | 36.9 | d | 636 |
| dd' | | | | 20.5 | 24.6 | 20.5 | d' | 648 |

Figure 4.6 Flow paths of six selected soil particles I – VI during the cutting process of Ede sand soil.

Particle velocity distribution

For selected soil particles between two successive frames of I – VI as shown in Figure 4.5 and 4.6 the average velocity could be calculated over a short interval of time.

For Wageningen clay soil the interval of time was 96 ms and for Ede sand soil it was 36 ms.

Figure 4.7 with Table 4.6 and Figure 4.8 with Table 4.7 show the average particle velocity distribution of Wageningen clay soil and Ede sand soil respectively.

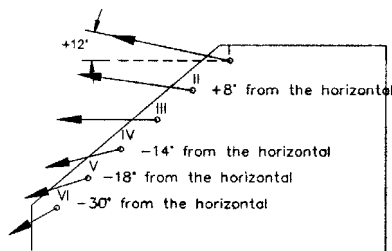


Table 4.6 Average velocity of particles for Wageningen clay soil

| Particle number | I | II | III | IV | V | VI |
|-----------------|------|------|------|------|------|------|
| Velocity (cm/s) | 96.3 | 91.9 | 78.8 | 61.3 | 52.5 | 43.8 |

Figure 4.7 Particles average velocity distribution for Wageningen clay soil

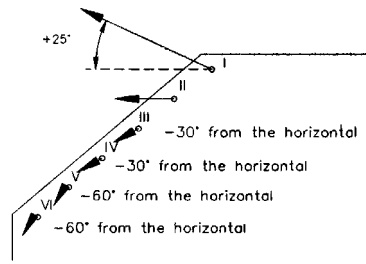


Table 4.7 Average velocity of particles for Ede sand soil

| Particle number | I | II | III | IV | V | VI |
|-----------------|-------|------|------|------|------|------|
| Velocity (cm/s) | 113.9 | 45.6 | 22.8 | 22.8 | 11.4 | 11.4 |

Figure 4.8 Particles average velocity distribution for Ede sand soil

4.1.4 CONCLUSION

The energy absorbed by the loosened soil during the cutting process was related to clay content. The absorbed energy increased as the content of clay in the tested soil block increased.

It was also observed that the cutting process was dependent on the kind of soil in terms of crack formation in the remaining part of soil block and the shape of thrown soil. In case of cutting Wageningen clay soil (cohesive soil) no crack was seen or very small cracks were generated; besides velocity of the thrown soil was small. This is because the clay caused larger resistance against mutual soil particle motion.

In the case of cutting Ede sand soil (soil with highest sand content) crumbling was found at the top of the thrown block with higher velocities and some cracks were found in the remaining part of the soil.

4.2 ANALYSIS OF DYNAMIC TYRE – SOIL SYSTEM UNDER FIELD CONDITIONS AND IN LABORATORY EXPERIMENTS

4.2.1 INTRODUCTION

Mechanical compression of soils by tyre loads is still subject to much discussion and research. The transmission of total stresses as effective stresses on the solid phase of the soil is a time dependent process, because the decrease of pore water pressure is a function of the hydraulic conductivity of the soil (Lebert et al, 1988).

Most laboratory research has been carried out with relatively long periods of stress application and slow deformation rates, which are often most convenient for laboratory equipment. Therefore these experiments can only be associated with very slow vehicle speeds.

Horn et al (1988) described that the tractor speed of wheeling and the number of passes cause different degrees of compaction. But there is a lack of information about the process in detail, that occurs during loading in structured soils.

4.2.2 FIELD EXPERIMENTS

The field experiment of Horn et al (1988) for analysing the effect of stress duration on the pressure transmission of soil under running wheels is presented in the next section.

4.2.2.1 Materials and methods

Horn et al (1988) used the following soil properties in the field experiment. The used soil was a transitional red – brown earth, ameliorated by deep ploughing to 30 cm. It had two horizons, the A – horizon was sandy clay loam, while the B – horizon consists of sandy clay. The bulk density was 1.22 and 1.46 g/cm³ respectively. After the last cultivation the soil was spray irrigated with 80 mm of water at 50 mm/h by a lateral move irrigator and covered with a polythene sheet to allow redistribution of water.

Each wheeling was on a different plot at water contents of the ameliorated soil just below or above the casagrande lower plastic limit (21% w/w) and a suction between 6 or 12 kPa that is field capacity. Two different kinds of speed were used, (slow (0.7 km/h) and fast (4.5 km/h)).

Forward speed and wheel slippage were calculated from measurements of distance and time. The wheeling was one pass by a single rear wheel of a 100 kW tractor with 18.4 – 38 size water ballasted tyre, an inflation pressure of 140 kPa and contact area of 3,600 cm². In each plot stress transducers were installed at 20 and 35 cm depths. After a transducer was inserted its hole was firmly back – filled with soil. The transducers measured vertical stress (σ_v) or horizontal stress (σ_h) with at least two replicates at each depth.

Wheeling signals from the transducers in various horizons of the soil profile were recorded simultaneously each 0.1s by a field data logger. The stresses were calculated by applying individual calibration curves for each transducer. Water contents at 20 cm depth after wheeling were also measured. Bulk density and air permeability after wheeling were measured at 20 cm on soil cores taken in metal rings of 100 mm diameter.

4.2.2.2 Results and discussion

In Figure 4.9 the mean vertical stress at 20 cm depth is shown for the two tyre speeds. At the slowest speed the stresses lasted longer and the shape of the graph resembled a flattened sine wave.

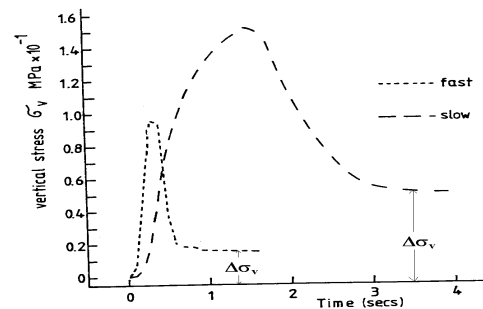


Figure 4.9 Change of vertical stress with time for two tractor speeds (Horn et al, 1988)

Average vertical stress at 20 cm depth changed significantly with speed (from 0.2 – 0.6 MPa). Which means the vertical stress increased when the speed is lowered. However at a water content above the lower plastic limit the vertical stress increased when the speed increased.

At 35 cm depth an increase in speed resulted in a decrease of σ_v . Thus the maximum vertical stresses decline as speed increased for the subsoil. The longer periods of stress application at lower speeds allowed a greater opportunity for subsoil stress to reach the maximum value.

Hence increasing speed resulted in lower maximum vertical stress in the subsoil.

Because soil compaction is a time dependent process increasing speed resulted in decreasing increments of bulk density values. Wheeling also caused considerable surface soil deformation. The formation of ruts and the mean rut depth decreased when speed increased. In general faster forward speeds of a tractor should minimise damage to the soil structure.

4.2.3 LABORATORY EXPERIMENTS

Lebert et al (1988) also showed the effect of stress duration on the pressure transmission of tilled soil by laboratory experiments. Pressure transmission is affected not only by load intensity but also by speed. In their experiment, the load and time dependent settlement of the undisturbed and predried soil samples have been simulated by a confined compression test with a load range of 10 to 800 kPa.

They analysed, that at constant load, pressure will be transmitted deeper down the soil profile with the longer stress duration at the soil surface (Fig. 4.10)

Horn et al (1988) also showed the longer the stresses are applied at the soil surface the greater the permanent deformation $\Delta\sigma_v$, as shown in Fig. 4.9.

Thus fast wheeling protects soil structure from compaction especially in soils with low hydraulic conductivity.

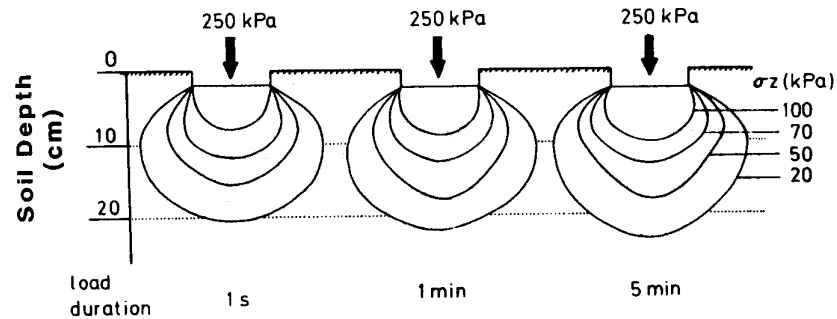


Figure 4.10 Time dependent alteration of the stress lines (Lebert et al, 1989)

4.3 LABORATORY EXPERIMENTS OF THE SHEAR BOX TEST

4.3.1 INTRODUCTION

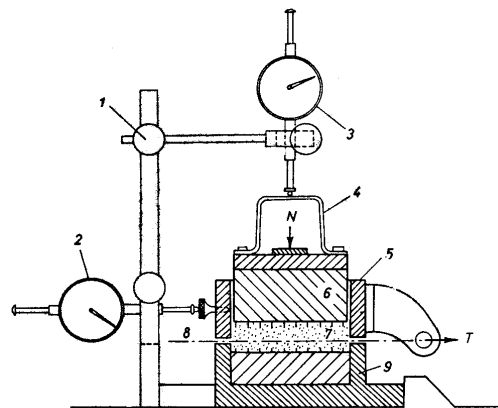
The direct shear test is used to measure the shear strength of a soil under drained conditions. A square specimen of soil is placed in a square box that is divided horizontally into two frames. The specimen is confined under a vertical or normal stress and a horizontal force is applied so as to fail the specimen along a horizontal plane at its midheight.

Generally a minimum of three specimens each under a different normal stress are tested to establish the relation between shear strength and normal stress. The magnitude of normal stresses used depends on the range of stresses anticipated for design. Because of the difficulties involved in controlling drainage of the soil specimen during the direct shear test, only the drained test method in which complete consolidation is permitted under each increment of normal and shear stress shall be used.

4.3.2 Materials and methods

The apparatus consists of a square metal box split across the middle into two parts, one fixed the other movable in the horizontal direction. The soil specimen is held between two indented porous stones or metal grilles.

Dimensions of the shear box are selected with respect to the size of the grains in the soil under test. For sand and silty sand a box of (6 * 6) or (10 * 10 cm) is used. Coarse gravel or rubble are tested in large size (30 * 30 cm) boxes, types of apparatus with a surface 1 m² are also known for both in-situ and laboratory experiments. The complete experimental setup of the shear box is shown in Figure 4.11



1-pressure screw; 2-dial gauge to measure horizontal displacement; 3-dial gauge to measure vertical displacement; 4-measuring frame; 5-moving frame; 6-pressing block; 7-soil sample; 8-shear surface; 9-bottom frame

Figure 4.11 The experimental setup of shear box test (Kezdi, 1980)

During the test a vertical confining load is first applied to the specimen through a rigid top block. Then a gradually increasing horizontal shearing force is applied through the upper movable part until the sample fails. Both the horizontal shear displacement and the vertical deformation are measured by precise dial gauges.

The loading causes the void ratio of the specimen to decrease. If the voids are filled only with air compression occurs almost instantaneously, whereas in water saturated soils consolidation may take a very long time.

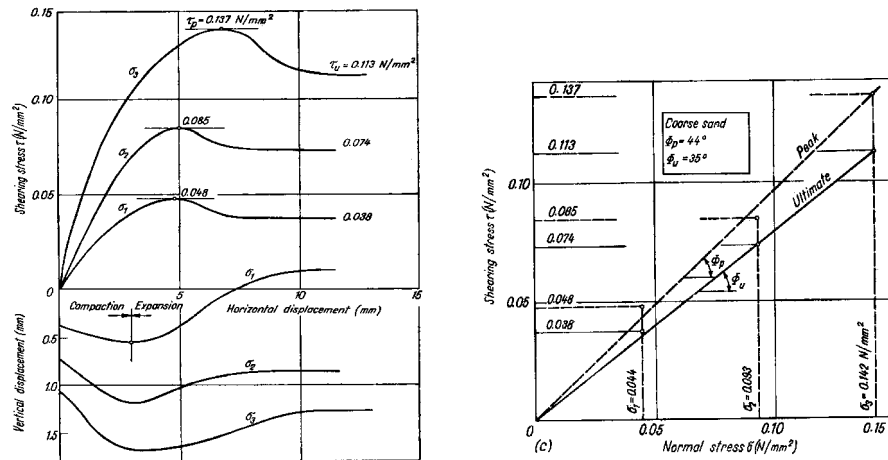
The direct shear test can be performed by a continuous duration of the shear force. This is applied in a stepwise manner; the vertical and horizontal displacements are read off and the next load step is applied thereafter (stress control method).

Another experimental technique consists of a relative displacement at a constant speed between the two shear box frames and the measurement of the shear force is recorded (strain control method).

4.3.3 RESULTS AND DISCUSSION

Fig 4.12 shows results obtained with the strain control method. The soil here was coarse sand. For various constant normal loads the horizontal forces that cause the specimen to fail in shear were measured and the corresponding stress values calculated.

In Fig. 4.12 a the shearing resistance and the vertical displacement (expansion or compaction) of the sample are plotted against the horizontal displacement. By reading off the ultimate shear stress values from the stress – strain curves and plotting them against the corresponding normal stresses we obtain the Coulomb lines as a result and hence the shear strength parameters ϕ and c can be determined graphically (Fig. 4.12 b).



a) Shear test results

b) Calculated shear strength

Figure 4.12 Shear test results of coarse sand with different normal stresses (a) and calculated shear strength; Mohr – Coulomb line (b) (Kezdi, 1980)

In general the following points are discussed for laboratory experiments of the shear box test.

1. The direct shear test is simple and fast to operate. Because thin specimens are used in the shear box, they facilitate drainage of pore water from a saturated sample in short time.
2. In some cases of shear box test the specimen is not failing along its weakest plane but along a predetermined or induced failure plane that is the horizontal plane separating the two halves of the shear box. This is the main draw back of this test. Moreover during loading the state of stress cannot be evaluated. It can be evaluated only at failure condition, Mohr's circle can be drawn at the failure condition only. Failure usually starts at the edge and propagates towards the centre which means failure is progressive with non uniform stress conditions in the specimen.
3. The friction angle (ϕ) of sand depends on the state of compaction, the coarseness of grains and the particle shape. It varies between 28 degrees (uniformly graded sands with round grains in very loose state) to 46 degrees (well graded sand with angular grains in dense state (Kezdi, 1980)).
4. The friction between sand particles is due to sliding and rolling friction and interlocking action.
5. The volume change in sandy soil is a complex phenomenon depending on particle size, particle shape, state and type of packing, etc. In general loose sands contract and dense sands expand in volume on shearing.

5 DISTINCT ELEMENT MODELLING (DEM)

5.1 INTRODUCTION

While soil is a multi-phase particulate medium it is generally modelled as a continuum. Problems occur with this assumption due to soil's inherent granular nature and consequent deformation and failure modes. The problem is particularly acute when local yield occurs in narrow shear zones, resulting in bifurcation behaviour such as fracture, cutting and sliding or dividing as a result of soil – machine interaction or dynamic loading cases.

In such cases it may be advantageous to treat soil as an assemblage of particles with the ability to break and reform contacts since each particle would have its own physical properties governed by physical laws. This method simulates the fracture process sequentially from the formation of small cracks to large slides. In the DEM soil is represented by a system of numerous discrete particles, the dynamic behaviour of each being calculated individually. This method is based on the concept that each particle satisfies the equation of motion and that particle interaction is simple. The discrete particulate modelling was first developed by Cundall (1971 and 1974) for the analysis of rock mechanics problems by using it to analyse the stability of fractured rock slopes. In his method the interaction of particles is viewed as a transient problem with the state of equilibrium developing whenever the internal forces balance.

Even though Cundall pioneered DEM for particles of any shape, Wakabayashi (1957) proposed a testing technique for assemblies of discs that enables the direct determination of contact forces between particles. Analysis of the force distribution in their test technique was described by Josselin de Jong and Verruijt (1969).

They have developed a method to determine the magnitude and the direction of the contact forces between particles, by measuring the rotation of polarised light through those particles made of photoelastic materials.

Other researchers (Serrano and Rodriguez-Ortiz, 1973) developed a numerical model for assemblies of discs and spheres.

In their model contact forces and displacements are calculated for equilibrium conditions assuming that the increments of contact forces are determined by incremental displacements of particle centres.

After ten years of intensive research Cundall (1971) developed a computer model, named 'BALL' to describe the behaviour of granular materials. This model is based on the basic elements of those structures, which are the particles themselves and their interactions. It can be used for both non-coherent particles and coherent particles. The model is validated by Cundall and Strack (1979) by comparing force vector plots obtained from the computer program 'BALL' with the corresponding plots obtained from the photoelastic analysis which was done by De Josselin de Jong and Verruijt (1969).

Cundall and Strack (1979 a and 1979 b) extended DEM to soil using two dimensional disc elements and three dimensional spheres.

The DEM has been used primarily to study the fabric and structure of granular media during loading and to aid the development of constitutive relations for soils using discs and spheres (Bathurst and Rothenburg, 1988 and Oner, 1984). In addition it has been used to study the flow of granular media down inclined chutes (Campbell and Brennen, 1983); slope stability (Uemura and Hakuno, 1987); liquefaction process (Tarumi and Hakuno, 1988) and stress around tunnel openings (Lorig and Brady, 1984).

Agricultural soils are structured and usually compacting. Thus structured soil plays a major role in plant growth. DEM work from the past didn't concentrate on this. In DEM simulation soil is represented by assemblies of discs or spheres with different particle size distribution which is analogous to the actual soil particle shape.

Tanaka et al (2000) presented a simulation of the reaction of tool penetration by representing soil as discs with two kinds of diameters in two dimensional states. In their simulation discs were randomly distributed and each disc was assumed rigid. An overlap between discs was allowed; this overlap causes a contact force and forces acting on a disc appear only when the disc contacts other disc or tool. Furthermore the magnitudes of forces depend on the relative positions and velocities of the discs to the others. In their work an elastic spring between discs is introduced in order to estimate the force produced by the contacts of mutual discs.

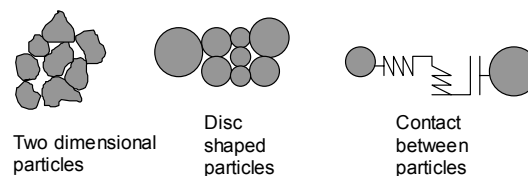
Momozu et al (2000) presented a simulation of the cutting process of a soil block by a pendulum type tool by modifying the conventional DEM model to be applicable for cohesive soil. In conventional DEM the particles have complete discreteness and normally resemble non – cohesive soil. However in his modification adhesion effect between particles is included in the normal direction between particles, when particles are departing from each other after contact. This is because actual soil particles are not completely discrete, especially the cohesive ones.

5.2 GRANULAR MATERIALS AND THEIR STRUCTURE

As the word “granular” in “granular material” implies, this material consists of discrete grains. Liquids and metals also consist of discrete molecules, but the discrete nature of granular materials is much more evident than that of metals and liquids. This is so because the ratio of a microscopic (particle) length scale over a macroscopic length scale is much larger for granular materials, Kruyt (1994). The concept of continuum mechanics is based on the assumption that this ratio is extremely small. This is the so-called continuum hypothesis (Batchelor, 1967).

The behaviour of granular structures depends on the individual particles and their interaction. In order to be able to model this on a microscopic level three approximations have to be done (Baars, 1995).

- Number of dimensions of particles
- Shape and size of particles
- Nature of contact between particles



A first approximation is made due to the number of dimensions. Three dimensional computer modelling consumes a lot of time and memory whereas two dimensional modelling is simple and consumes less time and memory. Therefore two dimensional modelling is selected for the present case.

The second approximation is made with respect to the particle shape. Analysis of a medium which consists of irregularly shaped particles is a major problem in the DEM studies. In early versions of the DEM model polygonal particles were often used (Meguro et al, 1991). The forces acting between these particles being assumed to be transmitted through contact between corners or edges. Moreover using such particles required much more computation time because of the complexity in judging the contact between particles. The most common and simplified shape is a disc or a sphere. For the present case a disc is selected as the best particle shape for two dimensional cases.

The third approximation is the description of contact behaviour between particles which includes: normal deformation, shear deformation and slip or crack. All differences between real measurements and model results have to be explained by those three approximations besides selecting the right input parameter values.

5.2.1 DESCRIPTION OF CONTACT BETWEEN DISCS (PARTICLES)

In conventional DEM model the equilibrium contact forces and displacements of a stressed assembly of discs are found through a series of calculations tracing the movements of the individual particles. These movements are the result of the propagation through the medium of disturbance originating at the boundaries which is a dynamic process. In describing this dynamic behaviour numerically, small time steps are taken over which velocities and accelerations are assumed to be constant.

The deformations of the individual particles are small in comparison with the deformation of a granular assembly as a whole. The latter deformation is due primarily to the movements of the particles as rigid bodies. In the 'BALL' program the particles are allowed to overlap one another at contact points. This overlap causes a contact force. Forces acting on a disc appear only when the disc contacts with other discs or wall/tool and the magnitude of forces depends on the relative positions and velocities of the disc to the others.

The judgement of contact of discs is based on the geometrical relationship between the discs and the disc/wall. In other words if the distance between two centres of two discs is smaller than the sum of the radii (Eqn 5.1) of these two discs it follows that the discs are contacting each other (see Fig. 5.1). Also in the case of the contact between the disc and the wall /tool, if the distance between the centre of the disc and the wall/tool is smaller than the radius of the disc it follows that the disc contacts the wall/tool (see Fig. 5.1, disc x contacting the lower wall ($x_2 < R_x$)).

Figure 5.4 shows the mechanical relationship in normal and tangential directions between contacting discs. The reaction force by the spring and viscosity resistance by the dashpot are calculated for a disc which is overlapped by another disc in both normal and tangential directions. Each disc particle receives contact forces from contacting particles/walls. The magnitude of the contact force is determined by the relative displacement and relative velocity of the disc particle. See Eqns (5.9 and 5.10).

The calculations performed in the distinct element method alternate between the application of Newton's second law to the discs and a force-displacement law at the contacts. Newton's second law gives the motion of a particle resulting from the forces acting on it. The force – displacement law is used to find contact forces from displacements.

5.2.1.1 The force – displacement law and equations of particle motion

In the general case of an assembly of many discs, the force – displacement law is applied at each contact of any disc and the vectorial sum of these contact forces is determined to yield the resultant force acting on that disc. When this has been accomplished for every disc, new accelerations are calculated from Newton's second law.

The force-displacement law will be presented for the case of two discs in contact, disc x and disc y in Figure 5.1

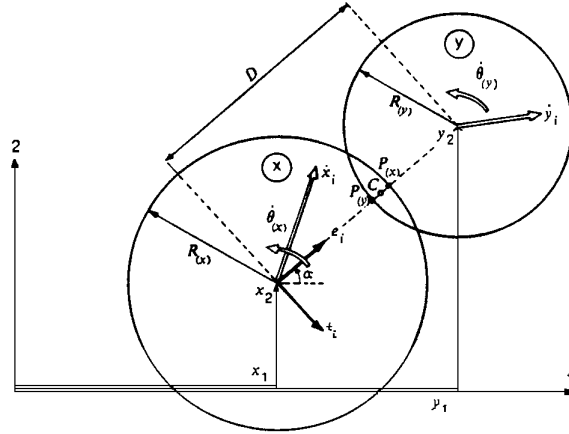


Figure 5.1 Contact between two discs (Cundall & Strack, 1979)

The co-ordinates of the disc centres are represented as $x_i = (x_1, x_2)$ and $y_i = (y_1, y_2)$ where the indices 1 and 2 refer to the co-ordinates of a Cartesian co-ordinate system as indicated in the figure above.

The components of the velocity vectors of discs x and y are $\dot{x}_i = (\dot{x}_1, \dot{x}_2)$ and $\dot{y}_i = (\dot{y}_1, \dot{y}_2)$ respectively and the angular velocities are $\dot{\theta}_x$ and $\dot{\theta}_y$, taken positive in counter clockwise direction.

Discs x and y have radii R_x and R_y and masses m_x and m_y . Points p_x and p_y are defined as the points of intersection of the line connecting the disc centres with the boundaries of discs x and y respectively. Two discs are taken to be in contact only if the distance D between their centres is less than the sum of their radii,

$$D < R_x + R_y \quad (5.1)$$

If the above condition is met, the relative displacement at contact C (Fig. 5.1) is determined by integration of the relative velocity. The relative velocity at the contact is defined as the velocity of point p_x with respect to p_y . The unit vector $e_i = (\cos \alpha, \sin \alpha)$ is introduced as pointing from the centre of disc x to the centre of disc y ,

$$e_i = (y_i - x_i) / D = (\cos \alpha, \sin \alpha) \quad (5.2)$$

and the unit vector t_i is obtained by a clockwise rotation of e_i through 90° i.e.

$$t_i = (e_2 - e_1) \quad (5.3)$$

The relative velocity of point p_x with respect to p_y expressed as,

$$\dot{X}_i = (\dot{x}_i - \dot{y}_i) - (\dot{\theta}_x R_x + \dot{\theta}_y R_y) t_i \quad (5.4)$$

The normal (\dot{u}_n) and tangential (\dot{u}_s) components of the relative velocities are the projections of \dot{X}_i on to e_i and t_i respectively,

$$\dot{u}_n = \dot{X}_i e_i = (\dot{x}_i - \dot{y}_i) e_i - (\dot{\theta}_x R_x + \dot{\theta}_y R_y) t_i e_i = (\dot{x}_i - \dot{y}_i) e_i \quad (5.5)$$

$$\dot{u}_s = \dot{X}_i t_i = (\dot{x}_i - \dot{y}_i) t_i - (\dot{\theta}_x R_x + \dot{\theta}_y R_y) t_i t_i = (\dot{x}_i - \dot{y}_i) t_i - (\dot{\theta}_x R_x + \dot{\theta}_y R_y) \quad (5.6)$$

Integration of the relative velocity component with respect to time gives the components Δu_n and Δu_s of the relative displacement increment,

$$\Delta u_n = (\dot{u}_n) \Delta t = \{(\dot{x}_i - \dot{y}_i) e_i\} \Delta t \quad (5.7)$$

$$\Delta u_s = (\dot{u}_s) \Delta t = \{(\dot{x}_i - \dot{y}_i) t_i - (\dot{\theta}_x R_x + \dot{\theta}_y R_y)\} \Delta t \quad (5.8)$$

These relative displacement increments are used with the force – displacement law to calculate increments of the normal and shear forces,

$$\Delta F_n = k_n \Delta u_n = k_n \{(\dot{x}_i - \dot{y}_i) e_i\} \Delta t \quad (5.9)$$

$$\Delta F_s = k_s \Delta u_s = k_s \{(\dot{x}_i - \dot{y}_i) t_i - (\dot{\theta}_x R_x + \dot{\theta}_y R_y)\} \Delta t \quad (5.10)$$

where

k_n and k_s represent the normal and shear stiffness, respectively.

Finally at each time step the force increments ΔF_n and ΔF_s are added to the sum of all force increments, F_n and F_s determined from previous time steps:

$$(F_n)_N = (F_n)_{N-1} + \Delta F_n \quad (5.11)$$

$$(F_s)_N = (F_s)_{N-1} + \Delta F_s \quad (5.12)$$

where the indices N and $N - 1$ refer to times t_N and t_{N-1} such that $t_N - t_{N-1} = \Delta t$.

The sign convention for the normal and shear forces acting on disc x is as shown on the Figure 5.2

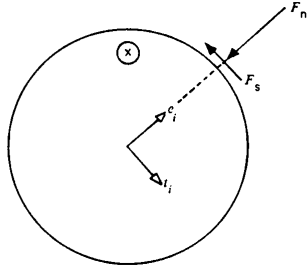


Figure 5.2 Sign convention for F_n and F_s (Cundall & Strack, 1979)

F_n and F_s are taken as positive in the directions opposite to e_i and t_i . The magnitude of the shear force found from Equation (5.12) is checked against the maximum possible value $(F_s)_{\max}$ defined as

$$(F_s)_{\max} = F_n \tan \phi + c \quad (5.13)$$

where

ϕ is the interparticle friction angle of the two discs in contact and c is the smaller of their cohesions.

If the absolute value of $(F_s)_N$ found from Equation (5.12) is larger than $(F_s)_{\max}$, then $(F_s)_N$ is equal to $(F_s)_{\max}$, preserving the sign obtained from Equation (5.12).

Once the normal and the shear forces have been determined for each contact of a disc, for example disc x , they are resolved into components in the directions 1 and 2, see Fig. 5.1. The sum of these contact force components gives the resultant forces $\sum F_{x1}$ and $\sum F_{x2}$. The resultant moment acting on disc x , $\sum M_x$ is taken positive if acting in the counter-clockwise direction and is found from $\sum M_x = \sum F_x R_x$, where summation is taken over all contacts of disc x . The resultant moments and forces acting on disc x are used with

Newton's second law to determine the new accelerations \ddot{x}_i and $\ddot{\theta}_x$.

The velocities \dot{x}_i and $\dot{\theta}_x$ used in the force – displacement law in Equations (5.9) and (5.10) are obtained as follows. The current resultant force and the moment at time t_N are assumed to act on disc x during the time interval Δt from $t_{N-1/2}$ to $t_{N+1/2}$.

Newton's second law applied to disc x is,

$$m_x \ddot{x}_i = \sum F_{x_i} \quad (5.14)$$

$$I_x \ddot{\theta}_x = \sum M_x \quad (5.15)$$

where, m_x and I_x represent the mass and moment of inertia of disc x respectively.

Taking \ddot{x}_i and $\ddot{\theta}_x$ constant over the time step Δt the expressions for the velocities are,

$$(\dot{x}_i)_{N+1/2} = (\dot{x}_i)_{N-1/2} + \left[\sum F_{x_i} / m_x \right]_N \Delta t \quad (5.16)$$

$$(\dot{\theta}_x)_{N+1/2} = (\dot{\theta}_x)_{N-1/2} + \left[\sum M_x / I_x \right]_N \Delta t \quad (5.17)$$

These new values for the velocities are used in the force – displacement law and the cycle is repeated for a new time increment.

The new values for velocities are used also to update the positions and rotations of the discs by a further numerical integration,

$$(x_i)_{N+1} = (x_i)_N + (\dot{x}_i)_{N+1/2} \Delta t \quad (5.18)$$

$$(\theta_x)_{N+1} = (\theta_x)_N + (\dot{\theta}_x)_{N+1/2} \Delta t \quad (5.19)$$

Body forces, such as gravitational forces may be included if so desired. In that case a term $m_x g_i$ is added to the force sum $\sum F_{x_i}$ in Equation (5.16), where $g_i = (g_1, g_2)$ represents the two components of the acceleration vector due to the body force.

Friction damping occurs during sliding when the absolute value of the shear force at any contact is $(F_s)_{\max}$. Contact damping operates on the relative velocities at the contacts and may be envisioned as resulting from dashpots acting in the normal and shear directions at contacts. The viscous damping in the shear direction is not applied when sliding occurs. In this case friction damping alone operates.

The coefficients of viscous contact damping in the normal and shear directions are represented by η_n and η_s . If contact damping is taken into account the damping forces must be included in the force sums in Equations (5.16) and (5.17) which become,

$$(\dot{x}_i)_{N+1/2} = (\dot{x}_i)_{N-1/2} + \left\{ \sum [F_{x_i} + D_{x_i}] / m_x \right\}_N \Delta t \quad (5.20)$$

$$(\dot{\theta}_x)_{N+1/2} = (\dot{\theta}_x)_{N-1/2} + \left\{ \sum M_x / I_x \right\}_N \Delta t \quad (5.21)$$

where $\sum D_{x_i}$ represents the sum of the components of the contact damping forces and

$\sum M_x$ includes the contribution of the contact damping forces to the moment sum.

The global components D_{x_i} are found from the normal D_n and the shear D_s components of the damping force at the contacts.

$$(D_n)_N = \eta_n \dot{u}_n = \eta_n (\dot{x}_i - \dot{y}_i)_{N-1/2} e_i \quad (5.22)$$

$$(D_s)_N = \eta_s \dot{u}_s = \eta_s \left\{ (\dot{x}_i - \dot{y}_i)_{N-1/2} t_i - (\dot{\theta}_x R_x + \dot{\theta}_y R_y)_{N-1/2} \right\} \quad (5.23)$$

In the original version of ‘BALL’ or the current version of DEM the contact damping coefficients η_n and η_s are taken to be proportional to the stiffness k_n and k_s with proportionality constant γ

$$\eta_n = \gamma k_n \quad (5.24)$$

$$\eta_s = \gamma k_s \quad (5.25)$$

5.2.1.2 Numerical stability

As a consequence of the explicit nature of the numerical scheme employed in the DEM programme, a time step must be selected small enough to make the numerical simulation stable. Its stability properties are analysed in Corkum & Ting (1986) for the constitutive relation at the contact as discussed here, that is less than the maximum critical value calculated from the following relations

$$\Delta t \leq \Delta t_{crit} = a \sqrt{\frac{m}{k_n}} \quad (5.26)$$

where

Δt is the input time step; Δt_{crit} is the critical time step calculated from the simulation; a is a proportionality constant; m and k_n are the mass and the stiffness of the particles, respectively.

5.3 PRINCIPLES OF DEM CALCULATION

The calculations performed in the distinct element method alternate between the application of Newton's second law to the discs and a force-displacement law at the contacts. Newton's second law gives the motion of a particle resulting from the forces acting on it. The force – displacement law is used to find contact forces from displacements.

This calculation is based on the idea that the chosen input time step (Eqn 5.26) may be so small that during a single time step disturbances can not propagate from any disc further than its immediate neighbours. The positions of each particle are determined step – by – step at intervals of this time step (Δt). The position and contact force on each particle determine the motion of the particle. Simulation is conducted by repeating the calculations of these two values. The concept of this algorithm is shown in Fig. 5.3

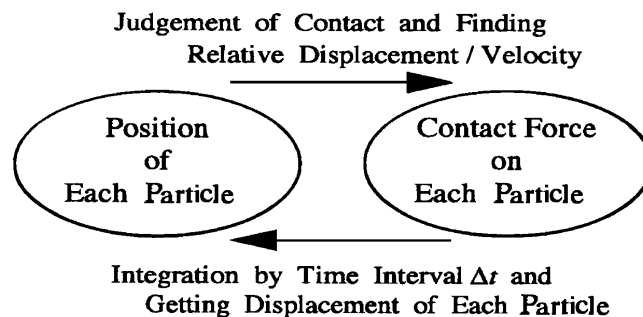


Figure 5.3 The calculation cycle of the DEM simulation algorithm (Adapted from: Tanaka et al, 2000)

5.4 REVIEW OF THE DEM MODELS

Although the distinct element modelling was first developed by Cundall (1971 and 1974) for the analysis of rock mechanics problems and later extended to soil using two – dimensional disc particles (Cundall and Strack, 1979 a) and three – dimensional spheres (Cundall and Strack, 1979 b), numerous other researchers have modified the conventional DEM model (Fig. 5.4) to improve its potentiality on different areas of expertise.

The DEM has been used primarily to study the fabric and structure of granular media during loading and to aid in the development of constitutive relations for soil using disc and sphere (Bathurst et al, 1988 and Oner, 1984).

In addition it has been used to study the flow of granular media down inclined chutes (Campbell and Brennen, 1983; Hawkins, 1983), stress around tunnel openings (Lorig and Brady, 1984), analysis of soil cutting (Momozu et al, 2000), blockage of cohesive particles in a hopper (Umekage et al, 1998), shear zone kinematics (Morgan et al, 1999), dynamic fracture analysis of ground and resistance against rolling at contacts (Iwashita and Oda, 1998), fracture analysis of media composed of irregularly shaped regions (Meguro et al, 1991), modelling in geomechanics (Sharma et al, 1999) and constitutive relations for cohesionless granular material (Kruyt, 1994).

Now we focus our attention on the review of some of the models which are in our areas of interest. Among them the models of Momozu (2000), Umekage and Shinkia (1998), Morgan (1999), Iwashita and Oda (1998) and Meguro and Hakuno (1991). Their models are very relevant for our areas of research but the optimal model is still under investigation. We here focus on areas of soil dynamics. For clear understanding, this review is classified into two parts: one is referring to the contact model of particles and the second is referring to the initial structure of those particles.

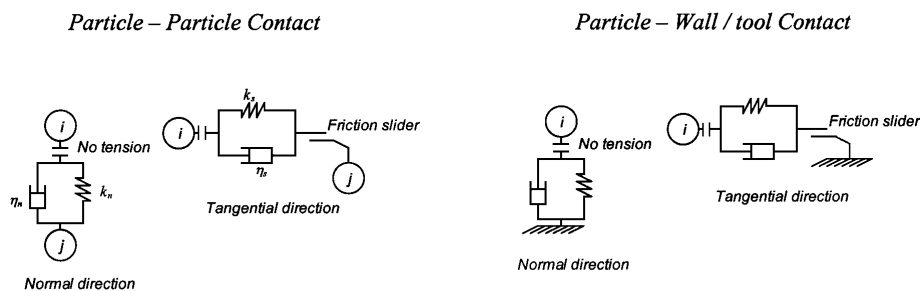


Figure 5.4 Mechanical contact model of Conventional DEM

5.4.1 REVIEW CONTACT MODEL OF PARTICLES IN DEM

The nature of contact between particles is one of the approximations used to explain the DEM model properties. In some cases the advantages and disadvantages of the model were analysed based on this contact properties. The two familiar drawbacks of the conventional DEM model are: it is used only for non – cohesive particles (Umekage and Shinkia, 1998; Momozu, 2000) and its high degree of particle rotation due to the circular shape of particles (Iwashita and Oda, 1998; Morgan, 1999)

In the conventional DEM model the particles are in a complete discreteness in which the effect of cohesion force between particles was ignored. However real soil particles have cohesive properties due to clay properties or pore water suction. Conventional DEM has a problem to determine the behaviour of cohesive soil. In order to be able to determine the behaviour of cohesive soil the DEM model has to be modified.

1. Momozu (2000) has modified the conventional DEM model by assuming the adhesion effects between particles. In his hypothesis such an adhesion force restricts the movements of soil particles in actual soil. In order to assume such adhesion effects he introduced ‘adhesion spring’ in the normal directions of particle contact and its effect was considered when the particles are departed from each other. See the mechanical contact model in Fig. 5.5.

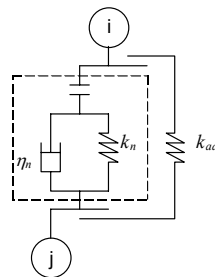


Figure 5.5 Contact model between two particles with adhesion spring in the normal direction, Momozu (2000)

If the co-ordinates (x_i, y_i) and (x_j, y_j) in Figure 5.6 are the centres of the contacting particles i and j respectively and overlap between particles is allowed, then the distance D between centres of the two particles where the adhesion acts can be calculated as:

$$D = \sqrt{(x_i - x_j)^2 + (y_i - y_j)^2} \quad (5.27)$$

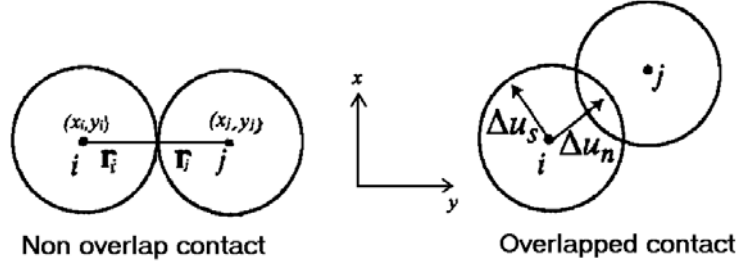


Figure 5.6 Particle – particle contact displacement components

The adhesion force will act between two particles which distance satisfies the following equation (with ‘ C_{ad} ’ is adhesion coefficient):

$$r_i + r_j < D \leq (1 + C_{ad})(r_i + r_j) \quad (5.28)$$

According to *Kyoto DEM* (Momozu, 2000) the conventional DEM model is applied when compression occurs between particles (Fig. 5.4), whereas a modified model (Fig. 5.5) is utilised when the particles start departing each other. Then the adhesion force F_{ad} is

$$F_{ad} = C_{ad}(r_i + r_j - D) \quad (5.29)$$

where

F_{ad} = adhesion force ; k_{ad} = adhesion spring ; D = distance between centers of particle i and particle j ; r_i, r_j = radii of particle i and particle j respectively.

2. Umekage et al (1998) also modified the conventional DEM in order to account for the effect of cohesion forces between particles. They introduced normal and shear cohesion forces between particles. In this case the cohesion force is defined as the attractive force which acts at the contact point in the opposite direction of separation only when the contacted particles move away from each other. Both the normal and the shear cohesion force have the same value.

When particles do not contact each other the cohesion force becomes zero.

The equations of the contact force of the particles in the normal and tangential directions are as follows. Fig. 5.7 shows the mechanical contact model with cohesion force.

$$[F_n]_t = [f_n]_t + [d_n]_t - (|\Delta x_n| - \Delta x_n / 2 |\Delta x_n|) [C_F]_t \quad (5.30)$$

$$[F_s]_t = [f_s]_t + [d_s]_t - \text{sign}([f_s]_t) [C_F]_t \quad (5.31)$$

where

$$[f_n]_t = [f_n]_{t-\Delta t} + k_n \Delta x_n ; \quad [d_n]_t = [d_n]_{t-\Delta t} - \eta_n \Delta \dot{x}_n ; \quad [f_s]_t = [f_s]_{t-\Delta t} + k_s \Delta x_s ;$$

$$[d_s]_t = [d_s]_{t-\Delta t} - \eta_s \Delta \dot{x}_s$$

In which F_n and F_s are the normal and tangential contact forces respectively; f_n and f_s are the normal and tangential dispersion forces; d_n and d_s are the normal and tangential damping forces; k_n and k_s are elastic spring constants in normal and tangential directions; η_n and η_s are viscous dashpots in normal and tangential directions; Δx_n and Δx_s are the increments of the relative particle displacement in normal and tangential directions;

$\Delta \dot{x}_n$ and $\Delta \dot{x}_s$ are the increments of the relative particle velocity in normal and tangential direction; C_F is the cohesion force that acts as the resistance force against the dispersion force. They assumed that the cohesion force is the resistance against particle dispersion so that the following conditions are required,

If $|f_n + d_n| < C_F$, $F_n = 0$; If $|f_s + d_s| < C_F$, $F_s = 0$;

If $|f_s| \geq [\mu f_n + C_F]$, $f_s = \text{sign}[f_s][\mu f_n + C_F]$ and $d_s = 0$ (for sign rule see what is explained for Eqns 5.12 and 5.13). The summation of contact force components in each direction gives the resultant force, $\sum ([F_n]_t + [F_s]_t)$. The resultant moment acting on the particles is found from $\sum (r[F_s]_t)$. These summations are taken over all contact points of the particle.

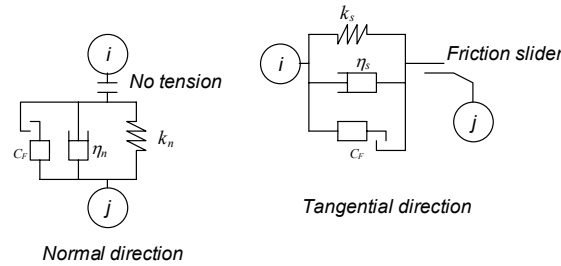


Figure 5.7 Contact model between two particles with cohesion effect, Umekage et al (1998)

3. Meguro et al (1991) improved the DEM model by introducing a new pore-spring model (Meguro's model) in which both transmission of the moment and rotation of the particles are considered. In their model an aggregate of particles connected by pore springs rotates as one body. Combining the DEM with this new pore-spring, they developed a new simulation program that uses arrays of different material parameters and called it "Extended Distinct Element Method (EDEM) or Modified Distinct Element Method (MDEM).

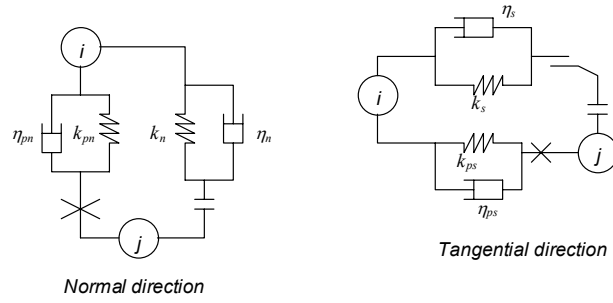


Figure 5.8 Contact model between two particles with pore – spring, Meguro et al (1991)

This Extended Distinct Element method (EDEM) is a numerical method applicable both to homogeneous and perfect discrete media and to complex, heterogeneous and continuous media (Meguro et al, 1991). Figure 5.8 shows the mechanical modelling of a medium for the EDEM model. The EDEM was developed by the introduction of modified pore-springs (k_{pn} and k_{ps}) and arrays of different material parameters to extend the application of the DEM.

The pore-spring used was established by Meguro based on Iwashita's model. With this pore-spring, rotation of particles and the transmission of moment can be taken into account. Moreover an aggregate of particles connected by pore-springs rotates as one body. For EDEM the equations of particle motion having the mass m and the moment of inertia I are as follows

$$m\ddot{u} + C\dot{u} + F = 0 \quad (5.32)$$

$$I\ddot{\phi} + D\dot{\phi} + M = 0 \quad (5.33)$$

In which F is the sum of all the forces acting on the particle; M is the sum of all the moments acting on it; C and D are the damping coefficients; u is the displacement vector; ϕ is the rotational displacement. Because two kinds of forces act on it (the force received from all the particles in contact and the force of all the pore material surrounding it), F and M are expressed as Equations (5.34) and (5.35):

$$F = F_p + F_{pore} + m[g + a] \quad (5.34)$$

$$M = M_p + M_{pore} \quad (5.35)$$

In which F_p is the sum of all the force vectors from all the particles in contact, F_{pore} is the force from all the pore material surrounding the particle.

M_p and M_{pore} are the respective sums of all the moments of all the particles in contact and of all the pore material surrounding the particle.

g is the acceleration due to gravity and a is the external acceleration acting on it.

4. Iwashita and Oda (1998) further modified the conventional DEM in which resistance against rolling at contacts is taken into account. He added an additional set of an elastic spring (k_r), a dashpot (C_r), a no tension joint and a slider (μ_r) at each contact, which respond to the moment M of the couple force.

Resistance against rolling is supplied by the elastic spring and the dashpot (Fig. 5.9).

The elastic spring yields rotational resistance equal to $k_r \theta_r$,

where k_r is the rotational stiffness and θ_r is the relative rotation by rolling.

These relative movements taking place at a contact during incremental deformation can in general be decomposed into two components: sliding and rolling.

The rolling component leads to the relative rotation between two particles with a common contact. The dashpot supplies rotational resistance equal to $C_r d\theta_r / dt$.

Where $d\theta_r / dt$ is the speed of relative particle rotation and C_r is the viscosity.

The sum of these resistances must be in equilibrium. The moment M satisfies an inequality of $|M| \geq \xi \Delta a F_n$. Where Δa is a length scale typical for a related contact surface and ξ is a non-dimensional coefficient (Sakaguchi et al, 1993). The contact model of the MDEM is shown in the Figure 5.9 below.

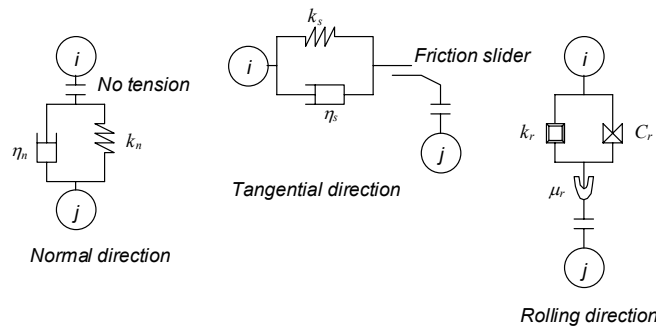


Figure 5.9 Contact model between two particles with rolling effect, Iwashita and Oda (1998)

5.4.2 REVIEW INITIAL STRUCTURE OF PARTICLES IN DEM

In the conventional DEM model the initial structure (arrangement) of particles is determined from randomly generated particles within specified boundaries (walls) in a manner at which positions and radii of such particles are given with respect to the x, y co – ordinate system (Cundall and Strack 1979). The particles are allowed to overlap one another at contact points. This overlapping behaviour takes the place of the deformation of individual particles. The magnitude of the overlap is related directly to the contact force in the way explained in section 5.2.1.1 and 5.5.1). It should be noted however that these overlaps are small in relation to the particle sizes.

1. Momozu et al (2001) used the conventional DEM model to develop a randomised initial arrangement of particles for the shearing simulation. At first the particle centres were regularly arranged in the calculation area. In this case the calculation area is defined as the area of the box which is larger in size than the shear box: 2.5 times the height of the shear box, with the same width as the shear box. In the calculation area particles were assumed to have the same radius (r_c) and being packed densely. After this step the radius of each particle was determined by

$$r_i = 0.5r_c + 0.5r_c R \quad (5.36)$$

where

r_i = radius of each particle; r_c = constant radius; R = random number between 0 and 1

He finally reached to the conclusion that the results obtained from the simulation were similar to the case of sand soil. The internal friction coefficient of the particle assembly which was obtained from the simulation was significantly different from the corresponding input value and the initial arrangement of particles was affecting the internal friction of elements.

2. Kruyt (1994) investigated the behaviour of granular assemblies by simulation of biaxial tests. The initial arrangement of particles is developed in such a manner that the particles were positioned inside a rectangular container without contacting each other. After that all walls (boundaries) were moved inwards at the same speed until the sample is compacted to a certain degree. The deformation of the particles is small, the overlap is specified to be smaller than a fraction of the particle radius. A typical assembly of discs after deformation is shown in Figure 5.10.

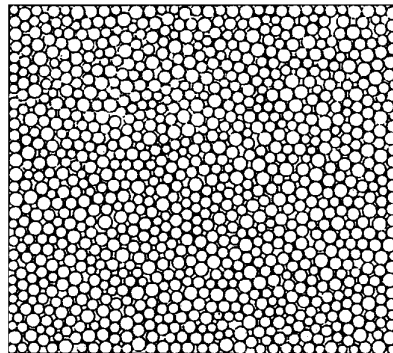


Figure 5.10 Assemblies of discs (Kruyt, 1994)

The disc radii were chosen according to a log-normal distribution (Prasher, 1987):

$$f(r; \alpha, \beta) = \frac{1}{r\sqrt{2\pi}\beta} \exp\left[\frac{-1}{2\beta^2} (\ln(r) - \ln(\alpha))^2\right] \quad (5.37)$$

where

parameters α and β are related to the mean radius \bar{R} and standard deviation $s\bar{R}$ of the probability distribution by $\alpha = \frac{\bar{R}}{\sqrt{1+s^2}}$ and $\beta^2 = \ln(1+s^2)$

The average radius \bar{R} is 1mm, and two cases were considered for the standard deviation of the disc radii ($s = 0.125$ and $s = 0.25$)

3. Morgan and Boettcher (1999) also investigated the character of deformation in the simulated assemblages, especially in relation to interparticle deformation mechanisms, localisation tendencies and geometries of micro-structures. The study mainly focused on the numerical simulation of the granular shear zone.

The initial particle assemblage was created by randomly generating a specified number of spheres of four different sizes: 500, 250, 125, and 62.5 μm within the 2D domain. Relative particle abundance was determined according to the following power law relationship, Sammis et al (1986) and Sammis and Biegel (1987)

$$N_i = N_{\max} \left(\frac{R_{\max}}{R_i} \right)^D \quad (5.38)$$

where

R_{\max} , R_i = maximum and incremental particle sizes; N_{\max} , N_i = maximum and incremental abundances; D = power law exponent.

The largest particles were generated first and the smaller ones squeezed into the remaining space with no overlap (Fig. 5.11)

Spherical particles centred on the x , y plane were used in these 2D simulations. The volume was then consolidated by moving the x and y boundaries of the domain inward until the desired isotropic mean stress (σ_m) was attained.

Deformation in this numerical assemblage is accommodated in large part by interparticle rolling. The distribution of rolling particles is strongly influenced by the particle size distribution and the geometry of particle packing.

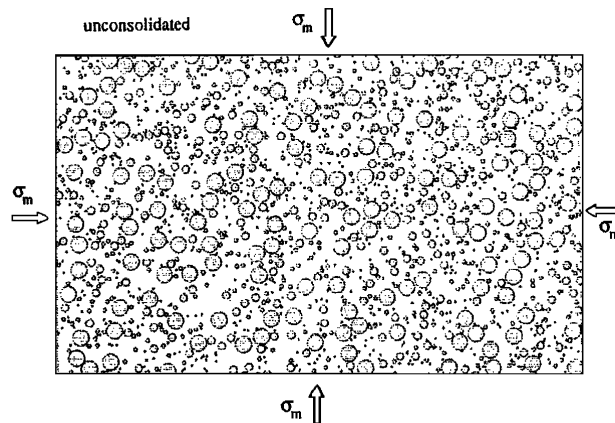


Figure 5.11 Initial structure of generated particles within the medium, Morgan and Boettcher (1999)

4. Sharma et al (1999) also studied the biaxial test simulation. The primary objective of his study was to investigate the microstructure and contact force distribution of soil particles during compaction. The generation of the initial structure of particles is described below. The program reads the particle information and its distribution data and generates an assembly of discs. Further the program locates these discs with respect to a fixed rectangular co-ordinate system.

Disc generation is accomplished using a random number generator that places non-overlapping discs of desired sizes corresponding to desired distribution at random $x - y$ locations within a specified size of circular regions within a box of specified size. He showed that if this assembly is hydrostatically compacted using strain controlled boundary conditions, a denser state of an assembly is obtained (Fig. 5.12 b).

The initially generated discs are an assembly of 1000 frictional discs of 20 different types in contact with a gradation of uniformly graded granular soils. The chosen normal and shear stiffness values ranged from 1.5 MN/mm for the largest size discs to 2.5 MN/mm for the smallest size discs, which are in conformity with real granular materials, Hakuno and Tarumi (1988).

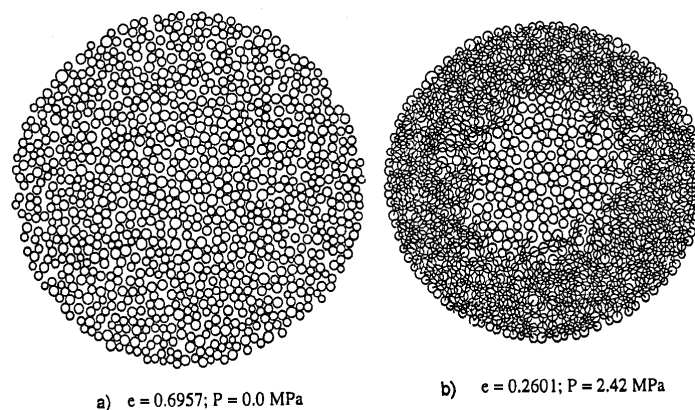


Figure 5.12 Discs and contact force distribution in the assembly at different stages of loading from initially generated non-overlapping discs (Sharma et al, 1999).

5.5 SELECTION OF APPROPRIATE DEM MODELS

For the present simulations two appropriate DEM models are selected based on the contact properties and initial arrangement of particles. The conventional DEM model (Fig. 5.4) is selected for the contact properties of completely discrete (non – cohesive) particles and their initial structure is very similar to the structure of non – cohesive natural soil.

For contact properties of adhesive particles which form soil clods during cutting, the modified DEM model (Fig. 5.5) of Momozu (Momozu et al, 2000) is selected. The two models (the conventional DEM model for non – cohesive particles property and the modified DEM model for cohesive particles property) are jointly said to be the ‘*Kyoto DEM*’.

The *Kyoto DEM* is the DEM software of the shear box test and the soil cutting test by a pendulum type machine that was originally composed by Dr. Momozu of the Kyoto University of Japan. For further understanding of *Kyoto DEM*, see the user related characteristics of *Kyoto DEM* in the next section (section 5.6.1.2). The force – displacement equations of the conventional DEM model used in the *Kyoto DEM* are explained below. For the modified part see the DEM review of Momozu (2000).

5.5.1 THE FORCE – DISPLACEMENT EQUATIONS IMPLEMENTED IN THE SELECTED DEM MODEL

The force – displacement equations explained for the *Kyoto DEM* program in the following section are in different capacity compared to the force – displacement equations explained in the original DEM program of ‘BALL’ (section 5.2.1 1). However some of the *Kyoto DEM* equations, for example, Eqns. 5.39 and 5.41 are in the same capacity as Equations 5.7 to 5.12. The only difference is that the damping forces (normal and tangential damping forces), are included in the *Kyoto DEM* program.

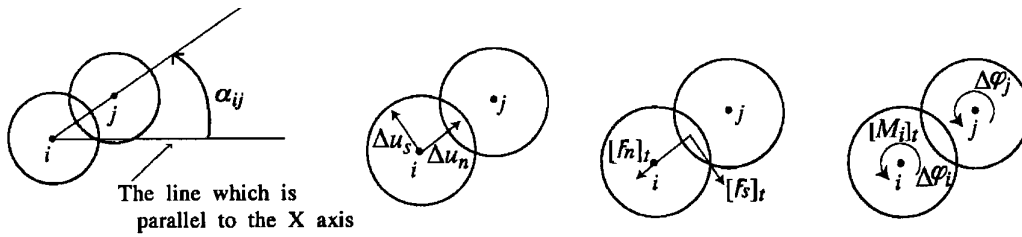


Figure 5.13 Particle – particle contact and direction of contact force and particles displacement (Tanaka et al, 2000)

The normal contact force F_n between two particles is expressed as,

$$[F_n]_t = [e_n]_t + [d_n]_t = [e_n]_{t-\Delta t} + k_n \Delta u_n + \eta_n [\Delta u_n / \Delta t] \quad (5.39)$$

$$\Delta u_n = (\Delta u_i - \Delta u_j) \cos \alpha_{ij} + (\Delta v_i - \Delta v_j) \sin \alpha_{ij} \quad (5.40)$$

where, $[e_n]_t = [e_n]_{t-\Delta t} + k_n \Delta u_n$ is analogous to Eqn. 5.11 which is further related with Eqns. 5.9 and 5.7. In other words Eqn. 5.39 is the scalar sum of Eqn. 5.11 and the normal damping force ($[d_n]_t$). In the normal direction the tension force is assumed to be zero as shown in the contact model (Fig. 5.4)

If $[e_n]_t < 0$, $[e_n]_t = [d_n]_t = 0$ implies no tension force

where

F_n is normal contact force ; t is time point; e_n is elastic force in the normal direction ; d_n is damping force in the normal direction; k_n is normal spring constant; η_n is normal damping coefficient; Δt is time step ;

Δu_n is normal relative displacement of particle i to particle j during Δt ;
 $\Delta u_i, \Delta u_j$ are horizontal displacements of particle i and j during Δt ;
 $\Delta v_i, \Delta v_j$ are vertical displacements of particles i and j during Δt ;
 α_{ij} is the angle between the line connecting the centres of the particles and the X – axis

The tangential contact force F_s between two particles,

$$[F_s]_t = [e_s]_t + [d_s]_t = [e_s]_{t-\Delta t} + k_s \Delta u_s + \eta_s [\Delta u_s / \Delta t] \quad (5.41)$$

$$\Delta u_s = -(\Delta u_i - \Delta u_j) \sin \alpha_{ij} + (\Delta v_i - \Delta v_j) \cos \alpha_{ij} + r_i \Delta \varphi_i + r_j \Delta \varphi_j \quad (5.42)$$

where, $[e_s]_t = [e_s]_{t-\Delta t} + k_s \Delta u_s$ is analogous to Eqn. 5.12 which is further related with Eqns. 5.10 and 5.8. In other words Eqn. 5.41 is the scalar sum of Eqn. 5.12 and the tangential damping force ($[d_s]_t$). In the tangential direction the particles slip against each other when the tangential force reaches the maximum friction force.

If $[e_n] < 0$, $[e_s]_t = [d_s]_t = 0$,

If $|[e_s]_t| > \mu [e_n]_t$, $[F_s]_t = [e_s]_t = \mu [e_n]_t$ also preserve sign of $[e_s]_t$ as it was explained in Equation (5.13), then slip or plastic deformation occurs

where

F_s is tangential contact force ; e_s is tangential elastic force ; d_s is tangential inelastic force ; k_s is tangential spring constant ; η_s is tangential damping coefficient ; t is time point ; Δt is time step ; Δu_s is tangential relative displacement of the particle i to the particle j during Δt ; μ is coefficient of sliding between two particles ; r_i , r_j are radii of particles i and j ;
 $\Delta \varphi_i$, $\Delta \varphi_j$ are rotational displacements of the particles i and j during Δt

The sign rule for relative displacement of the element i to the particle j is shown in Figure 5.13. In the normal direction, Δu_n is taken as positive for compression. In the tangential direction, Δu_s is taken as positive in the clockwise direction around the particle j .

$[F_n]_t$ and $[F_s]_t$ are taken as positive in the direction opposite to Δu_n and Δu_s (Fig. 5.13).

As for the rotational displacement $\Delta \varphi_i$ and the moment $[M_i]_t$, each value is taken as positive in the counterclockwise direction as shown in the Figure 5.13.

The contact forces in the normal and tangential direction are transformed into the forces in the horizontal, vertical and rotational directions. And next the contact forces caused by all of the particles which contact the particle i are summed up. Resultant forces which act on the particle i in the horizontal, vertical and rotational directions are obtained as

$$[X_i]_t = \sum_j \{ -(F_n)_t \cos \alpha_{ij} + (F_s)_t \sin \alpha_{ij} \} \quad (5.43)$$

$$[Y_i]_t = \sum_j \{ -(F_n)_t \sin \alpha_{ij} - (F_s)_t \cos \alpha_{ij} \} - m_i g \quad (5.44)$$

$$[M_i]_t = -r_i \sum_j \{ (F_s)_t \} \quad (5.45)$$

where

$[X_i]_t$ = horizontal resultant force on particle i at time t ; $[Y_i]_t$ = vertical resultant force on particle i at time t ; α_{ij} = angle between the X -axis and the common normal of two contacted particles i and j ; m_i = mass of single particle i ; r_i = radius of particle i ; g = gravitational acceleration
 $[M_i]_t$ = resultant moment on particle i at time t

The same procedure is operated in the calculation between the particle and the wall/tool.

Using the axial summation of contact forces from Equation 5.43 to 5.45, we calculated the accelerations of particle i in the horizontal, vertical and rotational directions as,

$$(\ddot{u}_i)_t = \frac{[x_i]_t}{m_i} ; (\ddot{v}_i)_t = \frac{[Y_i]_t}{m_i} ; (\ddot{\phi}_i)_t = \frac{[M_i]_t}{I_i} \quad (5.46)$$

where

\ddot{u}_i = acceleration of particle i in X -direction; \ddot{v}_i = acceleration of particle i in Y -direction; $\ddot{\phi}_i$ = angular acceleration of rotation of particle i

Integrating the accelerations over the time interval Δt and adding the values to the previous velocities, the velocities of particle i in each direction at time t are obtained as,

$$\begin{aligned} [\dot{u}_i]_t &= [\dot{u}_i]_{t-\Delta t} + [\ddot{u}_i]_t \Delta t ; [\dot{v}_i]_t = [\dot{v}_i]_{t-\Delta t} + ([\ddot{v}_i]_t - g) \Delta t ; \\ [\dot{\phi}_i]_t &= [\dot{\phi}_i]_{t-\Delta t} + [\ddot{\phi}_i]_t \Delta t \end{aligned} \quad (5.47)$$

where

$[\dot{u}_i]_t$, $[\dot{u}_i]_{t-\Delta t}$ are horizontal velocities of the particle i at t and $t - \Delta t$;
 $[\ddot{u}_i]_t$ is the horizontal acceleration of particle i at time t ;
 $[\dot{v}_i]_t$, $[\dot{v}_i]_{t-\Delta t}$ are vertical velocities of particle i at time t and $t - \Delta t$;
 $[\ddot{v}_i]_t$ is the vertical acceleration of particle i at time t ;
 g is acceleration due to gravity ; $[\dot{\phi}_i]_t$, $[\dot{\phi}_i]_{t-\Delta t}$ are rotational velocities of particle i at time t and $t - \Delta t$; $[\ddot{\phi}_i]_t$ is rotational acceleration of particle i at time t

The displacements of particle i in each direction at time t are given by integrating the velocities over the time interval Δt .

$$\begin{aligned} [\Delta u_i]_t &= \frac{1}{2}([\Delta u_i]_{t-\Delta t} + [\dot{u}_i]_t \Delta t) ; & [\Delta v_i]_t &= \frac{1}{2}([\Delta v_i]_{t-\Delta t} + [\dot{v}_i]_t \Delta t) ; \\ [\Delta \phi_i]_t &= \frac{1}{2}([\Delta \phi_i]_{t-\Delta t} + [\dot{\phi}_i]_t \Delta t) \end{aligned} \quad (5.48)$$

where

$$\begin{aligned} [\Delta u_i]_t, [\Delta u_i]_{t-\Delta t} & \text{ are horizontal displacements of particle } i \text{ at time } t \text{ and } t - \Delta t ; \\ [\Delta v_i]_t, [\Delta v_i]_{t-\Delta t} & \text{ are vertical displacements of the particle at time } t \text{ and } t - \Delta t ; \\ [\Delta \phi_i]_t, [\Delta \phi_i]_{t-\Delta t} & \text{ are rotational positions of the particle at time } t \text{ and } t - \Delta t \end{aligned}$$

Conducting these calculations for all particles new co-ordinates (positions) of the particles are determined after Δt from the previous time. For the new positions the contact conditions of each particle are investigated and new contact forces are found for contacting particles. Then the new displacement increments are obtained again during the next time interval. By repeating these calculations (Fig. 5.3) for a certain period of time the behaviour of particles is determined through simulation.

5.6 THE KYOTO DEM PROGRAM

Computer simulations of real problems have always been attractive because they provide a means of investigating model systems in order to gain understanding and to conduct “computer” experiments in cases where experimental systems are hard to probe. This is especially the case for granular systems where experiments with non – ideal materials are extremely hard to probe and a general theory is not available (Tijssens et al, 2003).

The *Kyoto DEM* is the DEM software of the shear box test and the soil cutting by a pendulum type machine that was originally written in ‘C’ language by Dr. Momozu of the Kyoto University of Japan. The software is composed for the purpose of studying the dynamic interaction between soil and agricultural machinery, soil deformation behaviour, soil strength, and soil material properties by considering soil as a discrete medium. The software is written in ‘C’ language which is a high level general purpose programming language developed in 1972 at AT&T Bell laboratories (Ritchie and Kernighan, 1978).

5.6.1 THE C PROGRAMMING LANGUAGE

C is a general purpose programming language (Ritchie and Kernighan, 1978). It has been closely associated with the Unix system, because ‘C’ was designed by Dennis Ritchie as a language in which to write the Unix operating system (Hanly et al, 1995). It was originally used primarily for systems programming. Besides it has been used equally well to write major numerical, text processing and data-base programs (Ritchie and Kernighan, 1978).

In ‘C’ the fundamental data objects are characters, integers of several sizes and floating point numbers. In addition, there is a hierarchy of derived data types created with pointers, arrays, structures, unions and functions. C provides the fundamental flow-control constructions required for well-structured program statement grouping; decision making (if); looping with the termination test at the top (while, for), or at the bottom (do); and selecting one of a set of possible cases (switch).

5.6.1.1 Main steps in creating the *Kyoto DEM* program

There are four fundamental steps in the creation of any *C* program, these are: ***Editing, Compiling, Linking, and Executing*** the program.

Editing: editing is the process of creating and editing *C* source codes - the name given to the program instructions we write.

Compiling: the compiler converts all source codes into languages that the computer can understand and detects and report errors in the conversion process. The input to this stage includes the files we produced during editing, which are usually referred to as source files. The compiler can detect a wide range of errors that are due to invalid or unrecognised program codes, as well as structural errors where for example, part of a program can never be executed. The output from the compiler is known as object code and is stored in files called object files which usually have names with the extension '***.obj***'. In Unix, object files have the extension '***.o***'

Linking: the linker combines the various files generated by the compiler, adds required code modules from program libraries supplied as part of *C* and welds everything into an executable whole. The linker can also detect and report errors, for example if part of the program is missing or a non-existent library component is referenced. In practice if the program is of any significant size, it will consist of several separate source code files, which can be linked together. The source files can be compiled separately, which makes eliminating the simple typographical errors a bit easier.

Furthermore, the whole program can usually be developed incrementally, this is how the *Kyoto DEM* software was developed. Each source file will have its own file name, and the set of source files that make up the program will usually be integrated under a project name, which is used to refer to the whole program.

A successful linking step will produce an executable file. In a Microsoft Windows environment, this executable file has '***.exe***' extension ; in Unix there will be no such extension, but the file will be an executable type.

Execution: the execution step is where we run our program, having completed all the previous processes successfully. Unfortunately this stage can also generate a wide variety of error conditions, ranging from producing the wrong output, through to sitting there and doing nothing. In all cases it's back to the editing process to check the source codes. The following diagram (Fig. 5.14) summarises all the above steps.

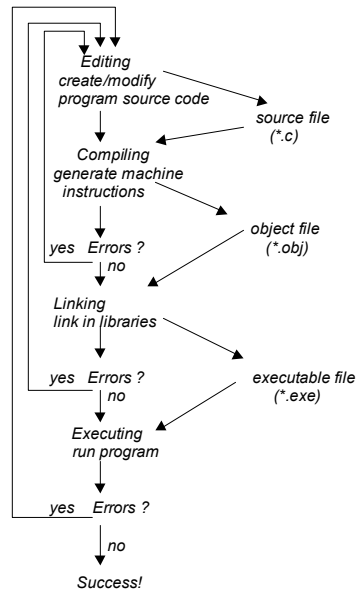


Figure 5.14 Main procedure of the *Kyoto DEM* program (Adapted from: Horton, 1997)

5.6.1.2 User related characteristics of the *Kyoto DEM* program

The *Kyoto DEM* program has two parts as explained above; these are the shear box test and the soil cutting by a pendulum type machines.

I *Shear box test*

The shear box test has three source code files. These are: *Input_Shear.c*, *Shear.c* and *Shear_Plot.c*. All these files are written in 'C' language.

Compiling the shear box test program

Compiler: gcc... with Visual Studio (C++)

CPU: Pentium III 266MHZ, Debian linux, with kernel version

RAM: 256MB

Input_shear.c

This program code prepares an executable '*Input*' file by displaying input parameter lists that help us to enter values of each parameter [normal spring constant between particles (k_n), tangential spring constant between particles (k_s), normal spring constant between particle and wall (k_{nw}), friction coefficient between particles (μ_{pp}), friction coefficient between particle and wall (μ_{pw}), shear velocity (V_{sh}), time step (Δt), precalculation time (t_{pre}), shearing time (t_{sh}), step output (s_{output}), particles mass (m_p), height of the shear box (h_b) and width of the shear box (w_b)].

% Input 'filename'
(% = *command prompt*)

'Input' generates the following five files. All these files are generated automatically when the program operates 'Input'.

filename.are, filename.cal, filename.chr, filename.exp, filename.con

These files contain the total information of all the particles. Let us see the contents of these files one by one.

'filename.are' contains the total number of particles generated at the first stages of consolidation, width and height of the shear box, maximum value of the co-ordinates in the x and y – direction (that helps to set the calculated area, particles that going out of the calculated area are ignored), height of the shear surface from the bottom of the shear box.

'filename.cal' contains the time step, shearing time, loading time and step output.

'filename.chr' contains normal and tangential spring constants of particle – particle and particle – wall contacts, normal and tangential damping coefficients of particle – particle and particle – wall contacts, friction angle of particle – particle and particle – wall contacts and particles mass.

'filename.exp' contains shear velocity and vertical load of the plate.

'filename.con' contains data before the first stages of consolidation. The particles are here consolidated due to their gravity weight; the contents are: total number of particles generated before consolidation, x and y – co-ordinates of all particles, radius of all particles, mass of all particles and moment of inertia of all particles.

For further elaboration see the example below.

For the executable file of 'Input' give a filename of 'cgps' and enter the following values for the parameters [$k_n = 80.7kN/m$, $k_s = 16.1kN/m$, $\mu_{pp} = 0.7$, $\mu_{pw} = 0.5$, $V_{sh} = 1mm/s$, $\Delta t = 0.00001$, $t_l = 3s$, $t_{sh} = 10s$, $m_p = 1700gm$, $h_b = 10cm$, $w_b = 10cm$, $S_{output} = 10000$].

Now see the contents of the above files

% Input 'cgps'

cgps.are = [104, 10cm, 10cm, 30cm, 50cm, 5cm respectively as explained above].

cgps.cal = [0.00001s, 10s, 3s, 10000 respectively]

cgps.chr = [80.7kN/m, 16.1kN/m, 80.7kN/m, 16.1kN/m, 100.8Ns/m, 45.1Ns/m, 100.8Ns/m, 45.1Ns/m, 0.7, 0.5, 1700gm respectively]

cgps.exp = [1mm/s, 10 kg]

```

cgps.con =
    part. no.  x-coord  y-coord  radius  mass  inertia
    0          1.000000  1.000000  0.920094  22.270253  9.426694
    1          3.000000  1.000000  0.697191  12.786892  3.107700
    2          5.000000  1.000000  0.891550  20.909898  8.310228
    .          .          .          .          .          .
    .          .          .          .          .          .
    .          .          .          .          .          .
    103        9.000000  39.105118  0.960064  24.247187  11.174597

```

Shear.c

This source file is the main program code of the shearing process. Shear started after the third stage of consolidation, by an executable file of '*Shear*'. That means after the particles are generated by '*Input*' the first stage of consolidation takes place due to gravity particles for a time of t_{pre} . The particles out of the box are removed and the remaining particles were consolidated again for the second time due to gravity for a time of t_{pre} . This is called the second stage of consolidation; after this stage the loading plate is applied for a time of t_{pre} and the system is consolidated for the third time and then shear is started.

% shear 'filename'

'*shear*' generates the main output of the shearing process: '*filename.dat*', '*filename_*.dat*', and '*filename_*.pos*'. It is generated as soon as shear started and ends when the simulation is over. The contents of these files: '*filename.dat*' contains time step, shear displacement, shear stress, vertical reaction stress and height of loading plate from the start of shear to the end of shear. This file is written as 'ASCII' file whose values are set apart by tabs. Furthermore it is a very huge file since it contains data for every time step for a duration of total shearing time. For instance, for the above example of shearing time and time step '*cgps.dat*' contains 10^6 data which need 53MB memory for a single simulation. Which is of course a very huge file to run in a normal PC. This is one of the drawbacks of DEM; it needs longer CPU time and large storage memory; '*filename_*.dat*' contains current calculated time, height of loading plate and shear distance; '*filename_*.pos*' contains remaining number of particles, *x* and *y* co-ordinates (position of particles) and radius of particles at the same time as '*filename_*.dat*' is generated.

% Shear 'cgps'

```
cgps_0001.dat = [0.1s, 11.030928, 0.01]
```

cgps_0001.pos =

```

    part. no  x-coord  y-coord  radius
    0          0.923498  0.893129  0.920094
    1          2.981003  0.688843  0.697191
    2          4.961491  0.865141  0.891550
    .          .          .          .
    .          .          .          .
    .          .          .          .
    42         8.266625  9.255822  0.641657

```

```

cgps.dat =
  time step    shear disp    shear stress    v. reaction stress    height of plate
  0.000000    0.000000    3946.061537    9749.300697    11.043348
  0.000010    0.000001    3378.496454    9748.717009    11.043348
  0.000020    0.000002    3378.496454    9747.749352    11.043348
  .           .           .           .           .
  .           .           .           .           .
  10.000000    0.010000    13300.00000    9807.588795    11.500000

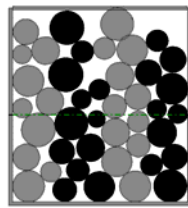
```

Shear_Plot.c

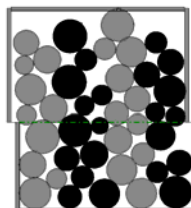
This program code prepares **'Plot'** for drawing snapshots at each output interval time. **'Plot'** generates the snapshots in the form of 'GIF' files as **'filename.gif'**. This output shows particle behaviour after shearing at that instance of time.

For the above example see the following snapshots at different time

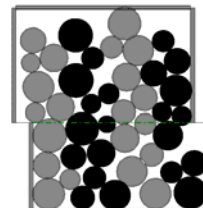
% Plot 'cgps1', 'cgps2', 'cgps3' generates snapshots of **cgps1.gif, cgps2.gif and cgps3.gif** for the simulation time of $t = 0, 5$ and 10 s respectively.



$t = 0$ s
cgps1.gif



$t = 5$ s
cgps2.gif



$t = 10$ s
cgps3.gif

II Soil cutting by pendulum type machine

Soil cutting by a pendulum type machine consists of nine source code files which are written in 'C' language

pendmain.c – main source file

contact.c – judgement of contacts between particles

force.c – calculation of contact force

tool_touch.c – contact judgement between particle and tool

pendulum.c – motion of pendulum

Inputgen.c – preparation of input parameter files

precalc.c – reading parameter files

snap_pos.c – plot of snapshots of particle motion

snap_vel.c – plot of snapshots of particle velocity vectors

Compiling the cutting simulator

Compiler: gcc... with Visual Studio (C++)

CPU: Pentium III 266MHZ, Debian linux, with kernel version

RAM: 256MB

Two executable programs are made out of the above source codes. One for the preparation of simulation which has the filename of '*INP*' and the other for the simulation process which has the filename of '*SIM*'.

'*INP*' is used to display parameter lists which help us to enter parameter values. Then it automatically generates three files with extension '*.chr*', '*.cal*' and '*.con*'.

% *INP* 'filename'

First display lists of parameters then we can enter the value of each parameter

[normal spring constant between particles (k_n), tangential spring constant between particles (k_s), normal spring constant between particle and wall (k_{nw}), adhesion spring constant (k_{ad}), coefficient of adhesion area (C_{ad}), coefficient of rolling friction (C_r), number of particles on the bottom layer (N_b), friction coefficient between particles (μ_{pp}), friction coefficient between particle and wall (μ_{pw}), time step (Δt), precalculation time (t_{pre}), simulation time (t_s) and step output (s_{output}),].

'*INP*' generates the following three files. All these files are generated automatically when the program operates '*INP*'.

filename.chr, *filename.cal*, *filename.con*

The contents of these files are:

'*filename.chr*' contains normal and tangential spring constants of particle – particle and particle – wall contacts, adhesion spring constant, coefficient of adhesion area, coefficient of rolling friction, normal and tangential damping coefficients of particle – particle and particle – wall contacts, friction coefficient of particle – particle and particle – wall contacts and number of particles.

'filename.cal' contains simulation time, precalculation time, time step, and step output
 'filename.con' contains particles number, initial position, radius, mass, and moment of inertia of all particles.

% SIM 'filename'

Now '**SIM**' generates three files at each time step where output interval is setting.

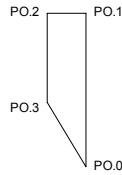
the particles position file, the tool position file, the tool force file

The particle position file is named '**filename.x**', where 'x' is a numeral that shows how many files '**SIM**' has to be made, which means '**filename.x**' has data at time of $(dt * s_{output} * x)$

seconds after pendulum started motion. The contents of this files are: particle number, particles x and y co-ordinate and particles x and y displacement, which are written as 'ASCII' files whose values are separated by tabs and show some information of each particle in a row of the file.

The tool position file is named '**filename_tool.x**', where 'x' is a numeral explained above for the particle position file. The contents of this file show coordinates of four points of the tool cross section as shown in the Figure below.

Where $PO.0, PO.1, PO.2, PO.3$ are different co-ordination points of the tool at calculation step. $PO.0 = (x_0, y_0), PO.1 = (x_1, y_1), PO.2 = (x_2, y_2), PO.3 = (x_3, y_3)$



The tool force file is named '**filename.dat**'. Its contents are: the total time steps, angular position of the tool, angular velocity of the tool, normal and tangential force of the tool and the work done by the tool. This file is an 'ASCII' file. Values are set apart by tabs.

The following example is shown for a brief understanding of the cutting simulator.

% INP 'cgppc' where '**cgppc**' is a file name.

Now we can enter values for the input parameters as follows,

$[k_n = 10kN / m, k_s = 2kN / m, k_{nw} = 10kN / m, k_{ad} = 2kN / m, \mu_{pp} = 0.7,$
 $C_{ad} = 0.05, C_r = 0.1, N_b = 20, \mu_{pw} = 0.5, \Delta t = 0.0001, t_{pre} = 2s, t_s = 1s,$
 $S_{output} = 100].$

The following three files are automatically generated by '**INP**'

cgppc.chr = [10000 , 2000 , 2000 , 0.05 , 0.1 , 12.92 , 5.78 , 12.92 , 5.78 , 0.7 , 0.5 , 345]
cgppc.cal = [1 , 2 , 0.0001 , 100]

cgppc.con =

| <i>part.no.</i> | <i>x-coord</i> | <i>y-coord</i> | <i>radius</i> | <i>mass</i> | <i>m.of inertia</i> |
|-----------------|----------------|----------------|---------------|-------------|---------------------|
| 0 | 6.125000 | 1.125000 | 1.125000 | 8.349764 | 5.283835 |
| 1 | 8.375000 | 1.125000 | 1.125000 | 8.349764 | 5.283835 |
| 2 | 10.625000 | 1.125000 | 1.125000 | 8.349764 | 5.283835 |
| . | . | . | . | . | . |
| . | . | . | . | . | . |
| . | . | . | . | . | . |
| 344 | 24.125000 | 40.096143 | 1.125000 | 8.349764 | 5.283835 |

% SIM 'cgppc'

Now **'SIM'** generates three files as stated above.

See content of particle position files. For example if we are interested to calculate **'cgppc.30'**, this file contains information of all particles after ($dt * s_{output} * 30$) seconds = ($0.0001 * 100 * 30$) seconds = 0.3 s after the pendulum started cutting.

cgppc.30 =

| <i>part.no</i> | <i>x-coord</i> | <i>y-coord</i> | <i>x-displ</i> | <i>y-disp</i> |
|----------------|----------------|----------------|----------------|---------------|
| 0 | 6.1249 | 1.1118 | 0.000518 | -0.000527 |
| 1 | 8.3754 | 1.1086 | -0.000264 | -0.000007 |
| 2 | 10.6264 | 1.1082 | 0.000211 | -0.000008 |
| . | . | . | . | . |
| . | . | . | . | . |
| . | . | . | . | . |
| 344 | 24.1250 | 40.0961 | 8.349764 | 5.283835 |

The contents of the tool position file **'cgppc_tool.30'** are

cgppc_tool.30 = [(12.492872, 42.257268), (12.691685, 48.253973),
(11.692234, 48.287109), (11.564481, 44.433733)]

In other words the tool is at this position at 0.3 s after the pendulum started motion.

The contents of the tool force file **'cgppc.dat'** are

cgppc.dat =

| <i>time step</i> | <i>ang. pos</i> | <i>angu. vel</i> | <i>n.force</i> | <i>t.force</i> | <i>torque</i> |
|------------------|-----------------|------------------|----------------|----------------|---------------|
| 0.00000 | 104.9999 | -0.0681 | 0.0000 | 0.0000 | 0.0000 |
| 0.00001 | 104.9999 | -0.1361 | 0.0000 | 0.0000 | 0.0000 |
| 0.00002 | 104.9998 | -0.2042 | 0.0000 | 0.0000 | 0.0000 |
| . | . | . | . | . | . |
| . | . | . | . | . | . |
| . | . | . | . | . | . |
| 1.00000 | -54.7959 | -105.4977 | -2.1618 | -0.1668 | -0.0278 |

Below it is explained how to develop the 'GIF' files by using '*Snap_pos.c*' or '*Snap_vel.c*'. After the simulation is over that means when '*SIM*' finished the cutting process, we obtain the simulated results in ASCII files. '*Snap_pos*' and '*Snap_vel*' read the ASCII data files and generate 'GIF' files.

% Snap_pos cgppc.30 ... generates the position of the particles after 0.3 s
% Snap_vel cgppc.30 ... generates the velocity vectors after 0.3 s

6 SIMULATION OF SHEAR BOX TEST AND SOIL CUTTING BY PENDULUM TYPE MACHINE USING *KYOTO DEM*

6.1 SIMULATION OF SHEAR BOX TEST

Introduction

The shear box test is a standard laboratory test which is often held for measuring the shear strength of the soil. This strength is explained with cohesion and interparticle friction angle. Numerous data are available from laboratory experiments of shear box tests and calculating the shear strength of soil based on continuum mechanics. See among these, Kezdi (1974 and 1980); Craig (1992) and Roberts (1996). Moreover results of these experiments are highly investigated. However data on the expertise of soil behaviour or soil reaction against loading or shearing based on discrete mechanics is very limited because of the difficulty of analysing motion of the individual particles and the numerous time and memory usage even for the fastest PC.

By nature soil is a granular material and has been considered as assemblies of discrete particles. Behaviour of such soil will be studied here using the discrete medium rather than continuous. Attention is focused on investigating deformation, shear strength and volume change properties of the simulation. Information regarding the micromechanics of the assembly, the shear strength, the volume change distribution at loading with different normal stresses and the effect of parameter variation is presented.

The process of shearing in between granular particles can be visualised with the help of plots indicating the curve trajectory for 1cm shear displacement, the volume change, snapshots that show the micro – structure of the assembly and the position distribution of the particles. The power and benefits of the distinct element method can be valued from the results of the simulation.

Shape and dimension of the shear box used for the simulation was a cube which has a cross section as shown in the Fig. 6.1

This chapter is intended to examine the feasibility of numerical simulation of granular particles by using the shear box test and the pendulum simulator.

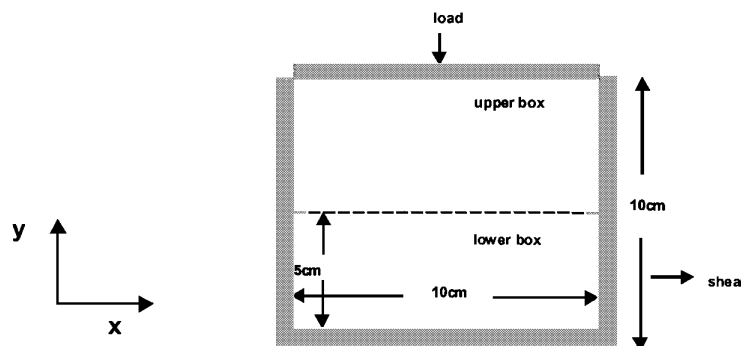


Figure 6.1 Cross section of the shear box

6.1.1 SELECTION OF PARAMETERS FOR THE SIMULATION

The mechanical behaviour of DEM particles depends on material constants dealing with contact properties such as normal and tangential stiffness, normal and tangential dashpot and interparticle friction coefficient values.

The selection of these constants is of great importance, in particular when the simulation is compared with the results of real tests, see Iwashita and Oda (1998). However until now we did not develop the right method to select the DEM parameters for a simulation without trial and error. Furthermore, model improvements made parameter selection a difficult task since the number of input parameters is increased simultaneously.

6.1.1.1 The normal stiffness value between particles

Efforts have been done to estimate the parameter value of one of the above basic material constants (normal stiffness value) based on Hertz's contact theory (Johnson, 1985). Next, tangential stiffness constant related with normal stiffness could also be estimated as has been shown by many researchers (for example Momozu et al (2000) and Umekage et al (1998)). Since the force – displacement laws and equations of particle motion explained in Chapter 5 section 5.2.1.1 and 5.5.1, are derived from the general contact theory, the normal stiffness of an elastic spring at the contact point between particles i and j can be estimated from the relation

$$\delta^3 = \frac{9}{16} F_n^2 \left(\frac{1-\nu_i^2}{E_i} - \frac{1-\nu_j^2}{E_j} \right)^2 \left(\frac{r_i r_j}{r_i + r_j} \right) \quad (6.1)$$

where

E_i , E_j and ν_i , ν_j are the modulus of elasticity and Poisson's ratio of particles i and j ; r_i and r_j are radius of particles i and j ; δ is the overlap displacement between the particles; F_n is the normal contact force between the particles

By assuming that all particles are made from the same material, modulus of elasticity of particles and Poisson's ratio of particles are the same, $E_i = E_j = E$ and $\nu_i = \nu_j = \nu$.

Thus the normal stiffness of particles is estimated as

$$k_n = \left(\frac{E}{1-\nu^2} \right) \left(\frac{r_i r_j}{r_i + r_j} \right)^{3/2} \delta^{1/2} \quad (6.2)$$

The normal stiffness estimated by the above method was best fit for analysing shearing behaviour of cohesionless granular soil, for example, sand. For cohesive soil the estimation was poor because of its low Young's modulus. The normal stiffness will become very low so that the load cannot be resisted anymore and the simulation will collapse.

6.1.1.2 The damping coefficient value between particles

The damping coefficient η of the dashpot is given by the critical damping condition of the vibration equation for computational stability,

$$\eta_n = 2\sqrt{m_{temp}k_n} \quad (6.3)$$

$$\eta_s = 2\sqrt{m_{temp}k_s} \quad (6.4)$$

where

η_n and η_s are the normal and the tangential damping coefficients of the particles, for m_{temp} see the following appendix A.

Appendix A (Momozu et al, 2001)

$$N_{layer} = (H_{box} - R_{max}) / (R_{max} * sqrt(3.0)) + 1;$$

$$i = N_{layer} \% 2;$$

if($i == 1$)

$$N_{temp} = (2N_{bed} - 1) * (N_{layer} - 1) / 2 + N_{bed};$$

else

$$N_{temp} = (2 * N_{bed} - 1) * N_{layer} / 2;$$

$$m_{temp} = m / N_{temp};$$

where

N_{layer} is number of layers ; H_{box} is height of the shear box (see Fig. 6.1) ;

R_{max} is maximum radius of the particles ; N_{bed} is number of particles at the bottom layer of the box and m is the mass of the particles in the box.

Table 6.1 Material properties of medium granular particles

| Parameters | Symbol | Value | Unit |
|--|------------|---------|------|
| Normal spring constant | k_n | 35.5 | kN/m |
| Normal dashpot | η_n | 33.9 | Ns/m |
| Tangential spring constant | k_s | 7.1 | kN/m |
| Tangential dashpot | η_s | 15.16 | Ns/m |
| Particle – particle friction coefficient | μ_{pp} | 0.577 | - |
| Particle – wall friction coefficient | μ_{pw} | 0.5 | - |
| Shear velocity | v_{sh} | 0.001 | m/s |
| Time step | Δt | 0.00001 | s |
| Precalculation time | t_{pre} | 3 | s |
| Shearing time | t_{sh} | 10 | s |
| Number of particles at bottom | N_{bed} | 10 | - |
| Vertical load | v_1 | 5 | kg |

6.1.2 GENERATION AND CONSOLIDATION OF THE INITIAL SAMPLE

The DEM simulation of the shear box test consists of three phases. The first phase is the automatic generation of the particles. The second phase is the consolidation of the generated particles and the third phase is the actual simulation of shearing.

In the first phase the program reads the particle information and its distribution data and generates randomised assembly of particles. The centres of particle are regularly arranged in a calculated area. In this case the height of the calculated area was 5 times as high as the height of the box and the width of the calculated area was 3 times the width of the shear box. In this phase particles are assumed to have a constant radius called r_c . The centre points are arranged equivalently to be most dense in the calculated area.

During the second phase the radius of each particle was decided by the following equation

$$r_i = 0.5r_{con} + 0.5r_{con}R \quad (6.5)$$

where

r_i is the radius of particle i ; r_{con} is a constant radius when particles are regularly arranged in a calculated area; R is a random number between 0 and 1 ($0 < R \leq 1$).

If we set $R = 1$ all the particles have the same radius.

After decision of particle radius, the friction coefficients μ_{pp} and μ_{pw} were applied to all particle – particle and particle – wall contacts respectively and then the assembly was equilibrated for a duration of t_{pre} due to gravity.

The particles beyond the box height were removed after the first consolidation and the remaining particles were consolidated again for the second time with the same duration t_{pre} by gravity; in this way the box was almost filled with particles.

After the second consolidation the assembly was compacted by the loading plate for a duration of t_{pre} and again consolidated for the third time. In this way the particles reached a denser state of arrangement. Figure 6.2 shows a snapshot of particle distribution at the beginning of shear.

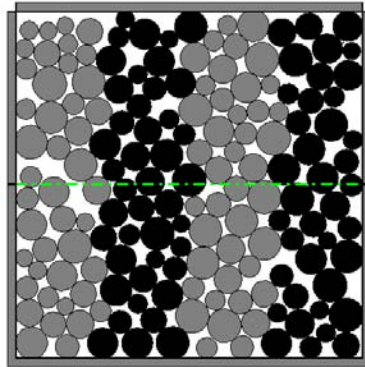


Figure 6.2 Snapshot of the initial arrangement of the particles inside the box.

6.1.3 THE SHEARING PROCESS

The shearing process started during the third phase and was completed after a constant shear velocity (V_{sh}) had been assigned to the lower box to impose shear conditions on the particles; in this case the upper box was fixed. Shear force and height of the loading plate were recorded during the process. Contact forces between particles and the right side wall of the upper box were summed up. The resultant force was assumed to be the shear force and this shear stress was solved by using equation:

$$\tau_t = \frac{F_{sh}}{[(W_{box} - D_{sh})d_{box}]} \quad (6.6)$$

where

τ_t = shear stress at time t ; F_{sh} = the shear force; W_{box} = width of shear box
 D_{sh} = shear distance; d_{box} = depth of the box

Shear stress was increasing linearly in almost all cases and failure rarely occurs. This is because particles moved so slowly that the dampers in the model could not work effectively. The volume change was computed from the differences of the height of the loading plate. Shearing has been performed by varying values of input parameters and the effect of these parameters has also been investigated. The normal stress selected for parameter investigation was $\sigma_n = 4.9kPa$ unless otherwise mentioned separately.

6.1.3.1 Effect of parameter variation on the shearing process

In this section the effect of some parameters (those parameters which are expected to affect the mechanical properties of the particles) was investigated in relation to the stress ratio-displacement and the volume change-displacement curves. The parameters in Table 6.1 are considered to be the default parameters of the simulation.

Effect of interparticle friction coefficient (μ_{pp})

When the interparticle friction coefficient increases then the shear stress of the particles was also increased, as is expected (see left in Fig. 6.3). Which means a larger friction angle between particles raises the shear stress. This is consistent with the property in which sliding dominates the plastic deformation of granular soil. However this larger friction angle is limited to a certain maximum, which was 35° at least in this case. Applying beyond this value means rotation of particles dominates the system and the shear stress becomes lower. In general the average volume change also increases as interparticle friction increases.

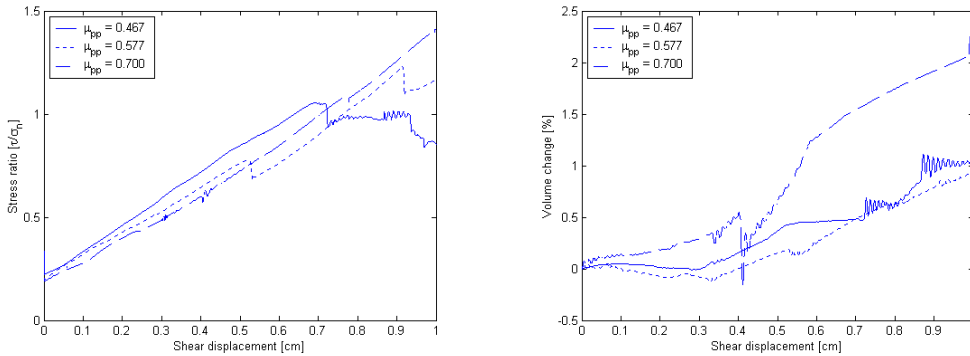


Figure 6.3 Effect of interparticle friction coefficient on the shearing of DEM particles

Effect of the normal spring constant (k_n)

The effect of the normal spring constant was investigated by simulating the shear stress behaviour and the volume change with $k_n = 17.75$ kN/m and $k_n = 71$ kN/m. All the other parameters are taken as a default parameter of Table 6.1 except the normal spring constant between the wall and the particles. For simplicity, we assume the normal spring constant between the particles and between the particle and the wall the same.

Equation (5.26) shows that the critical time step depends on the normal spring constant. The time step used in the simulation is less than the critical time step calculated by this equation.

The gradient of the $\frac{\tau}{\sigma_n}$ curve (left in Fig. 6.4) becomes steeper when the contact stiffness (k_n) increases. That means a model with a small contact stiffness needs larger shear displacement to reach the same peak stress. Therefore it is possible to consider that shear strength of DEM particles is independent of contact stiffness (Iwashita and Kojima, 1992).

However the contact stiffness influences the deformation mechanism since particles with small contact stiffness can move in the horizontal direction easier than those with large stiffness. The volume change also increases (negative to positive) as the particles have larger stiffness. These results are shown in Fig. 6.4, right

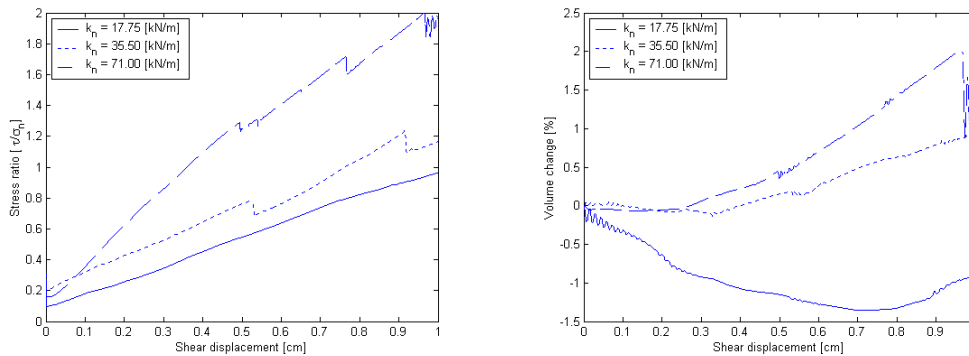


Figure 6.4 Effect of contact stiffness constant on shearing of DEM particles

Effect of tangential spring constant (k_s)

The effect of increasing tangential spring constant k_s from 7.1 kN/m (Table 6.1) to values of $k_s = 14.2$ kN/m and $k_s = 21.3$ kN/m was investigated by simulating the shear stresses and volume change behaviour. At least in this case increasing k_s has no significant effect on the shear stress ratio of the DEM particles (left in Fig. 6.5). More or less both tangential spring values mentioned above have almost the same peak stresses as the original one. However the volume change increases with increasing k_s (right in Fig. 6.5).

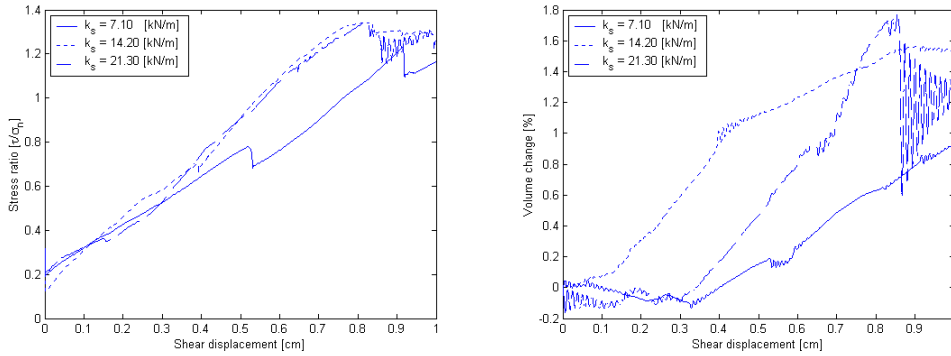


Figure 6.5 Effect of tangential spring constant on shearing of DEM particles

Effect of particle sizes (r)

The effect of the size of particles was investigated by performing additional simulations with distribution of coarse particles of radius $5 \leq r \leq 10$ mm and fine particles distribution of radius $1 \leq r \leq 2$ mm. The radius distribution of particles for the default case of the medium was $2 \leq r \leq 5$ mm. The shear stress of DEM particles slightly increases with increasing size of the particles (left in Fig. 6.6). Also interparticle contacts are dominated by large particle pairs which leave large pore spaces between them (see section 6.1.4.4). In case of smaller size particles, interparticle contacts are distributed among relatively large and small particle pairs. However large pore spaces are still occasionally present, but the system was more tightly packed. The volume change increases from coarse to fine during shearing (right in Fig. 6.6).

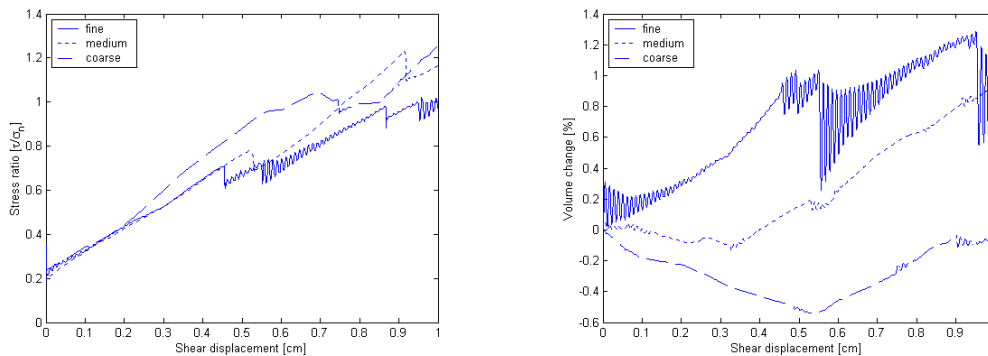


Figure 6.6 Effect of particle size distribution on shearing of DEM particles

6.1.4 OUTPUT AND DISCUSSION OF THE SHEAR BOX SIMULATION

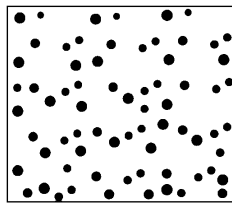
The following properties of DEM particles are investigated from the output of the shear box simulation: comparison check of input interparticle friction coefficient with output interparticle friction coefficient, shear strength, volume change, deformation behaviour (micro-mechanics of deformation) and failure property.

For simplicity we divided the simulation output into three parts, depending on the size distribution of the particles. Each part has its own material properties.

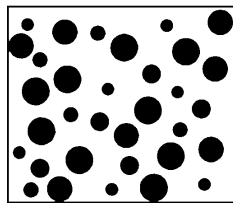
Part I.....Coarse granular particles with radius distribution of (5 – 10 mm)

Part II..... Medium granular particles with radius distribution of (2 – 5 mm)

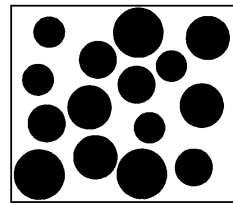
Part III.....Fine granular particles with radius distribution of (1 – 2 mm)



Fine: 1 to 2 mm



Medium: 2 to 5 mm



Coarse: 5 to 10 mm

6.1.4.1 Simulated maximum shear strength of DEM particles

Investigation of simulated shear strength of DEM particles was done by running a number of simulations with different normal stresses ($\sigma_1 = 9.8kPa$, $\sigma_2 = 14.7kPa$, $\sigma_3 = 19.6kPa$, $\sigma_4 = 24.5kPa$, $\sigma_5 = 29.4kPa$) and considering the corresponding maximum shear stresses within 1cm of shear displacement.

The simulated maximum shear strength is calculated from the linear regression of the maximum shear stress and the corresponding normal stress and has two parts: the cohesion and the simulated interparticle friction coefficient (the output interparticle friction coefficient). Since we are considering cohesionless particles here our attention is only focused on investigating the simulated interparticle friction coefficient.

Figure 6.7 a to 6.12 a show the shear stress increment behaviour during shearing of DEM particles. Because of the difficulties in manipulating 250 MB of memory for five simulations at once only three simulations for normal stresses of $\sigma_1 = 9.8kPa$, $\sigma_2 = 14.7kPa$ and $\sigma_3 = 19.6kPa$ are shown. The linear regression shown in Figure 6.7 b to 6.12 b are based on all the five normal stresses.

Part I Coarse granular particles (5 – 10 mm)

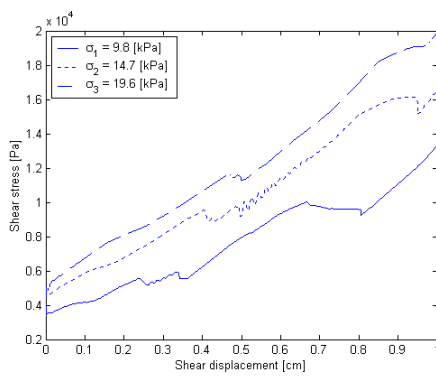
Simulation has been done for two selected input values of interparticle friction coefficients. These are 0.7 and 1.0. Such values are selected based on properties of coarse granular soil.

The material properties of coarse granular particles in Table 6.2 were used as an input value of the simulation.

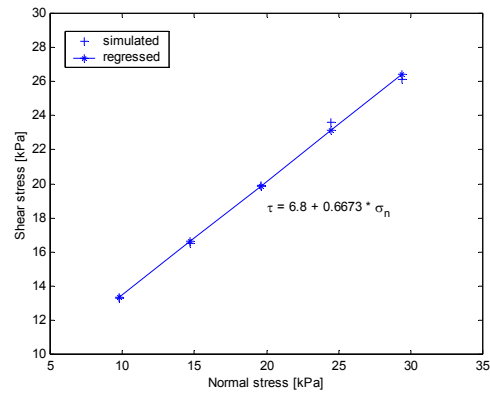
Table 6.2 Material properties of coarse granular particles

| Parameters | Symbol | Value | Unit |
|--|------------|---------|------|
| Normal spring constant | k_n | 80.7 | kN/m |
| Normal dashpot | η_n | 100.8 | Ns/m |
| Tangential spring constant | k_s | 16.1 | kN/m |
| Tangential dashpot | η_s | 45.1 | Ns/m |
| Particle – particle friction coefficient | μ_{pp} | 0.7 | - |
| Particle – wall friction coefficient | μ_{pw} | 0.5 | - |
| Shear velocity | v_{sh} | 0.001 | m/s |
| Time step | Δt | 0.00001 | s |
| Precalculation time | t_{pre} | 3 | s |
| Shearing time | t_{sh} | 10 | s |
| Number of particles at bottom | N_{bed} | 5 | - |
| Vertical load | v_l | 10 | kg |

Figures 6.7 and 6.8 show the shear stress increment curves and the linear regression for the calculation of the Mohr – Coulomb strength envelope.

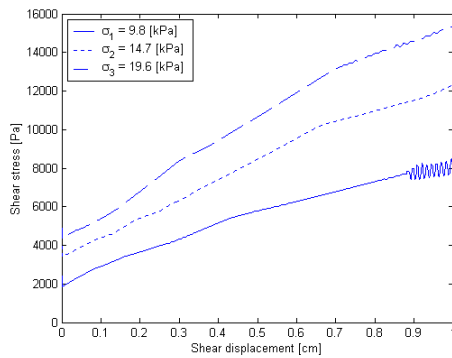


a) Shear stress increment

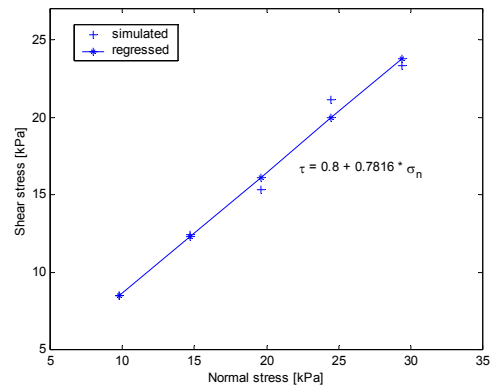


b) Regression equation

Figure 6.7 Shear stress increment (a) and regression equation (b) for $\mu_{pp} = 0.7$



a) Shear stress increment



b) Regression equation

Figure 6.8 Shear stress increment (a) and regression equation (b) for $\mu_{pp} = 1.0$

Part II Medium granular particles (2 – 5 mm)

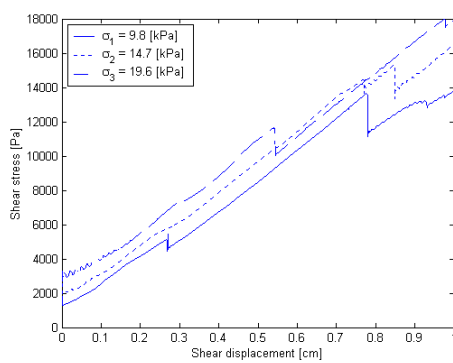
Simulation has been done for two selected input values of interparticle friction coefficients. These are 0.57 and 0.7. Such values are selected based on properties of medium granular soil.

The material properties of medium granular particles in Table 6.3 were used as an input value of the simulation.

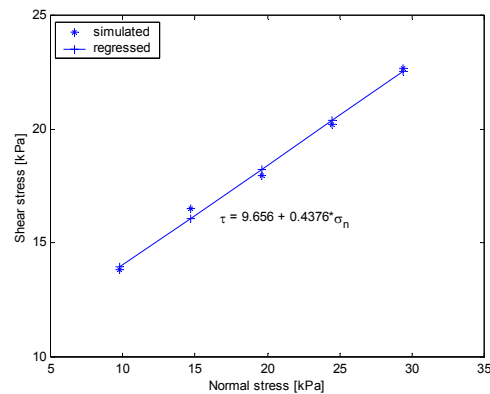
Table 6.3 Material properties of medium granular particles

| Parameters | Symbol | Value | Unit |
|--|------------|---------|------|
| Normal spring constant | k_n | 80.7 | kN/m |
| Normal dashpot | η_n | 49.6 | Ns/m |
| Tangential spring constant | k_s | 16.1 | kN/m |
| Tangential dashpot | η_s | 22.2 | Ns/m |
| Particle – particle friction coefficient | μ_{pp} | 0.57 | - |
| Particle – wall friction coefficient | μ_{pw} | 0.5 | - |
| Shear velocity | v_{sh} | 0.001 | m/s |
| Time step | Δt | 0.00001 | s |
| Precalculation time | t_{pre} | 3 | s |
| Shearing time | t_{sh} | 10 | s |
| Number of particles at bottom | N_{bed} | 10 | - |
| Vertical load | v_l | 10 | kg |

Figures 6.9 and 6.10 show the shear stress increment behaviour and the linear regression for the calculation of the Mohr – Coulomb strength envelope.



a) Shear stress increment



b) Regression equation

Figure 6.9 Shear stress increment (a) and regression equation (b) for $\mu_{pp} = 0.57$

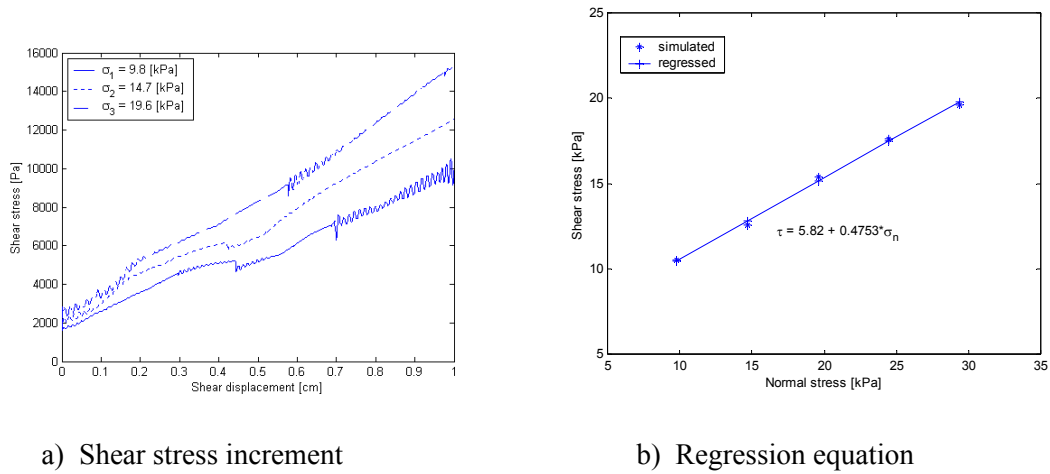


Figure 6.10 Shear stress increment (a) and regression equation (b) for $\mu_{pp} = 0.7$

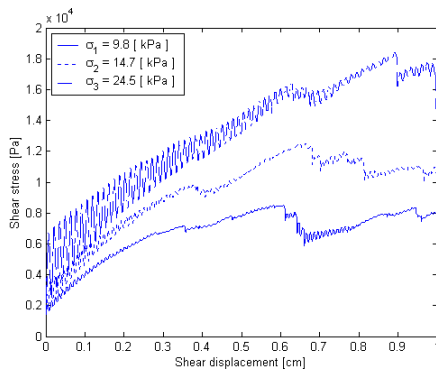
Part III Fine granular particles (1 – 2 mm)

Simulation has been done for two selected input values of interparticle friction coefficients. These are 0.466 and 0.57. Such values are selected based on properties of fine granular soil. The material properties of fine granular particles in Table 6.4 were used as an input value of the simulation.

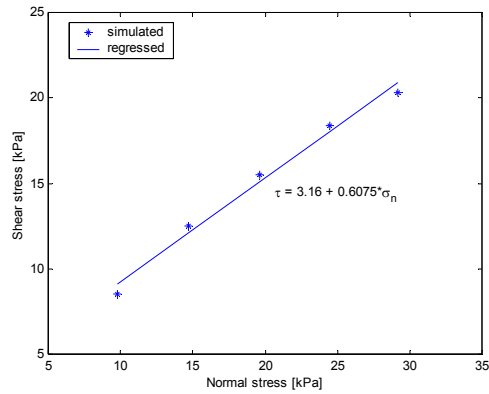
Table 6.4 Material properties of fine granular particles

| Parameters | Symbol | Value | Unit |
|--|------------|---------|------|
| Normal spring constant | k_n | 80.7 | kN/m |
| Normal dashpot | η_n | 19.5 | Ns/m |
| Tangential spring constant | k_s | 16.1 | kN/m |
| Tangential dashpot | η_s | 8.7 | Ns/m |
| Particle – particle friction coefficient | μ_{pp} | 0.466 | - |
| Particle – wall friction coefficient | μ_{pw} | 0.5 | - |
| Shear velocity | v_{sh} | 0.001 | m/s |
| Time step | Δt | 0.00001 | s |
| Precalculation time | t_{pre} | 3 | s |
| Shearing time | t_{sh} | 10 | s |
| Number of particles at bottom | N_{bed} | 25 | - |
| Vertical load | v_l | 10 | kg |

Figures 6.11 and 6.12 show the shear stress increment behaviour and the linear regression for the calculation of the Mohr – Coulomb strength envelope.

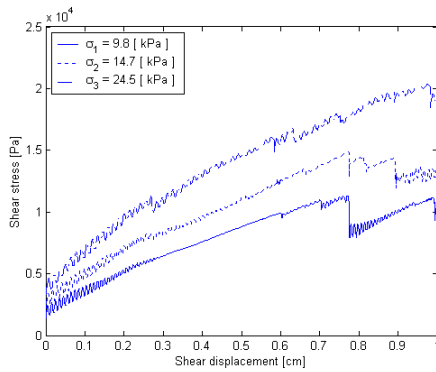


a) Shear stress increment

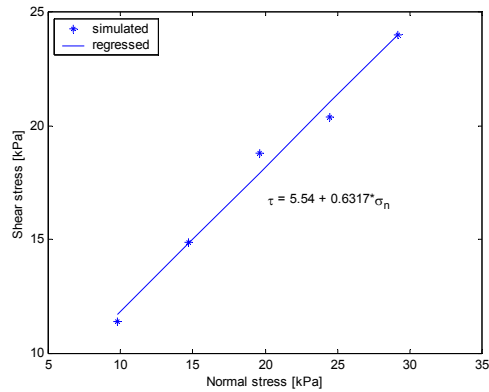


b) Regression equation

Figure 6.11 Shear stress increment (a) and regression equation (b) for $\mu_{pp} = 0.466$



a) Shear stress increment



b) Regression equation

Figure 6.12 Shear stress increment (a) and regression equation (b) for $\mu_{pp} = 0.57$

6.1.4.2 Discussion of simulated shear strength

According to the simulation output presented in the above section (6.1.4.1) simulated shear strength (the simulated interparticle friction coefficient) was generally lower than the input interparticle friction coefficient (μ_{pp}). See output summary in Table 6.5

Table 6.5 Output summary from shear box simulation

| Figure / (b) | Particle size distribution | Input μ_{pp} | Regression equation $\tau = c + \sigma \tan\phi$ |
|----------------|----------------------------|------------------|--|
| 6.7 | coarse | 0.7 | $\tau = 6.8 + 0.6673 \sigma$ |
| 6.8 | | 1.0 | $\tau = 0.8 + 0.7816 \sigma$ |
| 6.9 | medium | 0.57 | $\tau = 9.7 + 0.4376 \sigma$ |
| 6.10 | | 0.70 | $\tau = 5.8 + 0.4753 \sigma$ |
| 6.11 | fine | 0.466 | $\tau = 3.2 + 0.6075 \sigma$ |
| 6.12 | | 0.577 | $\tau = 5.5 + 0.6317 \sigma$ |

This was especially true for coarse and medium granular particles. For example, Fig. 6.8 b of coarse particles has a simulated value of 0.78 which is lower than the input interparticle friction coefficient of $\mu_{pp} = 1.0$. Fig. 6.7 b also shows a decrease from 0.7 to 0.667. The same is true for medium granular particles, (Fig. 6.10 b, lowered from 0.7 to 0.475 and Fig. 6.9 b, lower from 0.577 to 0.438).

There may be three possible reasons for the low simulated shear strength (simulated interparticle friction coefficient) values of DEM particles. The first reason is the ease with which the DEM particles (which are disc shaped) can roll easily. This means there was significant rotation of particles in the shear zone. The second reason may be the use of a completely discontinuous particle distribution and the third reason could be the degree of particle size distribution.

According to the first reason we now start to focus on the rotation of particles in the shear zone as illustrated in Fig. 6.24. The magnitude of such rotation increased with high μ_{pp} values. Scott (1996) confirmed if μ_{pp} is sufficiently high, then sliding will not occur and changes in contact configuration will occur only by particle rolling or separation.

Due to such a rotation of particles for high μ_{pp} values the shear strength decreased with increasing μ_{pp} whereas for the low μ_{pp} , the shear strength increased with increasing μ_{pp} . This is because sliding will be activated more readily for the low μ_{pp} surface than for the high μ_{pp} surface. Morgan (1999) showed that the percentage of sliding contacts will always be greater for the low μ_{pp} system. From the linear regression equations given in Table 6.5 it can be seen that a minor increase in the simulated interparticle friction coefficient $\tan \phi$ occurred when the input value of μ_{pp} was increased.

For example, in the case of coarse granular particles the simulated interparticle friction coefficient increased from 0.667 to 0.782 for the increase of μ_{pp} value from 0.7 to 1.0.

And from 0.438 to 0.475 for the increase of μ_{pp} value from 0.57 to 0.7 in the case of medium granular particles. In both cases the increase is minor which is expected and in agreement with Morgan (1999). Morgan states that if particle rotation was allowed the simulated shear strength increased rapidly over low values of interparticle friction coefficient ($\mu_{pp} < 0.2$) but levelled out over relatively higher μ_{pp} values. In other words for input values of interparticle friction coefficient which are greater than 0.3 ($\mu_{pp} > 0.3$), only minor increases (≤ 0.1 in magnitude in most cases) in simulated interparticle friction coefficient occurred due to increased frictional resistance at the few sliding contacts. In the present case the increase is 0.115 for coarse granular and 0.037 for medium granular particles, which agrees with the above statement.

The second possible factor contributing to the low simulated interparticle friction coefficient is the use of a completely discontinuous particle distribution. In real soil behaviour finer particles are generated during progressive particle fracture and will tend to fill the pore space. This increases the contact area and consequently the frictional resistance to shear deformation (Morrow and Byerlee, 1989).

In case of fine granular particles, Table 6.5, bottom, the simulated interparticle friction coefficient $\tan \phi$ is higher than the input μ_{pp} which is in contrast with that of coarse and medium granular particles. This is due to the very many fine particles generated in the system i.e., 2818 particles, packed densely. As a result “rolling” has decreased and “contact sliding” dominates the system. Due to this phenomena the shear strength significantly increases, see Fig. 6.11 b, from 0.466 to 0.608, and Fig. 6.12 b, from 0.577 to 0.632.

In general the above findings made clear, that simulated shear strength of DEM particles is highly dependent on the interparticle friction coefficient (μ_{pp}) and the particle size distribution.

6.1.4.3 Discussion of volume change of DEM particles

During shearing, the DEM particles tend to slide over one another. That leads to a volume increase (dilatancy) or tends to be tightly packed that leads to a volume decrease (compaction). This causes a change of the initial particles structure. The volume change of the DEM particles during shearing is measured by the ratio of incremental height (Δh) to initial height of the specimen (h). For simplicity we divided the simulation results into three parts, depending on the size distribution of the particles and each part has its own input particle material properties as was given in Table 6.2, 6.3 and 6.4 for coarse, medium and fine granular particles, respectively .

Part I.....Coarse granular particles with radius distribution of (5 – 10 mm)

Part II..... Medium granular particles with radius distribution of (2 – 5 mm)

Part III.....Fine granular particles with radius distribution of (1 – 2 mm)

Part I Coarse granular particles (5 – 10 mm)

Simulation was done for two selected input values of interparticle friction coefficient. These are 0.7 and 1.0; such values are selected based on properties of coarse granular soil.

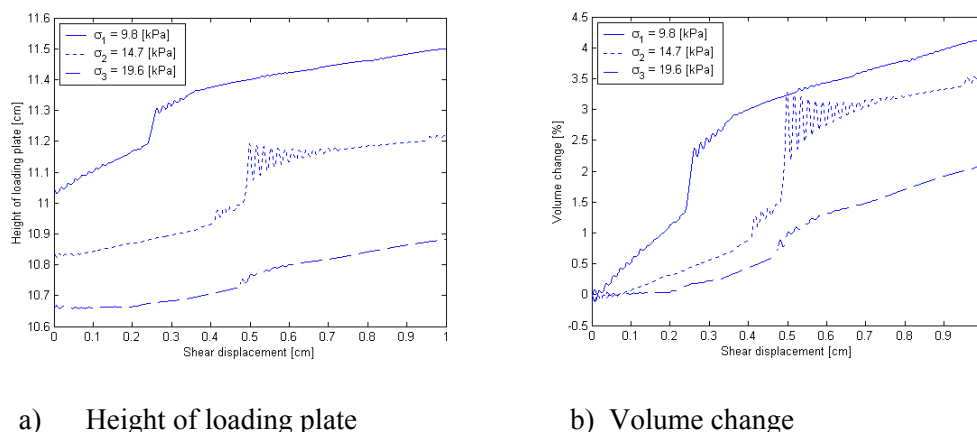
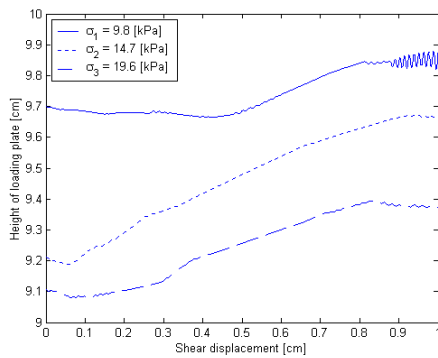
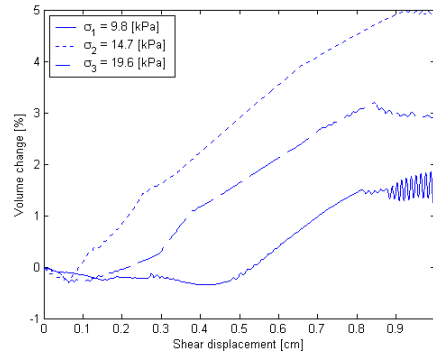


Figure 6.13 Height of loading plate (a) and volume change (b) for $\mu_{pp} = 0.7$



a) Height of loading plate

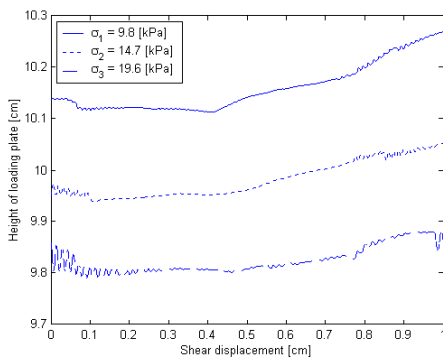


b) Volume change

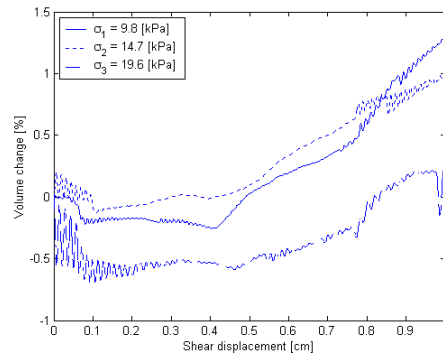
Figure 6.14 Height of loading plate (a) and volume change (b) for $\mu_{pp} = 1.0$

Part II Medium granular particles (2 – 5 mm)

Simulation was done for two selected input values of interparticle friction coefficient. These are 0.57 and 0.7; such values are selected based on properties of medium granular soil.

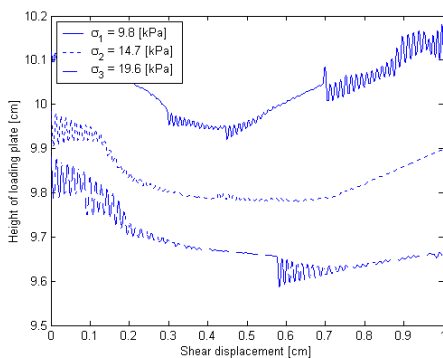


a) Height of loading plate

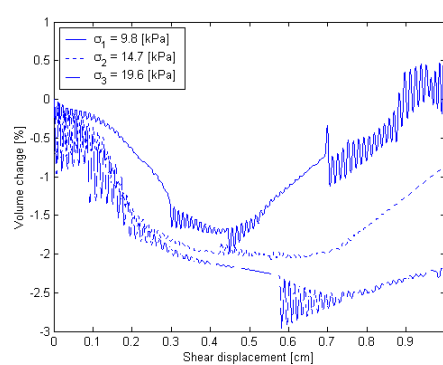


b) Volume change

Figure 6.15 Height of loading plate (a) and volume change (b) for $\mu_{pp} = 0.57$



a) Height of loading plate



b) Volume change

Figure 6.16 Height of loading plate (a) and volume change (b) for $\mu_{pp} = 0.7$

Part III Fine granular particles (1 – 2 mm)

Simulation was done for two selected input values of interparticle friction coefficients. These are 0.466 and 0.57; such values are selected based on properties of fine granular soil.

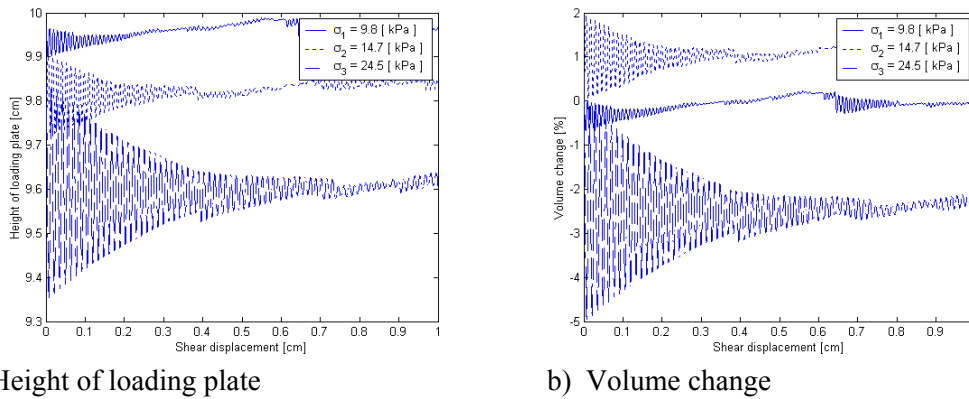


Figure 6.17 Height of loading plate (a) and volume change (b) for $\mu_{pp} = 0.466$

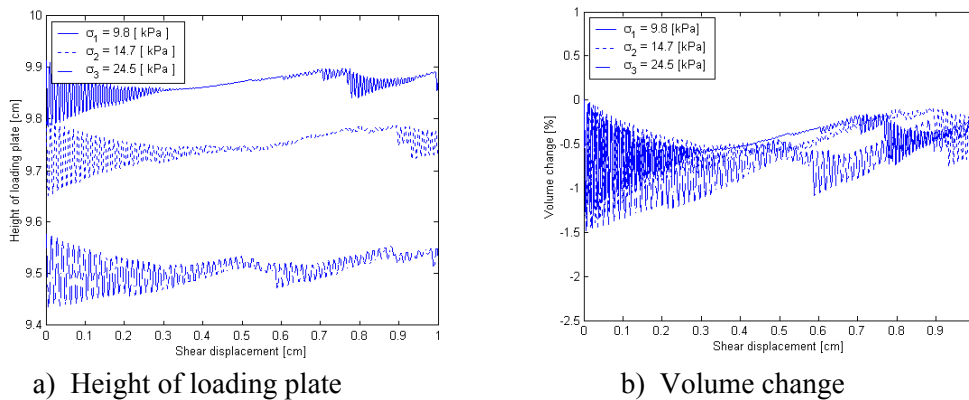


Figure 6.18 Height of loading plate (a) and volume change (b) for $\mu_{pp} = 0.57$

From the present output of the shear box simulation the degree of volume increase or decrease depends on the input interparticle friction coefficient (μ_{pp}) and the particle size distribution. Most of the results obtained from the present simulation show volume increase for coarse and medium granular particles and volume decrease for fine granular particles (see Fig. 6.13 b and 6.14 b for coarse granular particles, Fig. 6.15 b for medium granular particles and Fig. 6.18 b for fine granular particles).

As we see from Fig. 6.13 b to 6.18 b, in general the degree of volume change was decreased when the particle size was decreased. This may be due to the generation of many smaller particles in the medium and finer granular cases. These particles fill the voids between larger particles leading towards a tighter packing. One thing is clear: when the particle size decreases the number of particles increases.

In case of coarse granular particles, (Fig. 6.13 b and 6.14 b) for high μ_{pp} , volume increases with increasing μ_{pp} for instance when μ_{pp} increases from 0.7 to 1.0, with $\sigma_n = 19.6$ kPa, the volume increase from 2% to 3%. This minor increase is expected.

For almost all simulations of fine granular particles the volume change over about the first 30% of shearing fluctuates with large amplitude. Moreover the magnitude of this amplitude increases with increased level of the normal stress (σ_n).

The concept of dilatancy during shearing of DEM particles

Depending on the closeness of the particles in the box the sample is in a loose or a dense initial state. During shearing the density will change; a loose sample will compact while a dense one will dilate. This phenomenon of volume change induced by shear deformation is called dilatancy. In the context of classical plasticity theory plastic strains are derived from a plastic potential (detailed in Chapter 2). A plastic potential similar to the Mohr – Coulomb failure criterion is shown in Fig. 6.19, depicting the Mohr diagram for the strains (compressive strains are counted positive).

The arrow perpendicular to the plastic potential gives the direction of the plastic strains. A positive value for the angle of dilation ψ means that the plastic strains lead to an increase of volume and hence the particles become looser. So a dense particle packing will have a positive angle of dilation and a loose particle will have a negative angle of dilation.

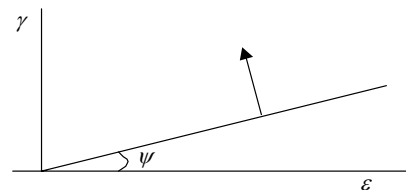


Figure 6.19 Mohr – Coulomb criterion depicting the plastic potential

6.1.4.4 Discussion of micro-mechanics of deformation DEM particles

At the beginning of the shearing process all DEM particles were moved into the direction of the applied shear velocity.

Particle stresses will vary with the distribution of contacts, forces and microstructures.

In case of coarse granular particles the system contains relatively many large particles and interparticle contacts are dominated by large particle pairs leaving large pore spaces between them. This is clearly seen on the snapshots of coarse granular particles, Fig. 6.20 and 6.21 for various σ_n levels.

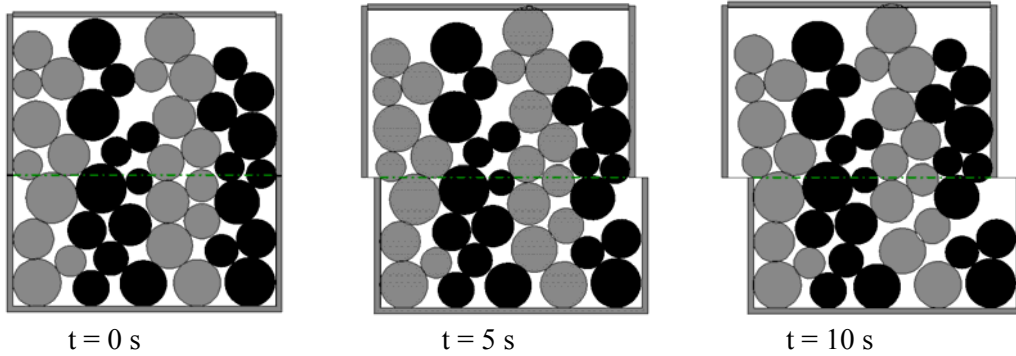


Figure 6.20 Snapshots of coarse particle behaviour, $\mu_{pp} = 0.7$, $\sigma_n = 9.8$ kPa

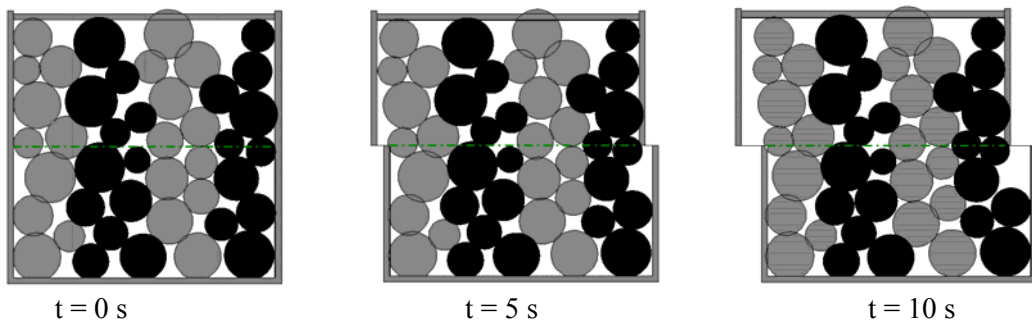


Figure 6.21 Snapshots of coarse particle behaviour, $\mu_{pp} = 0.7$, $\sigma_n = 49$ kPa

Whereas for medium granular particles, the system contains a higher number of particles and proportionally more relatively small particles. Besides interparticle contacts are distributed among large and small particle pairs. Also large pore spaces are still occasionally present but the system is apparently more tightly packed (see snapshots of medium granular particles, Fig. 6.22 and 6.23). Deformation proceeded with local slip points. These slip points increase in number with decreasing particle size. Furthermore, as smaller particles filled the pore spaces the variation in volume change was reduced (compare volume change of coarse granular particles, Fig. 6.14 b with volume change of medium granular particles, Fig. 6.15 b).

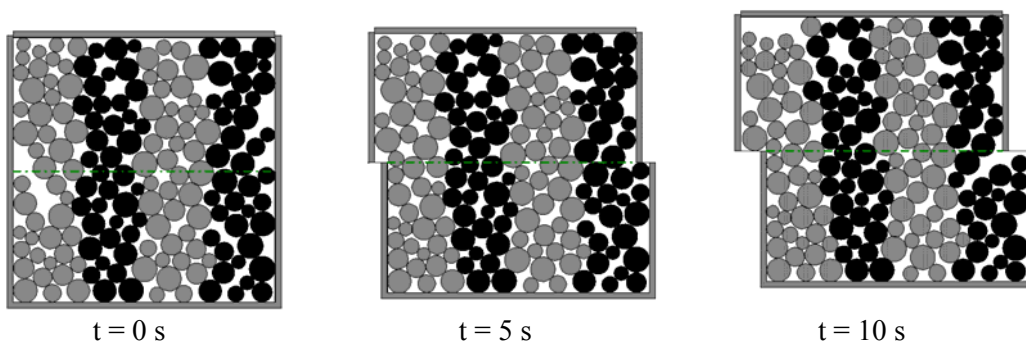


Figure 6.22 Snapshots of medium particle behaviour, $\mu_{pp} = 0.7$, $\sigma_n = 9.8$ kPa

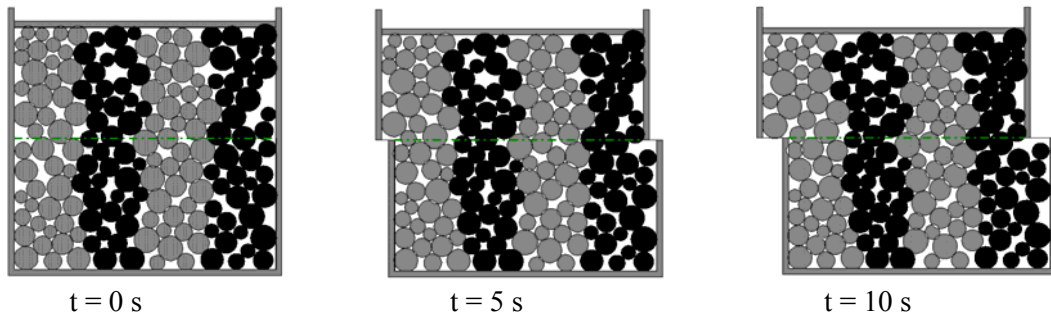


Figure 6.23 Snapshots of medium particle behaviour, $\mu_{pp} = 0.7$, $\sigma_n = 49$ kPa

For fine granular particles, the increased number of small particles dominates the system, pore space is not evident and the particles are quite densely packed. This implies the shear force is distributed over more contacts such that individual contacts carries a smaller contact force than that of coarse or medium granular particles.

In case of fine granular particles, at the beginning of shearing the amplitude of volume oscillation was larger especially for relatively higher normal stresses (see the volume change curves of fine granular particles, Fig. 6.17 and 6.18).

Generally particle deformation and configuration were accommodated through interparticle **sliding** and **rolling**. For instance if the shear force at the contact point is less than the critical force necessary to activate interparticle sliding, the moments acting on the particles may cause one or two particles to roll until the contact is favourably oriented and interparticle sliding is allowed. However sliding will be activated more readily for the low μ_{pp} with the same contact force which means that the percentage of sliding particles is higher for a low μ_{pp} than for a relatively higher one.

If μ_{pp} is high enough, rotation of particles (Fig. 6.24) dominates the deformation behaviour and change of contact configuration will occur due to this rolling. This is in line with Morgan (1999) and Scott (1996).

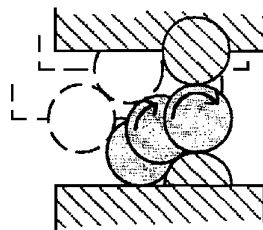


Figure 6.24 Illustration of particle rotation in the shear zone (Adapted from: Morgan, 1999)

6.1.4.5 Discussion of failure points of DEM particles

Failure appears to be highly influenced by interparticle sliding and rolling. This sliding and rolling behaviour is highly influenced by the input values of interparticle friction coefficient (μ_{pp}), particle size distribution and initial arrangement of particles.

Hence the percentage of sliding contacts will always be greater for the low μ_{pp} value (compare Fig. 6.25 a and Fig. 6.25 b ; arrows indicate sliding contacts). Normally sliding contacts increase for μ_{pp} values ranging between 0.1 and 0.4 for all particle size distributions (coarse, medium and fine). Moreover in fine granular particles failure also occurs for $\mu_{pp} = 0.466$ and 0.577 values. In this case, particles are more tightly packed and peak stress is equal to failure stress (see shear stress increment curves of fine granular particles, Fig. 6.26 b).

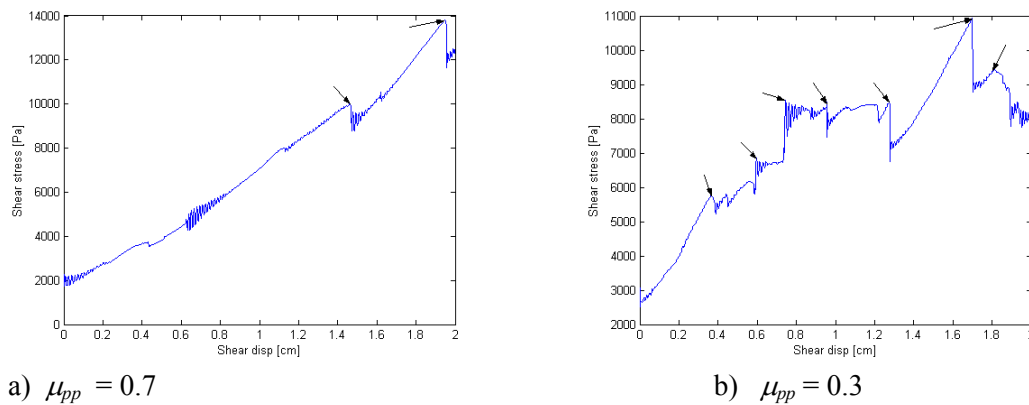


Figure 6.25 a, b. Stress trajectories that show sliding contacts for medium granular particles

At the failure point, trajectories of stress – displacement curves are characterised by a sudden drop in stress, accompanied by localised slip (see the failure curve, Fig. 6.26). However this behaviour varies depending on the input μ_{pp} and the particle size distribution. The failure force increases with increasing particle size.

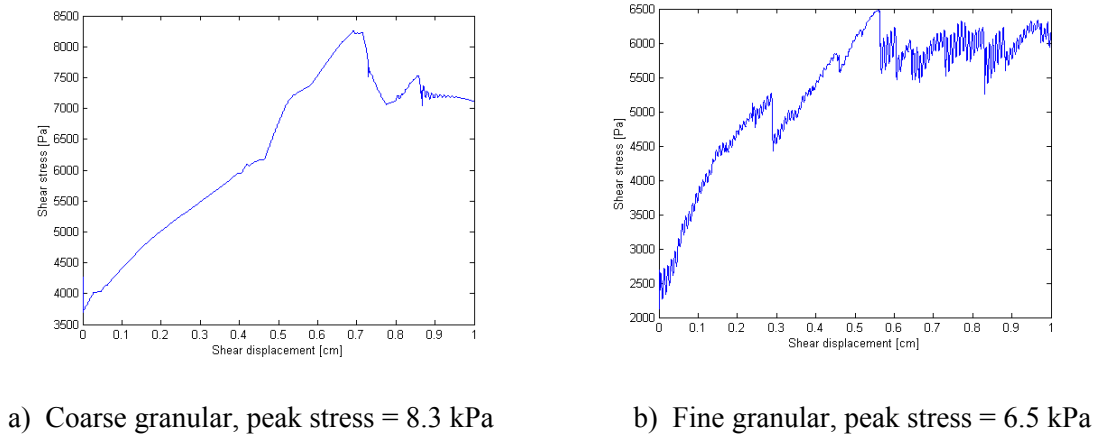


Figure 6.26 Stress trajectories that show failure behaviour for the coarse (a) and fine (b) granular particles $\sigma_n = 9.8$ kPa , $\mu_{pp} = 0.2$

6.2 SIMULATION OF SOIL CUTTING BY A PENDULUM TYPE MACHINE

With the advancement of modern computer performance, analysis of numerical simulation of soil cutting by a pendulum type machine has been one of the phenomena used to study the dynamic interaction between soil and agricultural machinery (Momozu et al, 2000). The numerical method according to DEM has the potential that the analysed object is assumed to be an assembly of distinct particles and its properties have been explained in detail in Chapter 5. DEM particle properties used in the simulation are listed in Table 6.6.

Table 6.6 Material properties of DEM particles

| Parameters | Symbol | Value | Unit |
|--|------------|--------|------|
| Normal spring constant | k_n | 10 | kN/m |
| Normal dashpot | η_n | 12.9 | Ns/m |
| Tangential spring constant | k_s | 2.0 | kN/m |
| Tangential dashpot | η_s | 5.8 | Ns/m |
| Particle – particle friction coefficient | μ_{pp} | 0.7 | - |
| Particle – wall friction coefficient | μ_{pw} | 0.5 | - |
| Adhesion spring | k_{ad} | 2.0 | kN/m |
| Coefficient of adhesion area | C_{ad} | 0.01 | - |
| Coefficient of rolling friction | C_r | 0.1 | - |
| Time step | Δt | 0.0001 | s |
| Precalculation time | t_{pre} | 2 | s |
| Simulation time | t_s | 1 | s |
| Number of particles at bottom | N_{bed} | 20 | - |
| Particle radius | r | 12.5 | mm |

6.2.1 GENERATION OF THE INITIAL SAMPLE

After the values of the input parameters (Table 6.6) were entered by using one of the executable program files ‘INP’, as was explained in the user related characteristics of *Kyoto DEM*, the particles were generated with their x, y - co-ordinates and the box filled as shown in Fig. 6.27.

In this case all the particles have the same radius in order to keep the system stable with the required shape of the box. Each particle was assigned by a number, in order to show the initial position arrangement of the particle.

The box has the shape of the soil block which was designed based on the laboratory experiment of soil block cutting by a pendulum type machine. All the geometric dimensions of either the soil block or the pendulum machine were equal to those of the laboratory experiment. For details, see Fissaha (1998).

After the particles were generated and filled into the box in the shape of a soil block, the system was consolidated by gravity for t_{pre} s.

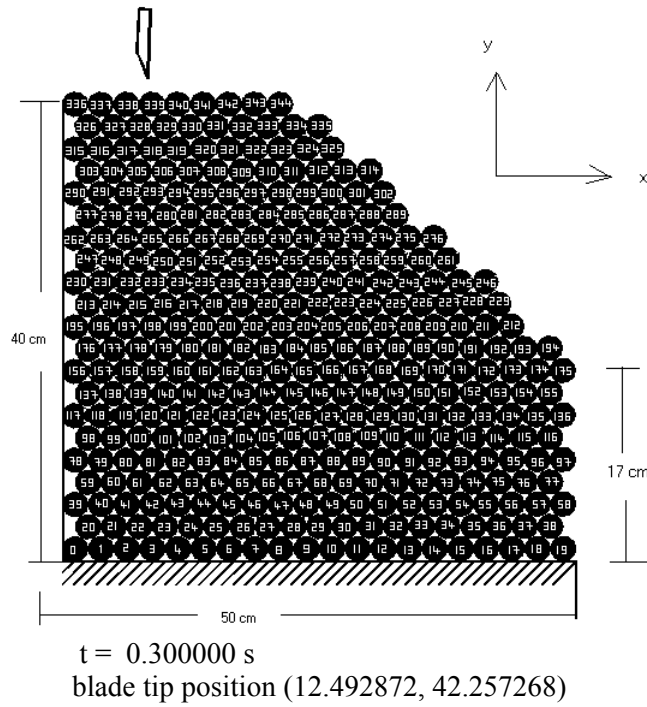


Figure 6.27 Initial arrangement of DEM particles in the form of a soil block

6.2.2 THE CUTTING PROCESS

The pendulum position was set at $+105^\circ$ as a starting position, the soil block was set such that the height of the soil allowed the blade to strike the soil block at $+72^\circ$ after a rotation of 33° . The bite length of the blade was 12.5 cm and its tip angle was 25° . The motion of the pendulum was controlled by the following equation when ‘SIM’ was operated:

$$I_0 \alpha_t = RF_t - Lmg \cos \theta_t + e \Delta \theta \quad (6.7)$$

where

I_0 = moment of inertia of the pendulum; α_t = angular acceleration of the pendulum;
 R = rotation radius of the blade ; F_t = resistance force against blade motion ;
 L = length from rotation axis to centre of gravity of the pendulum ; m = mass of the pendulum including the blade ; g = acceleration due to gravity ; θ_t = rotation angle of pendulum ; e = energy lost per unit degree of rotation by the pendulum.

The conventional *Kyoto DEM* was modified in order to analyse the behaviour of natural cohesive soil during cutting. In order to fulfil such task the cohesion properties of the DEM particles were investigated from the output of the cutting simulation.

The simulation was done for three different input values of the ‘adhesion coefficient’ (C_{ad}). These are (0.01, 0.05 and 0.10); for simplicity all the values of other parameters were kept constant as the default value of Table 6.6.

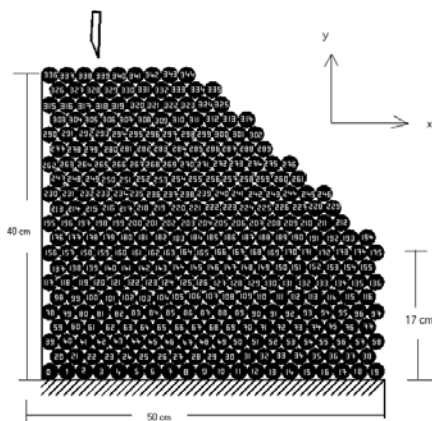
To investigate the adhesion property of the DEM particles, varying the coefficient of adhesion area is very important. According to the *Kyoto DEM*, increasing this value will also increase the adhesion force of the particles in the normal direction during separation as calculated in Eqn (5.29).

6.2.3 OUTPUT AND DISCUSSION OF THE CUTTING PROCESS

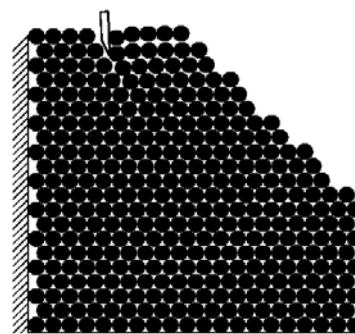
The output of the simulation was given in the form of snapshots, which show particle motions in the cutting processes, the x and y displacements of these particles, and the work done by the tool during the simulation.

Figure 6.28 to 6.30 show snapshots of the cutting process with three different C_{ad} values which were simulated within a duration of 0.1 s. The snapshots were taken with intervals of 0.02 s since the tool touched the soil block.

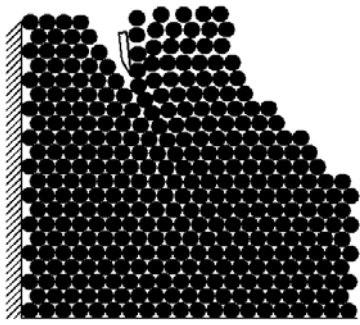
According to the present simulations, the motion of particles depends on the magnitude of the coefficient of adhesion area (C_{ad}). For a relatively small magnitude of coefficient of adhesion area, particle motions were dominated by scattering behaviour (Figure 6.28) and also particle displacement was relatively large. However this effect was decreasing when the coefficient of adhesion area was increasing (see from Fig. 6.28 to 6.30). For relatively large values of coefficient of adhesion area there was a resistance against the motion of these particles (Fig. 6.30) while particles moved together in a stucked manner and later formed soil clods.



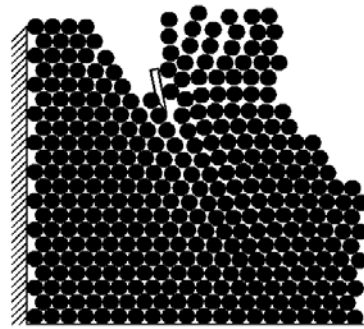
a) $t = 0.3$ s



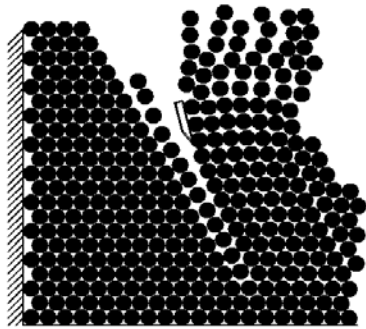
b) $t = 0.32$ s



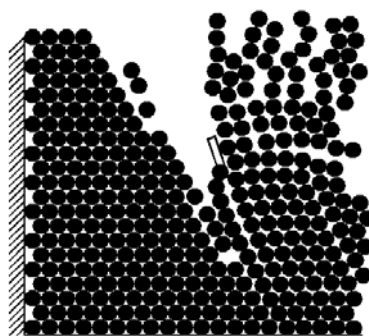
c) $t = 0.34$ s



d) $t = 0.36$ s

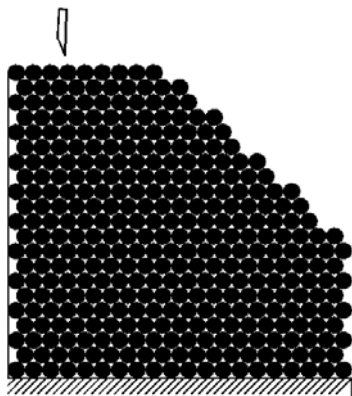


e) $t = 0.38$ s

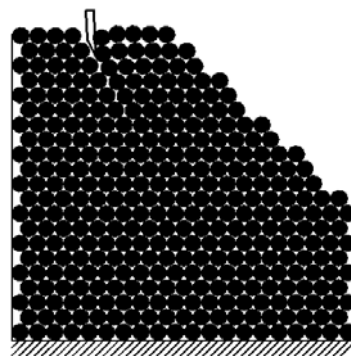


f) $t = 0.4$ s

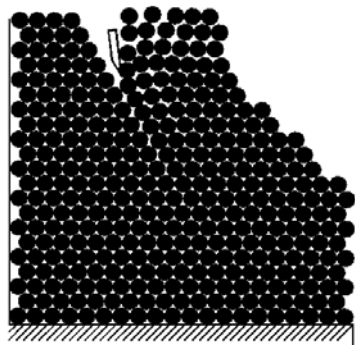
Figure 6.28 a,b,c,d,e,f. Snapshots of particles position distribution at different points of time during simulation, $C_{ad} = 0.01$



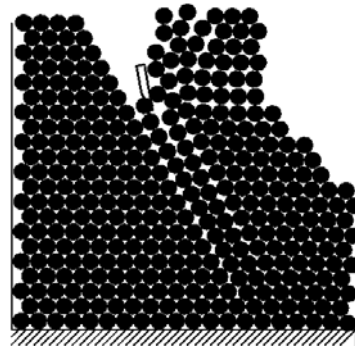
a) $t = 0.3$ s



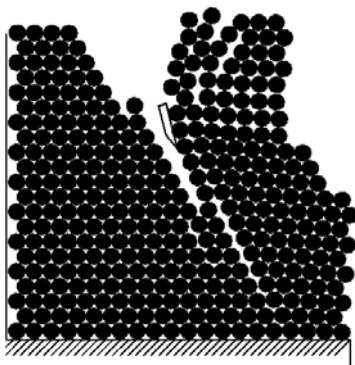
b) $t = 0.32$ s



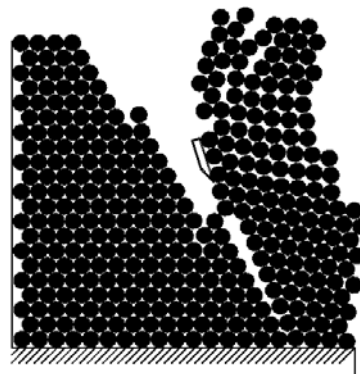
c) $t = 0.34$ s



d) $t = 0.36$ s

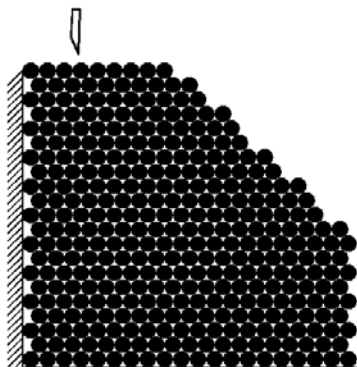


e) $t = 0.38$ s

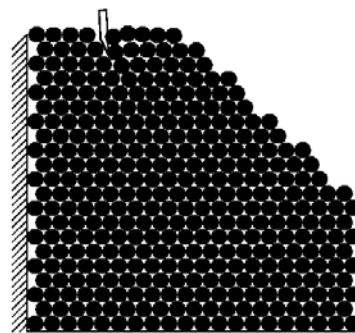


f) $t = 0.4$ s

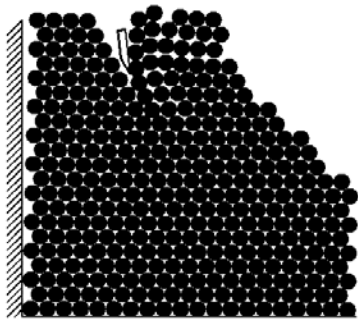
Figure 6.29 a,b,c,d,e,f. Snapshots of particles position distribution at different points of time during simulation, $C_{ad} = 0.05$



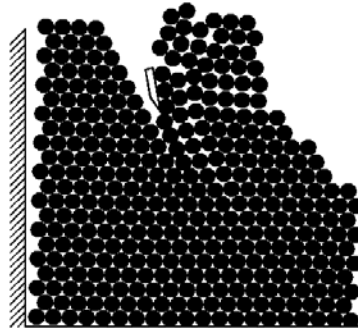
a) $t = 0.3$ s



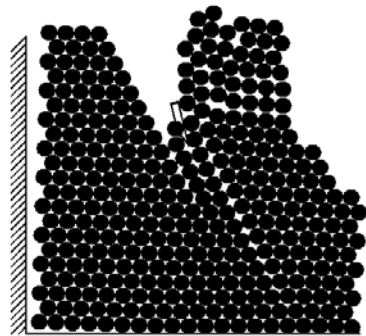
b) $t = 0.32$ s



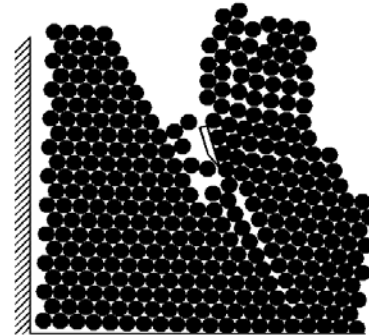
c) $t = 0.34$ s



d) $t = 0.36$ s



e) $t = 0.38$ s



f) $t = 0.4$ s

Figure 6.30 a,b,c,d,e,f. Snapshots of particles position distribution at different points of time during simulation, $C_{ad} = 0.100$

For all simulations of the cutting process, the particles motion was dominated by its displacements into x -direction.

The magnitude of displacement was higher on areas where the blade and the soil block have interactions; that concerns the particles at the top of the soil block, as assigned by higher numbers i.e., 250 – 350, see Fig. 6.31 for $C_{ad} = 0.01$.

This displacement decreased in magnitude for particles which were placed far from the cutting area (bottom end) and had no access to contact with the cutting tool. Particles were also displaced in the y -direction however this displacement was relatively small due to the direction of tool motion.

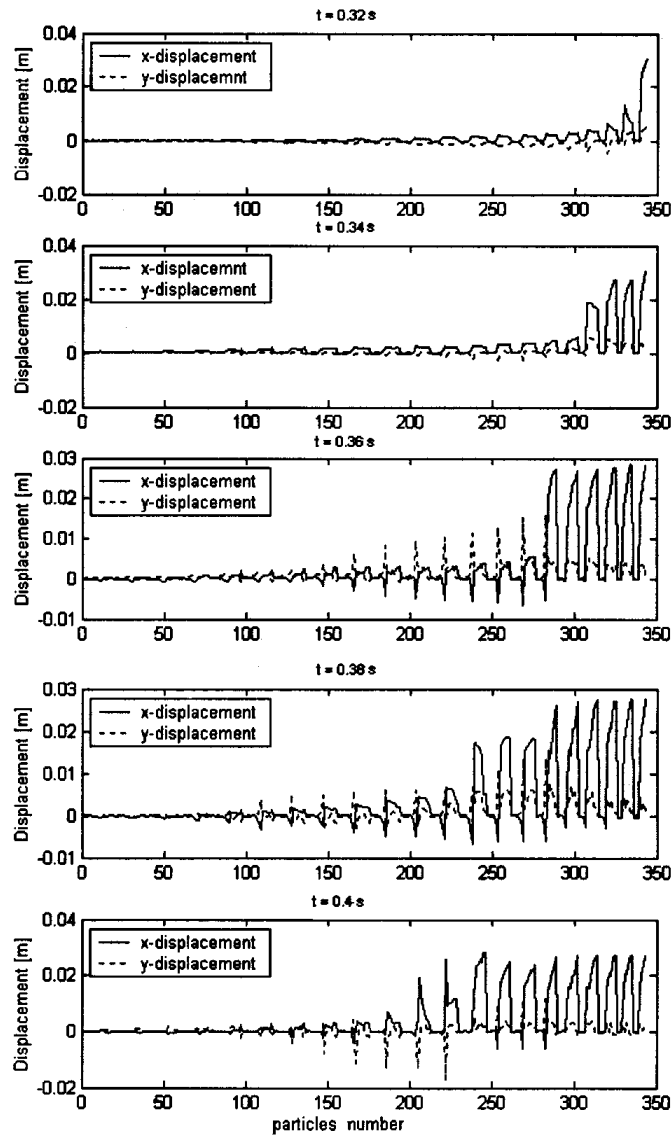


Figure 6.31 Particles displacement at different instants of time during cutting simulation for $C_{ad} = 0.01$, assigned particle number refers to its position in the soil block, see Fig. 6.27

The energy consumption by the cutting tool was also analysed during the simulation. The magnitude was very fluctuating ; one possible reason for this was the variation in material properties of the particles (Oida et al, 1995). But the magnitude of fluctuation is increased for increased values of the coefficient of adhesion area (Fig. 6.32). This means the energy consumption of the cutting tool is increased when the motion of the particles is restricted by an increasing coefficient of adhesion area.

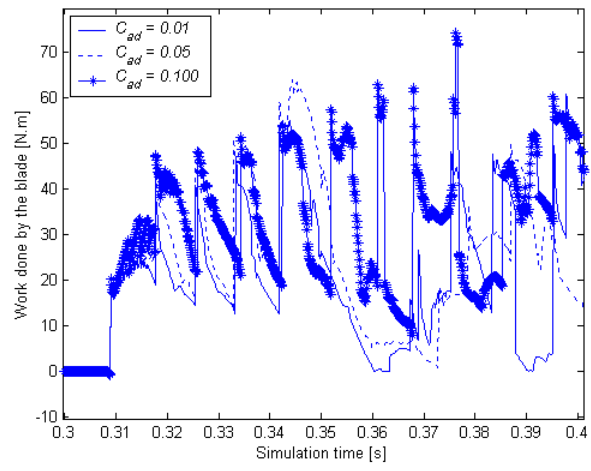


Figure 6.32 The energy consumption of the tool during the cutting process

7 DEM RESULTS FROM LITERATURE

7.1 INTRODUCTION

Computer simulations of real problems have always been attractive because they provide a means of investigating model systems in order to gain understanding and to conduct computer experiments in cases where experimental systems are hard to probe. This especially is the case with granular systems where experiments with non – ideal materials are extremely hard to probe and a general theory is not available (Tijskens et al, 2003). The DEM is well suited for such a task and its advantage over FEM is obvious. However, a realistic DEM simulation of granular soil demands a large number of disks which is beyond the current computational capability. Thus a balance has to be reached between a realistic simulation and practicality in computation.

In this section a review of still scarce DEM applications for agricultural purposes is presented. These applications are related to the study of tyre – soil interaction and soil – tool interaction during wedge or bar penetration. For recent results the reader is referred to Oida et al (1998 , and 1999); Tanaka et al (2000) and Huang et al (1992)

7.2 SIMULATION OF TYRE – SOIL SYSTEM USING DEM

The principle and merits of DEM were already described in the previous Chapters (5 and 6). It was explained that DEM was utilised to simulate the behaviour and reaction of an assembly of particles when the assembly was loaded or sheared. Oida et al (1999) show the effect of tyre reaction force on tyre performance by using the modified part of the *Kyoto DEM* for adhesive DEM particles. The virtual soil bin was prepared and filled by 8379 DEM particles to a height of 17 cm. A rigid wheel with a radius of 21 cm and a mass of 1.5 kg was put on the particle assembly. Next a vertical load of 8 N and a horizontal load of 6 N were applied to the wheel. Then the wheel was rotated on the surface of the particles assembly with an angular speed of 80 deg/s. The movement of the wheel is also governed by Newton’s Law. The DEM parameters in Table 7.1 were used for this preliminary simulations.

Table 7.1 Material properties of DEM particles

| Parameters | Symbol | Value | Unit |
|--|------------|-------|-------|
| Normal spring constant | k_n | 1.8 | kN/m |
| Tangential spring constant | k_s | 0.45 | kN/m |
| Adhesion spring constant | k_{ad} | 0.9 | kN/m |
| Particle – particle friction coefficient | μ_{pp} | 2.0 | - |
| Particle – wall friction coefficient | μ_{pw} | 1.8 | - |
| Vertical load | F_v | 8.0 | N |
| Horizontal load | F_h | 6.0 | N |
| Tyre velocity | v_t | 80.0 | deg/s |
| Total number of particles | n | 8379 | - |

Figure 7.1 shows simulated deformation results of the particles assembly by the rigid wheel with tyre lugs. As easily shown in the Figure holes made by lug prints can be found after running.

The volume change of particles assembly (corresponding to the soil compaction) is also observed on areas where the wheel and the particle assembly surface contacted each other and even deeper in the profile.

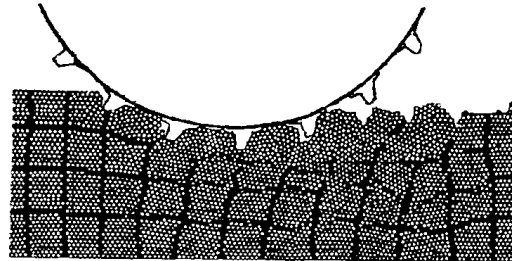


Figure 7.1 Deformation of particles assembly after wheeling (Oida et al, 1999)

Oida et al (1999) performed more simulations by using different sizes and masses of particles to analyse the vertical reaction forces of the wheel. In his simulation, two kinds of radii of particles were set to 2.0 mm and 2.5 mm in order to express moving restrictions such as interlocking of particles.

The density of particles was also tried to vary according to its depth. Three cases were considered: a standard case with constant density of 50000 kg/m^3 and normal spring constant of 12500 N/m ; an exponential case where the density increases exponentially with the depth (6000 to 120513 kg/m^3) and also the normal spring constants increase exponentially with depth from 1500 to 30128 N/m ; a linear case where the density increases linearly with the depth (6000 to 120000 kg/m^3) and also the normal spring constant increases linearly with depth from 1500 to 30000 N/m . The adhesion spring was set 20 % of the normal spring constant in each case. The friction coefficient was assumed as 0.52 between particles and also between particle and wheel surface.

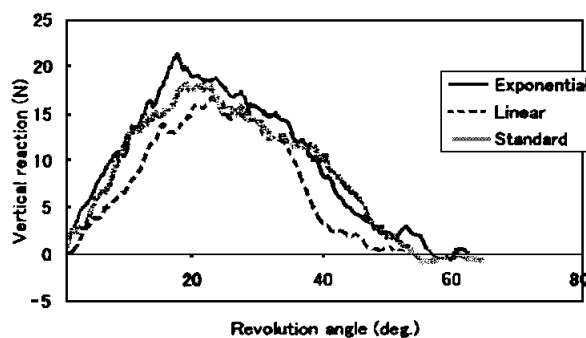


Figure 7.2 Distribution of vertical reaction forces along the contact surface in three cases of density variation with depth (Oida et al, 1999)

Figure 7.2 shows the simulated result of vertical reaction forces for three cases of density variations with depth when the pulling force of the wheel was 7.4 N. There is no significant difference between these force distributions of the three cases. As a result of the deformation of the particle assembly, the deep region was considerably deformed in the standard case. These force distribution patterns are surely similar to experimental results (Oida et al, 1991).

7.3 SIMULATION OF PENETRATION TEST USING DEM

A numerical technique which is known as the distinct element method (DEM) was developed by scientists (Huang et al, 1992 ; Tanaka et al, 2000) to simulate two – dimensional penetration tests in a granular material.

A series of simulated penetration tests of a 60° tip angle penetrometer was performed in a normally consolidated granular soil by Huang et al (1992).

The test was conducted by pushing the cone into the soil at a constant rate of 2 cm/s, while recording the penetration resistance at the tip.

The cone has a radius of 5 mm, the DEM region contains 12000 disks using a linear contact stiffness, the radius of the disks is ranging between 0.2 to 2 mm, specific gravity of 2.67, the coefficient of restitution is 0.25, normal contact stiffness of 300 MN/m² , tangential contact stiffness of 210 MN/m² and interparticle friction angle of 25° .

The penetrometer has a 60° tip angle which is the same as a standard cone penetrometer (Fig. 7.3). The disk assembly was normally consolidated under zero lateral strain conditions and under a vertical consolidation stress of $\sigma_{vc} = 1200$ kPa. Taking advantage of symmetry only one half of the penetrometer and soil mass was simulated.

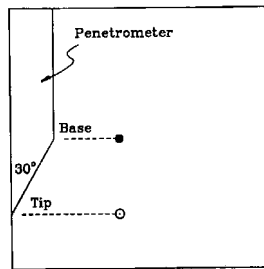


Figure 7.3 The standard penetrometer used in the simulation (Huang et al, 1992)

When we analyse the results of the test, at the penetration depth approximately $-3.5 R$ (where, R is the radius of the cone) a relatively constant penetration resistance was reached which is an indication of uniformity of the simulated assembly.

The directions of particle contacts and contact forces rotate towards the tip of the penetrometer and a substantial increase of contact forces was noticed as the penetrometer tip passes the initial state of penetration.

Figure 7.4 shows the distribution of normal contact forces within the assembly. The line thickness is proportional to the magnitude of contact force. The result shows that the contact forces are concentrated in the vertical direction below and around the face of the penetrometer tip. The contact forces between the particles and the penetrometer are low in areas immediately behind the penetrometer tip.

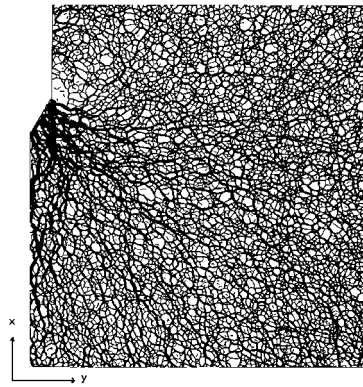


Figure 7.4 Distribution of normal contact force (Adapted from: Huang et al, 1992)

Tanaka et al (2000) also showed that the directions of particles contact and contact forces rotate towards the tip of the penetrating bar (Fig. 7.5)

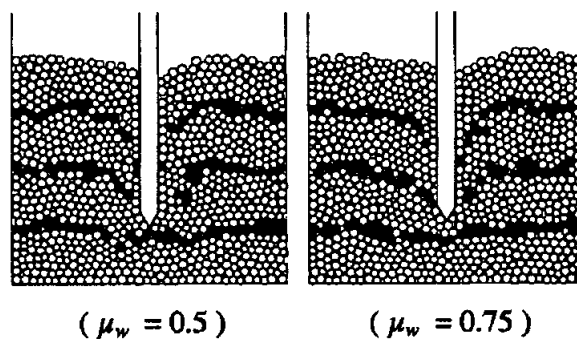


Figure 7.5 Particle behaviour during bar penetration for different particle wall friction coefficients μ_{pw} (Adapted from: Tanaka et al, 2000)

8 EVALUATION OF DEM RESULTS

8.1 COMPARISON BETWEEN FEM AND DEM RESULTS

8.1.1 INTRODUCTION

One can evaluate the FEM and DEM models by comparing their simulation results. However such a model comparison is fairly hard and very limited in quality since soil reacts very non – linearly when manipulated under dynamic load. Furthermore the distinctiveness of the nature of the medium in which the models work, together with their limitations on using different soil parameters, are an uneasy task to make the comparison very effective.

FEM operates on media which are continuous; here the assumed soil body is discretized into finite elements that are connected to each other at nodal points. Whereas DEM works on discrete medium, with the assumption that the soil body is an assembly of discrete disc particles which are contacting each other at contact points with possible overlap.

Much discussion has been presented in the previous Chapters about the fundamental procedures and working mechanisms of these two models (FEM & DEM). Detailed description of the models is not needed in this section; rather only a selected comparison of the simulation results to give the reader a general overview of the similarities and differences found between the models. Besides, such comparison may help to judge which model is relatively better in reflecting the real soil behaviour under dynamic loading or in case of dynamic tool – soil interactions. For this reason experimental results have been included in our comparisons. They can act as a check on real soil behaviour and so be used for benchmarking.

8.1.2 MODEL LIMITATIONS AND METHODS OF COMPARISON

8.1.2.1 Model limitations

All engineering simulation models have limitations. First of all it is important to be aware of and to understand all the limitations used in the two simulation models (FEM & DEM). Furthermore some of these limitations are specific to the type of simulation (shear box test, soil cutting and tyre – soil system etc.) used in the models, which means they are case – sensitive. Other limitations are local, which means they are limited to the program used in the current models.

In general the results obtained from these simulation models depend on all such limitations and the quality of the input data. Especially, care has to be taken by the user when results are applied to compare with results of a real laboratory test.

Below, a short list of significant limitations in model implementation is presented.

FEM model limitations

- Cannot be used for discrete particles (particles separated from each other by pores or voids)
- Only applicable for small deformations (strains)
- Insufficient to create the exact model geometry of the problem of interest
- Precision of simulation results depends on the number of nodes, input parameters and the coarseness of the discretized mesh. Increasing such values consume lots of computer memory and require longer calculation time
- Output is stored only for a few selected nodes or stress points

DEM model limitations

- Cannot be used for a large number of particles even with the fastest PC because of its required longer CPU time and large storage memory
- The big number of input parameters used and the difficulty to attach the right values to them
- It is a rather new method and still needs lots of improvement

8.1.2.2 Methods of comparison

Comparison of simulation results of FEM and DEM models can be made by the two commonly used comparison methods which are quantitative and qualitative.

Quantitative method

Quantitative descriptions of simulation of FEM and DEM models are rarely used in agriculture because of the complexity of agricultural processes, for example, soil –tool interaction in tillage processes. Deformation and failure patterns in tillage processes depend on many complex factors such as tool shape, working depth, forward speed, soil type, soil moisture content, soil porosity and structure, etc., which can all vary widely (Koolen, 1977).

Moreover some of the simulation results, for example the forces required to move the tool (in the soil – tool interaction) are frequently not quantitatively assessed (Fissha, 1998). So, in general unfortunately the idea of full quantitative description of such agricultural processes like soil – tool interaction, or tyre – soil system has still not been reached (Fissha, 1998). The other basic problem why not to use quantitative comparison in FEM and DEM simulation results is the very big magnitude differences between the two results.

Since DEM is best working for non – cohesive soil, the forces necessary to shear (in case of shear box test) or to cut (in case of even cohesive soil by applying the modified part of *Kyoto DEM*) are very low in magnitude when compared with the forces of either FEM results or actual results. Oida et al (1998) showed some examples of these magnitude comparisons by using DEM simulation of soil deformation and reaction under a track shoe.

By selecting the DEM simulation parameters by matching the simulated soil deformation with the actual deformation pattern, the simulated soil reaction force (max 15 N) was smaller than the actual one (about 170 N). Tanaka et al (2000) also showed the resistance force during bar penetration using the DEM model producing a much lower value (1.5 N) than that of the experimental one (20 N).

However there could be some chances of comparison between FEM and DEM results using ratios of stresses rather than single force or stress. The author has shown some efforts to compare the stress ratios of the curves at failure points by using FEM and DEM results of the shear box simulations (compare Fig. 8.3 with 8.4). From this Figures it might be concluded that if the magnitude of the input parameters is rightly assessed there could be a chance of similarity between these stress ratios, quantitatively. Furthermore Iwasita and Kojima (1992) showed that peak value stress ratio and number of slidings at contact point are almost quantitatively equal to the one obtained from the laboratory tests of Oda and Konishi (1974). But in general all DEM simulation results are in one way or another less in magnitude than that of FEM or experimental results. Therefore this method of ratio comparison could not be used for the current simulation results of FEM and DEM models.

Qualitative method

The qualitative descriptive method is a very common method to compare model simulation results. Many researchers used qualitatively described methods to compare their simulation results either with other, similar, simulation models or with experimental results (Momozu et al, 2000; Tanaka et al, 2000; Oida et al, 1999).

In this thesis the qualitative descriptions of some of the results produced in the simulations (shear box, soil cutting, tyre – soil system and tool penetration) are selected for comparison of FEM and DEM simulation results.

8.2 TYPES OF SIMULATION AND RESULTS SELECTED FOR COMPARISON

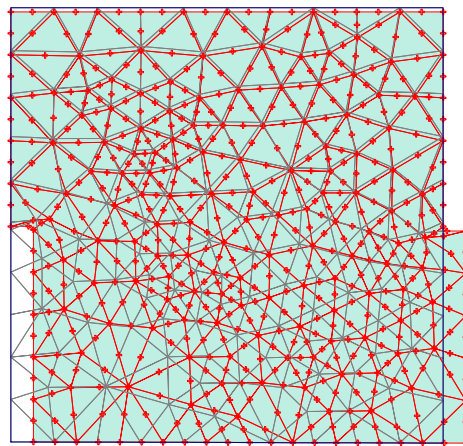
8.2.1 SHEAR BOX SIMULATION

Based on our previous discussion of FEM results (of shear box tests in Chapter 3 and DEM results of shear box test in Chapter 6) among the many simulation results, deformation behaviour or particle displacement vectors, shear stresses and failure properties, stiffness and volume change during shear were selected for our comparison purpose.

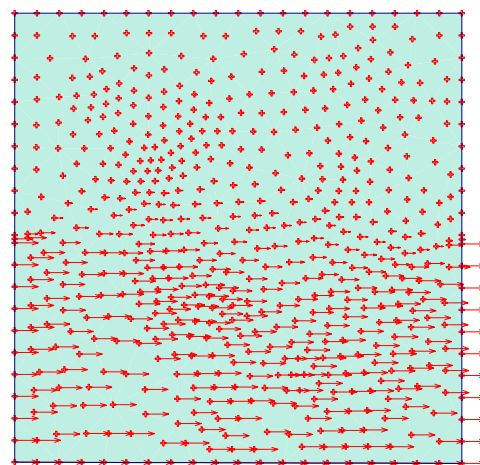
Furthermore these results stand for the basic output to determine the micromechanics of deformation for granular soils. Comparison has been taken place at different stages of shearing.

8.2.1.1 Deformation behaviour and particle displacement vectors during shearing

During FEM simulation of the shear box test, soils are deformed in the direction of shearing (Figure 8.1). Especially soil particles in the lower box are displaced horizontally, the direction in which the shear velocity is applied. Similar behaviour has occurred when shearing with DEM particles (Fig. 8.2). The length of each vector represents the magnitude of the displacement.

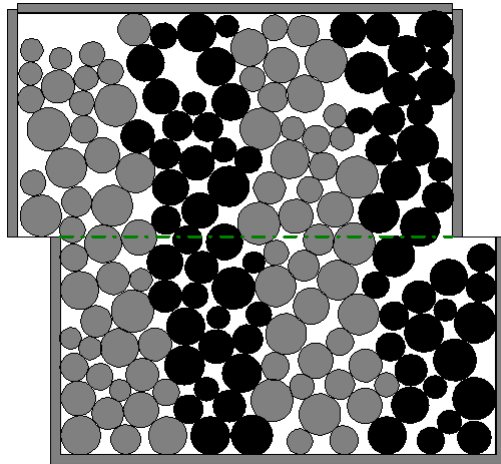


a) Deformed mesh with nodes relative to undeformed mesh after shearing

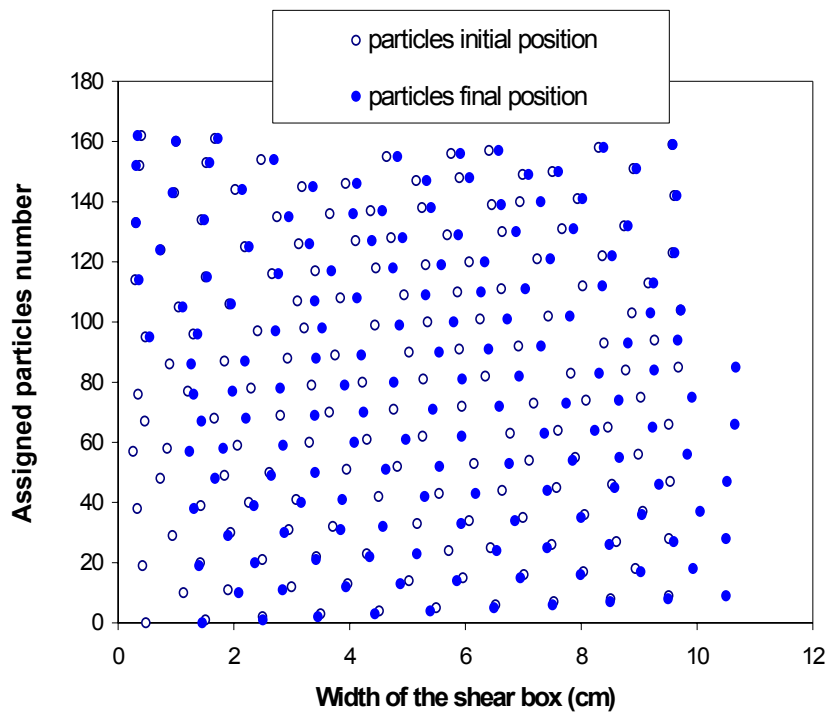


b) Horizontal displacement vectors distribution at nodal points

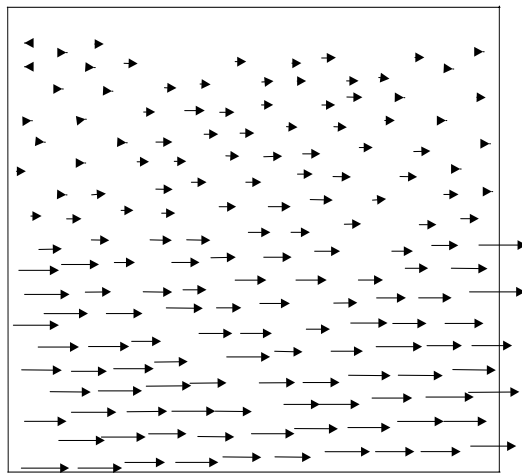
Figure 8.1 FEM results of deformation behaviour (a) and nodal displacement vectors (b) of Silty loam soil (Table 3.2) after shearing for 1 cm



a) Deformation behaviour of medium granular particles after shearing for 1 cm



b) Displaced position of DEM particles relative to initial position of DEM particles in the shear box



c) Horizontal displacement vectors direction of DEM particles after shearing; the length of the arrow shows the magnitude of its displacement

Figure 8.2 DEM results of deformation behaviour (a), particles displaced position (b) and horizontal displacement vectors direction (c) of medium granular DEM particles (Table 6.3) after shearing for 1 cm

8.2.1.2 Shear stresses and failure properties

According to FEM or analogous laboratory results from literature review (Chapter 4) of shear box tests of granular soils the shear stresses of such soils are made up, in general of two components: firstly the frictional resistance to the relative movement between the particles which is the sliding friction coefficient (μ_{pp}); secondly the structural resistance due to the interlocking of the particles (c). Since the conventional *Kyoto DEM* is working best for cohesionless soil we skip the second term.

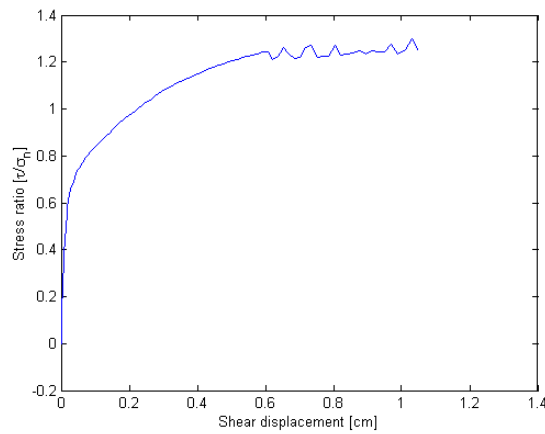
During FEM simulation of the shear box test (as it was explained in Chapter three) the shear stress is increased when the interparticle friction angle is increased (Fig. 3.31). Similar behaviour has occurred when increasing interparticle friction angle of DEM particles (Fig. 6.3). However this may not be true for interparticle friction angles beyond 40° . In this case the shear strength of DEM particles was decreased because of the increased particles rotation in the shear zone. Besides these, Mehrabadi et al (1992) show the potential of DEM for calculating the shear stress of loosely and densely packed granular particles respectively. Although not included here, their results are in line with shear stresses of loose and dense sand of FEM simulation results.

When we compare failure properties, for example failure forces from FEM simulation results can easily be determined from the stress – displacement (stress ratio – displacement in the present case) curves rather than that of DEM simulation results. From FEM output of stress ratio – displacement curves one can easily determine the maximum failure force (Fig. 8.3). If we further increase the displacement after reaching the failure point then the force increases gradually and hardening continues (see hardening law in section 1.4.2). Besides, the curve trajectories are very smooth as shown in Fig. 8.3.

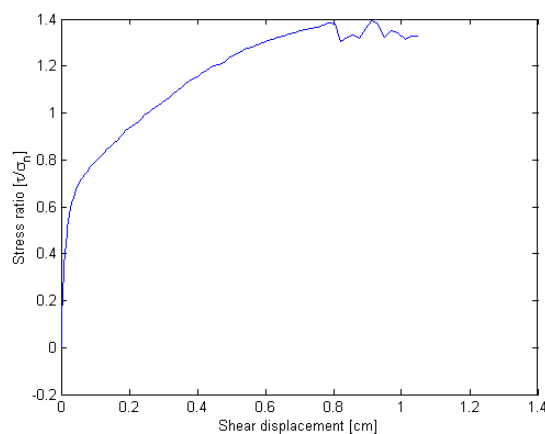
Whereas in the current DEM simulation, failure has been reached only locally after large displacement which means for example, we can determine the failure force within the range of 1 cm shearing displacement (Fig. 8.4). If we further increase the shearing displacement, the failure force goes up steeply. This last increase of failure force is caused by the right wall of the shear box. Besides, these failure forces are indicated by sudden drops in stresses in the shear zone. The periodicity and magnitude of these stress drops varied with both interparticle friction angle and particle size (Fig. 6.25).

If we compare both FEM and DEM simulation results with benchmarking laboratory test results of granular soil, failure behaviour from FEM simulation results was similar with the failure of loose granular soil and failure from DEM simulation results was similar with that of dense granular soil.

In general for all results from simulation and from laboratory tests failure stress increases as interparticle friction angle increases and the patterns also coincide.

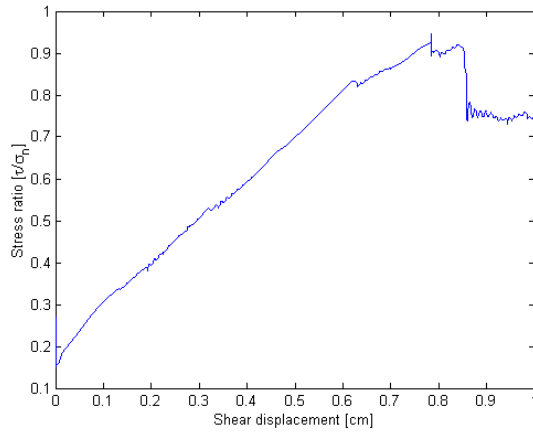


a) $\phi = 35$

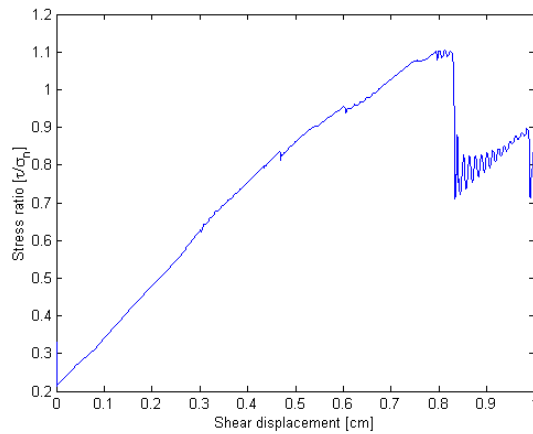


b) $\phi = 40$

Figure 8.3 FEM results of shear stress trajectory of Silty loam soil, for interparticle friction angle of 35° (a) and that of 40° (b)



a) $\mu_{pp} = 0.4$



b) $\mu_{pp} = 0.5$

Figure 8.4 DEM results of stress ratio trajectory for medium granular particles; interparticle friction coefficient μ_{pp} of 0.4 (a) and that of 0.5 (b)

8.2.1.3 Volume change and stiffness

The volume change was not analysed from FEM calculations of shear box test since the selected soil has no dilatancy. However when we see literature reviews of shearing test of real granular soil (Craig, 1992); (Kezdi, 1980) we notice that a dense soil tends to dilate, whereas a loose soil will decrease in volume. This is qualitatively similar with our DEM results. See the comparison in Fig. 8.5.

Analysis of volume change during shearing of DEM particles is considered in two cases. In the first case, the material constants are chosen so that the behaviour of the model corresponds to that of loosely packed DEM particles; while in the second case, the material constants are chosen so that the model behaviour corresponds to a densely packed sample.

In the first case, to start shear it is only necessary to make the particles slide upon one another. The small slip surface lies approximately in the same plane. In the second case (dense soil) a shear displacement is possible only if the particles do not merely slip along the plane of shear but also move upwards and roll over one another (dilatancy). These are similar behaviours of shearing DEM particles as it has been shown in Fig. 8.5 a. During shear of loosely packed DEM particles volume was decreased and for that of densely packed particles volume was increased (dilatancy).

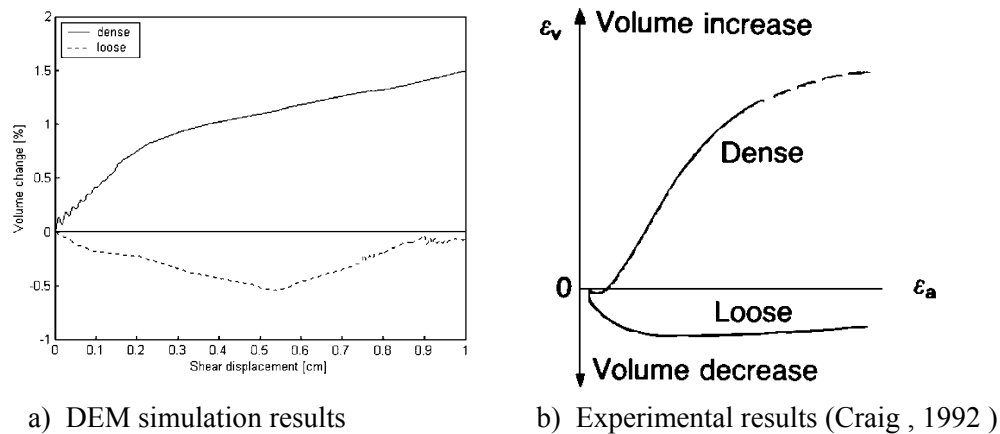


Figure 8.5 a, b. Volume change behaviour of granular soil during shear

Iwashita and Kojima (1992) also showed the potential of DEM models by using a laboratory test of simple shear with artificial DEM particles. He analysed that the results (the shear stress and the volume change behaviour) from DEM simulations were qualitatively similar with that of the analogous laboratory tests, see Figure 8.6.

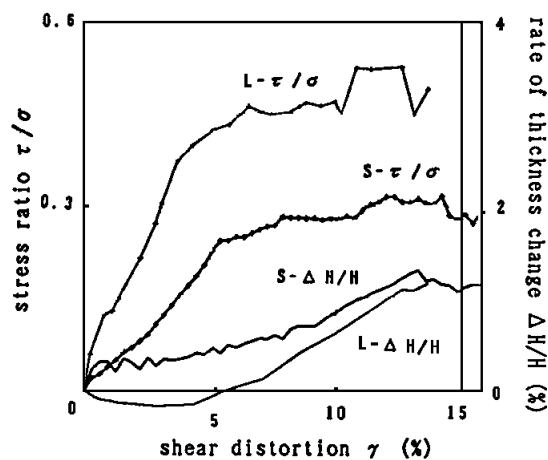


Figure 8.6 Comparison between DEM simulation results (S) and laboratory test results (L) of a simple shear test (Iwashita and Kojima, 1992)

The other important parameter that can influence the deformation mechanisms of granular soil is the normal contact stiffness between the particles. This parameter has a significant effect on simulation of DEM particles and can be considered as an important parameter, despite its effect was minimum on deformation using FEM simulation. During FEM simulation of very stiff soil, failure has been reached in an earlier stage than that of less stiff soil (Fig. 3.25). In DEM also similar behaviour occurs. So a DEM model with a soft contact stiffness needs larger shear displacement to reach the peak state than that of hard contact stiffness.

In case of DEM simulation of soft stiffness particles, the particles move mainly in the horizontal direction and few of them move vertically; while in the case of a hard stiffness (twice the value of soft stiffness) they move in both directions as if they were rolling over other particles. For the latter case the specimen shows a dilatation (Fig. 8.7).

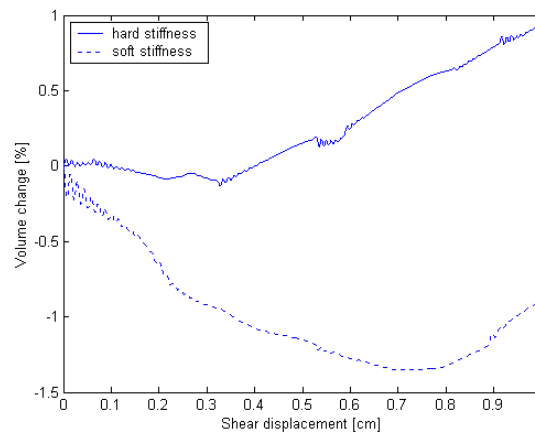


Figure 8.7 Volume change of DEM particles during shearing for different stiffness

For the same loading force a soft contact stiffness allows large overlapping at the contact between particles, while a hard stiffness allows relatively lower overlapping. And according to the shear force, soft particles can move easier than the hard ones in horizontal direction. Therefore the contact stiffness has an important influence in the deformation mechanism during DEM simulation.

In general based on the above comparisons one can conclude that the deformation mechanisms, the shear stresses and the volumetric behaviour of the DEM model are in good qualitative agreement with the observed behaviour of real granular soil.

8.2.2 SIMULATION OF SOIL CUTTING

In this section, among the FEM simulation results of soil cutting by a pendulum type machine, particle displacement vectors during the cutting process and particle velocity vectors at initial and final stages of cutting are analysed in order to compare them with those of DEM simulation results. The 6 cm long and 25 degree tip angle blade is assumed for the cutting process (Fig. 4.2). In the FEM simulation the tool is used to move 7 cm inside the Wageningen clay soil (Table 3.1) for a duration of 0.05 s. The soil block is discretised with a finite element mesh of 158 elements and 346 nodes.

The soil elements with the nodes very close to the tip and the area in front of the cutting blade surface are selected for analysing the displacement and velocity vectors. These nodes are the first which meet with the blade when the blade is in action.

Table 8.1 shows these nodes with the corresponding x and y displacement of the particles for the first three steps of the initial stage of the cutting process.

8.2.2.1 Particles displacement direction

When the blade has displaced its first 0.7 mm (first step in the cutting process, nodes 60, 63 and 62 show the direction of the tool displacement, Fig 8.8) inside the soil. Then the soil particles at the top surface (for example node 61) move upward. Those in front of the tool surface (node 59 and 64) move with relatively large magnitude in horizontal direction and less magnitude in downward directions but the soil particles around the tip of the tool (node 58) move in downward direction. This behaviour of particles displacement at the initial stage of cutting is also seen at DEM particles cutting process.

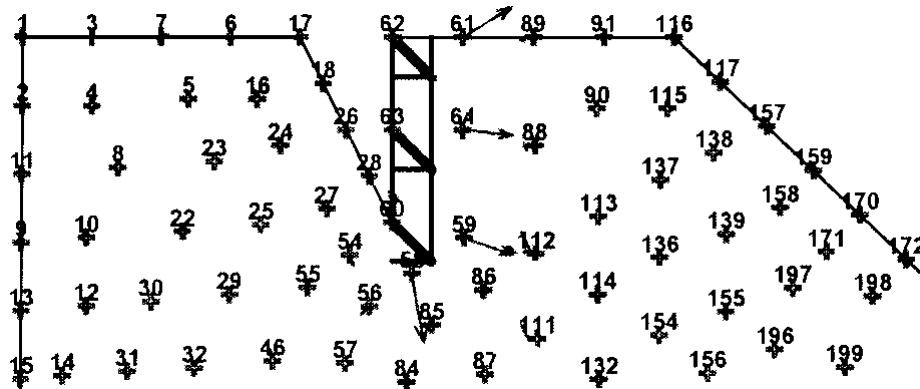


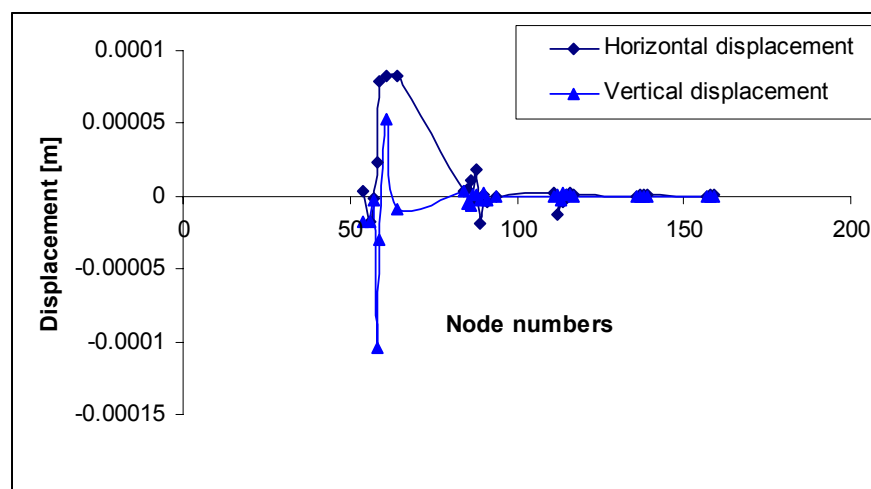
Figure 8.8 Soil particles displacement direction at the initial stage of cutting (first step, tool moves from 0 to 0.7 mm), FEM simulation results

Table 8.1 shows the horizontal and vertical displacements of all the selected nodes at the time of the first three steps of the cutting process.

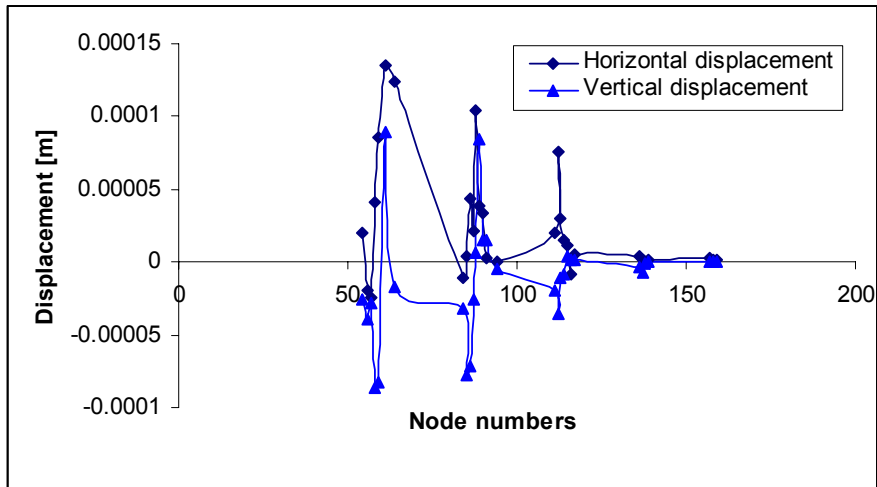
Table 8.1 Selected nodes with their corresponding displacements

| Node No. | First step | | Second step | | Third step | |
|----------|------------|------------|-------------|------------|------------|------------|
| | x-disp (m) | y-disp (m) | x-disp (m) | y-disp (m) | x-disp (m) | y-disp (m) |
| 54 | 3.85E-06 | -1.74E-05 | 1.99E-05 | -2.54E-05 | 2.31E-05 | -2.15E-05 |
| 56 | -1.72E-05 | -1.73E-05 | -1.97E-05 | -3.88E-05 | -4.88E-06 | -5.55E-05 |
| 57 | -1.34E-06 | -2.8E-06 | -2.44E-05 | -2.87E-05 | -3.35E-05 | -1.12E-05 |
| 58 | 2.27E-05 | -0.000104 | 4.1E-05 | -8.65E-05 | 3.65E-05 | -9.47E-05 |
| 59 | 7.95E-05 | -3.03E-05 | 8.5E-05 | -8.22E-05 | 9.57E-05 | -8.7E-05 |
| 61 | 8.27E-05 | 5.24E-05 | 0.000136 | 8.98E-05 | 8.03E-05 | -2.01E-05 |
| 64 | 8.3E-05 | -8.93E-06 | 0.000124 | -1.65E-05 | 0.000125 | -2.81E-05 |
| 84 | 2.94E-06 | 3.68E-06 | -1.05E-05 | -3.15E-05 | -2.34E-05 | -3.92E-05 |
| 85 | 4.89E-06 | -5.76E-06 | 3.92E-06 | -7.76E-05 | 4.58E-06 | -7.65E-05 |
| 86 | 1.09E-05 | -6.85E-06 | 4.3E-05 | -7.11E-05 | 4.28E-05 | -9.03E-05 |
| 87 | -2.18E-06 | 9.38E-07 | 2.11E-05 | -2.63E-05 | -4.44E-07 | -5.43E-05 |
| 88 | 1.83E-05 | 9.71E-07 | 0.000104 | 6.6E-06 | 8.38E-05 | 2.3E-05 |
| 89 | -1.85E-05 | -2.47E-06 | 3.89E-05 | 8.46E-05 | 0.000111 | 0.000124 |
| 90 | 1.36E-06 | 1.99E-06 | 3.39E-05 | 1.53E-05 | 7.56E-05 | 4.73E-05 |
| 91 | -3.92E-06 | -2.75E-06 | 2.53E-06 | 1.46E-05 | 6.27E-05 | 0.000103 |
| 94 | -3.62E-07 | 1.51E-07 | 6.91E-07 | -5.27E-06 | 1.11E-05 | -3.77E-05 |
| 111 | 2.37E-06 | -5.67E-07 | 2.05E-05 | -1.93E-05 | 4.92E-05 | -5.11E-05 |
| 112 | -1.29E-05 | 1.35E-06 | 7.54E-05 | -3.62E-05 | 4.95E-05 | -5.82E-05 |
| 113 | -2.32E-06 | -2.56E-06 | 3.01E-05 | -1.05E-05 | 7.73E-05 | -1.92E-05 |
| 114 | -3.46E-06 | 2.33E-06 | 1.45E-05 | -7.99E-06 | 5.87E-05 | -3.77E-05 |
| 115 | 5.92E-07 | 5.19E-07 | 1.12E-05 | 4.15E-06 | 4.46E-05 | 1.38E-05 |
| 116 | 1.96E-06 | 1.07E-06 | -8.84E-06 | 1.52E-06 | 2.68E-05 | 3.43E-05 |
| 117 | 3.83E-07 | 4.44E-08 | 5.49E-06 | 2.1E-06 | 2.51E-05 | 1.87E-05 |
| 136 | -1.28E-07 | -1.25E-07 | 3.78E-06 | -3.41E-06 | 5.16E-05 | -1.24E-05 |
| 137 | 1.32E-06 | -3.71E-07 | 1.22E-06 | -6.83E-06 | 6.03E-05 | 3.46E-06 |
| 138 | 4.77E-07 | 2.77E-08 | 4.33E-07 | -7.53E-07 | 2.02E-05 | 1.64E-06 |
| 139 | 4.45E-07 | -3.73E-08 | 1.24E-06 | -3.7E-07 | 1.77E-05 | -2.9E-06 |
| 157 | 2.66E-07 | -2.01E-08 | 2.25E-06 | -3.03E-07 | 1.61E-06 | -5.88E-06 |
| 158 | 5.48E-07 | -1.54E-08 | 9.71E-07 | -9.08E-08 | 6.07E-06 | 6.23E-07 |
| 159 | 4.26E-07 | 5.22E-08 | 1.21E-06 | -3.47E-08 | 4.84E-06 | 6.5E-07 |

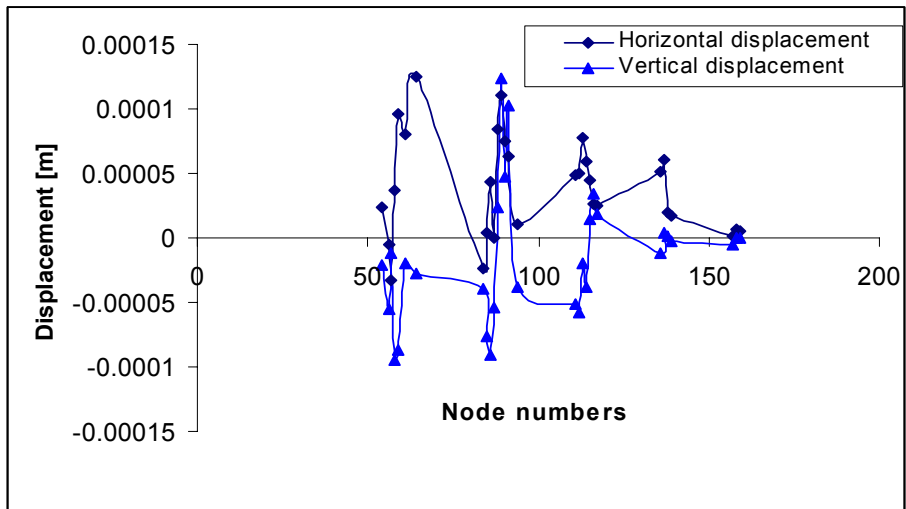
Figure 8.9 shows the particles displacement magnitude distribution at the first three initial steps of the first stage of cutting.



a) First step (tool moves from 0 to 0.7 mm)



b) Second step (tool moves from 0.7 to 1.4 mm)



c) Third step (tool moves from 1.4 to 2.1 mm)

Figure 8.9 a,b and c. Soil particles displacement at the first three initial stages of cutting; FEM simulation results

From Figure 8.9 it follows that the particle displacement increases in both directions when the tool displacement increases. However the magnitude of displacement increases more in horizontal direction than in the vertical direction. This is similar with DEM results of particles displacement behaviour during cutting (Fig. 8.10).

Besides in both simulations (FEM and DEM) the number of particles displaced also increases when the tool displacement increases. This can clearly be seen from the Figures 8.9 and 8.10.

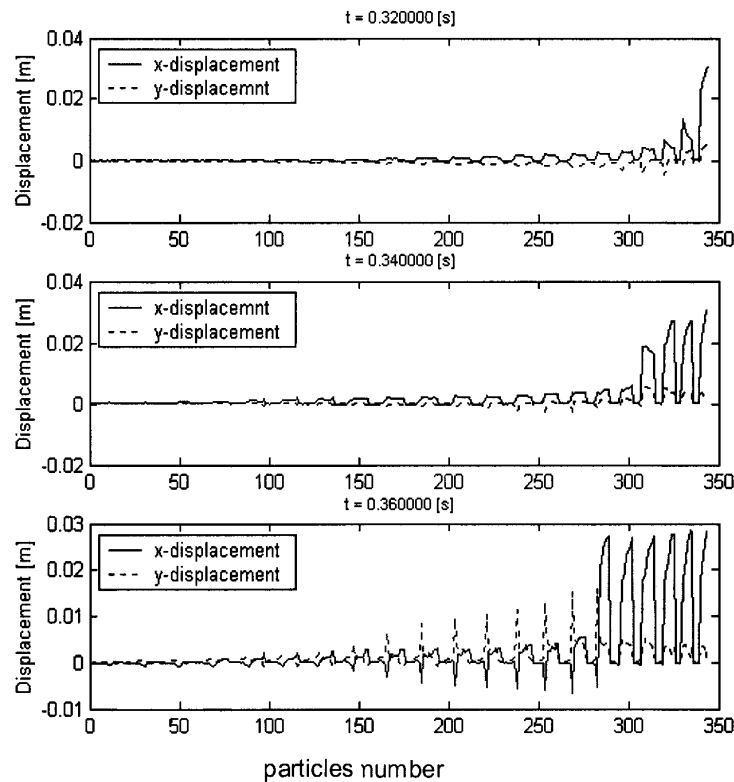


Figure 8.10 Soil particles displacement at the first three initial steps of cutting DEM particles by using pendulum type machine. With increasing simulation time, the number of particles with horizontal displacement increases

8.2.2.2 Particles velocity vector

Figures 8.11, 8.12 and 8.13 show the velocity distribution vectors of the soil particles for the above three steps of initial stage of the cutting processes simulated with FEM.

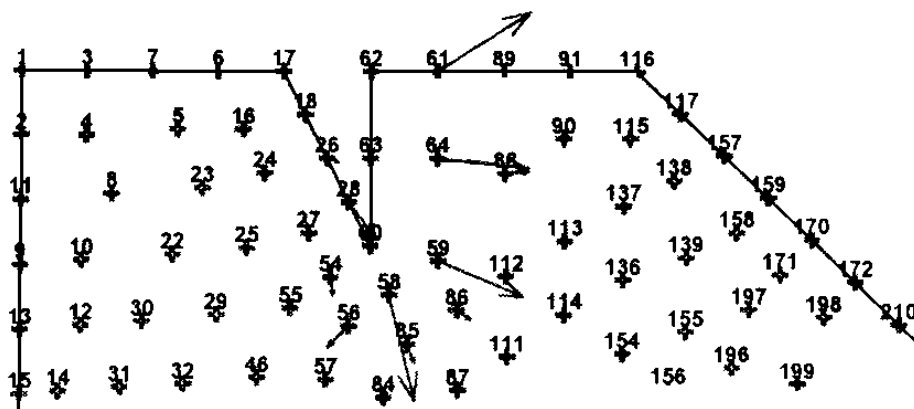
These velocity distribution vectors are similar with those of DEM particles, especially at the first step of the initial stage of cutting (compare Fig. 8.11a with Fig. 8.15 a). The magnitude of the velocity vectors decreases with increasing relative positions of the particles to the cutting tool.

Table 8.2 shows the horizontal and vertical velocity magnitude distribution of the selected nodes during the first three initial steps of cutting

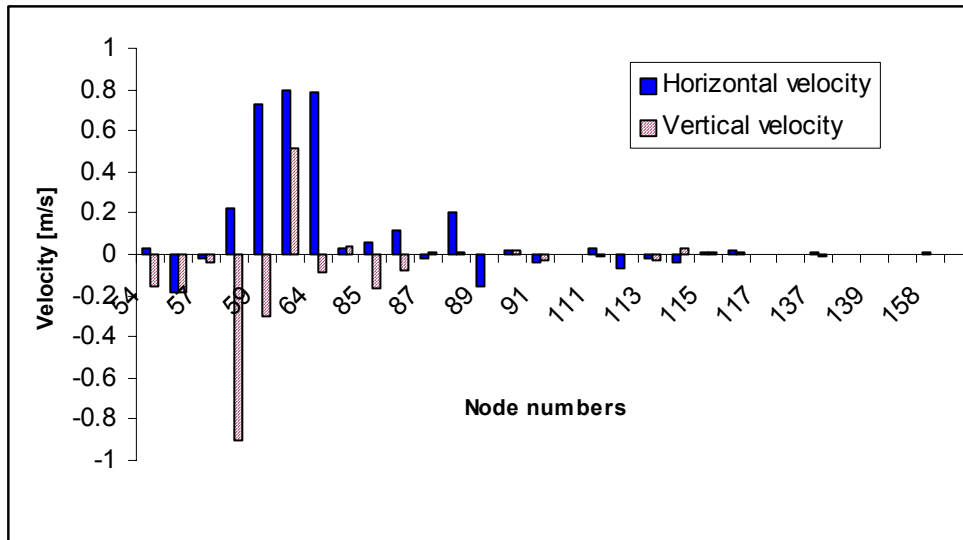
Table 8.2 Selected nodes with their corresponding velocities

| Node No. | First step | | Second step | | Third step | |
|----------|----------------------|----------------------|----------------------|----------------------|----------------------|----------------------|
| | V _x [m/s] | V _y [m/s] | V _x [m/s] | V _y [m/s] | V _x [m/s] | V _y [m/s] |
| 54 | 0.02552 | -0.157047 | 0.171785 | -0.207595 | 0.214095 | -0.170129 |
| 56 | -0.183522 | -0.186823 | -0.103226 | -0.294104 | -0.055822 | -0.477558 |
| 57 | -0.018151 | -0.033987 | -0.225988 | -0.248717 | -0.259304 | -0.068143 |
| 58 | 0.226238 | -0.905558 | 0.31501 | -0.700609 | 0.302939 | -0.742787 |
| 59 | 0.73218 | -0.304278 | 0.64545 | -0.683321 | 0.804876 | -0.686592 |
| 61 | 0.794413 | 0.511795 | 1.04944 | 0.667523 | 0.598002 | -0.285423 |
| 64 | 0.78908 | -0.086666 | 0.958562 | -0.130326 | 1.03627 | -0.259013 |
| 84 | 0.031188 | 0.034327 | -0.117157 | -0.311191 | -0.1848 | -0.303864 |
| 85 | 0.06094 | -0.161986 | -0.009323 | -0.542353 | 0.08483 | -0.68039 |
| 86 | 0.120003 | -0.081735 | 0.356679 | -0.642778 | 0.336115 | -0.698457 |
| 87 | -0.019315 | 0.007116 | 0.199807 | -0.262897 | -0.042674 | -0.435378 |
| 88 | 0.207716 | 0.010855 | 0.88682 | 0.061963 | 0.622966 | 0.202516 |
| 89 | -0.151508 | 0.001957 | 0.398362 | 0.797195 | 0.956412 | 0.940657 |
| 90 | 0.017539 | 0.022467 | 0.331998 | 0.143523 | 0.606193 | 0.414847 |
| 91 | -0.04232 | -0.029172 | 0.060385 | 0.181011 | 0.565024 | 0.893931 |
| 94 | -0.004129 | 0.001659 | 0.013521 | -0.061196 | 0.089514 | -0.331494 |
| 111 | 0.026778 | -0.00805 | 0.194632 | -0.188171 | 0.396562 | -0.436537 |
| 112 | -0.06815 | -0.00211 | 0.645873 | -0.336106 | 0.393732 | -0.456482 |
| 113 | -0.022495 | -0.028463 | 0.320897 | -0.08835 | 0.594245 | -0.165148 |
| 114 | -0.03613 | 0.024639 | 0.172447 | -0.100683 | 0.475908 | -0.301197 |
| 115 | 0.0068 | 0.006298 | 0.114067 | 0.034721 | 0.385751 | 0.143177 |
| 116 | 0.019321 | 0.01039 | -0.089099 | 0.0227 | 0.310137 | 0.305441 |
| 117 | 0.003656 | 0.000524 | 0.056254 | 0.022675 | 0.227838 | 0.181372 |
| 136 | -0.001985 | -0.001574 | 0.050101 | -0.034472 | 0.46801 | -0.106647 |
| 137 | 0.013191 | -0.005081 | 0.021263 | -0.059509 | 0.557166 | 0.046949 |
| 138 | 0.004542 | 0.000386 | 0.002633 | -0.008966 | 0.21275 | 0.028941 |
| 139 | 0.004068 | -0.000515 | 0.012016 | -0.002875 | 0.181077 | -0.030909 |
| 157 | 0.002642 | -0.000282 | 0.022148 | -0.003731 | 0.014785 | -0.048217 |
| 158 | 0.005071 | -0.000183 | 0.007953 | -0.000483 | 0.065979 | 0.004384 |
| 159 | 0.003959 | 0.00052 | 0.01077 | -0.000556 | 0.047303 | 0.008821 |

Figures 8.11, 8.12, 8.13 and 8.14 show the velocity vectors direction and their corresponding magnitudes at different stages of cutting process during FEM simulation.

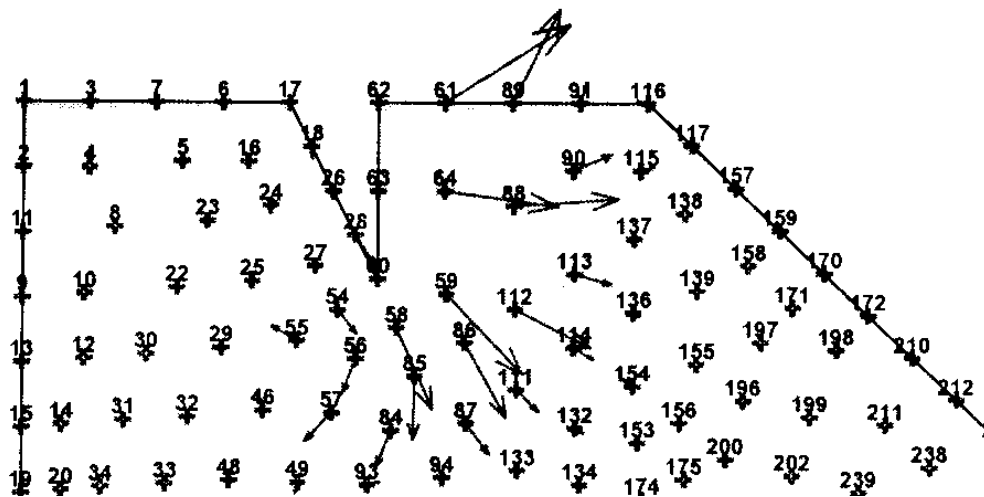


a) Velocity vectors, tool displaced (0 – 0.7 mm)

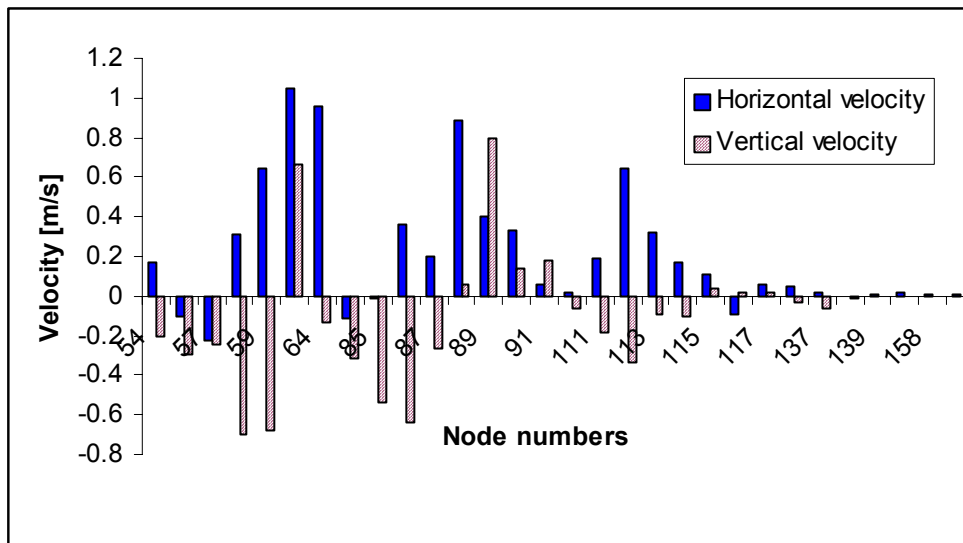


b) Magnitude distribution of the above velocity vectors

Figure 8.11 a, b. Velocity vectors with their magnitude at first step of cutting

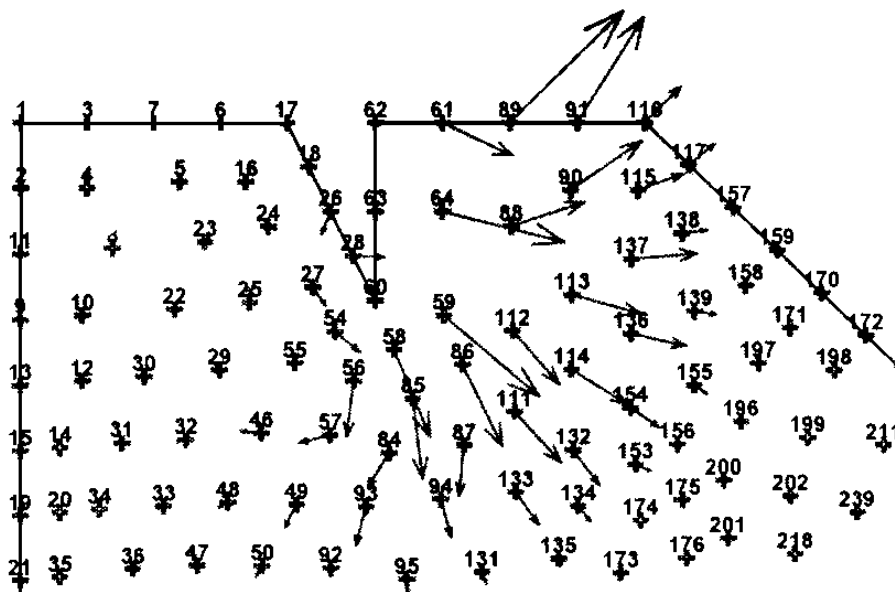


a) Velocity vectors, tool displaced (0.7 – 1.4 mm)

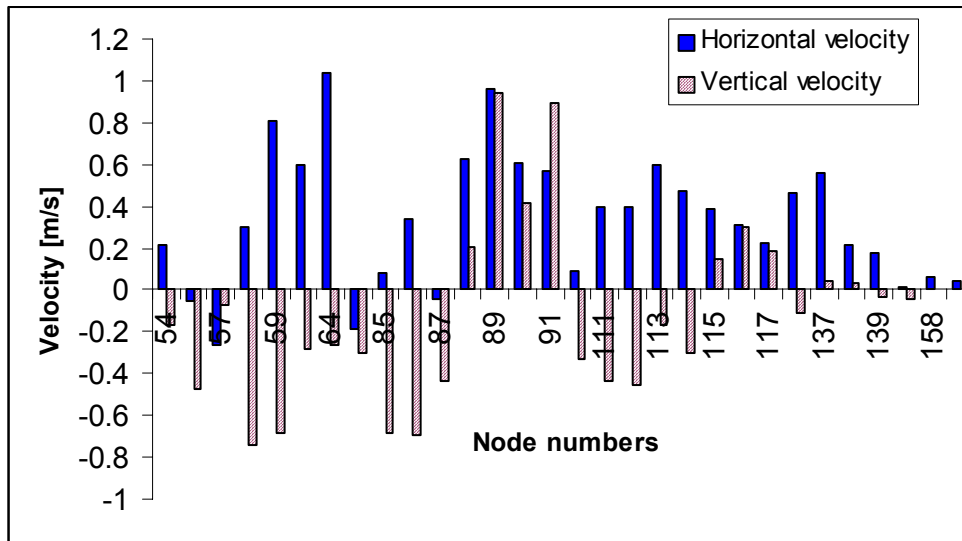


b) Magnitude distribution of the above velocity vectors at second step of cutting

Figure 8.12 a, b. Velocity vectors with their magnitude at second step of cutting



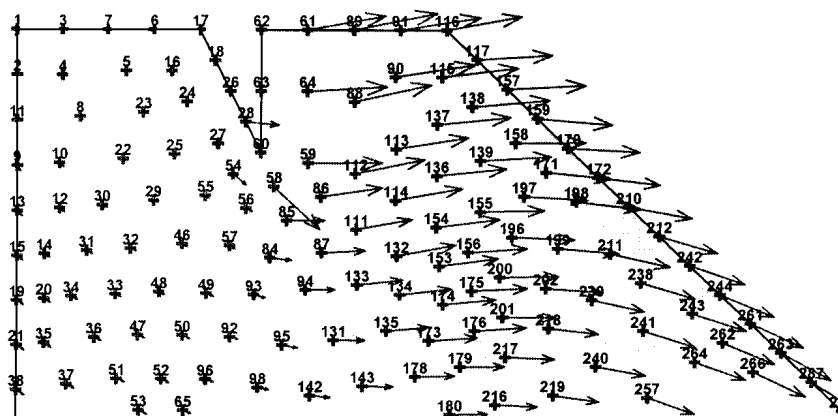
a) Velocity vectors, tool displaced (1.4 – 2.1 mm)



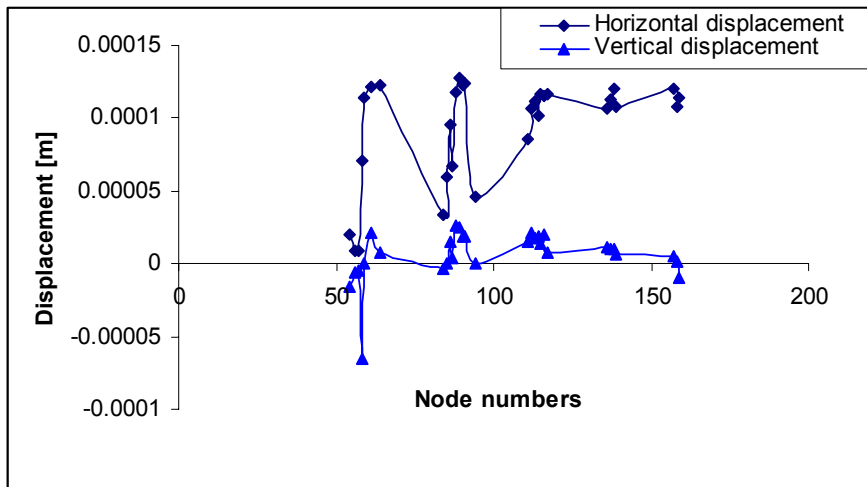
b) Magnitude distribution of the above velocity vectors at third step of cutting

Figure 8.13 a, b. Velocity vectors with their magnitude at the third step of cutting

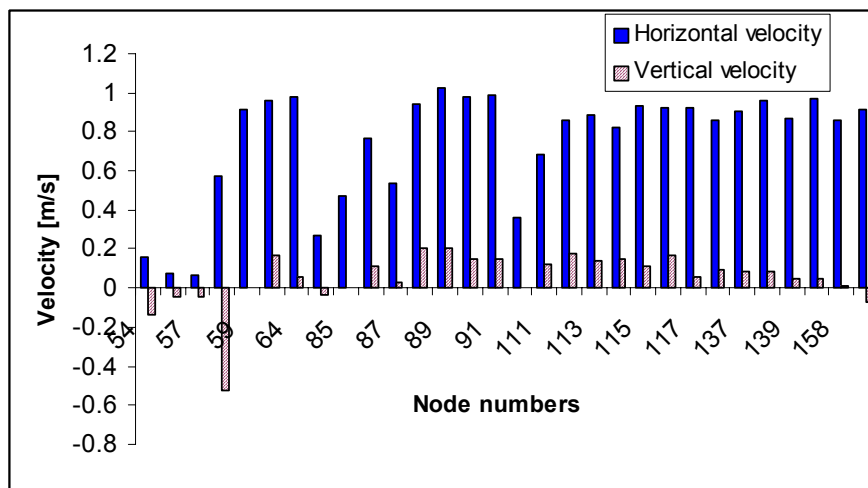
When we analyse the displacement and the velocity vectors distribution at the final step of cutting (after 70 mm of tool displacement), during FEM simulation, almost all the particles with the above selected nodes are displaced in horizontal direction with relatively large magnitude (Fig. 8.14 b). This can be seen especially from the velocity distribution (Fig. 8.14 a for velocity vectors and Fig. 8.14 c, for their magnitude).



a) Velocity vectors at the final stage, tool displaced (69.3 – 70.0 mm)



b) Displacement distribution of soil particles at the final stage of cutting



c) Velocity vectors distribution at the final stage of cutting

Figure 8.14 a, b, c. Displacement and velocity distribution at the final stage of cutting

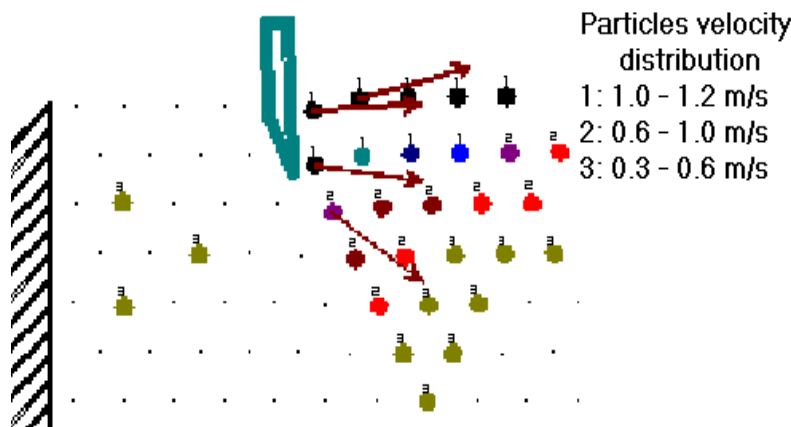
However, this has been true only for the above selected nodes. For other nodes, not shown here, the motion of the soil particles would be largely downward, especially those soil particles at the right bottom of the soil block (see Fig. 3.34 d).

Moreover during FEM simulation of cutting the particle velocity vectors have an almost equal distribution of motion in the downward, upward and horizontal directions at the first step of cutting (Fig. 8.11 a). Downward and upward motion of particles dominate during the intermediate stage and horizontal motion of particles dominates the system till the end of the cutting action or the final step of cutting (Fig. 8.14 a), except for particles at the right bottom of the soil block. All particle motions are determined from the initial positions of the particles before cutting.

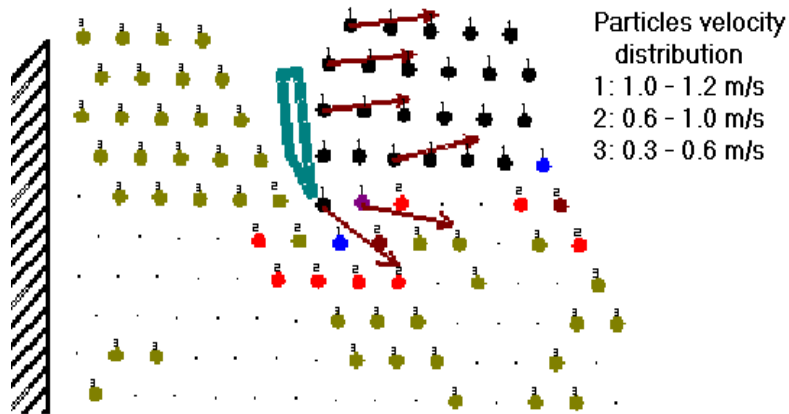
In case of DEM simulation of cutting, the DEM results show similar behaviour with those of FEM at the first step of the initial stage of cutting (Fig 8.15 a). Upward motion dominates at the intermediate stage (Fig 8.16 a). Downward motion of particles dominates during the final stage (Fig. 8.16 b).

The increased downward motion of particles at the final stage of cutting during DEM simulation is perhaps explained by soil particles falling down due to gravity; which is similar with the real laboratory test. For the DEM results presented in this section the DEM parameters used are of Table 6.6, with adhesion coefficient of $C_{ad} = 0.1$, unless otherwise mentioned explicitly.

Particle velocity distribution at the initial stage of cutting



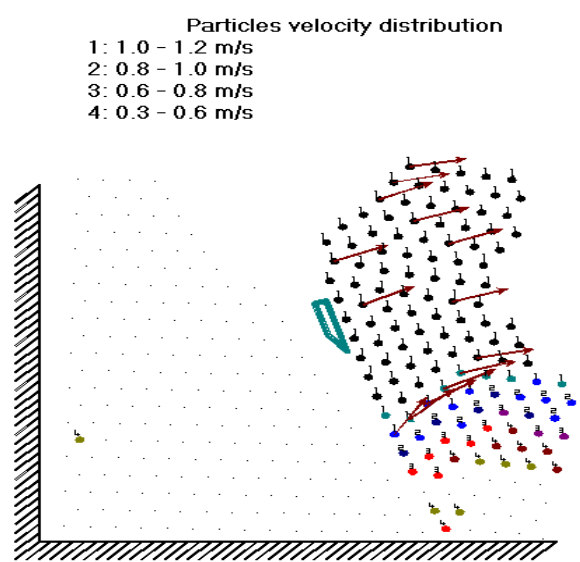
a) Velocity vectors at first step, after 0.2 s of tool – particles contact



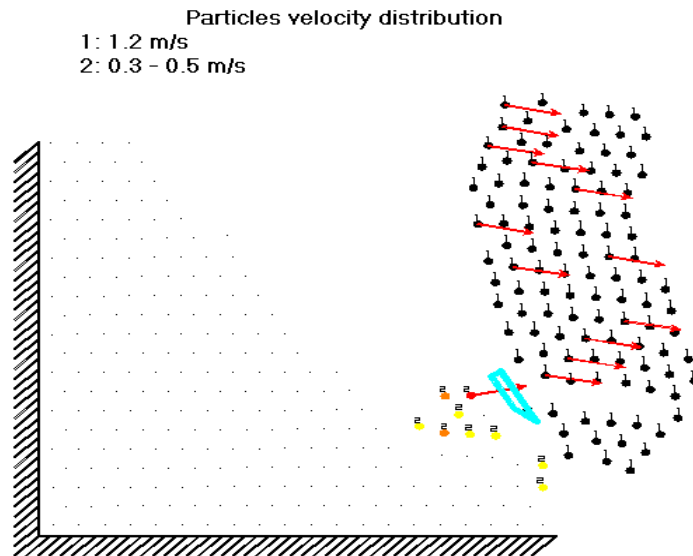
b) Velocity vectors at second step, after 0.4 s of tool – particles contact

Figure 8.15 a, b. Velocity vectors distribution at the first two steps of the initial stage of cutting process; DEM results

Particle velocity distribution at intermediate and final stages of cutting



a) At intermediate stage, shows upward motion



b) At final stage, shows downward motion

Figure 8.16 a, b. DEM particles velocity distribution at intermediate and final stages of cutting

After running and analysing a number of soil cutting simulations by DEM and FEM models, the general pattern of particles velocity vectors distribution has become clear. Figure 8.17 shows the general patterns of DEM and FEM particle velocity vectors distribution at different stages of the cutting process. In Fig. 8.17 double arrows show the dominant distribution and the single arrow shows a relatively normal distribution concerning an almost equal number of particles.

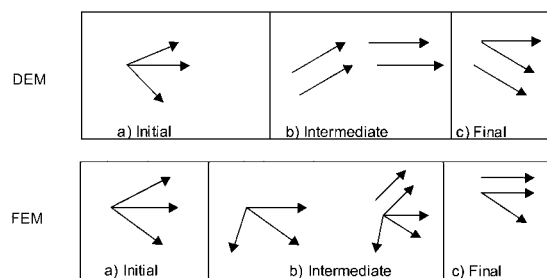
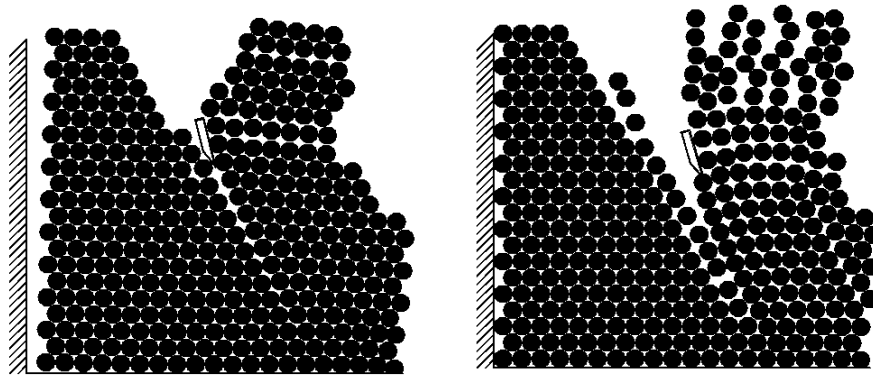


Figure 8.17 The general pattern of DEM and FEM particles velocity vectors distribution at different stages of the cutting process

By comparing the results of DEM and FEM simulations with the benchmarking laboratory test results, we can easily judge the advantages of DEM over FEM simulation models. DEM results show more behaviour similar to the real soil laboratory tests than FEM results during soil cutting, for both adhesive and non - adhesive DEM particles.



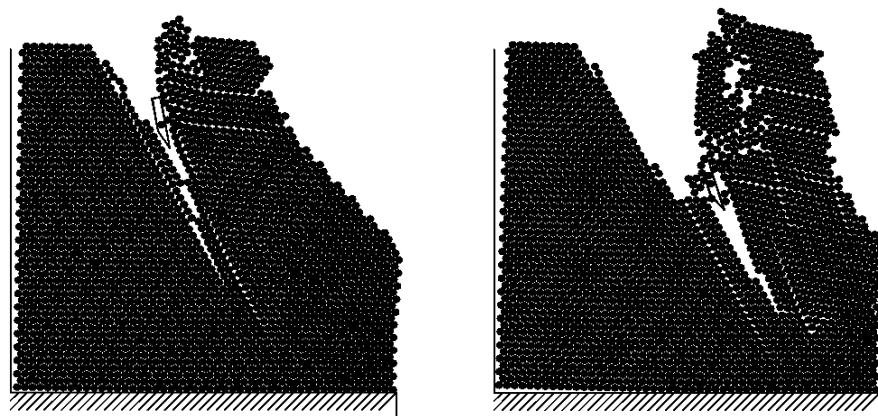
a) Adhesive particles ($C_{ad} = 0.1$)

b) Non – adhesive particles ($C_{ad} = 0.01$)

Figure 8.18 a, b. Particles behaviour during cutting of DEM particles assembly, where C_{ad} is coefficient of adhesion area ($N_{bed} = 10$, $\mu_{pp} = 0.7$, $r = 10$ mm)

During cutting of adhesive DEM particles we do not see much scattering of particles during the process (Fig. 8.18 a), whereas for non-adhesive DEM particles, scattering of particles dominates the cutting process (Fig. 8.18 b). This scattering behaviour of soil particles is also seen in laboratory test of cutting Ede sand soil (Fig. 4.4 b).

In case of adhesive DEM particles cutting, particles are displaced more or less together by forming soil clods. Cracks are preceding the blade motion (Fig. 8.19 a, b), which is similar with the laboratory results (Fig. 4.4 a)



a) $\mu_{pp} = 0.466$

b) $\mu_{pp} = 0.36$

Figure 8.19 a, b. Particles behaviour during cutting of DEM particles assembly ($C_{ad} = 0.1$, $N_{bed} = 50$, $r = 4.5$ mm)

8.2.3 SIMULATION OF TYRE – SOIL SYSTEM

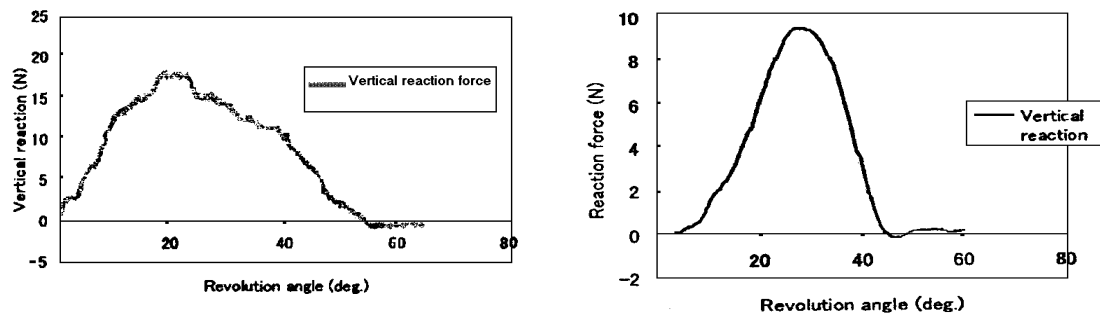
8.2.3.1 Vertical stress and volume change

During FEM simulation of the tyre – soil system soil vertical reaction stresses (total stresses in this case) increased on areas around the tyre – soil contact (Fig. 3.8 a). Soil plastic cap points (soil compaction) were seen on areas where such vertical stresses were greater than the preconsolidation stress of the soil.

In case of DEM simulation of tyre performance, the volume change of the particles assembly (soil compaction) is observed on areas where the wheel and the particle assembly surface contacted each other and even deeper in the profile (Oida et al, 1999).

This behaviour of DEM particles is similar to the previously mentioned FEM results of soil compaction. Figure 8.20 also shows the distribution of the vertical reaction force along the wheel-tyre contact surface from the DEM model. For detailed information of tyre performance by the DEM model, see Chapter 7.

The DEM parameters (Table 7.1) were selected by a trial and error method in such a way that the simulated values approach the experimental values. The vertical reaction force distribution pattern from DEM simulation results is similar to that of the experimental result of the rigid wheel of mass 7 kg, pull force of 7.4 N and wheel rotation angular speed of 36 deg / s on silty sand soil with moisture content of 10 % (Oida et al, 1991).



a) DEM results (Adapted from: Oida et al, 1999)

b) Experimental results (Adapted from: Oida et al, 1991)

Figure 8.20 Distribution of vertical reaction force during tyre – soil simulation from DEM (a) and experiment (b)

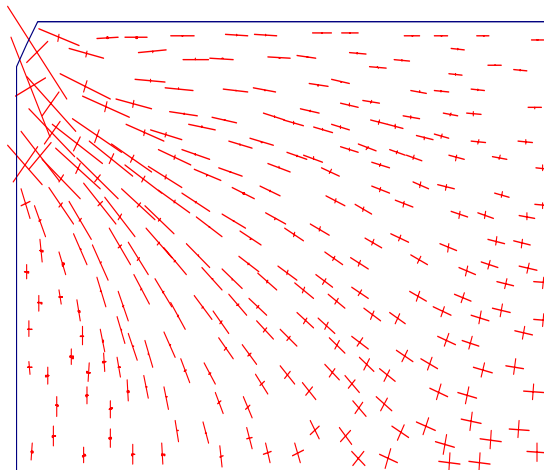
8.2.4 SIMULATION OF PENETRATION TEST

8.2.4.1 Resistance force and particle motion during penetration

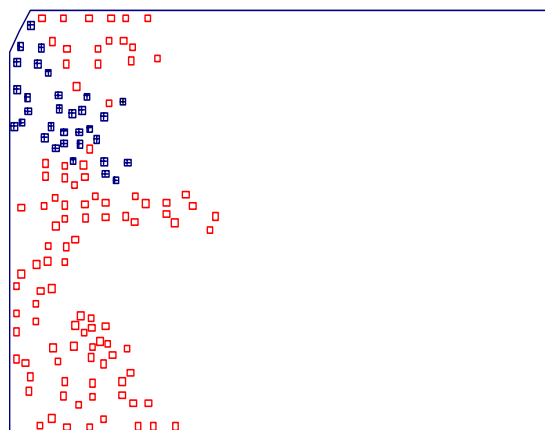
Among the FEM simulations of penetration, analysis of a 60° tip angle wedge penetration into Silty loam soil of Table 3.2 with wedge height of 20 cm, wedge width of 23 cm, a constant penetration velocity of 20 cm/s, time step of 0.0001 s, duration of penetration of 1 s, and penetration depth of 10 cm was selected to compare soil behaviour during penetration with that of DEM simulation.

During FEM simulation of the 60° wedge penetration, the soil particles are moving in the direction of the wedge displacement and the maximum total stress is concentrated at the tip and the front surface of the wedge (Fig. 8.21 a).

Because of such concentration of stresses, soil compaction (cap failure points) occurred at the tip and around the surface of the wedge (Fig. 8.21 b).



a) Total stress distribution



□ Mohr - Coulomb failure point
■ Plastic cap failure point (compaction)

b) Failure points

Figure 8. 21 a, b. Silty loam soil behaviour during penetration of a 60 degree wedge; FEM results

The DEM simulation of penetration of a 60 degree tip angle penetrometer into normally consolidated granular soil was analysed by Huang et al (1992). For detailed information of the simulation see Chapter 7 section 7.1.2.

When we analyse the results of this simulation, the contact forces appear to be concentrated on the vertical direction below and around the face of the penetrometer tip and the contact forces are low in the area immediately behind the penetrometer tip (Fig. 7.4).

This behaviour of DEM particles during penetration are analogous to the total stress concentration at the tip and surface of the wedge during FEM simulation of a 60° tip angle wedge penetration. These contact forces are decreasing in magnitude when the distances of the particles from the penetrometer surface are increasing, which is the same as total stresses decreasing for soil particles far from the penetrating wedge.

When penetration starts (Fig. 8.22) during DEM simulation displacement of particles by the penetrating bar is accompanied by a rise of the particles surface near the place of penetration. This behaviour of DEM particles during penetration is analogous to soil deformation behaviour during initial penetration of wedges (Fig. 3.15 b). During FEM simulation of penetration, soil can be deformed or compacted based on the deformability or compactability of the soil (Koolen and Kuipers, 1983)

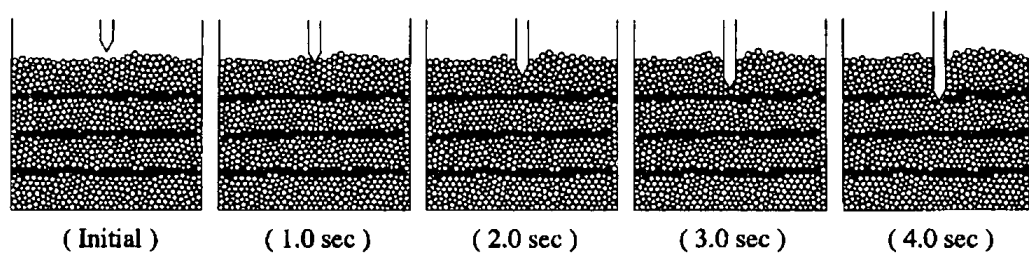


Figure 8.22 Behaviour of DEM particles at different points of time during penetration (Tanaka et al, 2000)

For the FEM simulation results of the current penetration test, the resistance force of the soil is increasing when the depths of penetration increases (Fig. 8.23). It seems that the curve is very smooth when we compare it with that of the DEM simulation result.

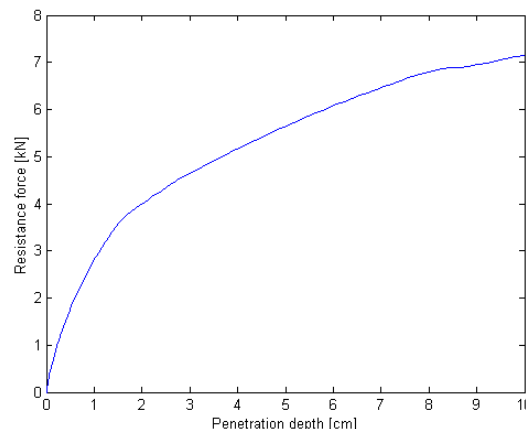


Figure 8.23 Resistance force during FEM simulation of penetration into silty loam soil

Figure 8.24 shows the curve of penetration resistance versus depth of the penetrometer tip during penetration. After a penetration of 1.75 cm, the penetration resistance fluctuates with less magnitude and a relatively constant value is reached which is an indication of uniformity of the simulated particulate assembly (Huang et al, 1992). This is analogous to the obtained steady state condition after large depth of penetration of a wedge into incompactible soil (Koolen and Kuipers, 1983).

In general, DEM simulation results showed, that penetration resistance increases when depth of the penetrometer increases. Curve fluctuation of the penetration resistance also occurs in DEM simulation. One possible reason for such a fluctuation was the lack of cohesion effect as explained by (Tanaka et al, 2000) due to the no – tension joint in the contact model (Fig. 5.3). Which means a frequent small change of resistance given by one particle would cause even a big change of penetration resistance.

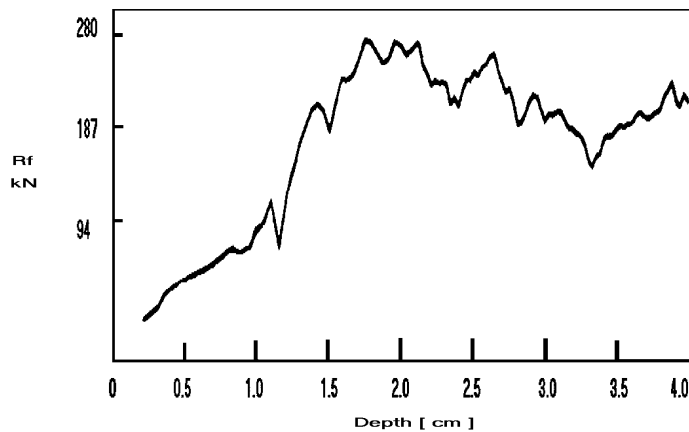


Figure 8.24 Resistance force versus depth during DEM simulation of penetration (Adapted from: Huang et al, 1992)

The DEM simulation indicates that fine particles around the penetrometer tip experience a sharp increase of contact stresses. This may result in crushing of the particles during penetration of real granular soil (Huang et al, 1992) .

8.2.5 DISCUSSION AND CONCLUSION

Even though the FEM simulation model has many advantages, like its easiness of considering soil as a continuum medium without any holes or gaps, being very advanced, well known and easily available, it has also many basic limitations as explained before to show real granular soil behaviour and properties.

Whereas the DEM simulation model, although being not very advanced and having also some limitations, the results from this model show very convincing granular soil properties. Despite those limitations the DEM models have also many advantages over the FEM models.

In the DEM model the soil medium is represented by assemblies of discrete particles with pores (voids) which represent true soil structure. Moreover in the DEM model (since it is not yet very advanced) there are many possibilities to modify and adjust the soil properties. For example concerning the cohesion force between particles as has been introduced in *Kyoto DEM* for cohesive soil properties.

Comparison of DEM simulation results with analogous FEM simulation results demonstrate qualitatively similar behaviour. Moreover particles behaviour from DEM results are in good agreement with that of experimental or laboratory test results. Therefore it is not erroneous to conclude that DEM has the potential capability to model granular soils better than that of FEM.

In other words DEM is a potentially useful and a more realistic method for simulating the deformation mechanisms of granular soil since its results are more convincing and similar to the behaviour of real granular soil during laboratory tests and in the field.

9 GENERAL DISCUSSION AND CONCLUSION

Agricultural soil is structured, has a certain strength and is usually compacting, thus structured soil plays a major role in plant growth (McKenzie and McGarry, 1999; Lebert et al, 1988; Gysi et al, 1999; Koolen, 1999). Although soil structure and soil mechanical properties have been extensively studied, they are still the least understood of soil characteristics affecting crop production, sustainability, environmental quality and tillage requirements. For an agricultural engineer concerned with soil compaction soil structure is assessed by indirect measurement of parameters related to soil mechanical properties.

The assessment of soil mechanical properties when soil interacts with different dynamic loading systems, for example tyre – soil system, wedge penetration, shearing and soil block cutting by pendulum type machine, can be treated using the two basic soil models (FEM and DEM). A number of scientists used such models particularly FEM to approximate the soil mechanical behaviour when soil interacts with agricultural machinery or tillage tools (see section 3.9.3). However modelling these dynamic load – soil systems (for example tyre – soil interaction) with FEM still remains complicated (Barneveld, 2000).

In this thesis, analysis of FEM and DEM of the previously mentioned loading systems is presented. Our focus is to evaluate simulation results and to determine the type of model which best reflects the real soil properties during such load – soil interactions, despite their limitations. This can be done based on the model simulation results (output).

Plaxis, one of the best examples of the finite element method (FEM) is used to treat soil during load – soil interactions, by assuming soil as a continuous medium. Plaxis has a number of limitations (see section 8.1.2.1) despite its advantages to treat dynamic load – soil interactions (Plaxis for the dynamic module version 7.2). Almost all agricultural processes are dynamic processes; tyre – soil interaction and tool – soil interaction are best examples. Therefore the basis of prediction of a good set of soil properties (stresses and deformations) under load – soil interactions using the finite element method is the choice of the right constitutive model in connection with the proper assessment of model parameters. However besides all the limitations of FEM modelling, determination of the right model parameters and their values still remains challenging.

The available models in Plaxis can roughly be divided into first order (the linear elastic model and the Mohr – Coulomb model) and high order models (Cam - Clay type model and Hardening – Soil model). The first order model (Mohr – Coulomb in this thesis) is characterised by a simple relationship between increments of stress and increments of strain with only a few model parameters (see section 2.3.1.1). Parameters of like E , ν , ψ , c and ϕ are the basic model parameters of the Mohr – Coulomb model. Measuring values for these model parameters is not an easy task. Besides data for such parameters are hardly available particularly for agricultural soil. Therefore all parameter values are taken based on different assumptions as explained in this thesis.

Furthermore the high order model (Cam - Clay in this thesis) has a more complex formulation based on hardening plasticity and has more parameters (see section 2.5.2.1). Parameters of c , ϕ , p_c , κ^* and λ^* are the basic model parameters of the Cam – Clay type model. The same explanation of what is stated for Mohr – Coulomb model works for that of Cam – Clay type model about determining and availability of parameter values.

It is often believed that performing finite element calculations is only useful if results of extensive laboratory testing are available from which model parameters can be determined directly. However laboratory tests are more costly and proper sampling is difficult. In general all deviation of the FEM calculation from the actual results is perhaps caused by the inaccuracy in measuring the correct input soil parameter values applied in the calculation.

Distinct Element Method (DEM) is one of the best tools used to treat soil under load – soil interactions by assuming soil as discontinuous (discrete) medium. This is the basic difference of DEM from FEM. The medium is represented as an assembly of discrete particles with the possibility of cyclic contact and failure by updating contact interactions throughout the simulation. DEM has a potential capability to represent the real soil medium from the beginning. In the same way as for FEM, a number of scientists also used DEM to treat granular materials in general since DEM has many other applications than soil. However very few are in the areas of Agricultural Engineering. DEM is a very recent model in comparison with FEM, and still needs lots of improvement to increase its potentiality despite the many modifications done till now.

Although DEM is potentially rich to represent the real soil medium, it has also limitations (8.1.2.1) and is not applicable in all circumstances. Selecting the right contact model and determining the right model parameters inclusive validation still needs lots of investigation. The initial particle arrangement, the mechanical contact modelling and determination of the right model parameters with associated parameter values are the main features on which the model results are dependable. All these features are still under investigation. Particularly a method of determining the right model parameters with correct estimated values is very challenging. In this thesis k_n , k_s , C_{ad} , μ_{pp} and r_i are the most influential parameters of the DEM model results. For example if DEM is modified depending on our domain of interest (see section 5.4), the number of input parameters is increased. This all needs the right assessment of input values which further increases the problem in model studies, since parameter values are given by trial and error methods.

Mostly, parameter values are selected by assumption of similar patterns of soil behaviour during laboratory tests (Oida et al, 1999). In this thesis some assumptions are made to estimate the spring constant value (k_n) of sand soil using the Hertz contact theory (Eqn 6.2).

From k_n , k_s could easily be estimated from the relation ($k_s = \frac{1}{5}k_n$). This is a generally accepted estimate by many scientists (Momozu, 2001; Umekage, 1998). But still the theory is applicable for only sand soil with high Young's module (E) value and large overlap between particles (δ) relative to their radius (r_i). For cohesive soil which has a very low E value compared with that of sand soil, the estimated k_n value could be very low and such a value does not bear the applied load during load – soil interaction. Then the calculation fails.

In DEM simulation, the interparticle friction coefficient (μ_{pp}) is one of the most influential parameters in the study of micromechanics of particle deformation. That means, interparticle sliding and rolling appear to be highly influenced by the input values of μ_{pp} . A number of scientists concluded that the output interparticle friction angle, estimated from linear regression (Coulombs failure envelope) is lower than the input interparticle friction angle (Momozu et al, 2001; Morgan, 1999).

Therefore the interparticle friction coefficient obtained from DEM simulation should not be used directly as an input of the interparticle friction coefficient between soil particles. This conclusion agrees with some of the results presented in this thesis. However in contrast to this, the author has estimated the range of the input interparticle friction coefficients of granular soil from DEM simulation of the shear box test (see Table 6.5). The results in Table 6.5 at least imply a possibility of estimating the input interparticle friction coefficient of granular soil directly from the DEM simulation of shear box test. This under the condition that all the input parameter values are rightly assessed.

In general, and still under investigation until now, there is no such method to estimate the input DEM model parameter values directly from the real soil properties. However the DEM simulation results presented in this thesis are in good qualitative agreement with the real soil properties under the same conditions of load – soil interaction. Which means, DEM simulation results presented in this thesis are in better qualitative agreement with laboratory experimental results than similar simulation results of FEM presented in this thesis (refer Chapter 8). Due to the low magnitude values of DEM results, quantitative comparison could not be carried out at least in this case. This with exception of the failure point indication by using quantitative comparison of stress ratios given in this thesis.

The DEM results presented in this thesis have been compared with similar FEM results and laboratory test results from literature review. They are selected as benchmarking for those FEM and DEM simulation results.

Although DEM seems still on its early stage of development relative to comparison with FEM, the results are very promising and pointing their high potential capability for analysing the actual soil properties during load – soil interactions, when at least some of the limitations are removed and a better method for determining the right model parameter values is reached.

RECOMMENDATIONS ON FURTHER STUDIES

A number of improvements still has to be made regarding FEM and DEM simulation models, to further analyse and determine the best simulation results, from which the potentiality of the models is increased with respect to proper selection and validation of the real granular soil properties. By using the very latest FEM simulation models other than Plaxis, for example MSC.MARC, ABAQUS/Explicit interactive version 6.3 (released in 2002) we can minimise the limitations of the FEM models used in this thesis and improve the results.

The FEM simulation model of Plaxis can be used for analysis of small deformation but this limitation is removed in the FEM simulation model of MSC.MARC. Which enables to apply relatively large deformations. Besides, simulation of this model is computationally intensive which means minimising the time spent during the simulation. It can be applied with many options of operating systems (Windows 2000, Linux, Windows NT etc.).

ABAQUS/Explicit: Interactive version 6.3 (released in 2002) has also many advantages over the FEM simulation model Plaxis used in this thesis. One advantage is the use of a central difference rule to integrate the equations of motion explicitly through time, using the kinematics conditions at one increment to calculate the kinematics conditions at the next increment. In other words ABAQUS/Explicit uses explicit time integration rather than implicit time integration which is used in Plaxis.

This explicit time integration used in ABAQUS/Explicit has many advantages over implicit integration. The explicit method is especially a well suited to solve high speed dynamic events that require many small increments to obtain high resolution solution. If the duration of the event is short the solution can be obtained efficiently. Contact conditions and other extremely discontinuous events are readily formulated in the explicit method and can be enforced on a node – by – node basis without iteration. ABAQUS/Explicit reduces the computational costs by speeding up the simulation.

Therefore, by considering all the above benefits of the very advanced FEM simulation models we can increase our possibilities of using such simulation models on the areas of load – soil interactions.

On the other hand DEM models also need lots of improvement first in the initial arrangement of particles, second in the mechanical contact modelling and third in assessment of the right parameter values. In general the magnitude of the DEM simulation results is very low when compared with that of FEM simulation results or laboratory experimental results. For example, in order to increase the magnitude of shear stress of DEM particles during shearing simulation or to increase the work done by the pendulum cutting blade we have to improve the initial arrangement of particles for the former case and the mechanical contact modelling for the latter case.

During shearing of real soil, finer particles are generated which will tend to fill the pore spaces, increasing the contact area and consequently the frictional resistance to shear deformation. This phenomenon would be most apparent for fine granular particles where smaller particles contribute relatively more to the area of the assemblage (see section 6.1.4.2). DEM still needs improvements on its application for cohesive soil. Although the assumption of an adhesion spring (on the normal direction of the contact modelling of DEM particles) decreases the scattering of DEM particles and rather forms soil clods during cutting, the magnitudes of the normal as well as the tangential forces of the cutting blade are very low when compared with that of FEM or laboratory experimental results.

Developing methods to estimate the right model parameter values that correlate with the real soil properties is one of the main features that scientists on this area of expertise have to focus on. DEM also needs improvements on reducing the number of model parameters. Especially at the time of modification. This has to be done by using degrees of sensitivity of parameters which help to concentrate on the selected (most influential) parameters. Attention should also be given to mechanisms to reduce the computational time of DEM simulations.

Finally current advancement in computer technology together with the possibilities of moving from 2D modelling to 3D modelling will enhance the potential capability of DEM over the coming years.

SUMMARY

Although soil structure and soil mechanical properties have been extensively studied during load – soil interactions, they are still the least understood in agricultural soil mechanics. They directly or indirectly affect crop production, environmental quality and tillage requirements. Agricultural soil is structured, has a certain strength and is often tilled by machinery or compacted by vehicles. Agricultural soil structure and strength affect the growth of roots and rooting patterns which directly or indirectly affect the quantity and the quality of the crop yield. Tillage and compaction are processes that affect soil structure and strength. Besides, soil water content at the time of tillage and traction, tractor loads, implement design, speed and tyre size, type and inflation are important parameters which affect soil structure and soil mechanical properties.

There is no doubt that a good investigation of soil structure and soil mechanical properties during load – soil interaction is highly dependent on the type of the methods (models) used to accomplish such a task. The two basic soil models used for the assessment of soil structure and soil mechanical properties are the well known finite element method (FEM) and the distinct element method (DEM) which is relatively new and still under investigation.

This thesis covers an extensive review of the two models (FEM and DEM) for analysis of application of the models for dynamic loading cases like tyre – soil system, wedge penetration, shear box test and soil cutting by a pendulum type machine. Moreover the thesis covers the evaluation of the two models by showing some basic qualitative comparisons of the simulation results to show the potential capability of the models and to determine our first priority of the models based on similarities between the model results and the real soil mechanical properties under the same conditions of load – soil interaction.

FEM simulations

Plaxis, one of the best examples of the finite element method (FEM) is used to treat soil during load – soil interactions, by assuming soil as a continuous medium. Plaxis has a number of limitations despite its advantages to treat the dynamic load – soil interactions common in agricultural processes.

The basis of a good prediction of soil properties (stresses and deformations) under load – soil interactions using the finite element method is the choice of the right constitutive model in connection with the proper assessment of model parameters. However besides all the limitations of FEM model, determination of the right model parameters and their values still remains challenging. The available models in Plaxis can roughly be divided into first order (the linear elastic model and the Mohr – Coulomb model) and high order models (Cam - Clay type model and Hardening – Soil model).

The first order model (Mohr – Coulomb model in this thesis) is characterised by a simple relationship between increments of stress and increments of strain with only a few model parameters. Parameters of Young's modulus, Poisson's ratio, dilatancy, cohesion and internal friction angle are the basic model parameters of the Mohr – Coulomb model. Measuring values of such model parameters is not an easy task.

Besides, data for such parameters are hardly available particularly for agricultural soil. Therefore all parameter values are taken based on different assumptions as explained in this thesis. The soil under investigation for the Mohr – Coulomb model is the Wageningen clay soil.

On the other hand the high order model (Cam - Clay type model, in this thesis) has a more complex formulation based on hardening plasticity and has more parameters. Parameters of cohesion, internal friction angle, dilatancy, preconsolidation stress, swelling index and compression index are the basic model parameters of the Cam – Clay type model. The same explanation of what is stated about the Mohr – Coulomb model works for that of Cam – Clay type model about determination and availability of parameter values. The soil under investigation for the Cam – Clay type model is the Silty loam soil.

In general all deviation of the FEM calculation results from the actual results is perhaps caused by the inaccuracy in measuring soil parameter values which is the main problem in FEM calculation as explained above.

DEM simulations

Distinct element method (DEM) is one of the best tools used to treat soil during load – soil interactions by assuming soil as discontinuous (discrete) medium. This is the basic difference of DEM from FEM: its assumption of the medium as an assembly of discrete particles with the possibility of cyclic contact and failure by updating contact interactions throughout the simulation. DEM has a potential capability to represent the real soil medium from the process beginning. In the same way as FEM, also a number of scientists used DEM to treat granular materials based on the area of their interest. However very few are in the areas of Agricultural Engineering. DEM is a very recent model in comparison with FEM, and still needs lots of improvement to increase its potentiality despite the many modifications already done until now.

Although DEM is potentially rich to represent the real soil medium it has also limitations and is not applicable in all circumstances. Determining the optimum initial arrangement of particles, which represents the actual initial soil structure, having the right contact model and determining the right model parameters with their right parameter values still need lots of investigation.

The initial particle arrangement, the mechanical contact modelling and determination of the right model parameters with their right parameter values are the main features on which the model results are dependable. All these features are still under investigation. Particularly a method of determining the right model parameters with their estimation of parameter values is very challenging. In this thesis the contact stiffness between particles, the tangential stiffness between particles, the adhesion coefficient between particles, the interparticle friction coefficient and the particle size are turned out to be the most influential parameters of the DEM model results.

Conclusion

Despite all the limitations of the DEM model, its simulation results presented in this thesis are in a good qualitative agreement with FEM simulation results or analogous laboratory experimental results of real soil under the same conditions of load – soil interaction. Therefore it is not erroneous to conclude that DEM has the high priority and good potential capability for assessing soil structure and studying fundamental soil mechanical properties during dynamic load – soil interaction.

SYMBOLS

| | |
|--|---|
| u_f | displacement column matrix of any point in an element |
| N | shape function matrix |
| u | nodal displacement column matrix of an element |
| ε | strain vector at any point in an element |
| B | element strain matrix |
| σ | stress vector at any point in an element |
| C | a constitutive matrix depending on the material properties of the element |
| f_n | element nodal force column matrix |
| k | element stiffness matrix |
| K | global stiffness matrix |
| U | column matrix composed of nodal displacements |
| F | global load column matrix caused by external forces |
| f_x, f_y, f_z | body forces in x, y and z axis respectively |
| $\varepsilon_{xx}, \varepsilon_{yy}, \varepsilon_{zz}$ | principal strains in x, y and z axis respectively |
| E | Young's modulus of the material |
| ν | Poisson's ratio |
| τ_{xy} | shear stress |
| γ_{xy} | shear strain |
| D | stiffness matrix |
| G | shear modulus |
| $\sigma_x, \sigma_y, \sigma_z$ | principal stresses in x, y and z axis respectively |
| ε_v | volumetric strain |
| σ_{oct} | octahedral normal stress |
| τ_{oct} | octahedral shear stress |
| ε_{oct} | octahedral normal strain |
| γ_{oct} | octahedral shear strain |
| σ'_{ij} | deviator stresses |
| ε'_{ij} | deviator strains |
| K | bulk modulus (page 16) |
| $\Delta\sigma$ | incremental stress |
| $\Delta\varepsilon$ | incremental strain |
| τ | shear stress |
| c | cohesion |
| ϕ | angle of internal friction |
| $d\varepsilon_{ij}$ | total strain increment |
| $d\varepsilon_{ij}^e$ | elastic strain increment |
| $d\varepsilon_{ij}^p$ | plastic strain increment |
| k | yield constant (page 20) |
| v_p | penetration velocity |

| | |
|------------------------|--|
| k_0 | failure constant |
| $d\sigma_{ij}^e$ | elastic stress increment |
| M | mass matrix |
| C | damping matrix (page 22) |
| u, \dot{u}, \ddot{u} | displacement, velocity and acceleration vectors |
| α_R, β_R | Rayleigh coefficients |
| c_i | interface cohesion |
| R | strength reduction factor |
| c_{soil} | soil cohesion |
| ϕ_i | angle of friction of the interface |
| ϕ_{soil} | angle of internal friction of the soil |
| α, β | constants that determine numerical time integration |
| t | time |
| Δt | time interval or time step |
| θ | a constant that determine the accuracy of the numerical time integration |
| Δt_{crit} | critical time step |
| ζ | multiplying factor |
| B | average length of an element (page 27) |
| S | surface area of an element |
| ρ | density of the material |
| $\dot{\epsilon}$ | strain rates |
| $\dot{\epsilon}^e$ | elastic strain rate |
| $\dot{\epsilon}^p$ | plastic strain rate |
| f | yield function |
| g | plastic potential function |
| λ | plastic multiplier |
| E_t | tangent modulus |
| T | rotational matrix |
| T^T | transpose of matrix |
| α | a switch constant (page 28) |
| ψ | dilatancy angle |
| $\dot{\epsilon}_V^p$ | increment of plastic volumetric strain |
| $\dot{\gamma}^p$ | plastic distortion increment |
| K_0 | coefficient of lateral earth pressure |
| χ | degree of saturation |
| S_w | suction in the soil water |
| p' | mean effective stress |
| λ^* | modified compression index |
| κ^* | modified swelling index |
| p_c, p_{pre} | preconsolidation stress |
| σ_v, σ_h | vertical and horizontal stresses respectively |
| δt | time step |
| n | number of additional steps |
| \bar{f} | surface function of the stress state |

| | |
|--------------------------|---|
| q | deviatoric stress |
| σ_{ij} | stress tensor |
| m | number of dynamic sub steps |
| σ'_x, σ'_y | horizontal and vertical effective stresses respectively |
| γ_w | wet soil density |
| γ_d | dry soil density |
| L | vertical load |
| T_{IP} | tyre inflation pressure |
| r | radius of the loaded area |
| IP | inflation pressure |
| P | total force on the wedge |
| P_1 | normal resistance force of the wedge |
| P_2 | tangential resistance force of the wedge |
| N | normal force (page 62) |
| T | tangential force (page 62) |
| α | wedge angle (page 62) |
| μ' | coefficient of soil – metal friction |
| v_l | low penetration velocity |
| v_h | high penetration velocity |
| σ_n | vertical pressure |
| ε_v^e | elastic volumetric strain |
| F | footing force (page 94) |
| r | radius of elastic boundary (page 95) |
| β | tip angle (page 100) |
| R | rotation radius |
| γ | setting angle (page 100) |
| H | working depth |
| L | bite length (page 100) |
| I_0 | moment of inertia of the pendulum |
| α_t | angular acceleration of the pendulum |
| R | distance from axis to blade tip (page 101) |
| F_t | resistance force against blade motion |
| L | length from rotation axis to centre of gravity of the pendulum (page 101) |
| m | mass of the pendulum (page 101) |
| g | acceleration due to gravity (page 101) |
| θ_t | rotational angle of the pendulum |
| e | friction energy lost by the pendulum bearings |
| E_{abs} | energy absorbed by the soil loosening process |
| Δh | change in heights between the starting and stop position of the pendulum |
| $\Delta\theta$ | rotation angle during pendulum motion |
| $\Delta\sigma_v$ | change in vertical stress |
| x, y | discs x and y respectively |
| x_i, y_i | centre co-ordinates of discs x and y respectively |
| \dot{x}_i, \dot{y}_i | velocity vectors of discs x and y respectively |
| \ddot{x}_i, \ddot{y}_i | acceleration vectors of discs x and y respectively |

| | |
|--------------------------------------|--|
| $\dot{\theta}_x, \dot{\theta}_y$ | angular velocities of discs x and y respectively |
| $\ddot{\theta}_x, \ddot{\theta}_y$ | angular accelerations of discs x and y respectively |
| R_x, R_y | radii of discs x and y respectively |
| m_x, m_y | masses of discs x and y respectively |
| D | distance between centres of disc x and disc y (page 113) |
| e_i | unit vector |
| u_n, u_s | normal and tangential displacements of discs |
| \dot{u}_n, \dot{u}_s | normal and tangential velocities of discs |
| $\Delta u_n, \Delta u_s$ | increments of normal and tangential displacements |
| $\Delta F_n, \Delta F_s$ | increments of normal and tangential forces |
| $(F_n)_N, (F_s)_N$ | total sum of normal and tangential forces |
| k_n, k_s | normal and tangential stiffness between discs (particles) |
| η_n, η_s | normal and tangential damping coefficients |
| γ | proportionality constant (page 117) |
| m | mass of particle (page 117) |
| a | proportionality constant |
| r_i, r_j | radii of particles I and j respectively |
| k_{ad} | adhesion spring |
| C_{ad} | adhesion coefficient |
| F_{ad} | adhesion force |
| F_n, F_s | normal and tangential contact forces |
| f_n, f_s | normal and tangential dispersion forces |
| d_n, d_s | normal and tangential damping forces |
| $\Delta x_n, \Delta x_s$ | normal and tangential increments of relative particle displacement |
| $\Delta \dot{x}_n, \Delta \dot{x}_s$ | normal and tangential increments of relative particle velocity |
| C_F | cohesive force |
| μ | interparticle friction coefficient (page 121) |
| I | moment of inertia (121) |
| C, D | damping coefficients (page 122) |
| ϕ | rotational displacement (page 122) |
| F_p | sum of all the force vectors from all the particles in contact |
| F_{pore} | force from the pore material |
| M_p | sum of all the moments from all the particles in contact |
| M_{pore} | moments from all the pore material |
| a | external acceleration acting on the particle (page 122) |
| M | sum of all the moments acting on the particle (page 122) |
| k_r | elastic spring (page 122) |
| F | sum of all the forces acting on the particle (page 122) |
| c_r | dashpot |
| μ_r | slider at contact |

| | |
|--------------------------------------|---|
| θ_r | relative rotation by rolling |
| r_c | constant radius |
| R | random number between 0 and 1 (page 124) |
| R_{\max}, R_i | maximum and incremental particle size |
| N_{\max}, N_i | maximum and incremental abundance |
| D | power law exponent (page 125) |
| σ_m | isotropic mean stress |
| e | void ratio (page 126) |
| e_n, e_s | normal and tangential elastic forces |
| $\Delta u_i, \Delta u_j$ | horizontal displacements of particles i and j |
| $\Delta v_i, \Delta v_j$ | vertical displacements of particles i and j |
| α_{ij} | angle between the line connecting the centres of particles and x-axis |
| $\Delta \varphi_i, \Delta \varphi_j$ | rotational displacements of particles i and j |
| $[X_i]_t$ | horizontal resultant force on particle i |
| $[Y_i]_t$ | vertical resultant force on particle i |
| $[M_i]_t$ | resultant moment on particle i |
| \ddot{u}_i, \ddot{v}_i | acceleration of particle i in x and y direction |
| $\ddot{\phi}_i$ | angular acceleration of rotation of particle i |
| k_{mw} | normal spring constant between particle and wall |
| μ_{pp} | interparticle friction coefficient |
| μ_{pw} | particle – wall friction coefficient |
| V_{sh} | shear velocity |
| t_{pre} | precalculation time |
| t_{sh} | shearing time |
| S_{output} | step output |
| m_p | particle mass |
| h_b | height of shear box |
| w_b | width of shear box |
| cgps | coarse granular particles simulation |
| c_r | rolling friction coefficient (page 137) |
| N_b | number of particle at bottom layer |
| t_s | simulation time |
| INP | input |
| SIM | simulation |
| cgppc | coarse granular particles pendulum cutting |
| E_i, E_j | Young's modulus of particles i and j |
| σ' | stress vector transformed in to another co-ordinate system |
| ν_i, ν_j | Poisson's ratio of particles i and j |
| δ | overlap displacement between particles |
| N_{layer} | number of layers |

| | |
|--------------------|--------------------------------------|
| H_{box} | height of shear box |
| R_{max} | maximum radius of particles |
| ε_{ij} | tensorial shear strains |
| τ_t | shear stress at time t |
| F_{sh} | shear force |
| D_{sh} | shear distance |
| d_{box} | depth of the shear box |
| F_v | vertical load |
| F_h | horizontal load |
| n | total number of particles (page 168) |
| σ_{vc} | vertical consolidation stress |
| R | radius of the cone (page 170) |

Note: page numbers are used to identify those symbols with more than one definition

REFERENCES

- Anandarajah, A., and Lu, N. 1991. Structural analysis by distinct element method, *Journal of engineering mechanics*, Vol. 117, ASCE.
- Aruga, K., Iwaoka, M., Sakai, H., and Kobayashi, H. 2000. The dynamic analysis of soil deformation caused by a semi-legged vehicle, *Proceedings of a Symposium organised by IUFRO*, Kuala Lumpur, Malaysia.
- Atkison, J.H., and Bransby, P.L. 1978. *An introduction to critical state soil mechanics*, McGraw-Hill, London, UK.
- Baars, S. 1995. *Communications on hydraulic and geotechnical engineering, discrete element analysis of granular media*, Report, Delft University, The Netherlands.
- Barneveld, A. 2000. *FEM based soil stress and strain analysis aimed at plant growth factors*, PhD thesis, Wageningen University, The Netherlands.
- Barneveld, A. 1994. *Determination of agricultural soil parameters that can be used in Plaxis finite element code*. Second international conference on soil dynamics, Cranfield University, UK.
- Batchelor, G.K. 1967. *An introduction to fluid mechanics*, Cambridge University Press, UK.
- Bath, and Jurgen, K. 1982. *Finite element procedures in engineering analysis, engineering and engineering mechanics* Seri, Prentice-Hall, Inc.
- Bathurst, R.J., and Rothenburg, L. 1988. Micromechanical aspects of isotropic granular assemblies with linear contact interactions, *Journal of Applied mechanics*, Vol. 55, pp 17-23.
- Bishop, A.W. 1966. The strength of soils as engineering materials, Sixth Rankin lecture, *Geotechnique* 16 (2): 91-128.
- Bland, D.R. 1960. *The theory of linear viscoelasticity*, Pergamon Press Ltd, London, UK.
- Bjarne, S. 1992. *The C++ programming language*, 2nd ed., Reading Massachusetts, Addison-Wesley Publishing Company.
- Blume, H.P., Eger, H., Fleischhauer, E., Hebel, A., Reij, C., and Steiner, K.G. 1998. Towards sustainable land use, *Advances in Geoecology* 31, Volume 1, Catena Verlag gmbh.
- Brain, W.K., and Dennis, M.R. 1978. *The C programming language*, Bell Laboratories, Murray Hill, New Jersey, Prentice-Hall, Inc.
- Braja, M.D. 1997. *Advanced soil mechanics*, 2nd ed., Washington DC, Taylor & Francis.
- Braja, M.D. 1995. *Fundamentals of soil dynamics*, Elsevier Science Ltd.

- Braja, M.D. 1994. Principles of geotechnical engineering, third edition, Pws Publishing company, Boston, USA.
- Brinkgreve, R.B.J. 2000. Beyond 2000 in computational mechanics, ten years of Plaxis international, Balkema, Rotterdam, The Netherlands.
- Brinkgreve, R.B.J. 1994. Geomaterial models and numerical analysis of softening, PhD thesis, Delft University The Netherlands
- Britto, A.M., and Gunn, M.J. 1987. Critical state soil mechanics via finite elements, Ellis Horwood Limited, Chichester, England.
- Brussaard, L., Kooistra, M.J. 1993. Soil structure/Soil biota interrelationships, Elsevier Science Publishers B.V., Amsterdam, The Netherlands.
- Burland, J.B. 1965. The yielding and dilating of clay, *Geotechnique*, Vol. 15, 211-214.
- Burland, J.B. 1967. Deformation of soft clay, Dissertation, Cambridge University.
- Campbell, C.S., and Brennen, C.E. 1983. Computer simulation of shear flows of granular material, mechanics of granular materials: New models and constitutive relations, Elsevier Science Pub. Amsterdam, 313-326.
- Canada Department of Agriculture, 2001. Glossary of terms in soil science, publication 1459.
- Carol, P., Claude, L., Sylvio, T., and Marc, J.R. 1999. Improving FEM performance for soil – tool interaction problem, Proc, the 13th intern. conf. of ISTVS, Munich, Germany.
- Casaverde, L., Iwashita, K., Tarumi, Y., and Hakuno, M. 1989. Distinct element analysis for rock avalanche, *Journal of Earthquake Engineering*, Vol. 6, pp131-140.
- Chancellor, W.J. 1977. Compaction of soil by agricultural equipment, Division of Agricultural Science, University of California, USA.
- Chi, L., and Kushwaha, R.L., and Shen, J. 1993. An elastoplastic constitutive model for agricultural cohesive soil, *Canadian Agr. Eng.* 35 (4) 245-251.
- Chung, T.J., and Lee, J.K. 1975. Dynamics of viscoelastoplastic soil under a moving wheel, *Journal of Terramechanics*, Vol. 12, pp 15-31.
- Corkum, B.T., and Ting, J.M. 1986. The discrete element method in geotechnical engineering, dept. civil Eng. Univ. Toronto, Ontario, Canada.
- Craig, R.F. 1992. Soil mechanics, Fifth edition, Chapman & Hall.
- Cundall, P.A. 1971. A computer model for simulating progressive large scale movements in blocky rock systems, Proc. Symp. Int. Soc. Rock. Mech.
- Cundall, P.A. 1974. A computer model for rock mass behaviour using interactive graphics for the input and output of geometric data, Rep. AD/ A-001 602, US National Tech.Inf.

- Cundall, P.A., and Strack, O.D.L. 1979a. A discrete numerical model for granular assemblies, *Geotechnique* 29 pp 47-65.
- Cundall, P.A., and Strack, O.D.L. 1979b. The distinct element method as a tool for research, depart. civil. and mineral Eng. Univ. of Minnesota, Minneapolis, USA.
- Cundall, P.A., and Strack, O.D.L. 1979. A discrete numerical model for granular assemblies, *Journal of Geotechnique* Vol. 29, pp 47-65.
- Dawidowski, J.B., and Koolen, A.J. 1987. Change in soil water suction conductivity and dry strength during deformation of wet undisturbed samples, *Soil and Tillage Research* , 9, pp, 169 – 180.
- Josselin de Jong, G., and Verruijt, A. 1969. Etude photo elastique d'un empliment de disques, *cahiers du group, Francais de Rheologie*, Vol. II.
- Deitel, H.M., and Deitel,P.J. 1994. C++ how to program, New Jersey, Prentice Hall international, Inc.
- Dexter, A.R., Emerson,W.W., and Bond, R.D. 1978. Modification of soil structure, Chichester, John Wiley & Sons Ltd.
- Dexter, A.R. 1979. Prediction of soil structures produced by tillage, *Journal of Terramechanics*, Vol.16, pp 117-127.
- Drescher, J., Horn.R., and Boodt, M. 1988. Impact of water and external forces on soil structure, selected papers of the first workshop on soil physics and soil mechanics.
- Drucker, D.C., Gibson,R.E., and Henkel, D.J. 1955. Soil mechanics and work hardening theories of plasticity, *Proc, ASCE*, Vol. 81, Paper No. 298, pp 1 – 14.
- Drucker, D.C., and Prager, W. 1952. Soil mechanics and plastic analysis or limit design, *app. math.* 10 (2): 157-165.
- Duncan, J.M., and Chang, C.Y. 1970. Non-linear analysis of stress and strain in soils, *Journal of soil mechanical foundation*, Div. Amer. Soc. Civil. Eng., 96: 1629-1653.
- Febo, P. 1999. Research and experiences on agricultural tires to minimise soil compaction, sc-dlo, Wageningen, The Netherlands.
- Ferrez, J.A., Liebling, Th. M., and Muller, D. 1999. Dynamic triangulation's for granular media simulations, *Statistical Physics and spatial statistics*, Springer, Berlin.
- Fielk, J.M. 1997. Finite element modelling of the interaction of the cutting edge of tillage implements with soil , Pro, the 3rd intern. con. on soil dynamics, Tiberias, Israel.
- Francois, D., Pineau, A., and Zaoui, A. 1998. Mechanical behaviour of materials, volume 2: viscosity, damage, fracture and contact mechanics, Kluwer Academic Publishers, Dordrecht, The Netherlands.

- Fredlund, D.G., and Rahardjo, H. 1993. Soil mechanics for unsaturated soils, John Wiley and Sons, Inc, New York, USA.
- Gladwell, G.M.L. 1980. Contact problems in the classical theory of elasticity, Sijthoff & Noordhoff, Alphen aan de Rijn, The Netherlands.
- Gotoh, H., and Sakai, T. 1997. Numerical simulation of sheetflow as granular material, Journal of Waterway, Port, Coastal and Ocean Engineering
- Gregory, S., and Doug, B. 1996. A foundation for C programmers: C++ the core language, Cambridge, O' Reilly & Associates, Inc.
- Gysi, M., Ott, A., and Fluhler, H. 1999. Influence of single passes with high wheel load on a structured unploughed sandy loam soil, Soil Tillage Research, Vol. 52, pp 141-151.
- Hakuno, M., Tarumi, Y. 1988. A granular assembly simulation for the seismic liquefaction of sand , struc. Eng. Japan Society of Civil Engineers, 5 (2) pp 333 – 342.
- Hanly, R.J., Koffman, B.E., and Horvath, C.J. 1995. C programming design for engineers, Addison – Wesley Inc.
- Hawkins, G.W. 1983. Simulation of granular flow, mechanics of granular materials, Elsevier Science Pub. Amsterdam, The Netherlands, pp 305-312.
- Harris, W.L. 1971. The soil compaction process. In: Barnes, K.K., ed., Compaction of agricultural soil, pp 9-44. Am Soc. Agr. Eng. St. Joseph, MI.
- Higashitani, K., and Nakagawa, K.H. 1998. Deformation of aggregates depositing on a plate in a viscous fluid simulated by a modified discrete element method, Journal of Advanced Powder Technology, Vol. 9, pp 345-361.
- Hill, R. 1950. The mathematical theory of plasticity, Oxford University press, London, UK.
- Hillel, D., Warrick, A.W., Baker, R.S., and Rosenzweig, C. 1998. Environmental soil physics, Academic Press, San Diego, USA.
- Horn, R., Blackwell, P.S., and White, R. 1988. The effect of stress duration on pressure transmission in an ameliorated red-brown earth under irrigation. Proceeding 11th ISTRO conference, Edinburgh.
- Horn, R., and Wiermann, C. 1999. Input parameters for soil mechanical properties theory and first approach, sc-dlo, Wageningen, The Netherlands.
- Horton, I. 1997. Beginning C , Wrox, Press Ltd, Canada.
- Huang, A.B., Ma, M.Y., and Lee, J.S. 1992. A micromechanical study of penetration tests in granular materials, Advances in micromechanics of granular material, Elsevier.
- Hugh, F. 1963. Advanced mechanics of materials, Longmans, Green and co ltd. London.

- Hughes, TH.J.R. 1987. The finite element method, linear static and dynamic analysis, Prentice hall Int.
- Irving, H.S. 1992. Mechanics of fluid, 3rd ed., Singapore, McGraw-Hill, Inc.
- Iwashita, K., and Hakuno, M. 1990. Modified distinct element method simulation of dynamic cliff collapse, Journal of Earthquake Engineering, Vol. 7, pp133-142.
- Iwashita, K., and Oda, M. 1998. Couple stress developed in shear bands (1)—Particle rotation and couple stress in granular media, Proceedings of the 12th engineering mechanics conference, California, USA.
- Iwashita, K., and Oda, M. 1998. Rolling resistance at contacts in simulation of shear bands development by DEM, Journal of Engineering Mechanics.
- Iwashita, K., Oda, M., Kakiuchi, T. 1997. Importance of particle rotation in the mechanics of granular materials, Powders, and grains, Balkema, Rotterdam, The Netherlands.
- Iwashita, K., and Kojima, T. 1992. Distinct element simulation of simple shear test of granular assembly, Advances in micromechanics of granular materials, Elsevier.
- Jaeger, J.C. 1964. Elasticity, fracture and flow, London, Butler and Tanner LTD.
- Jaeger, J.C., and Cook, N.G.W. 1979. Fundamentals of rock mechanics, Chapman and Hall, UK.
- Jan, G., and Jerzy, L. 1990. Soil physical conditions and plant roots, CRC Press Inc, USA.
- Janbu, N. 1963. Soil compressibility as determined by Oedometer and triaxial tests, European conference on soil mechanics and foundation engineering, Wiesbaden, Germany 1: 19-25.
- John, D.N., and Debra, J.M. 1992. Expansive soils problems and practice in foundation and pavement engineering, John Wiley & Sons, Inc.
- John, P.W., and Chongmin, S. 1996. Finite-Element modelling of unbounded media, John Wiley & Sons Ltd.
- Johnson, K.L. 1985. Contact mechanics, Cambridge University Press, New York.
- Karczewski, T. 1978. The influence of speed on soil compaction by wheels of agricultural machinery. SIAE Technical report No. 5 Scotland.
- Kezdi, A. 1980. Handbook of soil mechanics, Vol. 2, Elsevier, Amsterdam.
- Kezdi, A. 1974. Handbook of soil mechanics, Vol., 1, Elsevier, Amsterdam.
- Kirby, J.M. 1989. Shear damage beneath agricultural tires: A theoretical study, Journal of Agricultural Engineering Research, Vol. 44, pp 217-230.
- Klajj, M.C. 1975. The meaning of pore pressures in soil with respect to soil strength, MSc thesis, Wageningen Agr. Univ. Wageningen The Netherlands, pp 47 In Dutch

- Kondner, R.L. 1959. Study of vibratory cutting penetration and compaction of soils. Tech. Rpt. 6 John Hopkins University, USA.
- Konijn, N.J.M. 1978. Resistance of soil against compaction in a soil profile. MSc. thesis, Wag. Agr. Univ. Wageningen, The Netherlands, pp 55. In Dutch.
- Koolen, A.J. 1977. Soil loosening processes in tillage analysis, systematics and predictability, PhD thesis, Wageningen University, Wageningen The Netherlands.
- Koolen, A.J. 1999. The compactive action, initial conditions, modelling and immediate effects, sc-dlo, Wageningen, The Netherlands.
- Koolen, A.J., and Van den Akker, J.J.H. 2000. On the use of agricultural soil data required in soil deformation models, *Advances in GeoEcology*, Catena Verlag, Reiskirchen, The Netherlands.
- Koolen, A.J., and Van den Boogaert, G.H.P.L. 1997. Transformation of three agricultural soil models into a model for the Plaxis Finite Element code, *Proceeding of the third international conference on soil dynamics*, Tiberias Israel.
- Koolen, A.J., and Kuipers, H. 1983. *Agricultural soil mechanics*, Advanced Series in Agricultural Sciences, Springer Verlag, Berlin Germany.
- Koolen, A.J., and Vaandrager, P. 1984. Relationships between soil mechanical properties, *Journal of Agricultural Engineering Research*, Vol. 29, pp 313-319.
- Kostritsyn, A.K. 1956. Cutting of a cohesive medium with knives and cones. *Natl. Inst. Agr. Engin., Eng. Translation* 58.
- Kruyt, N.P. 1994. Aspects of constitutive relations for cohesionless granular materials, PhD thesis, University of Twente, Hengelo, The Netherlands.
- Langen, H. 1991. Numerical analysis of soil structure interaction, PhD thesis, Delft University, The Netherlands.
- Larson, W.E., Blake, G.R., Allmaras, R.R., Voorhees, W.B., and Gupta, S.C. 1989. *Mechanics and related processes in structured agricultural soils*, NATO ASI Series, Vol. 2, Kluwer Academic Publishers, Dordrecht The Netherlands.
- Lebert, M., Burger, N., and Horn, R. 1988. Effects of soil structure and stress duration on pressure transmission in tilled soil. *Proceedings 11th ISTRO conference*, Edinburg.
- Lebert, M., Burger, N., and Horn, R. 1989. Effects of dynamic and static loading on compaction of structured soil, *Mechanics and related processes in structured agricultural soil*, NATO ASI Series, Kluwer Academic publishers.
- Lebert, M., and Horn, R. 1990. A method to predict the mechanical strength of agricultural soils, *Soil and Tillage Research*, Vol. 19, pp 275-286.

- Lerink, P. 1994. Prediction of the immediate effect of traffic on field soil qualities, PhD thesis Wageningen University, The Netherlands.
- Lorig, L.J., and Brady, B.H.G. 1984. A hybrid computational scheme for excavation and support design in jointed rock media, Cambridge England, pp 105-112.
- Marshall, T.J., and Holmes, J.W. 1992. Soil physics, Second Edition, Cambridge University Press, UK.
- McKyes, E. 1989. Agricultural engineering soil mechanics, Elsevier, Amsterdam, The Netherlands.
- McKenzie, D.C., and McGarry, D. 1999. Soil assessment and yield map interpretation: some case studies. The Australia cottongrower, 20 (2), p 46 – 51.
- McKyes, E. 1985. Soil cutting and tillage, developments in agricultural engineering 7, Elsevier, Science Publishers B.V., Amsterdam, The Netherlands.
- Meguro, K., and Iwashita, K., and Hakuno, M. 1991. Fracture analyses of media composed of irregularly shaped regions by the extended distinct element method, Journal of Earthquake Engineering, Vol. 8, pp 131-142.
- Mehrabadi, M.M., and Loret, B., and Nemat – Nasser, S. 1992. A constitutive model for granular materials based on micromechanics. Advances in micromechanics of granular material, Elsevier.
- Mitchell, J.K. 1993. Fundamentals of soil behaviour, 2nd ed., New York, John Wiley & Sons, Inc.
- Momozu, M., Oida, A., and Nakashima, H. 2001. Simulation of shear box test by the distinct element method, Proc. 6th Asian – Pasific con. of ISTVS, Bangkok Thailand.
- Momozu, M., Oida, A., and Koolen, A.J. 2000. Analysis of soil cutting process by the distinct element method, Proceedings of the international agricultural engineering conference, Bangkok, Thailand.
- Momozu, M., Oida, A., and Tanaka, H. 1995. Construction of model of mechanical soil behaviour by means of distinct element method, Landmaschinen, TU Munchen.
- Momozu, M., Oida, A., and Yamazaki, M. 1997. Simulation of interaction between soil and rotary blade by modified distinct element method, Pro. 7th European Conf. ISTVS, pp 572-579.
- Morgan, J.K., and Boettcher, M.S. 1999. Numerical simulations of granular shear zones using the distinct element method, Journal of Geophysical Research, Vol. 104, pp 2703-2719.
- Morgan, J.K. 1999. Numerical simulations of granular shear zones using the distinct element method, Journal of Geophysical Research, Vol. 104, pp 2721-2732.

- Morrow, C.A., and Byerlee, J. 1989. Experimental studies of compaction and dilatancy during frictional sliding on faults containing gouge, *Journal of structural geology*, 11 pp. 815-825.
- Norwegian Geotechnical Society. 1967. Proceedings of the geotechnical conference on shear strength, properties of natural soils and rocks, Aas and Wahls Boktrykkeri, Oslo, Norway.
- Oda, M., and Konishi, J. 1974. Microscopic deformation mechanism of granular material in simple shear, *Soils and Foundations*, Vol 14, No. 4 , pp 25 – 38.
- Oda, M., Iwashita, K., and Kakiuchi, T. 1997. Importance of particle rotation in the mechanics of granular materials, *Powder and Grains*, Balkema, Rotterdam The Netherlands.
- Oida, A., Schwanghart, H., and Ohkubo, S. 1999. Effect of tyre lug cross section on tyre performance simulated by distinct element method, Pro. 13th inter. con. of ISTVS, Munich, Germany.
- Oida, A., Schwanghart, H., Ohkubo, S., and Yamazaki, M. 1998. Simulation of soil deformation and reaction under a track shoe by distinct element method, Symposium, actual tasks on agricultural engineering, Opatija, Croatia
- Oida, A., Tanaka, H., and Momotsu, M. 1995. Construction of model of mechanical behaviour by Distinct Element Method, Division of Environmental Science and Technology, Graduate School of Agriculture, Kyoto Univ. Kyoto, Japan
- Oida, A., Satohh, A., Itoh, H., and Triratanasirichai, T. 1991. Three dimensional stress distribution on a tire – sand contact surface, *Journal of Terramechanics*, 28 (4) pp 319 – 330.
- Olsen, H.J. 1999. Measuring of shear properties on large soil samples, sc-dlo, Wageningen, The Netherlands.
- Oner, M. 1984. Analysis of fabric changes during cyclic loading of granular soils, Pro. 8th World Con. Earthquake Eng. Sanfrancisco, California 3, 55-62.
- Othman, S. 1999. Tire-soil interaction modelling in DADS environment, national advanced driving simulator and simulation centre, the University of Iowa.
- Plaxis, B.V. 2000. The dynamic module of the finite element method, Version 7.2.
- Plaxis, B.V. 1998. The Finite Element Code for soil and rock analysis, version 7.
- Plaxis, B.V. 1994. Finite element method material models manual, version 5.
- Prasher, C. L. 1987. Crushing and grinding process handbook, John Wiley & Sons.
- Poodt, M.P. 1999. Soil stresses caused by agricultural tyres during sugar beets harvesting, MSc. thesis, Wag. Agr. Univ. Wageningen, The Netherlands, In Dutch.

- Prager, W. 1959. Introduction to plasticity, Addison-Wesley, Reading MA, USA
- Revut, I.B., and Rode, A.A. 1981. Experimental methods of studying soil structure, New Delhi, Amerind Publishing CO. Pvt. Ltd.
- Ritchie, M.D., and Kernighan, W.B. 1978. The C programming language, Bell laboratories, Murray Hill, New Jersey, Prentice – Hall , Inc.
- Roberts, J. 1996. Understanding soil mechanics, Delmar Publisher.
- Sakaguchi, E., Kawakami, S., and Tobita, F. 1994. Simulation of flowing phenomena of grains by distinct element method, Journal of Agricultural Engineering Research, Milano, Italy.
- Sakaguchi, H., Ozaki, E. and Igarashi, T. 1993. Plugging the flow of granular materials during the discharge from a silo, International Journ. modern physics, B(7), 1949-1963.
- Sammis, C.G., Osborne, R.H., Anderson, J.L., Banerdt, M., and White, P. 1986. Self-similar cataclasis in the formation of gouge, pure applied geophysics 124, 53-78.
- Sammis, C.G., and Biegel, R. 1987. The kinematics of gouge deformation, pure applied geophysics, 125, 777-812.
- Sanglerat, G., Olivar, G., and Cambou, B. 1984. Practical problems in soil mechanics and foundation engineering, 1. Developments in geotechnical engineering 34A. Physical characteristics of soils, plasticity, settlement calculations, interpretation of in situ tests. Amsterdam, The Netherlands, Elsevier science publishers B.V.
- Schjonning, P. 1999. Mechanical properties of Danish soils. A review of existing knowledge with special emphasis on soil spatial variability. "Experience with the impact of subsoil compaction on soil, crop growth & environment and ways to prevent subsoil compaction" Wageningen, The Netherlands.
- Schofield, W. 1968. Critical state soil mechanics, McGRAW-HILL, London.
- Schwanghart, H., Oida, A., Ohkubo, S., and Yamazaki, M. 1998. Simulation of soil deformation and reaction under a track shoe by distinct element method, Symposium Actual Task on Agricultural Engineering, Opatija, Croatia.
- Scott, D.R. 1996. Seismicity and stress rotation in granular model of the brittle crust, Nature 381 pp 592 –595.
- Serrano, A.A., and Rodriguez – Ortiz, J.M. 1973. A contribution to the mechanics of heterogeneous granular media, Pro. Symp. Plasticity and Soil Mechanics, Cambridge, UK.
- Sharma, V.M., Saxena, K.R., and Woods, R.D. 1999. Distinct element modelling in geomechanics, Balkema, Rotterdam, The Netherlands.

- Shen, J., and Kushwaha, R.L. 1998. Soil-machine interactions, a finite element perspectives, Marcel Dekker Inc, New York, USA.
- Sluys, L.J. 1992. Wave propagation localisation and dispersion in softening solids, dissertation, Delft University of Technology.
- Smith, I.M., and Griffith, D.V. 1982. Programming the finite element method, second edition John Wisley & Sons UK.
- Smith, I.M. 1982. Programming the finite element method with applications to geo-mechanics, John Wiley & Sons.
- Soane, B.D., and Van Ouwerkerk, C. 1994. Soil compaction in crop production, Elsevier, Amsterdam, The Netherlands.
- Sohne, W.H. 1958. Fundamentals of pressure distribution and soil compaction under tractor tyres, Agricultural engineering 39 (5) pp 276 – 281.
- Sohne, W.H. 1953. Pressure distribution in the soil and soil deformation under tractor tyres, Grundlagen landtechnik 5 , pp 49 – 63.
- Sullivan, M.F., and Robertson, J.K., and Henshall, J.K. 1999. Shear effects on gas transport in soil, Soil Tillage Research, Vol. 50, pp 73-83.
- Tadesse, D. 2000. Plaxis calculations of soil stresses under tyre-soil system with Mohr-Coulomb and Cam-Clay type soil models, technical report, Wageningen University, The Netherlands.
- Tadesse, D. 1999. Distinct Element Method results, high speed video camera images and crack propagation films of modified single rotary tine, MSc thesis, Wageningen Univ. Wageningen, The Netherlands.
- Tanaka, H., Momozu, M., Oida, A., and Yamazaki, M. 2000. Simulation of soil deformation and resistance at bar penetration by the distinct element method, Journal of Terramechanics 37, pp 41 – 56.
- Tarumi, Y., and Hakuno, M. 1988. A granular assembly simulations for the seismic liquefaction of sand, Proc. Japan Soc. Civil. Eng. Vol. 398, pp 129-138.
- Terzaghi, K., Ralph, B.P., and Gholamreza, M. 1996. Soil mechanics in engineering practice, 3rd ed., New York, John Wiley & Sons, Inc.
- Thornton, C. 1993. Powders and grains 93, Proc. 2nd intern. conf. on powder and grains, Balkema, Rotterdam.
- Tijink, F.G.J. 1988. Load-bearing processes in agricultural wheel-soil systems, PhD Thesis, Wageningen University, The Netherlands.
- Tijsskens, E., Ramon, H., and Baerdemaeker, de J. 2003. Discrete element modelling for process simulation in agriculture, Journal of sound and vibration 266, pp 493 – 514.

- Timoshenko, S.P., and Goodier, J.N. 1984. Theory of elasticity, third edition, McGraw-Hill Int.
- Ting, J.M., Corkum, B.T. 1988 a. Strength behaviour of granular materials using discrete numerical modelling, Proc. 6th Int. Conf. Numerical methods in Geomechanics.
- Ting, J.M., Corkum, B.T., Kauffman, C.R., and Greco, C. 1989. Discrete numerical model for soil mechanics, Journal of Geotechnical Engineering, Vol. 115, ASCE.
- Uemura, D., and Hakuno, M. 1987. Granular assembly simulation for ground collapse, Bulletin of the Earthquake Research Institute, Univ. Tokyo 62 pp 19-59.
- Uemura, D., and Hakuno, M. 1988. Granular assembly simulation with Cundall's model for the dynamic collapse of the foundation of a structure, Proc. Japan Soc. Civil Eng. pp 155-164.
- Umekage, T., Shinkai, T., Yuu, S., and Abe, T. 1998. Numerical simulation for blockage of cohesive particles in a hopper using the distinct element method and its correlation with experimental results of real cohesive granular materials, Advanced Powder Technology, Vol. 9, No. 4 pp 331-344.
- Van den Akker, J.J.H., Arvidsson, J., and Horn, R. 1999. Experiences with impact and prevention of subsoil compaction in the European community, sc-dlo, Wageningen, The Netherlands.
- Van den Berg, P. 1994. Analysis of soil penetration, PhD, thesis, Delft University Press, The Netherlands.
- Vermeer, P.A., and Borst, R. 1984. Non associated plasticity for soils concrete and rock, Heron, Volume 29, No. 3, Delft University of Technology, The Netherlands.
- Wakabayashi, T. 1957. Photo-elastic method for determination of stress in powdered mass, Process. 7th Japan National Congr. Appl. Mech.. 153- 192.
- Weisstein, E.W. 1999. CRS Concise Encyclopaedia of Mathematics, Boca Raton, CRS Press LLC.
- Whitlow, R. 1995. Basic soil mechanics, 3rd ed., Burnt Mill Harlow, Long man Scientific and Technical.
- Wiermann, C., Way, T.R., Horn, R., Bailey, A.C., and Burt, E.C. 1999. Effect of various dynamic loads on stress and strain behaviour of Norfolk sandy loam, Elsevier Science B.V.
- Williams, J.R., and O'Connor, R. 1999. Discrete element simulation and the contact problem, Archives of computational methods in engineering 6 (4) pp 279 - 304
- William, R.G., and Glen, E.V.B. 1968. Soil dynamics in tillage and traction, Agricultural research service, United States Department of Agriculture, USA.

- Wu, T.H. 1971. Soil dynamics., Boston, Allyn and Bacon, Inc.
- Young, D.H., and Roger, A.F. 1996. University physics, 9th ed., Reading Massachusetts, Addison-Wesley Publishing Company, Inc.
- Yuu, S., Umekage, T., Shinkai, T., and Abe, T. 1998. Numerical simulation for blockage of cohesive particles in a hopper using the distinct element method and its correlation with experimental results of real cohesive granular materials, Journal of Advanced Powder Technology, Vol. 9, pp 331-344.
- Zienkiewicz., and Taylor. 1991. The finite element method, fourth edition, volume 2, solid and fluid mechanics, dynamics and non-linearity, McGraw-Hill (UK).
- Zienkiewicz, O.C. 1991. The finite element method, solid and fluid mechanics, dynamics and non-linearity, Volume 2, 4th edition, McGraw-Hill, London.

SAMENVATTING

Hoewel de structuur en de mechanische eigenschappen van de bodem veel onderzocht zijn voor bodem-belasting interacties, zijn deze in de landbouwgrondmechanica het minst begrepen. Zij beïnvloeden direct of indirect de gewasopbrengsten, de kwaliteit van het milieu, en de grondbewerkingseisen. Landbouwgrond is gestructureerd, heeft een zekere sterkte, en wordt vaak bewerkt met machines of verdicht door voertuigen. De structuur en sterkte van landbouwgrond beïnvloeden de groei van de plantenwortels en het bewortelingspatroon, welke direct of indirect de kwantiteit en de kwaliteit van de gewasopbrengst beïnvloeden. Bewerking en verdichting zijn processen die de bodemstructuur en –sterkte beïnvloeden. Het bodemvochtgehalte tijdens bewerking en berijding, voertuiggewichten, werktuigontwerp, rijnsnelheid en maat, type, en spanning van banden zijn daarnaast parameters welke de structuur en de mechanische eigenschappen van de bodem beïnvloeden.

Een goede bestudering van de structuur en de mechanische eigenschappen van de grond gedurende belasting – grond interactie is ongetwijfeld sterk afhankelijk van het type van methodes (modellen) die gebruikt worden om deze taak uit te voeren. De twee basismodellen welke gebruikt worden voor het berekenen van de structuur en de mechanische eigenschappen van de bodem zijn de bekende Eindige-Elementen Methode (EEM) en de Discrete-Elementen Methode (DEM) welke relatief nieuw en in ontwikkeling is.

Dit proefschrift geeft een uitgebreid overzicht van de twee modellen (EEM en DEM) ten behoeve van de analyse van de toepassing van de modellen op dynamische belastingsgevallen zoals het band – grond systeem, wigpenetratie, de test met het lineaire afschuif-apparaat, en het snijden van grond met een slagapparaat van het slinger-type. Bovendien omvat het proefschrift een evaluatie van de twee modellen door de presentatie van een aantal fundamentele kwalitatieve vergelijkingen van de simulatie-resultaten, uitmondend in het tonen van de potentiële mogelijkheden van de modellen en het bepalen van de eerste prioriteit van de modellen, gebaseerd op de overeenkomsten van de model-resultaten en de mechanische eigenschappen van reële grond bij gelijke condities van belasting – bodem interactie.

EEM simulaties

Plaxis, een van de beste voorbeelden van de eindige elementen methode (EEM), is gebruikt voor de behandeling van de grond gedurende belasting – bodem interacties, met de aanname dat de grond een continu medium is. Plaxis heeft een reeks van beperkingen ondanks zijn voordelen bij de berekening van dynamische belasting- bodem interacties welke in de landbouw processen algemeen zijn.

De basis van een goede voorspelling van bodem eigenschappen (spanningen en deformaties) tijdens belasting – bodeminteracties door het gebruiken van EEM is de keuze van het juiste constitutieve model, in samenhang met het geven van de juiste waarden aan de model parameters. Echter, naast alle tekortkomingen van EEM, blijft de bepaling van de juiste model parameters en hun waarden een uitdaging. De beschikbare modellen in Plaxis kunnen globaal ingedeeld worden in eerste-orde (het lineair-elastische model en het Mohr-Coulomb model) en hogere-orde modellen (Cam-Clay modeltype en het versterking grondmodel).

Het eerste orde model (in dit proefschrift het Mohr-Coulomb model) is gekarakteriseerd door een eenvoudig verband tussen spannings-incrementen en vervormings-incrementen met slechts enkele model parameters.

De parameters elasticiteitsmodulus, de dwarscontractie – coëfficiënt, dilatatiehoek, cohesie en hoek van inwendige wrijving zijn de basis parameters voor het Mohr-Coulomb model.

Het meten van deze model parameters is geen eenvoudige opgave. Bovendien zijn waardes voor deze parameters nauwelijks beschikbaar, in het bijzonder voor landbouwgrond. Daarom zijn waardes voor deze parameters gekozen op basis

van verschillende aannames, zoals uitgelegd in dit proefschrift. De bodem welke met het Mohr-Coulomb model bestudeerd wordt is “Wageningen” matig zware klei. Van de andere kant heeft het hogere orde model (in dit proefschrift het Cam-klei type) een meer complexe formulering, gebaseerd op plastische versterking, met meer parameters. De parameters cohesie, hoek van inwendige wrijving, dilatatiehoek, voorverdichtingsdruk, terugveringsindex en samendrukkingsindex zijn de basis parameters voor het model van het Cam-klei type. Dezelfde uitleg, gegeven bij het Mohr-Coulomb model, geldt voor het Cam-klei type waar het de bepaling en beschikbaarheid van parameter waardes betreft. De bodem welke gebruikt is bij het model van Cam-klei type is sterk zandige klei.

In het algemeen zijn de verschillen tussen EEM berekeningsresultaten en “waar” gedrag vooral veroorzaakt door onnauwkeurigheden bij het meten van de waardes van de bodem parameters, wat een hoofdprobleem is van de EEM berekening zoals hierboven omschreven.

DEM simulaties

De discrete elementen methode (DEM) is een van de beste hulpmiddelen die gebruikt zijn voor de behandeling van grond gedurende belasting – bodem interacties, dit door de aanname dat grond een discontinu (discreet) medium is. Dit is het fundamentele verschil tussen DEM en EEM: de veronderstelling dat het medium een samenstelling is van discrete delen met de mogelijkheid van cyclisch contact en verdwijnen van contact door herhaald berekenen van de contact-condities gedurende het verloop van de simulatie.

DEM heeft het potentiële vermogen om het werkelijke grondmedium weer te geven vanaf de aanvang van het proces. Zoals bij EEM gebruikten veel onderzoekers DEM voor de behandeling van korrelvormige materialen, gebaseerd op hun specifieke interesse gebieden. Slechts weinigen waren echter werkzaam in de landbouwtechniek. In vergelijking met EEM is DEM een zeer recent model, welke nog steeds veel verbetering behoeft ten einde zijn toepasbaarheid te verbeteren, ondanks de vele verbeteringen die al tot dusver bereikt zijn.

Ofschoon DEM een groot potentieel heeft om het werkelijke grondmedium weer te geven, heeft het ook beperkingen en is het niet onder alle omstandigheden toepasbaar. Veel onderzoek vragen nog: het bepalen van de optimale initiële rangschikking van de deeltjes, wat de initiële bodemstructuur bepaalt; het verkrijgen van het juiste contactmodel; het bepalen van de juiste modelparameters.

De initiële deeltjes rangschikking, het modelleren van het mechanische contact, en de bepaling van de juiste model parameters met hun juiste waardes zijn de hoofd-aspecten waarvan de modelresultaten afhangen. Al deze aspecten zijn nog in onderzoek. In het bijzonder het vinden van een methode voor voor het bepalen van de juiste model parameters met een schatting van hun waardes vormt een grote uitdaging. In dit proefschrift bleken normale veerconstante, tangenteel veerconstante, adhesie coëfficiënt, wrijvingscoëfficiënt tussen deeltjes en deeltjesgrootte de parameters te zijn welke de grootste invloed hebben op de DEM resultaten.

Conclusie

Ondanks alle beperkingen van het DEM model zijn de DEM simulatieresultaten die in dit proefschrift gepresenteerd zijn in goede kwalitatieve overeenstemming met de EEM simulatie resultaten of analoge resultaten van laboratorium experimenten met reële grond onder dezelfde condities van belasting – bodem interactie. Daarom is het niet onjuist om te concluderen dat DEM een grote prioriteit en potentie heeft waar het gaat om de simulatie van de structuur van de bodem en het bestuderen van de mechanische eigenschappen van de grond gedurende dynamische belasting – grond interactie.

CURRICULUM VITAE

Dawit Tadesse was born 2 January 1971 in Addis Ababa, Ethiopia. He had accomplished his ESLCE (Ethiopian School Leaving Certificate Examination) in 1989 with Distinction and in the same year he joined Addis Ababa University. In 1994, he graduated with B.Sc. degree in major Applied Physics and minor Computer and Mathematics from Addis Ababa University. In 1992, he had been a prize winner in the Mathematics Department of the University for successfully solving one of the prize questions and a certificate is awarded for the honour. He obtained his M.Sc. degree with Distinction in Agricultural Engineering with specialising Soil Technology from the Wageningen University in 1999.

From January 1999 onwards he has been posted to the Soil Technology group of Wageningen University as research assistance in Kyoto – Wageningen project for his Ph.D study.

He is a member of the following professional organisations: ASAE (American Society of Agricultural Engineers) and ISTRO (International Soil Tillage and Research Organisation)

Het onderzoek is uitgevoerd met een voltooid Training en Opleiding Plan bij de onderzoekschool
Production Ecology and Resource Conservation

